



AIR-TO-AIR MISSILE  
VECTOR SCORING

THESIS

Nicholas Sweeney, Major, USAF

AFIT/GE/ENG/12-38

DEPARTMENT OF THE AIR FORCE  
AIR UNIVERSITY

**AIR FORCE INSTITUTE OF TECHNOLOGY**

Wright-Patterson Air Force Base, Ohio

APPROVED FOR PUBLIC RELEASE; DISTRIBUTION UNLIMITED.

The views expressed in this thesis are those of the author and do not reflect the official policy or position of the United States Air Force, Department of Defense, or the United States Government.

This material is declared a work of the U.S. Government and is not subject to copyright protection in the United States.

AFIT/GE/ENG/12-38

AIR-TO-AIR MISSILE  
VECTOR SCORING

THESIS

Presented to the Faculty  
Department of Electrical and Computer Engineering  
Graduate School of Engineering and Management  
Air Force Institute of Technology  
Air University  
Air Education and Training Command  
In Partial Fulfillment of the Requirements for the  
Degree of Master of Science in Electrical Engineering

Nicholas Sweeney, B.S.E.E.

Major, USAF

March 2012

APPROVED FOR PUBLIC RELEASE; DISTRIBUTION UNLIMITED.

AIR-TO-AIR MISSILE  
VECTOR SCORING

Nicholas Sweeney, B.S.E.E.  
Major, USAF

Approved:

---

Maj Kenneth A. Fisher, PhD (Chairman)

---

date

---

Dr. Meir Pachter (Member)

---

date

---

Lt Col Michael J. Stepaniak, PhD  
(Member)

---

date

*Abstract*

An air-to-air missile vector scoring system is proposed for test and evaluation applications. Three different linear missile dynamics models are considered: a six-state constant velocity model and nine-state constant acceleration and three-dimensional coordinated turn models. All dynamics models include missile position and velocity in a Cartesian coordinate system, while the nine-state models also include acceleration. Frequency modulated continuous wave radar sensors, carefully located to provide spherical coverage around the target, provide updates of missile kinematic information relative to a drone aircraft. Data from the radar sensors is fused with predictions from one of the three missile models using either an extended Kalman filter, an unscented Kalman filter or a particle filter algorithm.

The performance of all nine model/filter combinations are evaluated through high-fidelity, six-degree of freedom simulations yielding sub-meter end-game accuracy in a variety of scenarios. Simulations demonstrate the superior performance of the unscented Kalman filter incorporating the continuous velocity dynamics model. The scoring system is experimentally demonstrated through flight testing using commercial off the shelf radar sensors with a Beechcraft C-12 as a surrogate missile.

## *Acknowledgements*

Numerous exceptional individuals have contributed to the successful completion of this research. First and foremost, I'd like to thank my family for their patience through some late nights and encouragement during successes and failures. Next, I'd like to thank my advisor, Ken Fisher, for his mentorship in guiding this research and promoting excellence. Additionally, the outstanding instruction of the professors in the Department of Electrical Engineering was indispensable to accomplishing this research. Their aptitude for teaching made the most complex concepts simple. Also, the ANT Center staff provided phenomenal support for this project. I'd like to offer a special thanks to Jared Kresge whose technical expertise was instrumental in adapting automotive sensors for a new function. Finally, many talented individuals deserve acknowledgment for their contributions to successful flight testing. Without the hard work and incredible troubleshooting skills of the highly dedicated members of the Have Splash test management team and support personnel, testing on the proposed missile scoring system would not have been possible.

Nicholas Sweeney

## *Table of Contents*

	Page
Abstract . . . . .	iv
Acknowledgements . . . . .	v
List of Figures . . . . .	ix
List of Tables . . . . .	xix
List of Abbreviations . . . . .	xxii
I. Introduction . . . . .	1
1.1 Motivation and Problem Description . . . . .	1
1.2 Assumptions . . . . .	1
1.3 Problem Approaches . . . . .	2
1.3.1 Global Positioning System . . . . .	2
1.3.2 Radar Sensors . . . . .	3
1.3.3 Laser Optics . . . . .	3
1.3.4 Infrared Sensors . . . . .	3
1.4 Research Contributions . . . . .	4
1.5 Thesis Outline . . . . .	5
II. Background . . . . .	6
2.1 Mathematical Notation . . . . .	6
2.2 Reference Frames . . . . .	7
2.3 Coordinate Transformations . . . . .	9
2.4 Kalman Filter . . . . .	11
2.4.1 Extended Kalman Filter . . . . .	14
2.4.2 Unscented Kalman Filter . . . . .	16
2.4.3 Particle Filter . . . . .	19
2.5 Radar Sensor . . . . .	22
2.6 Multilateration . . . . .	24
2.7 Velocity Vector Calculation from Speed Measurements . . . . .	27
2.8 Gating and Data Association . . . . .	28
2.9 Past Research . . . . .	30
2.9.1 Missile Tracking . . . . .	31
2.9.2 Related Estimation Problems . . . . .	34
2.10 Summary . . . . .	37

	Page
III. Methodology . . . . .	38
3.1 Aircraft Sensor Configuration . . . . .	38
3.2 System Model . . . . .	40
3.2.1 Missile Dynamics Models . . . . .	40
3.2.2 Observation Model . . . . .	45
3.3 Gating and Data Association Implementation . . . . .	46
3.4 Target Initialization . . . . .	46
3.5 Nonlinear Kalman Filter Implementation . . . . .	47
3.5.1 Extended Kalman Filter . . . . .	48
3.5.2 Unscented Kalman Filter . . . . .	50
3.5.3 Particle Filter . . . . .	51
3.6 Summary . . . . .	55
IV. Simulations . . . . .	56
4.1 Scenarios . . . . .	57
4.2 Truth Model . . . . .	59
4.3 Filter Tuning . . . . .	60
4.4 Noise Generation . . . . .	62
4.5 Dynamics Model Comparison . . . . .	65
4.6 Filter Comparison . . . . .	67
4.7 Missile Scoring Performance . . . . .	68
4.8 Summary . . . . .	73
V. Flight Test . . . . .	74
5.1 Scoring System Description . . . . .	74
5.2 Surrogate Missile . . . . .	78
5.3 Truth Data . . . . .	79
5.4 Test Execution . . . . .	80
5.5 Error Calculations . . . . .	82
5.6 Bias Reduction . . . . .	85
5.7 Sensor Maximum Range . . . . .	86
5.8 Flight Test Predictions . . . . .	86
5.9 C-12 Position Estimate Error . . . . .	87
5.10 C-12 Velocity Estimate Error . . . . .	97
5.11 Summary . . . . .	102
VI. Conclusions and Recommendations . . . . .	104
6.1 Summary of Results . . . . .	104
6.2 Future Work . . . . .	106
6.3 Summary . . . . .	109

	Page
Appendix A. Simulation Results . . . . .	110
A.1 Extended Kalman Filter Simulations . . . . .	110
A.2 Unscented Kalman Filter Simulations . . . . .	122
A.3 Particle Filter Simulations . . . . .	134
Appendix B. Flight Test Results . . . . .	146
B.1 Sensor Geometry: 90° Aspect Angle . . . . .	146
B.2 Sensor Geometry: 45° Aspect Angle . . . . .	161
B.3 Sensor Geometry: 20° Aspect Angle . . . . .	176
B.4 Sensor Geometry: 70° Aspect Angle . . . . .	180
Appendix C. Matlab Code . . . . .	181
C.1 Description of Software Programs . . . . .	181
C.2 Simulation Main Programs . . . . .	182
C.3 Simulation Subprograms . . . . .	211
Bibliography . . . . .	221

## *List of Figures*

Figure		Page
2.1.	Earth-Fixed Reference Frames [41] . . . . .	7
2.2.	Earth-Fixed Navigation Reference Frame [41] . . . . .	8
2.3.	Aircraft Body Reference Frame [41] . . . . .	9
2.4.	Linear Frequency Modulation in an FMCW Radar Sensor . . .	23
2.5.	FMCW Sensor Employing Varying Chirp Gradient to Resolve Range-Velocity Ambiguity . . . . .	24
2.6.	2D Trilateration [14] . . . . .	25
2.7.	Impact of Sensor Geometry on Precision of Position Calculation [24] . . . . .	26
2.8.	Calculation of 2D Velocity from Speed Measurements [26] . . . .	27
2.9.	Comparison of Errors using Three Different Estimation Tech- niques for 2D Robot Navigation [21] . . . . .	35
2.10.	Procedure for a Robust Kalman Filter [40] . . . . .	36
3.1.	Sampling-Importance Resampling Procedure . . . . .	54
4.1.	Scenario 1: Target Aircraft Non-maneuvering . . . . .	57
4.2.	Scenario 2: Target Aircraft Performing a 9G Descending Break- Turn . . . . .	58
4.3.	Scenario 3: Target Aircraft Performing a Vertical Climb . . . . .	58
4.4.	Statistical Properties of Random Sensor Noise Realization Uti- lized for all Scenario 1 Simulations . . . . .	63
4.5.	Statistical Properties of Random Missile Initialization Noise Uti- lized for all Scenarios . . . . .	64
4.6.	Unscented Kalman Filter Performance in Air-to-Air Missile Scor- ing Application with Continuous Velocity Dynamics Model (Tar- get Aircraft Non-maneuvering) . . . . .	69
4.7.	Unscented Kalman Filter Performance in Air-to-Air Missile Scor- ing Application with Continuous Velocity Dynamics Model (Tar- get Aircraft Executing a Defensive Break Turn) . . . . .	71

Figure		Page
4.8.	Unscented Kalman Filter Performance in Air-to-Air Missile Scoring Application with Continuous Velocity Dynamics Model (Target Aircraft Executing a Vertical Climb) . . . . .	72
5.1.	Sensor Platform Configuration (Simulates Installation Geometry on an F-16 Drone) . . . . .	75
5.2.	Actual Sensor Platforms Used in Testing . . . . .	75
5.3.	Sensor Mounting Brackets . . . . .	76
5.4.	Sensor Electrical Wiring Setup . . . . .	77
5.5.	Beechcraft C-12C (Surrogate Missile) . . . . .	78
5.6.	Surveyed Sensor Locations . . . . .	79
5.7.	C-12 Performing Low-Altitude Flyby Over Sensor Array . . . . .	80
5.8.	Tower Flyby Line at Edwards AFB, CA . . . . .	81
5.9.	Data Flow for Flight Test Error Analysis . . . . .	83
5.10.	Radar Sensor Measurement Bias Caused by Aircraft Size and GLite Location . . . . .	85
5.11.	Comparison of Flight Test Results and Simulation Predictions for Average Root Sum Square Error in Unscented Kalman Filter Estimates of C-12 Position (90° Drone Aspect Angle) . . . . .	89
5.12.	Illustration of False Target Impact on Errors in Unscented Kalman Filter Position Estimates (Data from Run 11 at 90° Drone Aspect Angle) . . . . .	90
5.13.	Illustration of False Target Speed Measurements (Data from Run 11 at 90° Drone Aspect Angle) . . . . .	91
5.14.	Comparison of Flight Test Results and Simulation Predictions for Average Root Sum Square Error in Unscented Kalman Filter Estimates of C-12 Position (45° Drone Aspect Angle) . . . . .	93
5.15.	Illustration of Increase in Sensor Measurement Noise as C-12 Approaches Sensor Overflight (Data from Run 1 at 45° Drone Aspect Angle) . . . . .	94
5.16.	Comparison of Flight Test Results and Simulation Predictions for Average Root Sum Square Error in Unscented Kalman Filter Estimates of C-12 Position (20° Drone Aspect Angle) . . . . .	96

Figure		Page
5.17.	Comparison of Flight Test Results and Simulation Predictions for Average Root Sum Square Error in Unscented Kalman Filter Estimates of C-12 Position (70° Drone Aspect Angle) . . . . .	97
5.18.	Comparison of Flight Test Results and Simulation Predictions for Average Root Sum Square Error in Unscented Kalman Filter Estimates of C-12 Velocity (90° Drone Aspect Angle) . . . . .	98
5.19.	Comparison of Flight Test Results and Simulation Predictions for Average Root Sum Square Error in Unscented Kalman Filter Estimates of C-12 Velocity (45° Drone Aspect Angle) . . . . .	100
5.20.	Comparison of Flight Test Results and Simulation Predictions for Average Root Sum Square Error in Unscented Kalman Filter Estimates of C-12 Velocity (20° Drone Aspect Angle) . . . . .	101
5.21.	Comparison of Flight Test Results and Simulation Predictions for Average Root Sum Square Error in Unscented Kalman Filter Estimates of C-12 Velocity (70° Drone Aspect Angle) . . . . .	102
A.1.	Extended Kalman Filter Performance in Air-to-Air Missile Scoring Application with Continuous Velocity Dynamics Model (Target Aircraft Non-maneuvering) . . . . .	110
A.2.	Extended Kalman Filter Performance in Air-to-Air Missile Scoring Application with Continuous Acceleration Dynamics Model (Target Aircraft Non-maneuvering) . . . . .	111
A.3.	Extended Kalman Filter Performance in Air-to-Air Missile Scoring Application with 3D Coordinated Turn Dynamics Model (Target Aircraft Non-maneuvering) . . . . .	112
A.4.	Extended Kalman Filter Performance in Air-to-Air Missile Scoring Application with Continuous Velocity Dynamics Model (Target Aircraft Executing a Defensive Break Turn) . . . . .	114
A.5.	Extended Kalman Filter Performance in Air-to-Air Missile Scoring Application with Continuous Acceleration Dynamics Model (Target Aircraft Executing a Defensive Break Turn) . . . . .	115
A.6.	Extended Kalman Filter Performance in Air-to-Air Missile Scoring Application with 3D Coordinated Turn Dynamics Model (Target Aircraft Executing a Defensive Break Turn) . . . . .	116

Figure		Page
A.7.	Extended Kalman Filter Performance in Air-to-Air Missile Scoring Application with Continuous Velocity Dynamics Model (Target Aircraft Executing a Vertical Climb) . . . . .	118
A.8.	Extended Kalman Filter Performance in Air-to-Air Missile Scoring Application with Continuous Acceleration Dynamics Model (Target Aircraft Executing a Vertical Climb) . . . . .	119
A.9.	Extended Kalman Filter Performance in Air-to-Air Missile Scoring Application with 3D Coordinated Turn Dynamics Model (Target Aircraft Executing a Vertical Climb) . . . . .	120
A.10.	Unscented Kalman Filter Performance in Air-to-Air Missile Scoring Application with Continuous Velocity Dynamics Model (Target Aircraft Non-maneuvering) . . . . .	122
A.11.	Unscented Kalman Filter Performance in Air-to-Air Missile Scoring Application with Continuous Acceleration Dynamics Model (Target Aircraft Non-maneuvering) . . . . .	123
A.12.	Unscented Kalman Filter Performance in Air-to-Air Missile Scoring Application with 3D Coordinated Turn Dynamics Model (Target Aircraft Non-maneuvering) . . . . .	124
A.13.	Unscented Kalman Filter Performance in Air-to-Air Missile Scoring Application with Continuous Velocity Dynamics Model (Target Aircraft Executing a Defensive Break Turn) . . . . .	126
A.14.	Unscented Kalman Filter Performance in Air-to-Air Missile Scoring Application with Continuous Acceleration Dynamics Model (Target Aircraft Executing a Defensive Break Turn) . . . . .	127
A.15.	Unscented Kalman Filter Performance in Air-to-Air Missile Scoring Application with 3D Coordinated Turn Dynamics Model (Target Aircraft Executing a Defensive Break Turn) . . . . .	128
A.16.	Unscented Kalman Filter Performance in Air-to-Air Missile Scoring Application with Continuous Velocity Dynamics Model (Target Aircraft Executing a Vertical Climb) . . . . .	130
A.17.	Unscented Kalman Filter Performance in Air-to-Air Missile Scoring Application with Continuous Acceleration Dynamics Model (Target Aircraft Executing a Vertical Climb) . . . . .	131

Figure		Page
A.18.	Unscented Kalman Filter Performance in Air-to-Air Missile Scoring Application with 3D Coordinated Turn Dynamics Model (Target Aircraft Executing a Vertical Climb) . . . . .	132
A.19.	Particle Filter Performance in Air-to-Air Missile Scoring Application with Continuous Velocity Dynamics Model (Target Aircraft Non-maneuvering) . . . . .	134
A.20.	Particle Filter Performance in Air-to-Air Missile Scoring Application with Continuous Acceleration Dynamics Model (Target Aircraft Non-maneuvering) . . . . .	135
A.21.	Particle Filter Performance in Air-to-Air Missile Scoring Application with 3D Coordinated Turn Dynamics Model (Target Aircraft Non-maneuvering) . . . . .	136
A.22.	Particle Filter Performance in Air-to-Air Missile Scoring Application with Continuous Velocity Dynamics Model (Target Aircraft Executing a Defensive Break Turn) . . . . .	138
A.23.	Particle Filter Performance in Air-to-Air Missile Scoring Application with Continuous Acceleration Dynamics Model (Target Aircraft Executing a Defensive Break Turn) . . . . .	139
A.24.	Particle Filter Performance in Air-to-Air Missile Scoring Application with 3D Coordinated Turn Dynamics Model (Target Aircraft Executing a Defensive Break Turn) . . . . .	140
A.25.	Particle Filter Performance in Air-to-Air Missile Scoring Application with Continuous Velocity Dynamics Model (Target Aircraft Executing a Vertical Climb) . . . . .	142
A.26.	Particle Filter Performance in Air-to-Air Missile Scoring Application with Continuous Acceleration Dynamics Model (Target Aircraft Executing a Vertical Climb) . . . . .	143
A.27.	Particle Filter Performance in Air-to-Air Missile Scoring Application with 3D Coordinated Turn Dynamics Model (Target Aircraft Executing a Vertical Climb) . . . . .	144

Figure		Page
B.1.	Air-to-Air Missile Scoring System Performance in Scoring C-12 Surrogate Missile using an Unscented Kalman Filter with Con- tinuous Dynamics Velocity Model (90° Drone Aspect Angle / Run 1) . . . . .	146
B.2.	Air-to-Air Missile Scoring System Performance in Scoring C-12 Surrogate Missile using an Unscented Kalman Filter with Con- tinuous Dynamics Velocity Model (90° Drone Aspect Angle / Run 2) . . . . .	147
B.3.	Air-to-Air Missile Scoring System Performance in Scoring C-12 Surrogate Missile using an Unscented Kalman Filter with Con- tinuous Dynamics Velocity Model (90° Drone Aspect Angle / Run 3) . . . . .	148
B.4.	Air-to-Air Missile Scoring System Performance in Scoring C-12 Surrogate Missile using an Unscented Kalman Filter with Con- tinuous Dynamics Velocity Model (90° Drone Aspect Angle / Run 4) . . . . .	149
B.5.	Air-to-Air Missile Scoring System Performance in Scoring C-12 Surrogate Missile using an Unscented Kalman Filter with Con- tinuous Dynamics Velocity Model (90° Drone Aspect Angle / Run 5) . . . . .	150
B.6.	Air-to-Air Missile Scoring System Performance in Scoring C-12 Surrogate Missile using an Unscented Kalman Filter with Con- tinuous Dynamics Velocity Model (90° Drone Aspect Angle / Run 6) . . . . .	151
B.7.	Air-to-Air Missile Scoring System Performance in Scoring C-12 Surrogate Missile using an Unscented Kalman Filter with Con- tinuous Dynamics Velocity Model (90° Drone Aspect Angle / Run 7) . . . . .	152
B.8.	Air-to-Air Missile Scoring System Performance in Scoring C-12 Surrogate Missile using an Unscented Kalman Filter with Con- tinuous Dynamics Velocity Model (90° Drone Aspect Angle / Run 8) . . . . .	153

Figure		Page
B.9.	Air-to-Air Missile Scoring System Performance in Scoring C-12 Surrogate Missile using an Unscented Kalman Filter with Con- tinuous Dynamics Velocity Model (90° Drone Aspect Angle / Run 9) . . . . .	154
B.10.	Air-to-Air Missile Scoring System Performance in Scoring C-12 Surrogate Missile using an Unscented Kalman Filter with Con- tinuous Dynamics Velocity Model (90° Drone Aspect Angle / Run 10) . . . . .	155
B.11.	Air-to-Air Missile Scoring System Performance in Scoring C-12 Surrogate Missile using an Unscented Kalman Filter with Con- tinuous Dynamics Velocity Model (90° Drone Aspect Angle / Run 11) . . . . .	156
B.12.	Air-to-Air Missile Scoring System Performance in Scoring C-12 Surrogate Missile using an Unscented Kalman Filter with Con- tinuous Dynamics Velocity Model (90° Drone Aspect Angle / Run 12) . . . . .	157
B.13.	Air-to-Air Missile Scoring System Performance in Scoring C-12 Surrogate Missile using an Unscented Kalman Filter with Con- tinuous Dynamics Velocity Model (90° Drone Aspect Angle / Run 13) . . . . .	158
B.14.	Air-to-Air Missile Scoring System Performance in Scoring C-12 Surrogate Missile using an Unscented Kalman Filter with Con- tinuous Dynamics Velocity Model (90° Drone Aspect Angle / Run 14) . . . . .	159
B.15.	Air-to-Air Missile Scoring System Performance in Scoring C-12 Surrogate Missile using an Unscented Kalman Filter with Con- tinuous Dynamics Velocity Model (90° Drone Aspect Angle / Run 15) . . . . .	160
B.16.	Air-to-Air Missile Scoring System Performance in Scoring C-12 Surrogate Missile using an Unscented Kalman Filter with Con- tinuous Dynamics Velocity Model (45° Drone Aspect Angle / Run 1) . . . . .	161

Figure		Page
B.17.	Air-to-Air Missile Scoring System Performance in Scoring C-12 Surrogate Missile using an Unscented Kalman Filter with Con- tinuous Dynamics Velocity Model (45° Drone Aspect Angle / Run 2) . . . . .	162
B.18.	Air-to-Air Missile Scoring System Performance in Scoring C-12 Surrogate Missile using an Unscented Kalman Filter with Con- tinuous Dynamics Velocity Model (45° Drone Aspect Angle / Run 3) . . . . .	163
B.19.	Air-to-Air Missile Scoring System Performance in Scoring C-12 Surrogate Missile using an Unscented Kalman Filter with Con- tinuous Dynamics Velocity Model (45° Drone Aspect Angle / Run 4) . . . . .	164
B.20.	Air-to-Air Missile Scoring System Performance in Scoring C-12 Surrogate Missile using an Unscented Kalman Filter with Con- tinuous Dynamics Velocity Model (45° Drone Aspect Angle / Run 5) . . . . .	165
B.21.	Air-to-Air Missile Scoring System Performance in Scoring C-12 Surrogate Missile using an Unscented Kalman Filter with Con- tinuous Dynamics Velocity Model (45° Drone Aspect Angle / Run 6) . . . . .	166
B.22.	Air-to-Air Missile Scoring System Performance in Scoring C-12 Surrogate Missile using an Unscented Kalman Filter with Con- tinuous Dynamics Velocity Model (45° Drone Aspect Angle / Run 7) . . . . .	167
B.23.	Air-to-Air Missile Scoring System Performance in Scoring C-12 Surrogate Missile using an Unscented Kalman Filter with Con- tinuous Dynamics Velocity Model (45° Drone Aspect Angle / Run 8) . . . . .	168
B.24.	Air-to-Air Missile Scoring System Performance in Scoring C-12 Surrogate Missile using an Unscented Kalman Filter with Con- tinuous Dynamics Velocity Model (45° Drone Aspect Angle / Run 9) . . . . .	169

Figure		Page
B.25.	Air-to-Air Missile Scoring System Performance in Scoring C-12 Surrogate Missile using an Unscented Kalman Filter with Con- tinuous Dynamics Velocity Model (45° Drone Aspect Angle / Run 10) . . . . .	170
B.26.	Air-to-Air Missile Scoring System Performance in Scoring C-12 Surrogate Missile using an Unscented Kalman Filter with Con- tinuous Dynamics Velocity Model (45° Drone Aspect Angle / Run 11) . . . . .	171
B.27.	Air-to-Air Missile Scoring System Performance in Scoring C-12 Surrogate Missile using an Unscented Kalman Filter with Con- tinuous Dynamics Velocity Model (45° Drone Aspect Angle / Run 12) . . . . .	172
B.28.	Air-to-Air Missile Scoring System Performance in Scoring C-12 Surrogate Missile using an Unscented Kalman Filter with Con- tinuous Dynamics Velocity Model (45° Drone Aspect Angle / Run 13) . . . . .	173
B.29.	Air-to-Air Missile Scoring System Performance in Scoring C-12 Surrogate Missile using an Unscented Kalman Filter with Con- tinuous Dynamics Velocity Model (45° Drone Aspect Angle / Run 14) . . . . .	174
B.30.	Air-to-Air Missile Scoring System Performance in Scoring C-12 Surrogate Missile using an Unscented Kalman Filter with Con- tinuous Dynamics Velocity Model (45° Drone Aspect Angle / Run 15) . . . . .	175
B.31.	Air-to-Air Missile Scoring System Performance in Scoring C-12 Surrogate Missile using an Unscented Kalman Filter with Con- tinuous Dynamics Velocity Model (20° Drone Aspect Angle / Run 1) . . . . .	176
B.32.	Air-to-Air Missile Scoring System Performance in Scoring C-12 Surrogate Missile using an Unscented Kalman Filter with Con- tinuous Dynamics Velocity Model (20° Drone Aspect Angle / Run 2) . . . . .	177

Figure		Page
B.33.	Air-to-Air Missile Scoring System Performance in Scoring C-12 Surrogate Missile using an Unscented Kalman Filter with Con- tinuous Dynamics Velocity Model (20° Drone Aspect Angle / Run 3) . . . . .	178
B.34.	Air-to-Air Missile Scoring System Performance in Scoring C-12 Surrogate Missile using an Unscented Kalman Filter with Con- tinuous Dynamics Velocity Model (20° Drone Aspect Angle / Run 4) . . . . .	179
B.35.	Air-to-Air Missile Scoring System Performance in Scoring C-12 Surrogate Missile using an Unscented Kalman Filter with Con- tinuous Dynamics Velocity Model (70° Drone Aspect Angle / Run 1) . . . . .	180

## *List of Tables*

Table		Page
3.1.	Radar Sensor Locations in Aircraft Body Frame . . . . .	40
4.1.	Summary of Nonlinear Kalman Filter Tuning Parameters . . .	62
4.2.	Comparison of Missile State Estimate Error Standard Deviation at Impact for Different Dynamics Models using an Extended Kalman Filter (Scenario 2) . . . . .	65
4.3.	Comparison of Missile State Estimate Error Standard Deviation at Impact for Different Nonlinear Kalman Filters (Scenario 1)	67
4.4.	Comparison of Missile State Estimate Error Standard Deviation at Impact for Different Nonlinear Kalman Filters (Scenario 2)	67
4.5.	Comparison of Missile State Estimate Error Standard Deviation at Impact for Different Nonlinear Kalman Filters (Scenario 3)	67
4.6.	Ensemble Mean Error Statistics for Missile States at Intercept using an Unscented Kalman Filter with Continuous Velocity Dy- namics Model (Scenario 1) . . . . .	69
4.7.	Ensemble Mean Error Statistics for Missile States at Intercept using an Unscented Kalman Filter with Continuous Velocity Dy- namics Model (Scenario 2) . . . . .	71
4.8.	Ensemble Mean Error Statistics for Missile States at Intercept using an Unscented Kalman Filter with Continuous Velocity Dy- namics Model (Scenario 3) . . . . .	72
5.1.	Slant Range Bins for Error Reporting . . . . .	84
5.2.	Maximum Range of COTS Frequency Modulated Continuous Wave Radar Sensors Versus a C-12 . . . . .	86
5.3.	C-12 Position Estimate Error per Slant Range Bin using an Unscented Kalman Filter with Continuous Velocity Dynamics Model (90° Drone Aspect Angle) . . . . .	89
5.4.	C-12 Position Estimate Error per Slant Range Bin using an Un- scented Kalman Filter with Continuous Velocity Dynamics Model (45° Drone Aspect Angle) . . . . .	93

Table	Page
5.5. C-12 Position Estimate Error per Slant Range Bin using an Unscented Kalman Filter with Continuous Velocity Dynamics Model (20° Drone Aspect Angle) . . . . .	96
5.6. C-12 Velocity Estimate Error per Slant Range Bin using an Unscented Kalman Filter with Continuous Velocity Dynamics Model (90° Drone Aspect Angle) . . . . .	98
5.7. C-12 Velocity Estimate Error per Slant Range Bin using an Unscented Kalman Filter with Continuous Velocity Dynamics Model (45° Drone Aspect Angle) . . . . .	100
5.8. C-12 Velocity Estimate Error per Slant Range Bin using an Unscented Kalman Filter with Continuous Velocity Dynamics Model (20° Drone Aspect Angle) . . . . .	101
A.1. Comparison of Missile State Estimate Mean Error at Impact for Different Dynamics Models using an Extended Kalman Filter (Scenario 1) . . . . .	113
A.2. Comparison of Missile State Estimate Error Standard Deviation at Impact for Different Dynamics Models using an Extended Kalman Filter (Scenario 1) . . . . .	113
A.3. Comparison of Missile State Estimate Mean Error at Impact for Different Dynamics Models using an Extended Kalman Filter (Scenario 2) . . . . .	117
A.4. Comparison of Missile State Estimate Error Standard Deviation at Impact for Different Dynamics Models using an Extended Kalman Filter (Scenario 2) . . . . .	117
A.5. Comparison of Missile State Estimate Mean Error at Impact for Different Dynamics Models using an Extended Kalman Filter (Scenario 3) . . . . .	121
A.6. Comparison of Missile State Estimate Error Standard Deviation at Impact for Different Dynamics Models using an Extended Kalman Filter (Scenario 3) . . . . .	121
A.7. Comparison of Missile State Estimate Mean Error at Impact for Different Dynamics Models using an Unscented Kalman Filter (Scenario 1) . . . . .	125

Table	Page
A.8. Comparison of Missile State Estimate Error Standard Deviation at Impact for Different Dynamics Models using an Unscented Kalman Filter (Scenario 1) . . . . .	125
A.9. Comparison of Missile State Estimate Mean Error at Impact for Different Dynamics Models using an Unscented Kalman Filter (Scenario 2) . . . . .	129
A.10. Comparison of Missile State Estimate Error Standard Deviation at Impact for Different Dynamics Models using an Unscented Kalman Filter (Scenario 2) . . . . .	129
A.11. Comparison of Missile State Estimate Mean Error at Impact for Different Dynamics Models using an Unscented Kalman Filter (Scenario 3) . . . . .	133
A.12. Comparison of Missile State Estimate Error Standard Deviation at Impact for Different Dynamics Models using an Unscented Kalman Filter (Scenario 3) . . . . .	133
A.13. Comparison of Missile State Estimate Mean Error at Impact for Different Dynamics Models using a Particle Filter (Scenario 1)	137
A.14. Comparison of Missile State Estimate Error Standard Deviation at Impact for Different Dynamics Models using a Particle Filter (Scenario 1) . . . . .	137
A.15. Comparison of Missile State Estimate Mean Error at Impact for Different Dynamics Models using a Particle Filter (Scenario 2)	141
A.16. Comparison of Missile State Estimate Error Standard Deviation at Impact for Different Dynamics Models using a Particle Filter (Scenario 2) . . . . .	141
A.17. Comparison of Missile State Estimate Mean Error at Impact for Different Dynamics Models using a Particle Filter (Scenario 3)	145
A.18. Comparison of Missile State Estimate Error Standard Deviation at Impact for Different Dynamics Models using a Particle Filter (Scenario 3) . . . . .	145

*List of Abbreviations*

Abbreviation		Page
WSEP	weapons system evaluation program . . . . .	1
KF	Kalman filter . . . . .	2
RCS	radar cross section . . . . .	2
TOF	time of flight . . . . .	2
GPS	Global Positioning System . . . . .	2
RF	radio frequency . . . . .	2
IR	infrared . . . . .	2
3D	3-dimensional . . . . .	2
JAMI	Joint Advanced Missile Instrumentation . . . . .	2
AOA	angle-of-arrival . . . . .	3
LOS	line-of-sight . . . . .	4
pdf	probability density function . . . . .	13
EKF	Extended Kalman Filter . . . . .	14
UKF	Unscented Kalman Filter . . . . .	16
PD	pulse-doppler . . . . .	22
FMCW	frequency-modulated continuous wave . . . . .	22
CW	Continuous wave . . . . .	22
EM	Electromagnetic . . . . .	22
LFM	linear frequency modulation . . . . .	23
MAWS	missile approach warning system . . . . .	31
MEMS	micro-electro-mechnamical system . . . . .	31
IMM	interacting multiple models . . . . .	32
EIKF	extended interval Kalman filter . . . . .	33
CV	constant velocity . . . . .	33
CA	constant acceleration . . . . .	33

Abbreviation		Page
CT	three-dimensional coordinated turn . . . . .	33
FOGMA	first-order Gauss-Markov acceleration . . . . .	33
FOV	field of view . . . . .	34
2D	2-dimensional . . . . .	34
RFID	radio frequency identification . . . . .	34
RMSE	root mean square error . . . . .	35
LFM	linear frequency modulation . . . . .	35
FSK	frequency shift keying . . . . .	35
RKF	robust Kalman filter . . . . .	36
AFB	Air Force Base . . . . .	46
GRDCS	Gulf range drone control system . . . . .	46
SIR	sampling-importance resampling . . . . .	53
EPF	extended particle filter . . . . .	54
UPF	unscented particle filter . . . . .	54
WGS 84	World Geodetic System 1984 . . . . .	59
RSS	Root Sum Square . . . . .	68
ECU	electronic control unit . . . . .	74
CAN	controller-area network . . . . .	74
PCMCIA	Personal Computer Memory Card International Association	77
GAINR	GPS Aided Inertial Navigation Reference . . . . .	79
GLite	GAINR Lite . . . . .	79
IMU	inertial measurement unit . . . . .	79
AGL	above ground level . . . . .	80
KIAS	knots indicated airspeed . . . . .	81
AA	aspect angle . . . . .	82
TSPI	time space position information . . . . .	83

# AIR-TO-AIR MISSILE VECTOR SCORING

## I. Introduction

This research proposes and analyzes an approach to reconstructing the flight path of an air-to-air missile relative to a drone aircraft. The challenging task of estimating the navigation parameters of a missile has numerous applications. By accurately tracking an inbound missile, aircraft can dispense countermeasures at the critical moment and perform evasive maneuvers. Additionally, a correct estimate of a missile's flight path is critical for missile test and evaluation to insure functionality and accuracy of weapons.

### *1.1 Motivation and Problem Description*

The United States Air Force air-to-air weapons system evaluation program (WSEP) conducts more than 300 live missile fires annually, targeting unmanned drone aircraft. In order to accomplish their mission, they require a scoring system capable of estimating the trajectory of the missile relative to the drone aircraft. When a missile fails to perform as expected, this scoring system is useful in analyzing whether a missile suffered a guidance failure, decoyed on aircraft countermeasures or lacked energy or maneuverability to complete the intercept.

### *1.2 Assumptions*

This research assumes only endgame vector scoring in close proximity to the aircraft is desired. Specifically, the feasibility and accuracy of missile estimation within 350 meters of the target aircraft is evaluated. Furthermore, the scope of this research is limited to the application of Kalman filtering techniques to estimate a

time history of the missile's position and velocity. A detailed discussion of Kalman filtering is included in Chapter II.

### ***1.3 Problem Approaches***

A Kalman filter (KF) computer algorithm separates the problem into two aspects, predicting missile behavior through modeling and performing updates by measuring missile parameters at discrete time intervals. However, accurately predicting missile behavior is difficult due to high maneuver-rates. Furthermore, measurements of missile navigation parameters are complicated by low radar cross section (RCS), high velocity and short time of flight (TOF).

There are numerous different approaches to consider for measuring missile navigation parameters. Some concepts for miss distance scoring systems include utilizing Global Positioning System (GPS), laser-optics, radio frequency (RF) or infrared (IR) measurements. Each of these has some inherent advantages and disadvantages.

*1.3.1 Global Positioning System.* The general concept of vector scoring with a GPS system is straight-forward. The 3-dimensional (3D) position of the aircraft and missile is measured using GPS and then used to derive the relative position between the missile and target. Velocity measurements are derived by calculating the change in position between each observation. This approach requires the installation of a GPS receiver on the missile to provide position updates. Due to short missile TOF, it is preferred that this GPS receiver acquires satellites prior to launch. Unfortunately, since air-to-air missiles are generally carried underneath the aircraft's wings or fuselage, GPS satellites are masked from view prior to launch. Attempts to provide GPS scoring must overcome this masking issue. The Joint Advanced Missile Instrumentation (JAMI) Program addresses this challenge.

Research in this area suggests measurements based on differential GPS can achieve an accuracy of 2 cm in test environments [38]. One potential drawback in this

estimation scheme is the potential for GPS satellite outages or jamming degrading or denying scores.

*1.3.2 Radar Sensors.* Using this approach, active omnidirectional antennas are installed on the drone aircraft transmitting in a spherical pattern. Depending on sensor type, these short range RF devices may provide range and/or range-rate of the missile as it approaches the aircraft. Using range measurements provided from four or more sensors suffices to calculate the 3D missile position using multilateration [10] , discussed in Section 2.6. Similarly, range-rate information from at least three sensors allows for determination of the missile’s instantaneous velocity vector as described in Section 2.7. When employing a Kalman filter algorithm, even a single valid range or radial-velocity measurement can improve the missile position and velocity estimate. However, missile position and velocity initialization using sensors requires simultaneous detection by at least four sensors. The selection of radar sensors and the geometry of the sensor configuration is critical for system performance and is discussed further in Chapters II and III.

*1.3.3 Laser Optics.* Implementing a laser vector scoring system involves installing a system of emitters on the target aircraft which transmit a spherical pattern of light energy around the target aircraft. In addition, missiles are enhanced with a high reflectivity coating to increase laser cross section. As the missile passes in close proximity to the aircraft, light energy reflected by the missile is registered by detectors and converted into range information. Radial velocity measurements from each detector are calculated using the change in range between updates. The combination of detector range and range-rate measurements are utilized in the same manner as the radar observations discussed previously.

*1.3.4 Infrared Sensors.* An IR scoring system relies on angle-of-arrival (AOA) information from a series of sensors to provide updates on missile position. In contrast to the radar and optics setups which are based on the concept of multilat-

eration, an AOA scoring system determines position using triangulation. Since the system is passive, it has some inherent advantages in threat detection if employed as part of a countermeasures system. However, in scoring air-to-air missiles, accuracy is significantly degraded by sensor geometry at long ranges.

#### **1.4 Research Contributions**

This research focuses on establishing the performance of an air-to-air missile scoring system utilizing a KF estimation algorithm along with a combination of RF sensors providing measurements of the missile's range and range-rate relative to the target aircraft. This approach is selected for the following reasons:

- It is not restricted by GPS jamming potentially employed on military ranges.
- GPS scoring requires major hardware modifications to the missile in order to incorporate a GPS receiver.
- The range of a scoring system using a laser optics approach is more limited than a RF scoring system due to the high laser power requirements to project the desired spherical light pattern. This problem can be mitigated if the laser tracks the incoming missile and focuses its laser energy, but this creates additional challenges based on missile speed and potentially high line-of-sight (LOS) rates.
- The range of an AOA scoring system is severely limited by sensor geometry unless extremely precise measurements of arrival angles are available.

This research addresses the following questions through analytical analysis, simulations and flight test:

- What is the optimal configuration of RF sensors?
- What is the accuracy and precision of this scoring system in reconstructing the last 350 meters of an air-to-air missile trajectory based on the performance of readily available RF sensors?

- How does performance vary using different missile dynamics models?
- How does accuracy and precision compare using different nonlinear Kalman filtering techniques?

### ***1.5 Thesis Outline***

Chapter II provides the mathematical background and prior research which is the foundation upon which this research is built. Chapter III records a detailed account of the methodology employed for air-to-air missile scoring. Chapter IV presents the simulations conducted along with an analysis of the simulation results. Chapter V explains the flight testing process and analyzes actual performance of the tested air-to-air scoring system. Chapter VI concludes the research with a summary of the most notable results along with a recommendation for future research in this area.

## II. Background

### 2.1 Mathematical Notation

This thesis uses the following mathematical notation:

- **Scalars:** Scalars are denoted by lower or upper case non-bold characters (e.g.,  $x$  or  $X$ )
- **Vectors:** Vectors are represented by lower case characters in bold font (e.g.,  $\mathbf{x}$ )
- **Matrices:** Matrices are denoted by upper case characters in bold font or upper case script characters (e.g.,  $\mathbf{X}$  or  $\mathcal{X}$ )
- **Vector Transpose:** A vector transpose is indicated by a superscript Roman  $T$  (e.g.,  $x^T$ )
- **Estimated Variables:** An estimated variable is designated by the use of a *hat* character (e.g.,  $\hat{x}$ )
- **Reference Frame:** If a variable's reference frame is designated, it is annotated by a superscript character (i.e.,  $\mathbf{x}^n$  is the vector  $\mathbf{x}$  in the  $n$  frame)
- **Direction Cosine Matrices:** A direction cosine matrix from frame  $i$  to frame  $n$  is represented by  $\mathbf{C}_i^n$
- **Discrete Time:** The subscript  $k$  is used to denote the  $k$ -th time step in a discrete time sequence (i.e.  $\hat{\mathbf{x}}_k$  is an estimate of the vector  $\mathbf{x}$  at time  $k$ )
- ***A priori* Estimate:** An estimate of a system's navigation parameters prior to incorporating a measurement update is designated with a superscript minus (e.g.,  $\hat{\mathbf{x}}^-$ )
- ***A posteriori* Estimate:** An estimate of a system's navigation parameters after incorporating a measurement update is designated with a superscript plus (e.g.,  $\hat{\mathbf{x}}^+$ )

## 2.2 Reference Frames

Fundamental to the estimation of missile position is a thorough understanding of coordinate reference frames. The following orthogonal, right-handed, reference frames are utilized in this research [39]:

- Earth-fixed inertial frame (i-frame)
- Earth frame (e-frame)
- Earth-fixed navigation frame (n-frame)
- Vehicle-fixed navigation frame (n'-frame)
- Body frame (b-frame)

Figure 2.1 depicts the relationship between the e-frame and i-frame. The Earth-fixed inertial frame approximates a theoretical true inertial reference frame where Newton's laws are valid. Its origin is located at the center of the earth and axes are non-rotating with respect to fixed stars. The x and y axes are located in the equatorial plane and the z-axis is coincident with the Earth's polar axis. This reference frame is

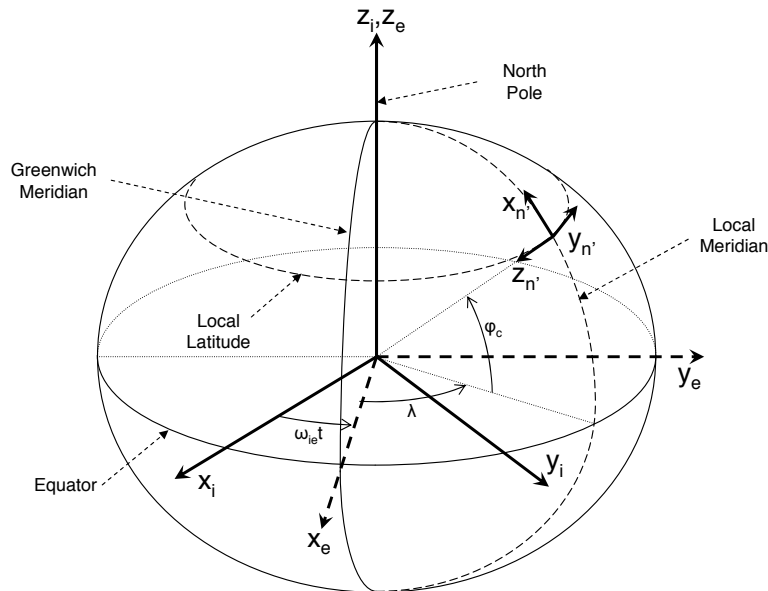


Figure 2.1: Earth-Fixed Reference Frames [41]

not truly inertial since the Earth rotates around the sun, but it serves as a sufficient approximation for terrestrial navigation. The Earth frame differs from the Earth-fixed inertial frame in that the  $x$  and  $y$  axes rotate with the Earth.

The Earth-fixed navigation frame, illustrated in Figure 2.2, is a local geographic reference frame with its origin chosen for convenience at a specific point on Earth. The  $x$ ,  $y$ , and  $z$ -axis point in the north, east, and down (NED) directions, respectively. The down direction is defined by the direction of the local gravity vector. The east, north, and up (ENU) navigation frame is a commonly used alternative to NED frame. As suggested by the name, the  $x$ ,  $y$ , and  $z$ -axis point in the east, north, and up directions, respectively. This research utilizes the NED frame during simulations, but transitions to the ENU frame for flight test. The vehicle-fixed navigation frame is identical to the Earth-fixed navigation frame except the origin is chosen at some fixed point on the vehicle.

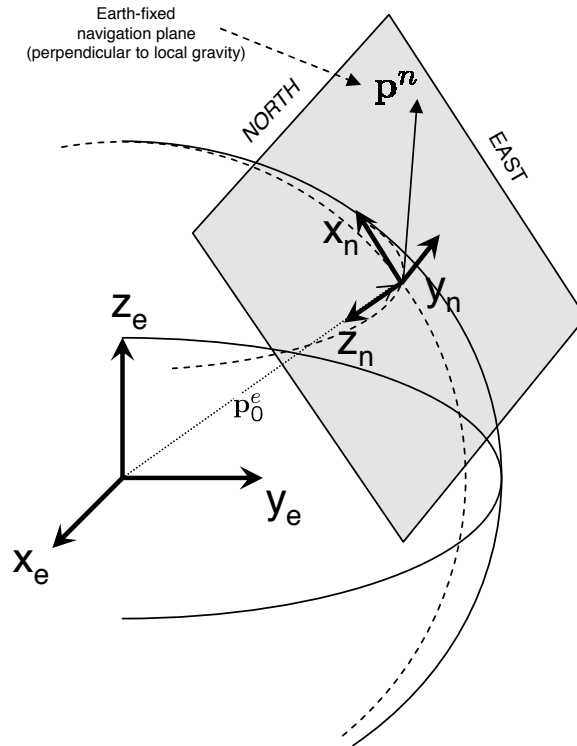


Figure 2.2: Earth-Fixed Navigation Reference Frame [41]

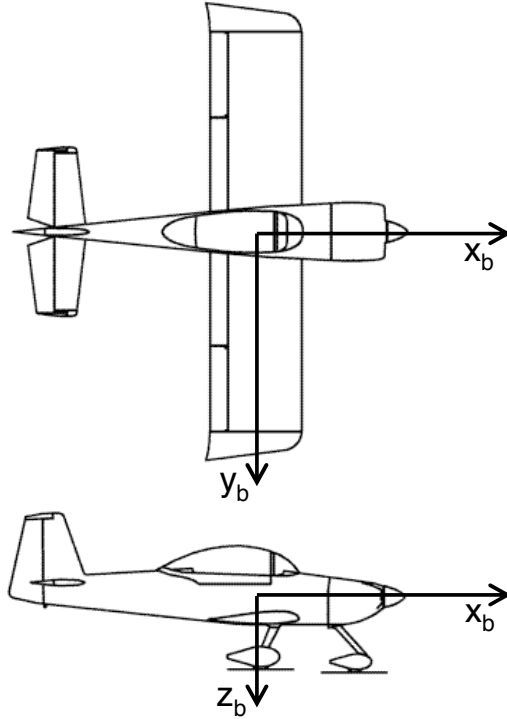


Figure 2.3: Aircraft Body Reference Frame [41]

Figure 2.3 depicts the aircraft body reference frame applied in this research. The body frame x-axis is out the nose of the aircraft, y-axis is out the right wing, and z-axis is out of the bottom of the vehicle. Roll, pitch, and yaw describe rotations about the x, y, and z-axis, respectively. The location of the origin is predetermined as a fixed point on the vehicle. In aircraft the center of gravity is a commonly used origin for the body frame.

### 2.3 Coordinate Transformations

Coordinate transformations provide an expression for the relationship between a vector in different reference frames. The two coordinate transformations pertinent to this research are direction cosine matrices (DCM) and euler angles. A DCM is a  $3 \times 3$  matrix used to express a vector in a different coordinate frame according to

$$\mathbf{r}^b = \mathbf{C}_a^b \mathbf{r}^a \quad (2.1)$$

where  $\mathbf{r}^a$  is a vector expressed in some arbitrary reference frame  $a$ ,  $\mathbf{r}^b$  is the same vector expressed in frame  $b$  and  $\mathbf{C}_a^b$  is the DCM from frame  $a$  to frame  $b$ . The element in the  $i$ -th row and the  $j$ -th column of  $\mathbf{C}_a^b$  represents the cosine of the angle between the  $i$ -th axis of frame  $a$  and  $j$ -th axis of frame  $b$  [39].

Euler angles provide a method for deriving the DCM to transform from one-coordinate system to another by performing a series of three rotations about different axes [39]. Rotations of  $\psi$  about the z-axis,  $\theta$  about the y-axis, and  $\phi$  about the x-axis are expressed mathematically by the DCMs

$$\mathbf{C}_1 = \begin{bmatrix} \cos \psi & \sin \psi & 0 \\ -\sin \psi & \cos \psi & 0 \\ 0 & 0 & 1 \end{bmatrix} \quad (2.2)$$

$$\mathbf{C}_2 = \begin{bmatrix} \cos \theta & 0 & -\sin \theta \\ 0 & 1 & 0 \\ -\sin \theta & 0 & \cos \theta \end{bmatrix} \quad (2.3)$$

$$\mathbf{C}_3 = \begin{bmatrix} 1 & 0 & 0 \\ 0 & \cos \phi & \sin \phi \\ 0 & -\sin \phi & \cos \phi \end{bmatrix} \quad (2.4)$$

When performing a transformation from a navigation frame to an aircraft body frame, the angle  $\psi$  represents the angle between the nose of the aircraft and north. Similarly, the angles  $\theta$  and  $\phi$  represent the pitch and roll of the aircraft, respectively. The product of these DCMs yields a transformation from the navigation frame to the body frame according to

$$\mathbf{C}_n^b = \mathbf{C}_3 \mathbf{C}_2 \mathbf{C}_1 \quad (2.5)$$

Using this DCM, a vector  $\mathbf{r}^n$  defined in the navigation reference frame is transformed into the body frame by

$$\mathbf{r}^b = \mathbf{C}_n^b \mathbf{r}^n \quad (2.6)$$

Deriving a DCM for a transformation in the opposite direction, from body frame to navigation frame, is easily accomplished by taking the transpose of  $\mathbf{C}_n^b$  (i.e.,  $\mathbf{C}_b^n = (\mathbf{C}_n^b)^T$ ).

## 2.4 Kalman Filter

Real-world systems are generally stochastic rather than deterministic because system models are imperfect, measurements available from sensors contain errors, and uncontrolled disturbances may exist. Therefore, a KF is a commonly used recursive, data processing algorithm which provides statistically optimal estimates of the states of a stochastic system. Implementing a KF requires the development of a system dynamics model and observation model. The dynamics model is designed to capture the typical behavior of the system in order to predict the changes in states of interest between measurement updates. The observation model provides the mathematical relationship between measurements and system states which is required to improve state estimates based on sensor data. Utilizing these models, the KF updates the state estimates by optimally weighting the dynamics and observation models according to their uncertainties. For example, if the sensor accuracy is poor, the gain in the KF algorithm adjusts to place more trust in the dynamics model.

Several assumptions are necessary to insure estimates are optimal. First, all system and measurement noises are accurately described by a Gaussian process. Second, noise sources are white, meaning their values are uncorrelated in time. Thirdly, a conventional KF assumes a linear system model in the general state space form

$$\dot{\mathbf{x}}(t) = \mathbf{F}(t)\mathbf{x}(t) + \mathbf{B}(t)\mathbf{u}(t) + \mathbf{G}(t)\mathbf{w}(t) \quad (2.7)$$

adequately represents the dynamics of the system. The variable  $\mathbf{x}(t)$  is a vector of system states,  $\mathbf{u}(t)$  is a vector of deterministic inputs, and  $\mathbf{w}(t)$  is a vector of zero-mean, white, Gaussian system noise sources. The matrices  $\mathbf{F}(t)$ ,  $\mathbf{B}(t)$ , and  $\mathbf{G}(t)$  describe how the state vector changes based on the current system states, inputs, and noise.

Since  $\mathbf{w}(t)$  is a vector of Gaussian processes, it is completely characterized by its mean and covariance. The noise covariance or strength, designated by the matrix  $\mathbf{Q}$ , is a tuning parameter adjusted to improve demonstrated filter performance. A higher  $\mathbf{Q}$  indicates more uncertainty in the dynamics model of the system. Finally, a conventional KF assumes a linear discrete-time observation model in the general state space form

$$\mathbf{z}_k = \mathbf{H}_k \mathbf{x}_k + \mathbf{v}_k \quad (2.8)$$

where  $\mathbf{z}$  is a vector of measurements, the matrix  $\mathbf{H}$  relates the measurements to current states, and  $\mathbf{v}$  is a vector of zero-mean, white, Gaussian measurement noise sources. The strength of the measurement noise vector is defined as

$$E[\mathbf{v}_k \mathbf{v}_k] = \mathbf{R} \quad (2.9)$$

where  $\mathbf{R}$  is a tuning parameter. The  $\mathbf{Q}$ -to- $\mathbf{R}$  ratio determines whether the filter places more faith in the dynamics model or observation model.

Since the KF is a discrete-time estimator, the dynamics model must first be converted from a continuous-time differential equation into an equivalent discrete-time difference equation. There are several methods available for performing this conversion. This research utilizes the Van Loan method [7]. First, using the parameters from the dynamics model in Equation (2.7), the matrix

$$\mathbf{M} = \begin{bmatrix} -\mathbf{F} & \mathbf{G}\mathbf{W}\mathbf{G}^T \\ \mathbf{0} & \mathbf{F}^T \end{bmatrix} \Delta t \quad (2.10)$$

is constructed where  $\Delta t$  is the propagation time step. Next, using software capable of matrix exponentials, solve for

$$\mathbf{N} = e^{\mathbf{M}} = \begin{bmatrix} \cdots & \phi^{-1}\mathbf{Q}_d \\ \mathbf{0} & \phi^T \end{bmatrix} \Delta t \quad (2.11)$$

Transposing the lower-right partition of  $\mathbf{N}$  yields the state transition matrix,  $\phi$ . Finally, the discrete-time noise strength,  $\mathbf{Q}_d$ , is obtained from the upper-right partition of  $\mathbf{N}$  through some basic linear algebra. Using these results, the equivalent difference equation for the dynamics model is

$$\mathbf{x}_k = \phi_{k-1}\mathbf{x}_{k-1} + \mathbf{B}_{k-1}\mathbf{u}_{k-1} + \mathbf{w}_{k-1} \quad (2.12)$$

where the discrete Gaussian, white noise sequence has strength  $\mathbf{Q}_{d_{k-1}}$ . The deterministic input is assumed constant over the propagation interval and therefore  $\mathbf{u}_{k-1}$  is identical to  $\mathbf{u}(t)$  evaluated at the current time. A first order approximation of  $\mathbf{B}_{k-1}$  is

$$\mathbf{B}_{k-1} = \mathbf{F}^{-1}(t)(\phi_{k-1} - \mathbf{I})\mathbf{B}(t) \quad (2.13)$$

where  $\mathbf{I}$  is the identity matrix.

All the necessary background is now in place to present the KF recursive algorithm. Since the state vector is a function of deterministic inputs and Gaussian processes, the state vector is also described by a Gaussian probability density function (pdf). Therefore, all the information about the state vector is captured by keeping track of its expected value,  $\hat{\mathbf{x}}$ , and covariance,  $\mathbf{P}$ . Using the discrete-time dynamics model, the equations for KF time propagations between samples are

$$\hat{\mathbf{x}}_k^- = \phi_{k-1} \hat{\mathbf{x}}_{k-1}^+ + \mathbf{B}_{k-1} \mathbf{u}_{k-1} \quad (2.14)$$

$$\mathbf{P}_k^- = \phi_{k-1} \mathbf{P}_{k-1}^+ \phi_{k-1}^T + \mathbf{Q}_{d_{k-1}} \quad (2.15)$$

After propagation the state  $\hat{\mathbf{x}}_k^-$  is referred too as the *a priori* estimate since it is prior to a measurement. Measurement updates are calculated using

$$\mathbf{K}_k = \mathbf{P}_k^- \mathbf{H}_k^T [\mathbf{H}_k \mathbf{P}_k^- \mathbf{H}_k^T + \mathbf{R}_k]^{-1} \quad (2.16)$$

$$\hat{\mathbf{x}}_k^+ = \hat{\mathbf{x}}_k^- + \mathbf{K}_k [\mathbf{z}_k - \mathbf{H}_k \hat{\mathbf{x}}_k^-] \quad (2.17)$$

$$\mathbf{P}_k^+ = \mathbf{P}_k^- - \mathbf{K}_k \mathbf{H}_k \mathbf{P}_k^- \quad (2.18)$$

where Equation (2.16) is the Kalman gain which optimally weights the dynamics model and observation model based on the state uncertainty after propagation,  $\mathbf{P}_{k+1}^-$ , and the strength of the measurement noise,  $\mathbf{R}$ . The updated state,  $\hat{\mathbf{x}}_k^+$ , is labeled the *aposteriori* estimate since it follows the measurement [18].

*2.4.1 Extended Kalman Filter.* Many real-world systems are not adequately modeled by a linear equation. An Extended Kalman Filter (EKF) deals with a nonlinear system by linearizing the dynamics about a nominal trajectory. Additionally, this nominal trajectory is updated based on the new state estimate after each measurement is incorporated. Furthermore, sensor measurements are frequently a nonlinear function of system states. An EKF linearizes the observation function about a nominal measurement, predicted according to the current *a priori* estimate. All EKF linearization is accomplished by using the first term of a Taylor series expansion at the point of interest.

This research is limited to linear missile dynamics models, but applies nonlinear observation models exclusively. In contrast to Equation (2.8), the general form for a nonlinear observation model with additive noise is

$$\mathbf{z}_k = \mathbf{h}[\mathbf{x}_k] + \mathbf{v}_k \quad (2.19)$$

where  $\mathbf{z}$  is the measurement vector,  $\mathbf{h}[\cdot]$  is a nonlinear operator, and  $\mathbf{v}$  is the noise vector.

In order to linearize this equation about a point of interest, a Jacobian matrix is calculated by taking the partial derivative of each of the nonlinear functions with respect to each of the states. Furthermore, the Jacobian is evaluated at the *a priori* estimate yielding

$$\mathbf{H}_k = \left. \frac{\delta \mathbf{h}}{\delta \mathbf{x}} \right|_{\hat{\mathbf{x}}_k^-} \quad (2.20)$$

Next, a nominal measurement is calculated by evaluating the nonlinear function at the *a priori* estimate according to

$$\mathbf{z}_{N_k} = \mathbf{h}[\hat{\mathbf{x}}_k^-] \quad (2.21)$$

Finally, a perturbation state,  $\delta \mathbf{z}$ , is defined as the difference between the realized measurement and nominal measurement

$$\delta \mathbf{z}_k = \mathbf{z}_k - \mathbf{z}_{N_k} \quad (2.22)$$

Since the dynamics model in this research is linear, the conventional KF time propagation equations are utilized. However, there is one small change in the KF measurement update equations for the EKF. The *aposteriori* estimate from Equation (2.17) is now calculated using

$$\hat{\mathbf{x}}_k^+ = \hat{\mathbf{x}}_k^- + \mathbf{K}_k \delta \mathbf{z}_k \quad (2.23)$$

The rest of the recursive algorithm is unchanged with the exception that the Jacobian matrix from Equation (2.20) now serves as  $\mathbf{H}$  in the KF measurement equations.

*2.4.2 Unscented Kalman Filter.* The Unscented Kalman Filter (UKF) provides another approach to dealing with nonlinear models. It improves on the accuracy of the EKF by capturing higher order effects while eliminating the need to calculate partial derivatives. The EKF is based on applying a first-order Taylor series approximation to linearize a nonlinear function. In contrast, the UKF relies on generating sigma points to represent the probability density function (pdf) of the state vector. The nonlinear function for system dynamics is then applied to transform the sigma points. The new set of sigma points, which represent the transformed pdf of the state vector, provides the required information to calculate the statistics of mean and covariance for the *a priori* estimate. Measurement updates are performed in a similar manner by transforming the sigma points through the nonlinear observation function and using the statistics of the sigma points to predict a measurement. The difference between the realized measurement and the prediction is then used to calculate the *a posteriori* estimate. The result is an estimator that accurately represents mean and covariance of the state vector to third order.

Since only linear dynamics models are utilized in this research, this background will only cover measurement updates with the UKF. To implement a UKF, sigma points are carefully chosen to capture the pdf using a fixed number of points based on the number of states in the system. The number of sigma points required is twice the number of states plus one. For a measurement update, the sigma points are calculated from the *a priori* estimate according to

$$\mathcal{X}_0 = \hat{\mathbf{x}}_k^- \quad (2.24)$$

$$\mathcal{X}_i = \hat{\mathbf{x}}_k^- + \sqrt[3]{(\lambda + L)\mathbf{P}_{x_k}^-|_i} \quad i = 1, 2 \dots L \quad (2.25)$$

$$\mathcal{X}_{i+L} = \hat{\mathbf{x}}_k^- - \sqrt[3]{(\lambda + L)\mathbf{P}_{x_k}^-|_i} \quad i = 1, 2 \dots L \quad (2.26)$$

where  $L$  refers to the number of states and the subscript  $i$  refers to the column number. The variable  $\lambda$  is a scaling parameter defined as

$$\lambda = \alpha^2(L + \kappa) - L \quad (2.27)$$

The  $\alpha$  term changes the spread of the sigma points and  $\kappa$  is a secondary tuning parameter which is set to zero in this research. After calculating the sigma points they are grouped into a matrix such that each sigma point is a column of the matrix. The complete set of sigma points is

$$\mathcal{X}_{L \times (2L+1)} = \begin{bmatrix} \mathcal{X}_0 & \mathcal{X}_1 & \dots & \mathcal{X}_{2L} \end{bmatrix} \quad (2.28)$$

Next, the sigma points are transformed through the nonlinear observation function shown mathematically by

$$\mathcal{Z}_k|_i = \mathbf{h}[\mathcal{X}_k|_i] \quad \forall i \in [0, 2L] \quad (2.29)$$

Now from the new sigma points,  $\mathcal{Z}_k$ , a measurement prediction and residual uncertainty is calculated using the equations

$$\hat{\mathbf{z}}_k = \sum_{i=0}^{2L} W_i^{(m)} \mathcal{Z}_k|_i \quad (2.30)$$

$$\mathbf{P}_{zz_k} = \sum_{i=0}^{2L} W_i^{(c)} (\mathcal{Z}_k|_i - \hat{\mathbf{z}}_k)(\mathcal{Z}_k|_i - \hat{\mathbf{z}}_k)^T + \mathbf{R}_k \quad (2.31)$$

where  $W^{(m)}$  and  $W^{(c)}$  are weighting terms for the mean and covariance, respectively, defined by

$$W_0^{(m)} = \lambda / (L + \lambda) \quad (2.32)$$

$$W_0^{(c)} = \lambda / (L + \lambda) + 1 - \alpha^2 + \beta \quad (2.33)$$

$$W_i^{(m)} = W_i^{(c)} = 1 / [2(L + \lambda)] \quad \forall i = 1, 2, \dots, 2L \quad (2.34)$$

The  $\beta$  term is a tuning parameter based on the type of distribution which represents the state estimate. For a Gaussian  $\beta = 2$ .

Before proceeding with an update, the cross correlation matrix between the state vector and measurements is required. This is calculated according to

$$\mathbf{P}_{xz_k} = \sum_{i=0}^{2L} W_i^{(c)} (\mathcal{Z}_k|_i - \hat{\mathbf{x}}_k^-) (\mathcal{Z}_k|_i - \hat{\mathbf{z}}_k)^T + \mathbf{R}_k \quad (2.35)$$

Kalman gain is now expressed in terms of cross correlation and residual uncertainty. This relationship is

$$\mathbf{K}_k = \mathbf{P}_{xz_k} \mathbf{P}_{zz_k}^{-1} \quad (2.36)$$

Finally, an update is performed using the Kalman gain to appropriately weight the dynamics model and measurement information. The equations for this update are

$$\hat{\mathbf{x}}_k^+ = \hat{\mathbf{x}}_k^- + \mathbf{K}_k (\mathbf{z}_k - \hat{\mathbf{z}}_k) \quad (2.37)$$

$$\mathbf{P}_{x_k}^+ = \mathbf{P}_{x_k}^- - \mathbf{K}_k \mathbf{P}_{zz_k} \mathbf{K}_k^T \quad (2.38)$$

*2.4.3 Particle Filter.* Conceptually, a particle filter is similar to a UKF because it utilizes sample points to represent a pdf of the state vector. However, unlike the sigma points in a UKF, the number of samples used is arbitrary, selected by the designer based on the specific problem. In general, the greater the nonlinearities in the system, the more sample points required to accurately capture the pdf.

The samples are a collection of discrete weighted particles designed to represent the pdf. There are several methods for accurately capturing the statistics of the pdf. In this research, the PF uses a combination of variable interval and variable weight particles. To initiate our filter, we assume the pdf of our state vector is normally distributed with an initial mean of  $\bar{\mathbf{x}}$  and covariance  $\mathbf{P}_{xx}$ . Next,  $NP$  particles are generated with locations defined by

$$\mathcal{X}_{k-1}^-|_i = \bar{\mathbf{x}} + \mathbf{n}|_i \quad \forall i \in [1, NP] \quad (2.39)$$

where  $\mathbf{n}$  represents random noise calculated using

$$\mathbf{n}|_i = \sqrt{\mathbf{P}_{xx}} \times \text{randn}(L) \quad \forall i \in [1, NP] \quad (2.40)$$

The variable  $L$  refers to the number of states and the `randn` command randomly generates a number from a normal distribution on the interval  $[0, 1]$ . When multiplied by the Cholesky square root of the covariance matrix, the random number generator produces the desired variation in particle interval to capture the state uncertainty.

The weight of each particle is specified by

$$\mathbf{W}_{k-1}^+|_i = \frac{1}{NP} \quad \forall i \in [1, NP] \quad (2.41)$$

In this instance all particles are weighted equally so the mean and covariance of the state vector is completely captured by the particle interval.

Next, the particles are propagated by passing them through the appropriate dynamics. For this research, all dynamics models utilized are linear in the general form of Equation (2.7). This leads to the calculation

$$\mathcal{X}_k^-|_i = \phi_{k-1} \mathcal{X}_{k-1}^+|_i + \mathbf{w}_{k-1}|_i \quad \forall i \in [1, NP] \quad (2.42)$$

The random noise,  $\mathbf{w}_{k-1}$ , is generated from

$$\mathbf{w}_{k-1}|_i = \sqrt{\mathbf{Q}_{d_{k-1}}} \times \text{randn}(L) \quad \forall i \in [1, NP] \quad (2.43)$$

This creates a random noise matrix with statistics matched to the specified discrete noise strength matrix,  $\mathbf{Q}_d$ .

In essence, by executing Equation (2.42) each of the particles is passed through the dynamics equation and then given a random kick due to process noise. During this transformation only the location of the particles change, the weights remain the same. The resulting statistics of the navigation states after propagation are calculated from

$$\hat{\mathbf{x}}_k^- = \sum_{i=1}^{NP} \mathbf{W}_k^-|_i \mathcal{X}_k^-|_i \quad (2.44)$$

$$\mathbf{P}_{x_k}^- = \sum_{i=1}^{NP} \mathbf{W}_k^-|_i (\mathcal{X}_k^-|_i - \hat{\mathbf{x}}_k^-)(\mathcal{X}_k^-|_i - \hat{\mathbf{x}}_k^-)^T \quad (2.45)$$

In Equation (2.44),  $\hat{\mathbf{x}}_k^-$  is just the weighted sum of the particles, while Equation (2.45) provides an expression for the *a priori* estimate covariance.

The next task is to apply a measurement update to the navigation states. In an analogous process to the UKF algorithm, measurements are predicted by transforming the particles through the observation function according to

$$\mathcal{Z}_k^-|_i = \mathbf{h}[\mathcal{X}_k^-|_i] \quad \forall i \in [1, NP] \quad (2.46)$$

Next, a residual for each of the particles is calculated using

$$\mathbf{r}_i = \mathbf{z}_k - \mathcal{Z}_k^-|_i \quad \forall i \in [1, NP] \quad (2.47)$$

where  $\mathbf{r}_i$  represents the residual of the  $i$ -th particle at time  $k$  (the subscript  $k$  is implied and is omitted for clarity). In addition, the weights of the transformed particles are adjusted based on their likelihood given the measurement realization and uncertainty. This effectively combines the statistical information from the realized measurement with the dynamics model prediction. Assuming a Gaussian measurement distribution, the likelihood of each particle is given by

$$L(\mathbf{r}_i) \propto e^{-\frac{\mathbf{r}_i^T \mathbf{r}_i}{\mathbf{R}^2}} \quad (2.48)$$

Using the resulting likelihood for each particle, the appropriate particle weighting is computed from

$$\mathbf{W}_k^+|_i = L(\mathbf{r}_i)\mathbf{W}_k^-|_i \quad \forall i \in [1, NP] \quad (2.49)$$

However, this procedure does not guarantee the sum of the weights is equal to one so an additional step is required to normalize the weights. In this relatively simple step each particle weight is divided by

$$\sum_{i=1}^N \mathbf{W}_k^+|_i \quad (2.50)$$

Since the location of the particles does not change during the measurement update the points are transferred according to

$$\mathcal{X}_k^+ = \mathcal{X}_k^- \quad (2.51)$$

This results in a new set of particle locations and weights to use for repeating the recursive filter algorithm. To calculate an *aposteriori* state estimate and uncertainty Equations (2.44) and (2.45) are applied using the post measurement weights and particle locations.

## 2.5 Radar Sensor

In this research the observation model is based on a group of sensors providing range and range-rate information. There are two different categories of radar sensors capable of providing the desired measurements: pulse-doppler (PD) and frequency-modulated continuous waveform (FMCW) radar. PD radars are less suitable for short range applications due to a blind zone in close proximity to the sensors. In addition, the FMCW sensors are generally lower in cost and complexity making them ideal for the application in this research.

Continuous wave (CW) radar functions by capitalizing on the Doppler effect. The CW radar outputs a constant frequency electromagnetic (EM) wave. When the EM wave reflects off a target and returns to the source, the frequency of the received signal is shifted based on the relative motion between the source and the target. If the target has a closing velocity the received frequency is higher while a receding target results in a lower received frequency. Based on this principle, target velocity along the sensor line-of-sight is calculated from doppler shift by

$$v = \frac{c(f_r - f_t)}{2f_t} \quad (2.52)$$

where  $f_t$  is the transmitted frequency,  $f_r$  is the received frequency, and  $c$  is the speed of light. In deriving Equation (2.52), it is assumed that  $c \gg v$ .

A FMCW sensor achieves range measurements in addition to range-rate by systematically varying the frequency of the transmitted signal. Linear frequency modulation (LFM) is a commonly employed technique in which the transmit frequency is modulated with a triangular waveform as shown in Figure 2.4 [30].

The bandwidth of the system is described by the frequency sweep range,  $f_{sweep}$ . Furthermore, the chirp time,  $T_{chirp}$ , corresponds to the time required to complete a sweep from the lowest to highest frequency (labeled  $T_{CPI}$  in Figure 2.4). However, this scheme results in an ambiguous range and range-rate measurement since the receiver does not know  $f_t$  for the the received signal at any instant in time. If we plot range versus velocity on an R-v diagram, the ambiguous combination of range and velocity describes a line.

In order to resolve the ambiguity, FMCW sensors vary chirp gradients by adjusting  $f_{sweep}$  and  $T_{chirp}$ . Typical sensors employ four different gradients enabling an unambiguous measurement of range and velocity by evaluating the intersection of lines on an R-v diagram as shown in Figure 2.5 [29].

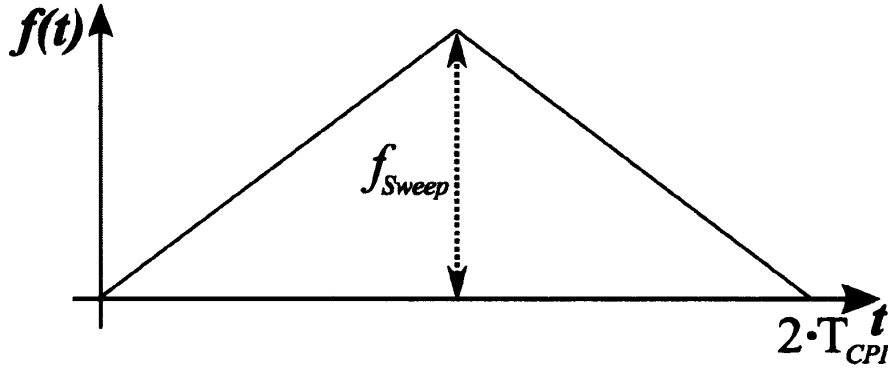


Figure 2.4: Linear Frequency Modulation in an FMCW Radar Sensor

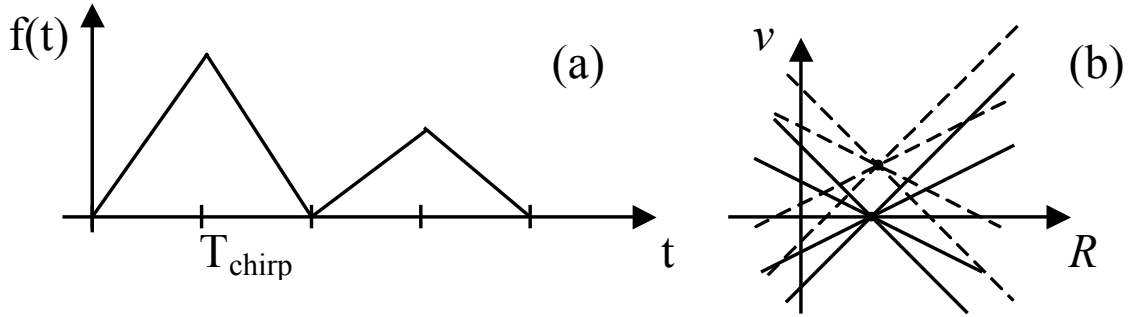


Figure 2.5: FMCW Sensor Employing Varying Chirp Gradient to Resolve Range-Velocity Ambiguity

The range and velocity resolution for an FMCW sensor are calculated by

$$\Delta R = \frac{c}{2f_{sweep}} \quad (2.53)$$

$$\Delta v = \frac{\lambda}{2T_{chirp}} \quad (2.54)$$

## 2.6 Multilateration

Estimating missile position based on sensor range measurements relies on the concept of trilateration. Figure 2.6 demonstrates a simple 2D case of trilateration where three sensors, P1, P2, and P3, measure range to a target located at point B. Given a single range measurement from sensor P1, the 2D position of the target is constrained to lie somewhere along the circle of radius  $r_1$  around the sensor. If a second sensor, P2, simultaneously provides a range measurement of  $r_2$ , the target position must be at an intersection of the two circles. As depicted in Figure 2.6, the intersection of the two circles limits the possible target location to two points, A and B. Finally, range from a third sensor, P3, uniquely identifies the 2D target location as point B. An inherent limitation in applying this approach is the sensors cannot be co-linear. For example, if we move the location of sensor P3 such that all sensors lie along a single straight line, their circles would all intersect at points A and B. In this case sensor P3 does not provide any additional information and the 2D position of

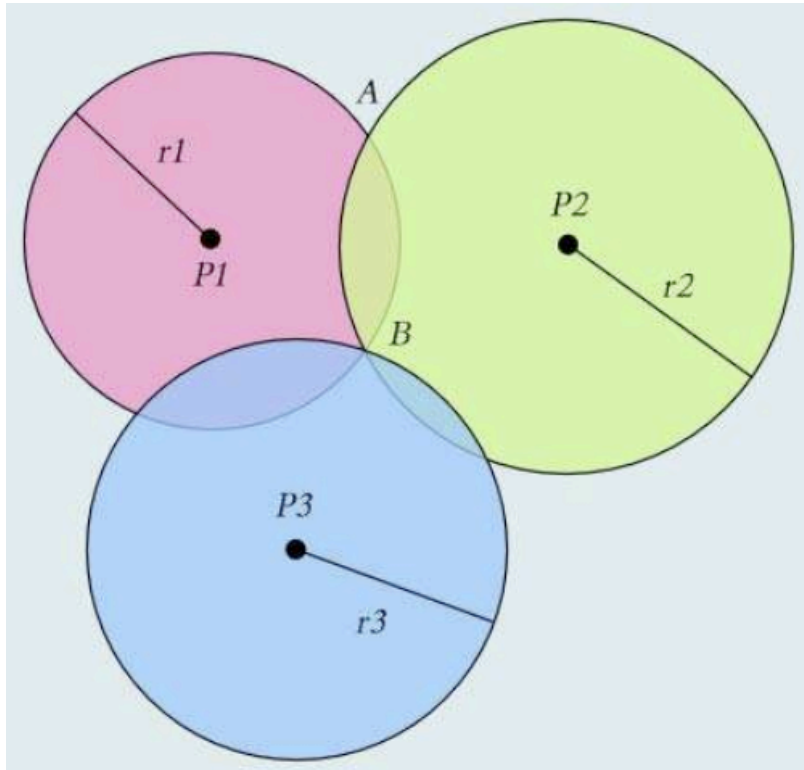


Figure 2.6: 2D Trilateration [14]

the target is not uniquely determined except in the trivial case in which the target is also co-linear with the sensors.

In 3D space, four non-coplanar sensors are required to uniquely define target location. The range from a single sensor describes a sphere around the object. Adding a second sensor constrains target position to the intersection of two spheres (i.e., a circle). Finally, by adding a third and fourth sensor range, the 3D position is further limited to a single point as discussed in the 2D example. In many applications three sensors are actually sufficient for updating 3D position because one of the two potential locations can be eliminated based on feasibility. As an example, GPS receivers determine user position by measuring ranges from multiple satellites. Although a minimum of four satellites are required to solve for receiver position, one of these satellites is actually necessary to determine an unknown clock bias to insure satellite ranges are accurate [24]. The remaining three satellites are sufficient to uniquely solve

for the user's location because only one of the two possible receiver locations is on the surface of the Earth [24]. The remaining point is somewhere in distant space and can be disregarded.

If all of the available range measurements are perfect, utilizing more than three sensors will not change the target location because all sensors' ranges will intercept at exactly the same point. However, in reality every sensor range measurement is corrupted by random noise. As a result, position accuracy is improvable by using range measurements from more than three sensors, referred to as multilateration [24]. This process assumes each sensor measurement is unbiased and applies a least-squares error estimation to calculate the target location [24].

When calculating position based on imperfect measurements sensor geometry is critical. Figure 2.7 illustrates the increase in error which results from suboptimal geometry. In Figure 7(a) the estimated target location is point A based on range measurements from sensors one and two. These sensors are configured such that their angular spacing from the target viewpoint is 90 degrees. The solid circles indicate the measured range between the target and each sensor while the dashed line represents measurement uncertainty (i.e., the true range from each sensor is expected to fall somewhere between their respective dashed circles). Based on this geometry, the

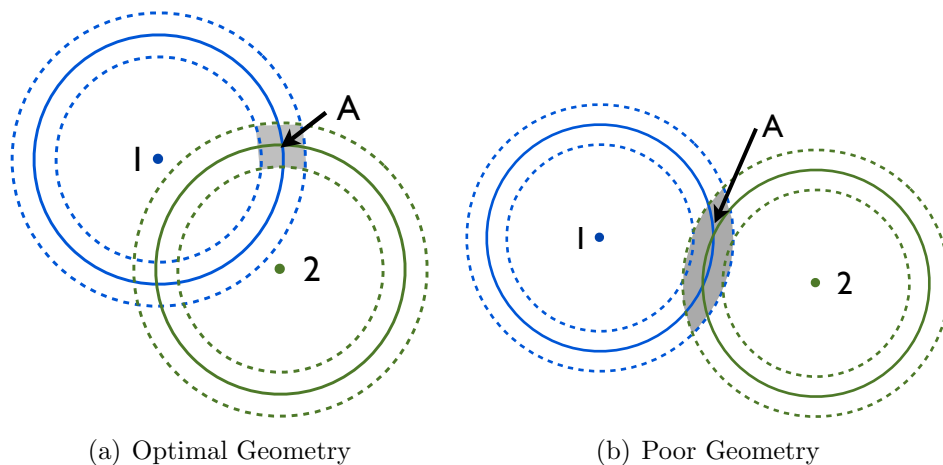


Figure 2.7: Impact of Sensor Geometry on Precision of Position Calculation [24]

gray shaded region indicates the region of uncertainty for the target location. Figure 7(a) represents the optimal geometry because area of uncertainty is minimized (i.e., the precision of the location estimate is maximized). In contrast, Figure 7(b) demonstrates the reduction in precision resulting when the sensor geometry is less than optimal. In a two sensor case, a 90 degree angular separation is desired between the sensors. However, for more than two sensors the best geometry is achieved when the angular spacing,  $\theta$ , is

$$\theta = \frac{360^\circ}{N}, N > 2 \quad (2.55)$$

where  $N$  is the number of sensors. For example, if you have three sensors the optimal configuration is an angular separation of  $120^\circ$  as viewed from the target. The concept is easily extended to 3D location precision.

### 2.7 Velocity Vector Calculation from Speed Measurements

A target's velocity vector is calculated by utilizing radial velocity measurements from multiple sensors in a process similar to multilateration. Figure 2.8 depicts a

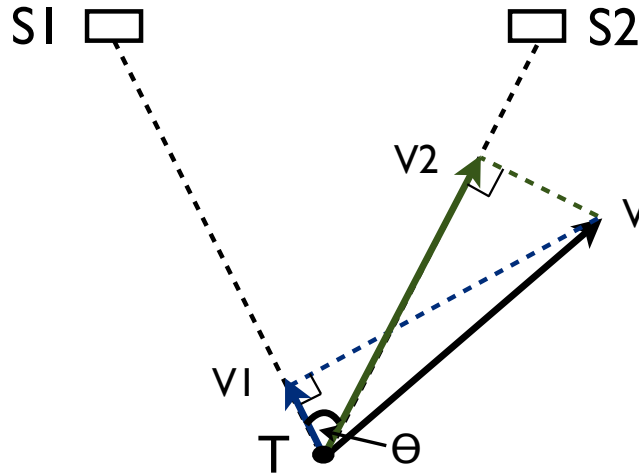


Figure 2.8: Calculation of 2D Velocity from Speed Measurements [26]

simple 2D scenario for illustration. In this example, two sensors,  $S1$  and  $S2$ , perform speed measurements of the target,  $T$ , along their LOS to the target. Assuming target and sensor positions are known, the velocity vector of the target is estimated by the projections  $v_1$  and  $v_2$  as depicted in Figure 2.8. By examining the geometry in the figure, it is apparent that a minimum of two sensors are required for a 2D velocity vector and the sensors cannot be positioned along the same LOS from the target (i.e., both sensors and the target cannot lie along a straight line). This process is extended to 3D by increasing the sensor count to three and insuring that all sensors are not co-planar with the target and no two sensors are co-linear with the target.

All of the geometry considerations relevant to multilateration also apply to precise velocity vector calculation. For example, in the 2D case depicted in Figure 2.8, the ideal geometry occurs when  $\theta = 90^\circ$ . The error in the calculated velocity vector increases as the angle decreases towards zero degrees [35].

## 2.8 Gating and Data Association

Tracking a target in a cluttered environment requires a method for eliminating false observations while associating valid observations with an existing target. Gating and data association techniques address this issue.

Gating approaches the task of distinguishing true target observations from clutter by evaluating the distance between the expected measurement and each received measurement. Two types of gating, square and ellipsoidal, are relevant to this research. Square gating is applied as a computationally cheap method to quickly eliminate observations far from the expected track location. To perform square gating the maximum eigenvalue of the residual covariance scaled by the selected gate size,  $\gamma$ , is evaluated according to [5]

$$emax = \sqrt{\max(\text{eig}(\gamma\mathbf{S}))} \quad (2.56)$$

The gate size is selected to achieve a desired probability that a true observation will fall within the selected gate. For example, choosing  $\gamma = 9.2$  provides a 99 percent chance that the true observation is within the gate [5]. The residual covariance is calculated from the *a priori* state covariance,  $\mathbf{P}_k^-$ , and the measurement model parameters using the formula [5]

$$\mathbf{S}_k = \mathbf{H}_k \mathbf{P}_k^- \mathbf{H}_k^T + \mathbf{R}_k \quad (2.57)$$

After computing *emax*, each measurement,  $\mathbf{z}_j$ , is compared to the expected target measurement,  $\hat{\mathbf{z}}$ , using the formula [5]

$$\hat{\mathbf{z}} - \text{emax} \leq \mathbf{z}_j \leq \hat{\mathbf{z}} + \text{emax} \quad (2.58)$$

The subscript  $j$  refers to the  $j$ -th measurement from the sensor. Every measurement outside this region is eliminated as a possible candidate for updating the target. If multi-target tracking is employed, these unused measurements are evaluated for updating alternate targets or initiating new targets.

Square gating only provides a coarse evaluation of potential observations because it's based on the residual covariance in the worst case direction of the measurement space. Ellipsoidal gating is used to further reduce observations relevant to the target by comparing the residual norm of each measurement to the gate size. The residual norm,  $d_j^2$ , is calculated by [12]

$$d_j^2 = \delta \mathbf{z}_j^T \mathbf{S}^{-1} \delta \mathbf{z}_j \quad (2.59)$$

where the time subscript,  $k$ , is intentionally omitted for clarity. If  $d_j^2 > \gamma$ , the observation is eliminated as an option for target update [12]. If multiple observations lie within the target's ellipsoidal gate, data association is applied to select the most likely candidate for target update.

There are two broad categories for data association, hard assignments and soft assignments. In a hard assignment a maximum of one observation is associated with each target. This is computationally simple, but performance is generally only satisfactory for basic tracking scenarios. In comparison, soft assignments allow association of multiple observations with a single target. This method is accomplished by probabilistic weighting of the measurements within the track's gate.

Although numerous different options are available for data association, this research applies the simplest technique, the global nearest neighbor (GNN). This hard assignment approach works well for our application involving a single-target in a low clutter environment. Based on GNN, the closest observation within each track's ellipsoidal gate is selected to perform the update. The closest observation is assessed by comparing the residual norm,  $d_j^2$ , for each observation surviving gating. [12]

## ***2.9 Past Research***

Missile state parameter estimation is a topic addressed by researchers in a variety of different applications. Some literature specifically addresses the problem of performing air-to-air missile scoring using various approaches such as radar, GPS, infrared or lasers. Other relevant literature applies similar concepts to the problem of tracking a ballistic missile trajectory for predicting impact location and performing an intercept. Although there are significant differences between these problems, there are also substantial similarities in approaches to solving the problems. For example, researchers commonly employ missile modeling in conjunction with Kalman filtering algorithms to estimate missile state parameters. Section 2.9.1 will summarize some of the research related to missile state parameter estimation to include scoring systems for test and evaluation, countermeasures systems for defeating air-to-air missiles, ballistic missile tracking approaches, and complex missile dynamics models.

Section 2.9.2 explores research with related methodologies, but not directly associated with missile state parameter estimation. Although the applications are

different, this research illustrates examples of utilizing multilateration, range-rate measurements, and Kalman filtering to estimate the position or velocity of a target.

*2.9.1 Missile Tracking.* DiFillippo and Campbell [8] present a concept for an active missile approach warning system (MAWS) similar to the end-game vector scoring system proposed in this research. The proposed MAWS utilizes a pulsed Doppler radar on the target platform to detect incoming missiles and direct the employment of countermeasures. The radar provides range and range-rate information to an EKF software algorithm to perform estimation of the missile parameters. DiFillippo and Campbell utilize a complex nonlinear missile dynamics model in the general form

$$\dot{\mathbf{x}}(t) = \mathbf{f}(\mathbf{x}, t) + \mathbf{w}(t) \quad (2.60)$$

This research expands on their work by considering additional missile dynamics models and evaluating alternate nonlinear Kalman filters such as the UKF and PF. Additionally, this research evaluates estimation performance using COTS, automotive-grade radar sensors. Furthermore, the authors mention the application of gating, but do not discuss specific implementation.

In 1997, Bradley received a patent on his invention of a miss distance vector scoring system [6]. The invention provides miss distance and miss direction in azimuth and elevation from the target. This device utilizes four omni-directional antennas emitting RF energy in a spherical pattern. Reflected energy is received by each of the four antennas and processed to provide direction and distance of the missile. This simple hardware only setup does not incorporate Kalman filtering or similar estimation techniques, nor does it model missile dynamics.

Minor and Rowe suggest a different approach to missile scoring using an integrated GPS receiver and micro-electro-mechanical system (MEMS) as an inertial sensor embedded in the missile or rocket [22]. Although there are advantages to this approach, there are also several disadvantages as outlined in Chapter I. Stadnik's

research, presented in [33], demonstrates the feasibility of implementing a GPS translator onto a missile system. However, a GPS based scoring system could incorporate the Kalman filter algorithms and missile dynamics models presented in this research to improve missile state estimation.

There is a significant body of literature exploring methods for passively tracking targets with IR sensors. Passive IR sensors do not offer an inherent advantage in test and evaluation applications, but do offer significant benefits for MAWS since they do not increase risk of detection. Dikic and Kovacevic [13] present a solution for air targets with two IR detectors. The IR sensors provide angle-only measurements to a filter based on interacting multiple models (IMM). An IMM algorithm uses a bank of Kalman filters, each with a different missile dynamics model. During target estimation, the algorithm can jump between the subfilters based on observed measurements to improve missile state estimation performance. This setup offers advantages when tracking a missile over an extended period of time involving multiple different phases of flight. For example, an air-to-air missile tracked from launch, through boost, coast, and endgame maneuvering would presumably demonstrate significantly different motion and a single dynamics model will not accurately capture all these phases. For end-game missile scoring, an IMM algorithm is unlikely to show significant performance improvement. The problem addressed by Dikic and Kovacevic is limited to estimating the scalar range from missile to target rather than a 3D vector solution. In related research, Xu, Wang, Zhao, and Guo propose a method for extracting range from a single IR sensor based on image processing [42].

The concept of single or combinations of IR sensors producing range information provides exciting implications for aircraft defensive systems. The air-to-air missile scoring system proposed in this research could be adapted to a MAWS system by substituting passive IR sensors for the FMCW sensors. However, performance will depend on the accuracy of the range measurements provided by the IR sensors.

A brief examination of research regarding ballistic missile tracking is also useful for considering approaches to missile vector scoring. Siouris, Chen, and Wang propose the tracking of an incoming ballistic missile using an extended interval Kalman filter (EIKF) [31]. Like many ballistic missile tracking approaches, the authors assume the availability of range, azimuth, and elevation measurements from a ground based radar system. Using this as the basis for their observation model combined with a nonlinear dynamics model, an EIKF algorithm is implemented. The EIKF was designed for nonlinear systems with parameter uncertainties that can be described by intervals. Conceptually, this is similar to the concept of switching between different dynamics models to model a missile during different phases of flight. There is a substantial amount of additional research available on different approaches to tracking a ballistic missile in which different dynamics models and filtering methods are explored. Much of the research is summed in Minvielle's article in [23]. The interested reader is also referred to [9] for a discussion of tracking ballistic missiles using IMM.

Any attempt to estimate missile state kinematic parameters using Kalman filtering must consider the appropriate missile dynamics model to obtain desired accuracy. Blackman and Popoli [5] outline several different missile models including constant velocity (CV), constant acceleration (CA), a three-dimensional coordinated turn (CT), and first-order Gauss-Markov acceleration (FOGMA). Several authors [28] [37] suggest hybrids of the CV and CA models by incorporating real-time switching between the dynamics models to improve tracking performance. More advanced missile models are proposed through research by other authors. Maybeck, Negro, Cusumano, and De Ponte develop a refined missile acceleration model by exploiting a knowledge of aerodynamically induced lift and drag forces of a nonthrusting missile employing proportional navigation guidance [17]. Their nonlinear missile dynamics model assumes additive, zero-mean, white, Gaussian noise. In addition, they utilize an observation model in which noise corrupted measurements of range, range-rate, and LOS angle are available. An EKF based on these models is proposed to assist in the precise tracking and prediction of the parameters of a threat missile.

The end-game air-to-air missile scoring system proposed in this paper intentionally does not utilize LOS angle measurements. This setup would require a more complex and expensive tracking radar which may be impractical for test and evaluation where drone aircraft destruction is anticipated. Additionally, the setup would require multiple tracking radars due to field of view (FOV) limitations and aircraft masking issues. Several of the dynamics models mentioned above are considered in this research, however, simpler linear models are selected over more complex nonlinear models like the one proposed in [17]. In missile testing, all the data processing is performed post-mission and highly accurate dynamics models for predictive purposes are unnecessary.

*2.9.2 Related Estimation Problems.* In the past, researchers applied trilateration in conjunction with Kalman filtering to a number of different navigation problems with highly successful results. Miah and Gueaieb use this approach for 2-dimensional (2D) navigation of a robot in [21]. In their work, a robot is equipped with a radio frequency identification (RFID) reader and three RFID tags are placed at known 3D locations in an indoor environment. This setup provides distance measurements between the robot and three known locations. Since the RFID tags are arranged in 3D space, three ranges does not uniquely identify the location of the robot, but the author uses a geometric approach based on Cayley-Menger determinants to solve the localization problem. Next, the author develops a dynamics model for the robot motion which includes zero-mean, white, Gaussian system noise. The dynamics model and observation model are implemented in an EKF and UKF to better estimate the robot position during navigation. Since this is a 2D navigation problem, the states of interest are the x and y position of the robot. The author concludes by performing an indoor navigation simulation and comparing the position estimates of the robot provided by trilateration alone, and trilateration in conjunction with the two proposed Kalman filters. The results are summarized in Figure 2.9. As illustrated in this figure, incorporating Kalman filtering reduces the root mean square

RMSES FOR OPEN PATH.				RMSES FOR CLOSED PATH.			
Run #	Trilateration	EKF	UKF	Run #	Trilateration	EKF	UKF
1	140 cm	34 cm	26 cm	1	140 cm	22 cm	15 cm
2	149 cm	31 cm	20 cm	2	146 cm	19 cm	12 cm
3	151 cm	44 cm	40 cm	3	145 cm	23 cm	30 cm
4	141 cm	22 cm	16 cm	4	143 cm	25 cm	19 cm
5	129 cm	21 cm	20 cm	5	154 cm	27 cm	29 cm
Average	141.8 cm	30.4 cm	24.4 cm	Average	145.6 cm	23.2 cm	21.0 cm

(a) Root Mean Square Error for Open Loop Robot Path (b) Root Mean Square Error for Closed Loop Robot Path

Figure 2.9: Comparison of Errors using Three Different Estimation Techniques for 2D Robot Navigation [21]

error (RMSE) significantly. The average RMSE for the UKF estimates are reduced by a factor of approximately 6.

This research paper proposes a similar method for performing air-to-air missile vector scoring. A multilateration observation model is incorporated into an EKF and UKF to improve missile state estimation. However, the missile state estimation problem is significantly more complex for a variety of reasons. First, the missile estimation problem is 3D and test and evaluation applications are interested in missile velocity as well as position. Additionally, modeling missile dynamics accurately is more challenging than capturing robot dynamics. The majority of the robot motion is controlled by deterministic inputs and hence, easy to model. However, the research by Miah and Gueaieb provides some useful insights by demonstrating the potential for significant improvement in state estimation by incorporating Kalman filtering rather than using trilateration stand-alone.

Tu and Kiang [40] propose a different strategy for applying trilateration and Kalman filtering to estimate the position, velocity and acceleration of a vehicle to avoid collision. The approach assumes a vehicle equipped with a minimum of three sensors providing range, radial velocity, and radial acceleration using hybrid linear frequency modulation (LFM)/frequency shift keying (FSK) echoed signals. Measurements from each sensor to a target vehicle are separately processed through a linear Kalman filter and then combined through the trilateration process to determine 2D

position, velocity, and acceleration of the target as illustrated in Figure 2.10. The authors demonstrate the effectiveness of this approach, referred to as a robust Kalman filter (RKF), in several scenarios. In related work, Klotz uses a network of FMCW sensors to trilaterate a target for vehicle collision avoidance [15]. He presents a solution using a least squares estimate of an overdetermined solution without a Kalman filter and an additional approach incorporating an EKF. Tu and Kiang compare their RKF solution to an EKF based approach and conclude the RKF performs better when the target vehicle is turning over a short period of time.

The method proposed in the next chapter for air-to-air missile vector scoring considers EKF, UKF, and PF based approaches in lieu of a RKF, but an RKF is an option for future work. Although the approaches cited in the collision avoidance automotive research are relevant to the proposed missile scoring system, they are simpler problems like robot navigation. Automotive collision avoidance is a 2D problem and the velocity and acceleration of the target vehicles does not approach the expected values for a missile.

The medical field contains research examples related to the relevant concept of converting multiple range-rate measurements into velocity. Torricelli, Scabia, Biagi, and Masotti [27] suggest a 2D vector Doppler system for use in observing patient

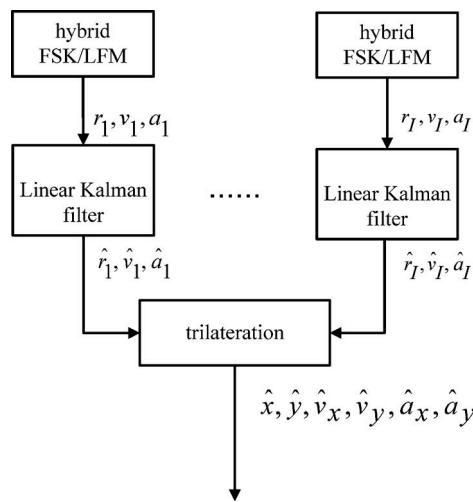


Figure 2.10: Procedure for a Robust Kalman Filter [40]

blood flow. Steel and Fish contribute to this field by studying the impact of range-rate measurement errors on the resulting estimated 2D or 3D velocity vectors [34]. These works are not based on Kalman filtering, but they provide insights into strategies for locating range-rate sensors and anticipating velocity error magnitude. The mathematical background for velocity calculations in Section 2.7 is taken directly from these conference papers.

### ***2.10 Summary***

This chapter began by covering the mathematical background required to understand the methods presented in the next chapter. The mathematical notation applied throughout this research was covered in great detail. The relevant coordinate reference frames were described along with transformations used to transition between reference frames. Additionally, the Kalman filter recursive data processing algorithm was presented along with an explanation of the three specific nonlinear Kalman filters applied in this research: an EKF, UKF, and PF. Furthermore, the basic operation of FMCW radar was described to familiarize the reader with the sensors used in the proposed missile scoring system. Moreover, the mathematical concepts required to determine target 3D position and velocity using multiple sensor measurements of range and range-rate were presented. Finally, this chapter introduced gating and data association to reduce the impact of radar clutter on missile state estimation.

The chapter concluded with a brief review of prior research to illustrate the contributions of this research with an academic framework. The past research was divided into two areas, work directly related to missile tracking and work employing similar methods for different types of estimation problems. In the next chapter, the methodology for implementing the proposed air-to-air missile scoring system is presented.

### III. Methodology

This research proposes an end-game missile scoring system which relies on short range radio frequency (RF) sensors to update missile position and velocity just prior to intercept. As introduced in Chapter I, this approach involves multiple, active directional antennas installed on a drone aircraft transmitting in a spherical pattern. FMCW radar sensors are utilized and therefore provide both range and radial velocity of an incoming air-to-air missile as discussed in Chapter II. The target platform and sensor locations upon the target platform are assumed to be known. During a live-fire test, the sensors' measurements may be broadcast to the ground as an air-to-air missile approaches and passes or impacts the drone.

Three different nonlinear Kalman filters are considered for translating the kinematic measurements from the RF sensors into estimates of the missile's position and velocity: an EKF, UKF, and PF. In order to initialize the filters, the air-to-air missile's position is passed from an external tracking source with some uncertainty (discussed in Section 3.4). The missile's position is improved near the intercept point through a Kalman filter based upon one of three missile dynamics models and using relative range and radial velocity measurement updates.

In the remainder of this chapter, Section 3.1 discusses the RF sensor type and location on the drone aircraft. Section 3.2 presents the missile dynamics models applied in the research along with the observation model for the sensor measurements. Section 3.3 explains the process applied to reduce the impact of clutter through gating and data association. Section 3.4 explains the approach for initializing missile parameters to begin Kalman filter estimation. Section 3.5 outlines the algorithms for the three nonlinear Kalman filters.

#### *3.1 Aircraft Sensor Configuration*

The results for this research are based on the performance of an existing automotive FMCW sensor with a one-sigma range resolution of  $0.01 \times$  range and a range-rate resolution of 0.25 meters per second [32]. A maximum sensor range of 350 meters

is assumed, although advertised range for the existing sensor is 240 meters against a truck sized target.

In order to overcome the short range of the radar sensors and high closure speed of the missile, each antenna transmits energy uniformly throughout its field of view rather than employing a sweeping pattern. The downside is measurements are limited to range and radial velocity, and no angular information is exploited.

The geometry of the sensor configuration is critical to the precision of state estimates. As explained in Section 2.6, multilateration precision is sensitive to changes in the geometry of the sensors relative to the target. For example, GPS is well known system which employs multilateration to calculate position. The position dilution of precision (PDOP) quantifies the increase in position uncertainty caused by a suboptimal satellite configuration [24]. The lowest PDOP is achieved when the satellites are distributed uniformly about the target [24]. Unfortunately, the placement of radar sensors on the target aircraft is constrained by the dimensions of the aircraft. However, the general principle of maximizing the angular spacing of the sensors as viewed from the incoming missile still applies. The same concept is relevant to velocity calculations.

This research assumes an F-16 aircraft is the platform for the vector scoring system. This aircraft has an approximate length and wingspan of 16 meters and 10 meters, respectively. To reduce errors in missile navigation states, seven antennas are located on the aircraft as follows: one directional antenna on the top and bottom of the nose section, one directional antenna on the top and bottom of each wingtip, and an omnidirectional antenna on the aircraft tail. Using this configuration, missile trajectories that approach in-plane with a wings level aircraft will create problems for scoring, but any trajectories from above or below will have excellent sensor visibility.

The locations of the sensors in the body frame are summarized in Table 3.1 where the origin of the body frame is defined by the geometric center of the aircraft.

Table 3.1: Radar Sensor Locations in Aircraft Body Frame

Sensor Number	Location	x (m)	y (m)	z (m)
1	Nose-Top	8	0	-0.5
2	Nose-Bottom	8	0	0.5
3	Lt Wing-Top	0	-5	0
4	Lt Wing-Bottom	0	-5	0.1
5	Rt Wing-Top	0	5	0
6	Rt Wing-Bottom	0	5	0.1
7	Tail	-8	0	-1

### 3.2 System Model

As previously discussed in Chapter II, implementing a KF requires the development of a system dynamics model and observation model. The dynamics model provides a prediction of the change in missile kinematic states over time. The observation model relates sensor measurements to current missile states corrupted by noise.

*3.2.1 Missile Dynamics Models.* There are numerous basic models used to predict missile motion between measurement updates. This research compares performance using three linear dynamics models: CV, CA, and CT.

*3.2.1.1 Constant Velocity.* Using a Cartesian coordinate frame, the CV model incorporates six navigation states to characterize the missile position and velocity yielding the state vector

$$\mathbf{x} = \begin{bmatrix} x & y & z & v_x & v_y & v_z \end{bmatrix}^T \quad (3.1)$$

The general continuous time linear form of the CV dynamics model is

$$\dot{\mathbf{x}}(t) = \mathbf{F}\mathbf{x}(t) + \mathbf{G}\mathbf{w}(t) \quad (3.2)$$

where

$$\mathbf{F} = \left[ \begin{array}{c|c} \mathbf{0}_{3 \times 3} & \mathbf{I}_{3 \times 3} \\ \hline \mathbf{0}_{3 \times 3} & \mathbf{0}_{3 \times 3} \end{array} \right] \quad (3.3)$$

$$\mathbf{G} = \left[ \begin{array}{c} \mathbf{0}_{3 \times 3} \\ \hline \mathbf{I}_{3 \times 3} \end{array} \right] \quad (3.4)$$

and the strength of the noise vector  $\mathbf{w}(t)$  is defined by

$$E[\mathbf{w}(t)\mathbf{w}(t + \tau)] = \mathbf{Q} = \begin{bmatrix} q & 0 & 0 \\ 0 & q & 0 \\ 0 & 0 & q \end{bmatrix} \quad (3.5)$$

The variable  $q$  is adjusted during filter tuning to improve performance.

In an inertial reference frame, the CV model assumes a constant velocity along each axis while acceleration along each axis is modeled by an independent, zero-mean, Gaussian, white noise. For this research the propagation time steps are in milliseconds, and the missile is tracked for a short duration of a couple seconds. Therefore, a flat Earth is assumed and missile propagation is performed in a local-level navigation frame with an origin on the surface of the Earth (i.e. n-frame approximates i-frame).

Converting the dynamics model into discrete time, the general form for the difference equation is

$$\mathbf{x}_k = \boldsymbol{\phi}\mathbf{x}_{k-1} + \mathbf{G}\mathbf{w}_{k-1} \quad (3.6)$$

This result is similar to Equation (2.12) except the deterministic input,  $u_k$  is zero for this estimation problem. Applying the Van Loan [7] method to solve for the state transition matrix,  $\boldsymbol{\phi}$ , and the noise strength matrix,  $\mathbf{Q}_d$ , yields [5]

$$\phi = \begin{bmatrix} 1 & 0 & 0 & T & 0 & 0 \\ 0 & 1 & 0 & 0 & T & 0 \\ 0 & 0 & 1 & 0 & 0 & T \\ 0 & 0 & 0 & 1 & 0 & 0 \\ 0 & 0 & 0 & 0 & 1 & 0 \\ 0 & 0 & 0 & 0 & 0 & 1 \end{bmatrix} \quad (3.7)$$

$$\mathbf{Q}_d = \begin{bmatrix} \frac{T^3}{3} & 0 & 0 & \frac{T^2}{2} & 0 & 0 \\ 0 & \frac{T^3}{3} & 0 & 0 & \frac{T^2}{2} & 0 \\ 0 & 0 & \frac{T^3}{3} & 0 & 0 & \frac{T^2}{2} \\ \frac{T^2}{2} & 0 & 0 & T & 0 & 0 \\ 0 & \frac{T^2}{2} & 0 & 0 & T & 0 \\ 0 & 0 & \frac{T^2}{2} & 0 & 0 & T \end{bmatrix} q \quad (3.8)$$

where the variable  $T$  represents the propagation time step which is determined by the sensor measurement rate.

*3.2.1.2 Constant Acceleration.* A CA model includes three additional navigation states to estimate acceleration along each axis. The resulting state vector is

$$\mathbf{x} = \left[ x \quad y \quad z \quad v_x \quad v_y \quad v_z \quad a_x \quad a_y \quad a_z \right]^T \quad (3.9)$$

The general continuous time linear form for the CA dynamics model is identical to Equation 3.2, with the new  $\mathbf{F}$  and  $\mathbf{G}$  matrices

$$\mathbf{F} = \begin{bmatrix} \mathbf{0}_{3 \times 3} & \mathbf{I}_{3 \times 3} & \mathbf{0}_{3 \times 3} \\ \mathbf{0}_{3 \times 3} & \mathbf{0}_{3 \times 3} & \mathbf{I}_{3 \times 3} \\ \mathbf{0}_{3 \times 3} & \mathbf{0}_{3 \times 3} & \mathbf{0}_{3 \times 3} \end{bmatrix} \quad (3.10)$$

$$\mathbf{G} = \begin{bmatrix} \mathbf{0}_{6 \times 3} \\ \mathbf{I}_{3 \times 3} \end{bmatrix} \quad (3.11)$$

The dynamic noise strength matrix,  $\mathbf{Q}$ , is in the same form as Equation (3.5). In this model the acceleration rate-of-change, or jerk, along each axis is modeled by an independent, zero-mean, Gaussian, white noise. Calculating the equivalent discrete time system for the the CA model results in [5]

$$\phi = \begin{bmatrix} 1 & 0 & 0 & T & 0 & 0 & \frac{T^2}{2} & 0 & 0 \\ 0 & 1 & 0 & 0 & T & 0 & 0 & \frac{T^2}{2} & 0 \\ 0 & 0 & 1 & 0 & 0 & T & 0 & 0 & \frac{T^2}{2} \\ 0 & 0 & 0 & 1 & 0 & 0 & T & 0 & 0 \\ 0 & 0 & 0 & 0 & 1 & 0 & 0 & T & 0 \\ 0 & 0 & 0 & 0 & 0 & 1 & 0 & 0 & T \\ 0 & 0 & 0 & 0 & 0 & 0 & 1 & 0 & 0 \\ 0 & 0 & 0 & 0 & 0 & 0 & 0 & 1 & 0 \\ 0 & 0 & 0 & 0 & 0 & 0 & 0 & 0 & 1 \end{bmatrix} \quad (3.12)$$

$$\mathbf{Q}_d = \begin{bmatrix} \frac{T^5}{20} & 0 & 0 & \frac{T^4}{8} & 0 & 0 & \frac{T^3}{6} & 0 & 0 \\ 0 & \frac{T^5}{20} & 0 & 0 & \frac{T^4}{8} & 0 & T & \frac{T^3}{6} & 0 \\ 0 & 0 & \frac{T^5}{20} & 0 & 0 & \frac{T^4}{8} & 0 & 0 & \frac{T^3}{6} \\ \frac{T^4}{8} & 0 & 0 & \frac{T^3}{3} & 0 & 0 & \frac{T^2}{2} & 0 & 0 \\ 0 & \frac{T^4}{8} & 0 & 0 & \frac{T^3}{3} & 0 & 0 & \frac{T^2}{2} & 0 \\ 0 & 0 & \frac{T^4}{8} & 0 & 0 & \frac{T^3}{3} & 0 & 0 & \frac{T^2}{2} \\ \frac{T^3}{6} & 0 & 0 & \frac{T^2}{2} & 0 & 0 & T & 0 & 0 \\ 0 & \frac{T^3}{6} & 0 & 0 & \frac{T^2}{2} & 0 & 0 & T & 0 \\ 0 & 0 & \frac{T^3}{6} & 0 & 0 & \frac{T^2}{2} & 0 & 0 & T \end{bmatrix} \mathbf{q} \quad (3.13)$$

3.2.1.3 *Three-dimensional Coordinated Turn.*

The CT model includes the same states as the CA model defined in Equation (3.9). The  $\mathbf{F}$  and  $\mathbf{G}$  matrices for the continuous time linear dynamics model are [5]

$$\mathbf{F} = \begin{bmatrix} \mathbf{0}_{3 \times 3} & \mathbf{I}_{3 \times 3} & \mathbf{0}_{3 \times 3} \\ \mathbf{0}_{3 \times 3} & \mathbf{0}_{3 \times 3} & \mathbf{I}_{3 \times 3} \\ \mathbf{0}_{3 \times 3} & \mathbf{A} & \mathbf{0}_{3 \times 3} \end{bmatrix} \quad (3.14)$$

$$\mathbf{A} = \begin{bmatrix} -\omega^2 & 0 & 0 \\ 0 & -\omega^2 & 0 \\ 0 & 0 & -\omega^2 \end{bmatrix} \quad (3.15)$$

$$\mathbf{G} = \begin{bmatrix} \mathbf{0}_{6 \times 3} \\ \mathbf{I}_{3 \times 3} \end{bmatrix} \quad (3.16)$$

During filter propagation, the angular turn-rate,  $\omega$ , is calculated after each update using the *a posteriori* estimate of missile velocity and acceleration in the formula

$$\omega = \frac{|\mathbf{v} \times \mathbf{a}|}{|\mathbf{v}|^2} \quad (3.17)$$

This model assumes the magnitude of the target velocity vector is constant, but the velocity components along each axis change as the target turns. Furthermore, a constant angular turn rate,  $\omega$ , is assumed over each propagation time step. The rate-of-change of the acceleration vector is defined as [5]

$$\dot{\mathbf{a}}(t) = -\omega^2 \mathbf{v}(t) + \mathbf{w}(t) \quad (3.18)$$

where  $\mathbf{v}(t)$  is the missile's velocity vector and  $\mathbf{w}(t)$  is a vector of independent, zero-mean, Gaussian, white noise sources. The strength of the noise vector,  $\mathbf{w}(t)$ , matches the form in Equation (3.5) and is tailorable by selecting an appropriate value for  $q$ .

In discrete time, the CT model state transition matrix is a function of  $\omega$  as described by [5]

$$\phi(\omega) = \begin{bmatrix} \mathbf{A}(\omega) & \mathbf{0}_{3 \times 3} & \mathbf{0}_{3 \times 3} \\ \mathbf{0}_{3 \times 3} & \mathbf{A}(\omega) & \mathbf{0}_{3 \times 3} \\ \mathbf{0}_{3 \times 3} & \mathbf{0}_{3 \times 3} & \mathbf{A}(\omega) \end{bmatrix} \quad (3.19)$$

where  $\mathbf{A}(\omega)$  is defined as

$$\mathbf{A}(\omega) = \begin{bmatrix} 1 & \frac{\sin \omega T}{\omega} & \frac{1 - \cos \omega T}{\omega^2} \\ 0 & \cos \omega T & \frac{\sin \omega T}{\omega} \\ 0 & -\omega \sin \omega T & \cos \omega T \end{bmatrix} \quad (3.20)$$

The closed form solution for the CT model's discrete noise strength,  $\mathbf{Q}_d$ , is intentionally omitted due to complexity. However, given a value of  $\omega$ , the numerical solution is relatively straight forward by application of the Van Loan method described in Chapter II. The interested readers is referred to [5] for details.

*3.2.2 Observation Model.* Range and range-rate measurements are a nonlinear function of system states. Therefore, this research utilizes a nonlinear measurement model with a vector of independent, additive, zero-mean, Gaussian, white noise sources in the general form of Equation 2.19 [18].

The range measurement from the  $i$ -th sensor is related to the system states according to

$$r_i = \sqrt{(x - x_i)^2 + (y - y_i)^2 + (z - z_i)^2} \quad (3.21)$$

The sensor coordinates,  $[x_i \ y_i \ z_i]$ , are easily defined in the aircraft body frame, but must be converted into the same reference frame as the missile state vector. In this research, the missile state vector is expressed in a local level Earth-fixed navigation

frame. In addition, radar radial velocity measurements from the  $i$ -th sensor are defined by

$$v_i = -\frac{(v_x - v_{x_i})(x - x_i) + (v_y - v_{y_i})(y - y_i) + (v_z - v_{z_i})(z - z_i)}{\sqrt{(x - x_i)^2 + (y - y_i)^2 + (z - z_i)^2}} \quad (3.22)$$

### ***3.3 Gating and Data Association Implementation***

The radar sensors for the missile scoring system are unlikely to see a large number of false returns in their operating environment for several reasons. First of all, the FMCW sensors are short range so the volume of airspace they observe is extremely limited. Secondly, a drone aircraft equipped with a missile scoring system for missile test and evaluation is generally operated in visual meteorological conditions for safety. However, the algorithm used in this research does include two features to limit the impact of false radar returns: gating and data association.

Square and ellipsoidal gating are applied sequentially as described in Section 2.8. Since multiple sensors are employed for this end-game missile scoring system, gating is applied to measurements from each sensor separately. If multiple measurements from a single sensor survive gating then GNN data association is applied as outlined in Section 2.8.

### ***3.4 Target Initialization***

The nonlinear KF algorithms used in this research are initialized by simulating missile position and velocity information from an external source. Most air-to-air missile test and evaluation ranges include a system which monitors missile position for safety. For example, missile testing performed at Tyndall Air Force Base (AFB) utilizes the Gulf range drone control system (GRDCS) [16]. This system provides position accuracy of approximately 15 meters in the x and y-axis and 45 meters in the z-axis. The data update rate is 20 Hz and velocity is determined by calculating the change in position over one time step. Based on the GRDCS system the missile state vector is set equal to truth with a random position and velocity error added to each

axis from a zero-mean normal distribution with the following standard deviations:  $\sigma_x = 15$ ,  $\sigma_y = 15$ ,  $\sigma_z = 45$ ,  $\sigma_{v_x} = 10$ ,  $\sigma_{v_y} = 10$  and  $\sigma_{v_z} = 10$ . Furthermore, the initial covariance matrix is set according to the GRDCS uncertainty as

$$P_0 = \begin{bmatrix} \sigma_x^2 & 0 & 0 & 0 & 0 & 0 \\ 0 & \sigma_y^2 & 0 & 0 & 0 & 0 \\ 0 & 0 & \sigma_z^2 & 0 & 0 & 0 \\ 0 & 0 & 0 & \sigma_{v_x}^2 & 0 & 0 \\ 0 & 0 & 0 & 0 & \sigma_{v_y}^2 & 0 \\ 0 & 0 & 0 & 0 & 0 & \sigma_{v_z}^2 \end{bmatrix} \quad (3.23)$$

An alternate approach is to initialize the target purely based on sensor measurements through multilateration as described in Section 2.6. A downside to this approach is it requires four measurements. If target detection probability is low, the multilateration procedure will not have sufficient information to initialize the target state vector [10]. Alternatively, if the sensors see large numbers of ghost targets, the multilateration process requires the tracking of multiple target hypotheses. Track scoring is one possible technique for making decisions on which track is the true target [5]. However, in a multiple target and high clutter environment this approach becomes computationally burdensome. Fortunately, in target scoring applications with short range sensors, a low clutter environment is probable.

### ***3.5 Nonlinear Kalman Filter Implementation***

As explained in Section 2.4, a conventional KF is inadequate to deal with the nonlinearities present in the system observation model. When performing estimation of nonlinear systems there is no single optimal approach for all problems. Some nonlinear filters may have an advantage in computational burden while another has superior precision or reduced complexity. Therefore, three different nonlinear Kalman filters are implemented in this research: an EKF, UKF, and PF. In Chapter IV their performance is compared to assess advantages when utilized in an end-game missile

scoring system. Appendix C includes the computer algorithms developed for this research. This software includes the main EKF, UKF, and PF programs along with all associated subprograms for performing the simulations detailed in Chapter IV.

Since all of the dynamics models considered in this research are linear, conventional KF Equations (2.14)-(2.16) are applied to propagate the state estimates in both the EKF and UKF filters. The PF uses a slightly different approach as outlined previously in Section 2.4.3.

*3.5.1 Extended Kalman Filter.* An EKF deals with nonlinearities in a system observation model by linearizing about a nominal measurement using a first-order Taylor series approximation. In order to linearize the observation model a Jacobian matrix is calculated as described in Section 2.4.1. The matrix is then evaluated at the *a priori* estimate according to Equation (2.20). For this end-game missile scoring application, when utilizing the CV missile dynamics model, the resulting  $H$  matrix is in the form

$$\mathbf{H} = \begin{bmatrix} \frac{\delta r_i}{\delta x} & \frac{\delta r_i}{\delta y} & \frac{\delta r_i}{\delta z} & \frac{\delta r_i}{\delta v_x} & \frac{\delta r_i}{\delta v_y} & \frac{\delta r_i}{\delta v_z} \\ \frac{\delta v_i}{\delta x} & \frac{\delta v_i}{\delta y} & \frac{\delta v_i}{\delta z} & \frac{\delta v_i}{\delta v_x} & \frac{\delta v_i}{\delta v_y} & \frac{\delta v_i}{\delta v_z} \end{bmatrix} \quad (3.24)$$

For the more complex nine state Kalman filters based on the CA or CT dynamics model, the general form of the  $H$  matrix is

$$\mathbf{H} = \begin{bmatrix} \frac{\delta r_i}{\delta x} & \frac{\delta r_i}{\delta y} & \frac{\delta r_i}{\delta z} & \frac{\delta r_i}{\delta v_x} & \frac{\delta r_i}{\delta v_y} & \frac{\delta r_i}{\delta v_z} & \frac{\delta r_i}{\delta a_x} & \frac{\delta r_i}{\delta a_y} & \frac{\delta r_i}{\delta a_z} \\ \frac{\delta v_i}{\delta x} & \frac{\delta v_i}{\delta y} & \frac{\delta v_i}{\delta z} & \frac{\delta v_i}{\delta v_x} & \frac{\delta v_i}{\delta v_y} & \frac{\delta v_i}{\delta v_z} & \frac{\delta v_i}{\delta a_x} & \frac{\delta v_i}{\delta a_y} & \frac{\delta v_i}{\delta a_z} \end{bmatrix} \quad (3.25)$$

The partial derivatives of Equations (3.21) and (3.22) used to populate the  $\mathbf{H}$  matrix are summarized below [36]<sup>1</sup>:

---

<sup>1</sup>The expressions  $r_i$  and  $v_i$  are substituted wherever possible to keep the length of the equations manageable.

$$\frac{\delta r_i}{\delta x} = \frac{x - x_i}{r_i} \quad (3.26)$$

$$\frac{\delta r_i}{\delta y} = \frac{y - y_i}{r_i} \quad (3.27)$$

$$\frac{\delta r_i}{\delta z} = \frac{z - z_i}{r_i} \quad (3.28)$$

$$\frac{\delta r_i}{\delta v_x} = \frac{\delta r_i}{\delta v_y} = \frac{\delta r_i}{\delta v_z} = 0 \quad (3.29)$$

$$\frac{\delta r_i}{\delta a_x} = \frac{\delta r_i}{\delta a_y} = \frac{\delta r_i}{\delta a_z} = 0 \quad (3.30)$$

$$\frac{\delta v_i}{\delta x} = -\frac{v_i(x - x_i)}{r_i^2} - \frac{v_x - v_{x_i}}{r_i} \quad (3.31)$$

$$\frac{\delta v_i}{\delta y} = -\frac{v_i(y - y_i)}{r_i^2} - \frac{v_y - v_{y_i}}{r_i} \quad (3.32)$$

$$\frac{\delta v_i}{\delta z} = -\frac{v_i(z - z_i)}{r_i^2} - \frac{v_z - v_{z_i}}{r_i} \quad (3.33)$$

$$\frac{\delta v_i}{\delta v_x} = -\frac{x - x_i}{r_i} \quad (3.34)$$

$$\frac{\delta v_i}{\delta v_y} = -\frac{y - y_i}{r_i} \quad (3.35)$$

$$\frac{\delta v_i}{\delta v_z} = -\frac{z - z_i}{r_i} \quad (3.36)$$

$$\frac{\delta v_i}{\delta a_x} = \frac{\delta v_i}{\delta a_y} = \frac{\delta v_i}{\delta a_z} = 0 \quad (3.37)$$

Next, nominal range and radial velocity measurements for each sensor are calculated by evaluating Equations (3.21) and (3.22) at the *a priori* estimate. As noted in Section 3.2.2, the coordinates of the sensors must be converted into the same reference frame as the missile state vector.

The perturbation state vector,  $\delta \mathbf{z}$ , contains the difference between the realized sensor measurements of range and radial velocity and the nominal. The size of  $\delta \mathbf{z}$  is dependent on the number of sensors with measurements that survive the gating process. For example, if sensors one and three detect the target and these measurements survive gating the resulting perturbation state vector is a four-by-one in the general form

$$\delta \mathbf{z} = \begin{bmatrix} \delta r_1 \\ \delta v_1 \\ \delta r_3 \\ \delta v_3 \end{bmatrix} \quad (3.38)$$

where  $\delta r_i$  represents the difference between the  $i$ -th sensor realized range measurement and calculated nominal measurement. Similarly,  $\delta v_i$  is the difference between the  $i$ -th sensor realized radial velocity measurement and nominal. A common discrete time subscript,  $k$ , is implied in Equations (3.24)-(3.38) and is intentionally omitted to avoid confusion with the sensor number subscript.

Finally, the *aposteriori* state estimate,  $\hat{\mathbf{x}}_k^+$ , and uncertainty,  $\mathbf{P}_k^+$  are updated using the resulting  $\mathbf{H}$  matrix and perturbation state vector according to Equations (2.16), (2.18) and (2.23).

*3.5.2 Unscented Kalman Filter.* Section 2.4.2 describes the UKF algorithm in detail. For this research, the initial sigma points locations are calculated after time

propagation using Equations (2.24)-(2.28). The scaling factor,  $\lambda$ , is determined by setting the tuning parameters  $\alpha$  and  $\kappa$  to 0.1 and zero, respectively.

Next, each sigma point is transformed into observation space by evaluating Equations (3.21)-(3.22) at their respective location. To clarify, each sigma point is a representation of the missile state vector (i.e., the weighted sum of all sigma points is the estimate of the state vector). Therefore, the missile location,  $[x \ y \ z]$ , and velocity,  $[v_x \ v_y \ v_z]$ , needed to evaluate Equations (3.21)-(3.22) comes directly from rows one through six of each sigma point.

After transforming all of the sigma points, a measurement prediction and uncertainty are calculated for the  $i$ -th sensor using Equations (2.30)-(2.34). Gating is then applied to the measurements from each sensor. The best surviving measurement from each sensor, as defined by GNN data association, is saved for missile state update. In addition, the transformed sigma points,  $\mathcal{Z}$ , from sensors with surviving measurements are saved for performing the *aposteriori* update. For example, if measurements are saved from sensors three and seven, the measurement vector,  $\mathbf{z}$ , is of the form

$$\mathbf{z} = \begin{bmatrix} r_3 \\ v_3 \\ r_7 \\ v_7 \end{bmatrix} \quad (3.39)$$

and  $\mathcal{Z} \in \mathbb{R}^{4 \times 2L+1}$ , where  $L$  is the number of missile states. Finally, the surviving measurements are used to calculate the *aposteriori* state estimate and uncertainty via Equations (2.30)-(2.38). Discrete time subscripts are again omitted in this section for clarity.

*3.5.3 Particle Filter.* Implementation of the PF is similar to the UKF. As discussed in Section 2.4.3, sample points replace the sigma points for representing the pdf of the missile state vector. For this application, the initial sample points are generated when the filter is initialized using data from the GRDCS. Equation (2.39) is

used to randomly generate the initial particle locations and all particles are weighted equally according to Equation (2.41).

Propagation of the missile state estimate in the PF is accomplished by transforming each particle through the linear dynamics function as illustrated in Equation (2.42). Random noise, consistent with the statistics of the noise sources in the dynamics model, is added to each particle as described in Section 2.4.3. As a result of particle propagation, the location of each particle changes while its weight remains the same. The *a priori* state estimate and uncertainty is determined from resulting particle locations as outlined in Equations (2.44) and (2.45).

Measurement updates for the PF are performed in an analogous fashion to the UKF. Each particle is transformed through Equations (3.21) and (3.22). The transformed particles are used to predict each sensor's measurement and the associated uncertainty. Gating is then applied to eliminate unlikely measurements from each sensor and the closest remaining measurements and associated particles are saved for state update. To perform the *aposteriori* update, the saved measurements are applied to adjust the particle locations and weights according to Equations (2.47)-(2.51). Finally, the updated state estimate,  $\mathbf{x}_k^+$ , and uncertainty,  $\mathbf{P}_{x_k}^+$ , are calculated from the new particle locations and weights using Equations (2.44) and (2.45).

Unfortunately, this application requires a large quantity of particles to avoid particle starvation. Particle starvation is often an issue in particle filters with uncertain dynamics models (i.e., large system noise,  $\mathbf{Q}$ ) and highly precise sensor measurements (i.e., low sensor noise,  $\mathbf{R}$ ). When a measurement update is performed, the weights of particles are adjusted based on their likelihood given the measurement realization according to Equations (2.48)-(2.50). A large ratio of system noise to sensor noise often results in the majority of the particles having zero weight. The resulting statistics for the missile state vector may be based on an insufficient number of particles and filter divergence may occur.

Particle resampling is a method used to mitigate particle starvation by eliminating particles with low importance weight and multiplying particles with high importance weight [20]. There are a number of different options for performing resampling, including sampling-importance resampling (SIR), residual resampling, and minimum variance resampling [20]. This research employs SIR after every measurement update.

The SIR method starts with  $NP$  particles, each with an associated weight,  $W_j$  (i.e.,  $W_1$  refers to the weight of particle one). Next, the weight of the particles are stacked as depicted in Figure 3.1 where the x-axis consists of particles one to  $NP$  and the y-axis is the cumulative sum of the weights. For example, the figure shows particle 7 with a weight of  $W_7$ . Next, a random draw is performed  $NP$  times from a uniform distribution between zero and one. Each random draw maps to one of the  $NP$  original particles. To perform the mapping, select a y value equal to the draw and then move horizontally across until reaching the cumulative sum of the weights line. Then, drop vertically down to the x-axis particle number. For example, if a random draw of 0.15 is selected it maps to particle number one as shown in Figure 3.1. By following this process SIR maps  $NP$  particles with variable weights into  $NP$  particles with constant weights by changing their locations so that the underlying statistics of the particles are comparable. Since the draw is random, the statistics will only be identical as  $NP$  approaches infinity.

Despite employing particle resampling, the PF still demonstrates issues when employed in this end-game missile scoring application. Due to the large  $\mathbf{Q}$ -to- $\mathbf{R}$  ratio, there are frequently only a small number of particles left after just one propagation and update. Therefore, when SIR is employed the new particles are based on relatively few original particles with high importance weight. The result is poor accuracy and potential instability. The brute force method for dealing with this issue is to utilize more particles. The PF implemented for this research employs 50,000 particles to avoid particle starvation and reduce the impact on estimation accuracy.

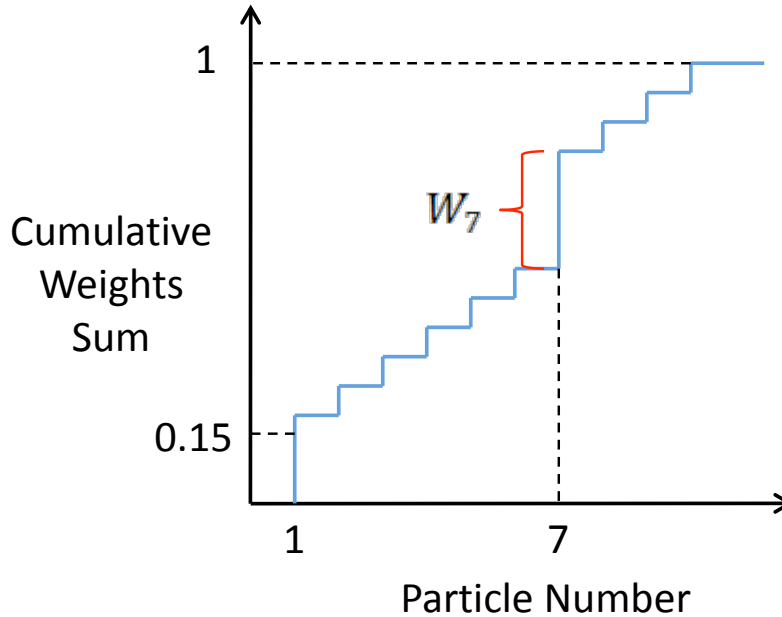


Figure 3.1: Sampling-Importance Resampling Procedure

Unfortunately, increasing particle numbers results in inefficiency and large computational burden. A 100 run Monte Carlo simulation using a PF with 50,000 particles takes approximately 48 mins and 9 seconds<sup>2</sup>. In contract, the EKF and UKF filters perform a 100 run Monte Carlo simulation in approximately 8.7 and 10.5 seconds, respectively. An alternative to increasing the particle number is available through the application of either an extended particle filter (EPF) or a unscented particle filter (UPF) [20]. The basic concept is to apply a bank of  $N$  EKF or UKF filters to move particles from low likelihood regions into high likelihood regions based on the measurement realization. This approach is not explored further in this research, but Merwe, Doucet, Freitas and Wan provide a comprehensive discussion on the EPF and UPF, including algorithms for implementation [20].

---

<sup>2</sup>Result based on the average execution time across all three scenarios described in Chapter IV using a CV dynamics model. The simulations are performed on a Macbook with a 2.13 GHz Intel Core 2 Duo processor.

### ***3.6 Summary***

This chapter documented the methodology applied to implement the proposed air-to-air missile scoring system. First, sensor placement on the drone aircraft was addressed and locations were proposed with justification. Next, three missile dynamics models were derived for implementation within the Kalman filter algorithm: a CV, CA, and CT. Also, the observation model was presented as a function of missile states based on the available sensor measurements of range and range-rate. The remainder of the chapter described the specific implementation of the three nonlinear Kalman filter algorithms: an EKF, UKF, and PF. The description included an explanation of the target initialization process and a discussion of gating and data association implementation. The final section of this chapter compares the processing speed of the three Kalman filter algorithms for the missile scoring application and foreshadows the topic of the next chapter. The next chapter provides the methodology and results from simulations designed to assess the overall performance of the scoring system and compare the three proposed missile dynamics models and Kalman filter algorithms.

## IV. Simulations

The proposed missile scoring solution is tested in three simulated scenarios to establish performance. Scenario 1 is a non-maneuvering target attacked vertically from below. Scenario 2 involves a tail-aspect attack against an aware adversary performing an aggressive 9G descending break-turn into the shooter. Scenario 3 is also a tail-aspect attack, but the target performs a 7G vertical maneuver. Section 4.1 discusses the scenarios in greater detail. Section 4.2 describes the truth model used to generate the scenarios and assess scoring performance.

A systematic approach to filter tuning is applied across all of the nonlinear filters evaluated in this research. Furthermore, target initialization error and sensor noise is randomly generated for each scenario and for each Monte Carlo run and then saved, so the same noise realization is used in all nonlinear filters. In other words, during the 100 run Monte Carlo analysis, each filter method is subjected to the same set of 100 sample functions of noise and 100 random initial hand-off errors. This approach insures valid conclusions are drawn when comparing the performance of different missile dynamics models and nonlinear Kalman filters. Section 4.3 outlines the tuning process and explains the justification behind the procedure. Section 4.4 provides samples of the randomly generated noise realizations to demonstrate statistical properties (i.e., sensor and initialization errors are shown to be normally distributed with desired mean and standard deviation).

Sections 4.5 and 4.6 compare the results from simulations to draw conclusions about which nonlinear KF and dynamics model provide the greatest precision in missile state estimates at impact. Since this research considers three scenarios, three dynamics models, and three nonlinear Kalman filters, there are a total of 27 simulation combinations. Only the highlights are addressed in this chapter, but Appendix A includes a comprehensive record of simulation results. All of the simulations consist of a 100 run Monte Carlo analysis where error mean and standard deviation are plotted for each of the missile position and velocity states.

Section 4.7 concludes this chapter by assessing the performance of the the best nonlinear KF and dynamics model combination from those considered in this research.

#### 4.1 Scenarios

Figure 4.1 depicts the flight profile for scenario 1. The target aircraft is wings-level, flying northbound at an altitude of 5000 meters and does not maneuver for the duration of the missile intercept. The shooter starts from a position one mile in front of the target on a southbound heading, at an altitude of 500 meters and a 70 degree pitch-up attitude. The true aircraft and missile trajectory are depicted for the entire simulation of approximately eight seconds.

Figure 4.2 illustrates the aircraft and missile 3D trajectory for scenario 2. The drone aircraft begins the simulation in a wings-level attitude, heading north, at an altitude of 5000 meters. After the simulation starts, the target rolls to approximately 120 degrees of bank and initiates a 9G, right-hand, descending turn. This break-turn maneuver is a common defensive tactic employed by an aircraft when targeted by a missile within visual range. Missile impact occurs as the target is passing through an easterly heading at an altitude of about 4300 meters. The shooter fires at the outset

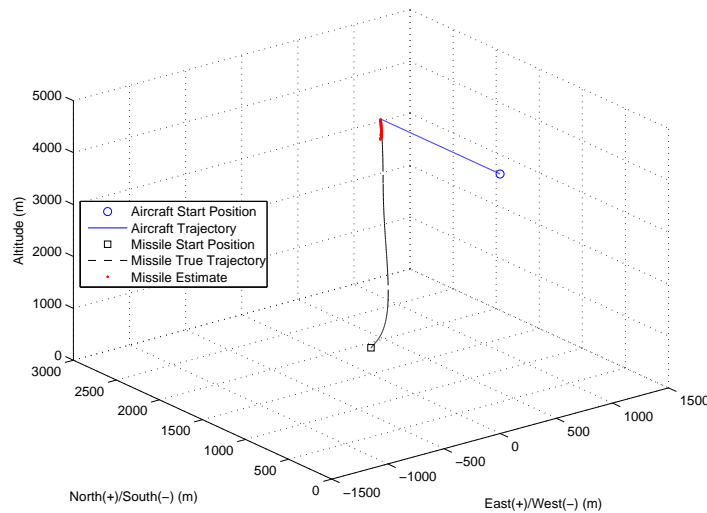


Figure 4.1: Scenario 1: Target Aircraft Non-maneuvering

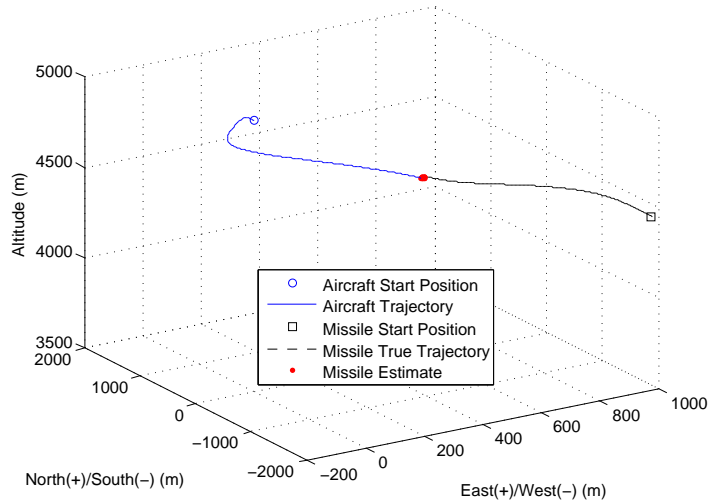


Figure 4.2: Scenario 2: Target Aircraft Performing a 9G Descending Break-Turn of the scenario from a three mile trail position, heading north, at an altitude of 5000 meters.

In scenario 3 the target starts the simulation wings-level, northbound, at an altitude of 5000 meters as shown in Figure 4.3. The shooter starts out two miles in trail with attitude and altitude identical to the target. When the simulation begins, the drone aircraft performs a 7G vertical pull-up while the shooter immediately fires.

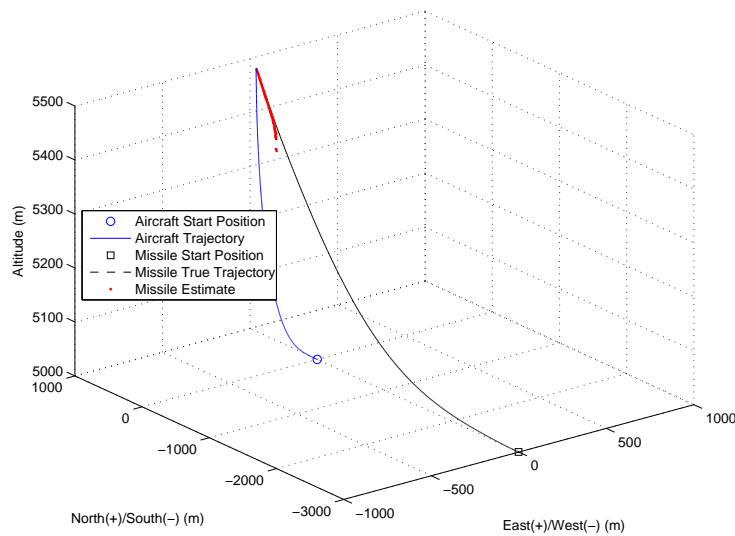


Figure 4.3: Scenario 3: Target Aircraft Performing a Vertical Climb

## 4.2 Truth Model

In order to provide realistic missile truth data in the presented dynamic scenarios, two separate simulation tools are employed: *Profgen* and *Argos 3.0*. *Profgen* takes a vehicle through a series of maneuvers to produce kinematic outputs. These kinematic outputs, which track the motion of an aircraft in six degrees-of freedom (6DOF), provide target information for use in *Argos*. *Argos* is a 6DOF missile simulation tool developed through collaboration between the National Air and Space Intelligence Center (NASIC) and the Air Force Research Laboratories (AFRL).

In *Profgen* [25], the user specifies the dynamic capabilities of the vehicle and directs maneuvers by stringing together basic profile elements such as horizontal and vertical turns, jinks, accelerations, and rolls. Since only the kinematic solution is of interest, *Profgen* models the vehicle as a point-mass body and considerations such as lift, drag, weight, and thrust are substantially reduced. *Profgen* outputs are specified in one of two coordinate frames, World Geodetic System 1984 (WGS 84) or Standard Navigation Unit, with five associated reference frames: inertial, Earth-centered Earth-fixed (ECEF), geodetic, wander-level, and body.

In this research, aircraft data is output in a WGS-84 ECEF reference frame and then externally converted into a local-level Earth-centered NED navigation frame for import into *Argos* and our nonlinear KF algorithms. *Argos* only utilizes target aircraft position and velocity information to compute missile trajectory. In contrast, the Kalman filter requires truth data on aircraft attitude in addition to position and velocity.

*Argos* [3] provides numerous options for missile models and coordinate frames for performing simulations. The simulation results in this research are obtained using an unclassified short-range missile and assuming a flat-Earth environment. The simulation is based in Matlab simulink and the resulting missile kinematic data is output in a NED local-level navigation frame. The true missile position is not known to the

filter, but it's used to generate noise corrupted sensor measurements and compute filter error.

### 4.3 Filter Tuning

The filter tuning is performed during scenario 2 because it represents the most dynamic scenario based on the degree of target maneuvers. Since the filter is required to operate without prior knowledge of the aircraft and missile profile, each filter's tuning parameters are held constant over all three scenarios. Four different parameters are varied during the tuning process: gate size,  $\gamma$ , dynamic noise strength,  $q$ , and two values in the observation noise strength matrix,  $\mathbf{R}$ . The sensor range and velocity noise are assumed to be uncorrelated, so the  $\mathbf{R}$  matrix from a single sensor measurement is in the general form

$$\mathbf{R} = \begin{bmatrix} r_{range} & 0 \\ 0 & r_{velocity} \end{bmatrix} \quad (4.1)$$

where  $r_{range}$  represents the uncertainty associated with sensor range measurements and  $r_{velocity}$  is the uncertainty in sensor velocity measurements. These variables are adjusted independently during the tuning process.

Tuning is initially conducted on the EKF filter using the CV dynamics model. The starting point for the adjustable parameters is selected based on an understanding of how each variable effects the estimation process along with knowledge of actual sensor characteristics. For example, a gamma value of 9.8 is an excellent initial guess because it insures that 99 percent of the true measurements will fall within the confines of ellipsoidal gating. In addition, sensor range measurement errors are 2.5 percent of target range while expected velocity measurement errors are just 0.25 meters per second. Therefore,  $r_{range}$  is an order of magnitude higher than  $r_{velocity}$  at a target range of 100 meters.

Based on this preliminary knowledge, multiple trials are conducted to assess the EKF filter parameters that provide the best position and velocity precision during scenario 2 using a 100 run Monte Carlo analysis. The result for the CV missile dynamics model is  $\gamma = 20$ ,  $q = 1,000$ ,  $r_{range} = 10$ , and  $r_{velocity} = 2$ . The large increase in gate size is not surprising since clutter measurements are low density and uniformly distributed. Therefore, there's a low probability that a clutter measurement will be incorporated into the missile state estimate even with a larger gamma value. As a result, using a larger gamma value provides the benefit of increasing the likelihood that true measurements survive gating without a significant risk of false measurements impacting missile state estimates. The dynamics noise value of 1,000 may appear large relative to  $\mathbf{R}$ , but converting to a discrete dynamics noise strength matrix based on a time step of 10 milliseconds results in

$$\mathbf{Q}_d = \begin{bmatrix} 0.0003 & 0 & 0 & 0.0500 & 0 & 0 \\ 0 & 0.0003 & 0 & 0 & 0.0500 & 0 \\ 0 & 0 & 0.0003 & 0 & 0 & 0.0500 \\ 0.0500 & 0 & 0 & 10 & 0 & 0 \\ 0 & 0.0500 & 0 & 0 & 10 & 0 \\ 0 & 0 & 0.0500 & 0 & 0 & 10 \end{bmatrix} \quad (4.2)$$

When performing filter tuning for different missile dynamics models, only the parameter for dynamics noise strength is adjusted. This varying of  $q$  places a different weight on the missile dynamics model when performing estimations of missile position and velocity. Under this limitation, EKF filter tuning is accomplished for the CA and CT missile models yielding  $q = 500,000$  and  $q = 800,000$ , respectively.

Since all of the nonlinear Kalman filters utilize identical dynamics and observation models, the same filter tuning parameters determined for the EKF are initially applied to the UKF and PF to facilitate performance comparison. This technique works well with the UKF, however, the PF exhibits instability due to particle starvation. As discussed in Section 3.5.3, particle starvation is exacerbated by highly

accurate measurements in the face of uncertain dynamics. In order to avoid this problem while keeping particle numbers to a reasonable level for simulation time constraints,  $r_{range}$  and  $r_{velocity}$  are both increased to 20. Table 4.1 summarizes the tuning parameters used in each filter.

Table 4.1: Summary of Nonlinear Kalman Filter Tuning Parameters

Filter-Dynamics Model	$\gamma$	$q$	$r_{range}$	$r_{velocity}$
EKF-CV	20	1,000	10	2
EKF-CA	20	500,000	10	2
EKF-CT	20	800,000	10	2
UKF-CV	20	1000	10	2
UKF-CA	20	500,000	10	2
UKF-CT	20	800,000	10	2
PF-CV (50,000 Particles)	20	1000	20	20
PF-CA (50,000 Particles)	20	500,000	20	20
PF-CT (50,000 Particles)	20	800,000	20	20

#### 4.4 Noise Generation

During simulations the missile state estimates are affected by randomly generated noise from three general areas. First, there is noise impacting the sensor measurements of range and radial velocity. Second, there are clutter measurements from false returns picked up by the sensors. Third, the initial target state vector contains random errors based on handoff from the GRDCS.

During algorithm testing, radar clutter is simulated separately for each sensor. During each measurement update, individual sensors return observations based upon the true missile position as well as clutter. The true (noise corrupted) observations are generated from truth data by adding random noise from a zero-mean, Gaussian distribution with variance defined by the sensor performance as described in Section 3.1. For clutter, the number of false observations are chosen from random, uniformly distributed integers over the interval [0,3]. Each clutter measurement takes on a value chosen from a random, uniform distribution over the sensor's minimum detection range and range-rate through its maximum detection range and range-rate.

In other words, false returns are modeled uniformly within the sensor volume rather than simulating clutter returns from multiple parts of the missile.

In order to guarantee valid comparisons between the various filter-missile model combinations, two of the three noise areas are seeded such that all filter-missile models see the same noise realizations for a specific run of a given scenario. The radar clutter is the only noise area not seeded because gating effectively eliminates its impact on the missile state estimates. To perform seeding, the sensor and initialization noise is randomly generated according to desired statistical properties during EKF-CV simulations for each of the three scenarios. This data is then saved so the other eight filter-missile model combinations use identical noise.

Figure 4.4 illustrates the statistical properties of the sensor noise from a single sensor during scenario 1. The histograms in Figures 5.4(a) and 5.4(b) depict the number of sensor noise values in each bin for sensor range and radial velocity measurements, respectively. The dashed line plots overlaid on the histograms illustrate the desired Gaussian distribution for comparison. In Figure 5.4(a) it is important to note the noise realizations are actually scaling values since sensor precision is based on target range (i.e., a value of 0.01 indicates the actual noise realization is one percent of the true range).

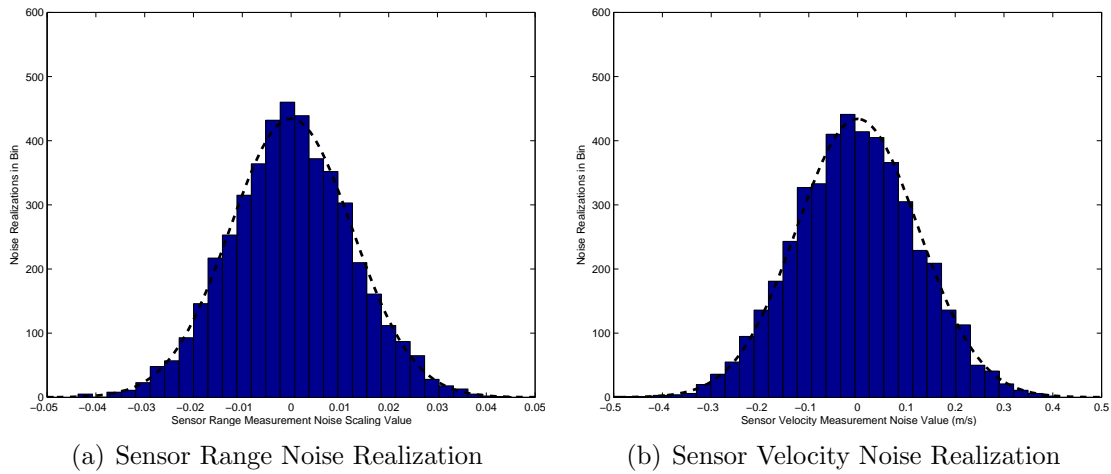
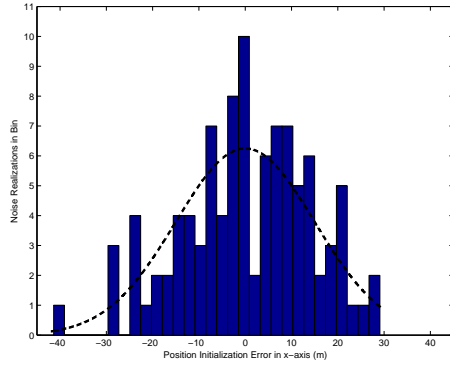
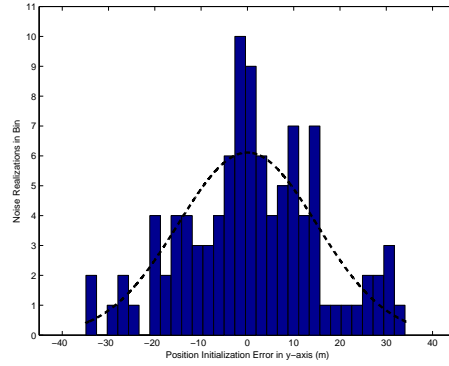


Figure 4.4: Statistical Properties of Random Sensor Noise Realization Utilized for all Scenario 1 Simulations

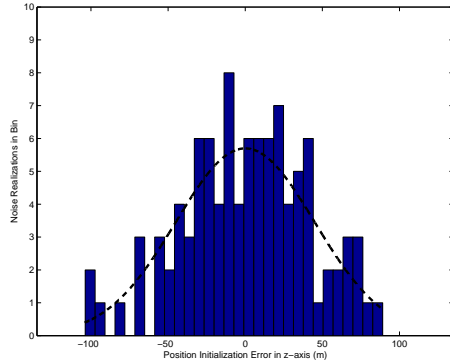
Figure 4.5 provides an illustration of the randomly generated missile state initialization error for the 100 simulated runs in scenario 1. These plots confirm that the initialization noise used in the simulations conform to the expected precision provided by the GRDCS.



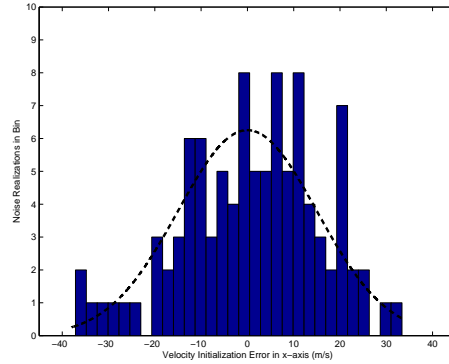
(a) Missile x-axis Position Initialization Noise



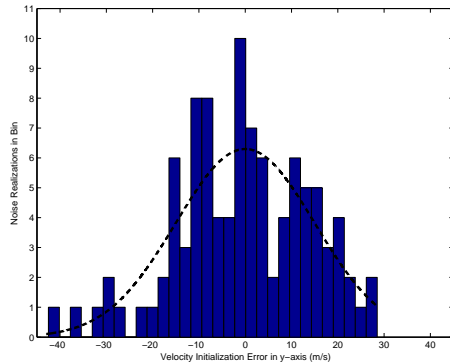
(b) Missile y-axis Position Initialization Noise



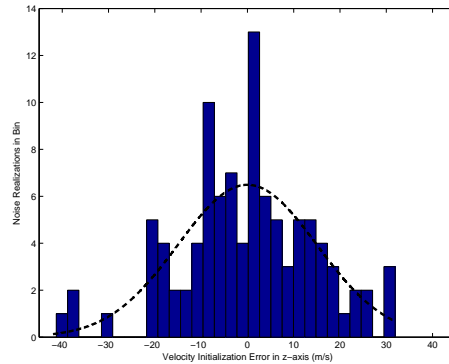
(c) Missile z-axis Position Initialization Noise



(d) Missile x-axis Velocity Initialization Noise



(e) Missile y-axis Velocity Initialization Noise



(f) Missile z-axis Velocity Initialization Noise

Figure 4.5: Statistical Properties of Random Missile Initialization Noise Utilized for all Scenarios

For example, in Figures 5.5(a) and 5.5(b) the x and y axis position error histogram approximates a normal distribution with a standard deviation of 15 meters. The z-axis position error plotted in Figure 5.5(c) follows a normal distribution with a standard deviation of 45 meters. Finally, the velocity error in all axes has a standard deviation of 15 meters per second.

#### 4.5 Dynamics Model Comparison

Of the three dynamics models evaluated, the CV provides the best performance in terms of precision. The precision is assessed by evaluating the missile state error standard deviation at missile impact over a 100 run Monte Carlo analysis. All simulations assume a 10 millisecond sensor measurement rate. Furthermore, the sensor measurements all occur simultaneously based on a common clock. According to the simulation results for the EKF and PF, the CV model exhibited a smaller standard deviation in at least five of the six missile navigation states at impact across all scenarios tested. Table 4.2 provides a sample of the results obtained for the EKF in Scenario 2, where initial filter tuning is conducted (see Appendix A for complete simulation results).

The worst case position precision for scenario 2 appears in the z-axis where the CV model exhibits an error standard deviation of 11.3 centimeters at impact. In comparison, the alternate dynamics models are significantly worse at 19.83 and

Table 4.2: Comparison of Missile State Estimate Error Standard Deviation at Impact for Different Dynamics Models using an Extended Kalman Filter (Scenario 2)

Missile State	CV Model Error Standard Deviation	CA Model Error Standard Deviation	CT Model Error Standard Deviation
$x$	0.0194 m	0.0224 m	0.0231 m
$y$	0.0762 m	0.1210 m	0.1099 m
$z$	0.1130 m	0.1983 m	0.1671 m
$v_x$	0.9391 $\frac{\text{m}}{\text{s}}$	1.9879 $\frac{\text{m}}{\text{s}}$	2.3412 $\frac{\text{m}}{\text{s}}$
$v_y$	6.2837 $\frac{\text{m}}{\text{s}}$	12.9057 $\frac{\text{m}}{\text{s}}$	9.1882 $\frac{\text{m}}{\text{s}}$
$v_z$	8.5262 $\frac{\text{m}}{\text{s}}$	19.7077 $\frac{\text{m}}{\text{s}}$	12.0386 $\frac{\text{m}}{\text{s}}$

16.71 centimeters. Similarly, the worst velocity precision occurs in the z-axis for all dynamics models. Once again, the CV model is much better with a standard deviation of 8.5262 meters per second. The CA shows greater than a 100 percent reduction in precision at 19.7077 meters per second. The CT models shows more than a 40 percent decrease in precision at 12.0386 meters per second.

The simulation results for the UKF are inconsistent, showing marginally higher precision with the CA dynamics models in about half of the missile states at impact. However, this is likely the result of filter tuning. The UKF adopted the same tuning parameters as the EKF and did not undergo independent tuning. One clear indication that the CV model provides better performance is revealed by examining the values of  $q$  used in the dynamics noise matrix for the different models. Filter tuning on the EKF-CV resulted in a  $q$  value of 1,000. In contrast, the CA and CT models used  $q$  values of 500,000 and 800,000, respectively. The large increase in  $q$  is effectively telling the filter to place less trust in the dynamics model and more faith in the measurements. In fact,  $q$  is so high that the filter is almost entirely ignoring the dynamics model.

The CV model also provides an advantage in simplicity and speed. Both the CA and CT model require the estimation of missile state acceleration in addition to position and velocity. These nine state filters result in increased computational complexity over the six state CV model. As a result, the CV filter algorithms will execute faster, especially in the case of the PF.

These results are not surprising since the radar sensors update at the high rate of 10 msec. Since the filter propagation intervals are so small, the missile velocity remains relatively constant over each interval and the CV model closely approximates missile dynamics.

## 4.6 Filter Comparison

An examination of the simulation results demonstrates the UKF is the ideal choice for this missile scoring application based on superior precision. Tables 4.3-4.5 compare the missile state estimate error standard deviation of each nonlinear Kalman filter for each of the three scenarios.

Table 4.3: Comparison of Missile State Estimate Error Standard Deviation at Impact for Different Nonlinear Kalman Filters (Scenario 1)

Missile State	EKF Error Standard Deviation	UKF Error Standard Deviation	PF Error Standard Deviation
$x$	0.0151 m	0.1005 m	0.2259 m
$y$	0.1503 m	0.1265 m	0.3086 m
$z$	0.0354 m	0.0323 m	0.0884 m
$v_x$	5.3800 $\frac{\text{m}}{\text{s}}$	4.7050 $\frac{\text{m}}{\text{s}}$	10.6083 $\frac{\text{m}}{\text{s}}$
$v_y$	9.4838 $\frac{\text{m}}{\text{s}}$	8.0019 $\frac{\text{m}}{\text{s}}$	19.3195 $\frac{\text{m}}{\text{s}}$
$v_z$	1.3355 $\frac{\text{m}}{\text{s}}$	1.1521 $\frac{\text{m}}{\text{s}}$	3.1860 $\frac{\text{m}}{\text{s}}$

Table 4.4: Comparison of Missile State Estimate Error Standard Deviation at Impact for Different Nonlinear Kalman Filters (Scenario 2)

Missile State	EKF Error Standard Deviation	UKF Error Standard Deviation	PF Error Standard Deviation
$x$	0.0194 m	0.0040 m	0.0244 m
$y$	0.0762 m	0.0310 m	0.1261 m
$z$	0.1130 m	0.0317 m	0.1363 m
$v_x$	0.9391 $\frac{\text{m}}{\text{s}}$	0.5608 $\frac{\text{m}}{\text{s}}$	2.6605 $\frac{\text{m}}{\text{s}}$
$v_y$	6.2837 $\frac{\text{m}}{\text{s}}$	2.4432 $\frac{\text{m}}{\text{s}}$	9.4397 $\frac{\text{m}}{\text{s}}$
$v_z$	8.5262 $\frac{\text{m}}{\text{s}}$	2.5532 $\frac{\text{m}}{\text{s}}$	10.3529 $\frac{\text{m}}{\text{s}}$

Table 4.5: Comparison of Missile State Estimate Error Standard Deviation at Impact for Different Nonlinear Kalman Filters (Scenario 3)

Missile State	EKF Error Standard Deviation	UKF Error Standard Deviation	PF Error Standard Deviation
$x$	0.0150 m	0.0052 m	0.0294 m
$y$	0.1521 m	0.1091 m	0.2684 m
$z$	0.2529 m	0.0673 m	0.1728 m
$v_x$	1.7028 $\frac{\text{m}}{\text{s}}$	0.5371 $\frac{\text{m}}{\text{s}}$	1.8390 $\frac{\text{m}}{\text{s}}$
$v_y$	11.8460 $\frac{\text{m}}{\text{s}}$	8.4909 $\frac{\text{m}}{\text{s}}$	20.8787 $\frac{\text{m}}{\text{s}}$
$v_z$	13.7464 $\frac{\text{m}}{\text{s}}$	3.6732 $\frac{\text{m}}{\text{s}}$	9.4543 $\frac{\text{m}}{\text{s}}$

These results are all based on a CV dynamics model since it provides the best performance. The UKF precision at missile impact outperforms the other Kalman filters in 17 of 18 state estimates across the three scenarios.

#### ***4.7 Missile Scoring Performance***

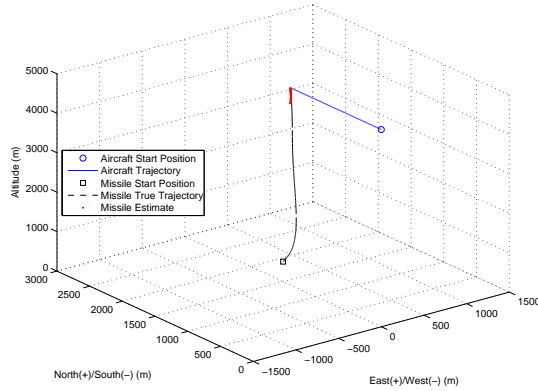
In order to assess the performance of the proposed missile scoring system, the accuracy and precision of the UKF-CV is evaluated in each of the three simulated scenarios. This filter-dynamics model combination is chosen based on its superior precision and reduced complexity over the other options considered.

The results from scenario 1 are recorded in Figure 4.6. Figure 4.6(a) provides a quick graphical reference of the flight profile covered in detail in Section 4.1 . The missile estimate from the proposed scoring system is overlaid on this plot, but is only depicted after the missile reaches the expected sensor range limit of 350 meters.

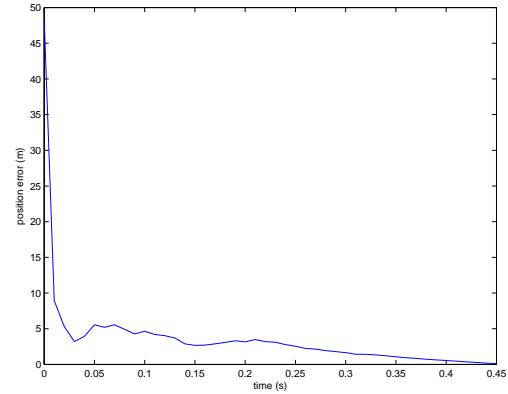
The Root Sum Square (RSS) position error for a single sample run is shown in Figure 4.6(b). The target is randomly initialized for the sample run in accordance with typical GRDCS range accuracies as discussed in Section 3.4. For the particular run shown, the position error is initially about 48 meters and the estimate improves to an end-game error on the order of centimeters. The continuous improvement in the position accuracy as the missile closes on the target is a result of better sensor geometry leading to improved observability of missile states. The final simulation time corresponds to missile impact with the target.

In addition, a 100 run Monte Carlo analysis is performed to evaluate the errors in the estimates of each of the six missile navigation states. Figures 4.6(c) and 4.6(d) record the results and the statistics are summarized in Table 4.6.

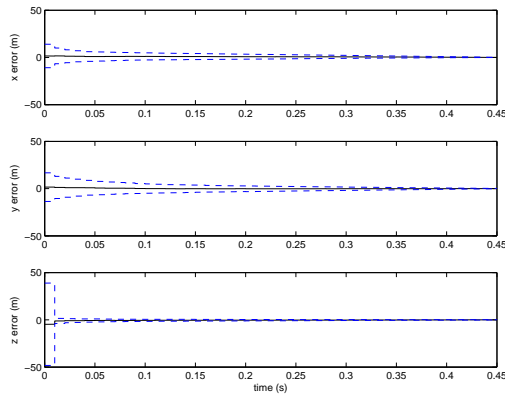
Despite large initialization errors in position, the ensemble mean error for all position states is less than two centimeters at impact and error standard deviation is below 13 centimeters. The ensemble mean error in all velocity states is less than one meter per second. The poorest velocity state precision appears in the y-axis where



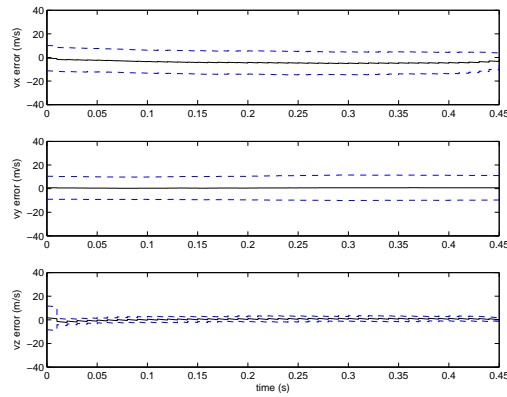
(a) 3D Aircraft and Missile Trajectory



(b) Root Sum Square Error in Missile Position Estimate (1 Run)



(c) Mean Error and Error Standard Deviation of Missile Position States (100 Runs)



(d) Mean Error and Error Standard Deviation of Missile Velocity States (100 Runs)

Figure 4.6: Unscented Kalman Filter Performance in Air-to-Air Missile Scoring Application with Continuous Velocity Dynamics Model (Target Aircraft Non-maneuvering)

Table 4.6: Ensemble Mean Error Statistics for Missile States at Intercept using an Unscented Kalman Filter with Continuous Velocity Dynamics Model (Scenario 1)

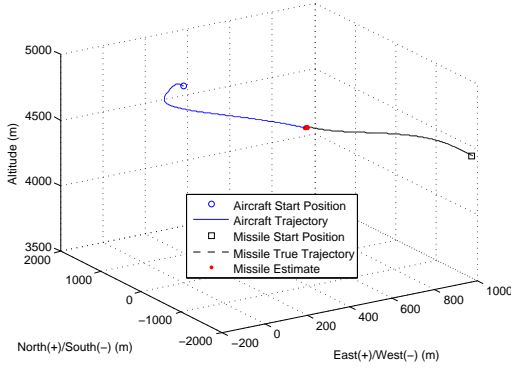
Missile State	Mean Error	Error Standard Deviation
$x$	0.0188 m	0.1005 m
$y$	0.0093 m	0.1265 m
$z$	-0.0166 m	0.0323 m
$v_x$	-0.8801 $\frac{\text{m}}{\text{s}}$	4.7050 $\frac{\text{m}}{\text{s}}$
$v_y$	-0.5921 $\frac{\text{m}}{\text{s}}$	8.0019 $\frac{\text{m}}{\text{s}}$
$v_z$	0.1685 $\frac{\text{m}}{\text{s}}$	1.1521 $\frac{\text{m}}{\text{s}}$

error standard deviation is 8.0019 meters per second. Figure 4.6(d) reveals that the z-axis velocity estimates are significantly better than the x or y-axis. This is a result of reduced observability in the x and y-axis due to the geometry of the intercept. Since the missile is approaching the drone aircraft vertically along the z-axis of the NED frame, the missile’s velocity component in the x and y-axis direction is almost perpendicular to the aircraft sensors’ line-of-sight (LOS). Therefore, radial velocity measurements from the sensors do not provide precise measurements of the  $v_x$  and  $v_y$  states.

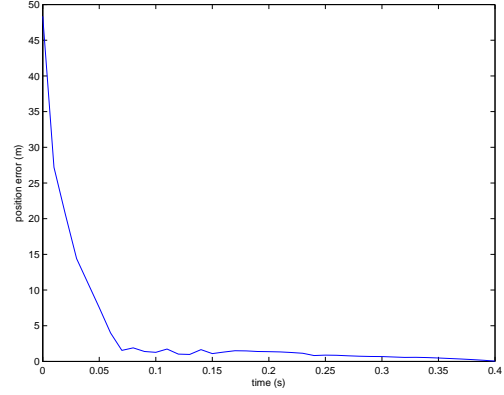
Figure 4.7 shows the results from scenario 2 where the target performs a defensive break-turn as illustrated in Figure 4.7(a). The RSS position error rapidly improves from about 48 meters to a few centimeters at impact for the single run shown in Figure 4.7(b). The results from a 100 run Monte Carlo analysis in Figures 4.7(c) and 4.7(d) illustrate errors in the navigation states. The ensemble statistics from this analysis are summarized in Table 4.7.

The filter performance in estimating position states is similar to scenario 1. The velocity states exhibit larger error standard deviations in the y and z-axis. Once again, this is the result of observability issues. The missile is approaching the target along the x-axis of the NED frame as the missile estimate is performed. As a result, the aircraft sensors do not provide precise measurements of missile velocity along the y and z-axis since these velocity components are nearly perpendicular to the sensors’ LOS.

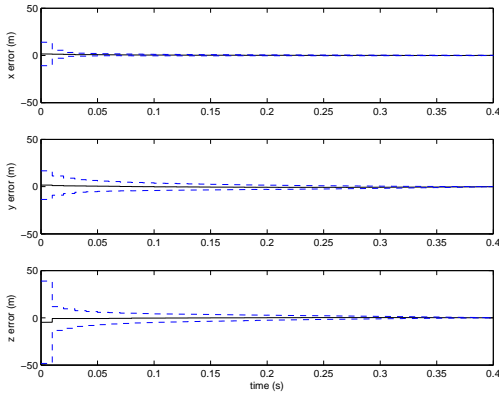
The results from the last scenario are recorded in Figure 4.8. In Figure 4.8(b) the missile position is randomly initialized based on typical GRDCS range accuracies to approximately 48 meters, but corrects to an accuracy of a few centimeters during the 0.39 second missile estimate for this sample run. Figures 4.8(c) and 4.8(d) show the results from the Monte Carlo analysis. The worst velocity observability occurs in the y and z-axis since the missile approaches along the x-axis of the NED frame. The results from the Monte Carlo analysis are summarized in Table 4.8.



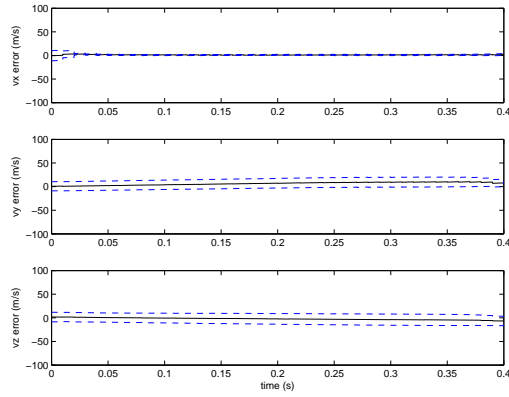
(a) 3D Aircraft and Missile Trajectory



(b) Root Sum Square Error in Missile Position Estimate (1 Run)



(c) Mean Error and Error Standard Deviation of Missile Position States (100 Runs)

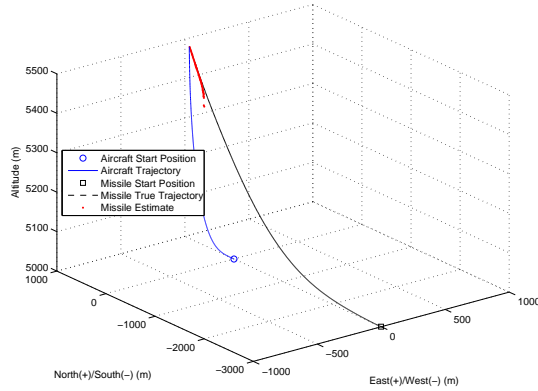


(d) Mean Error and Error Standard Deviation of Missile Velocity States (100 Runs)

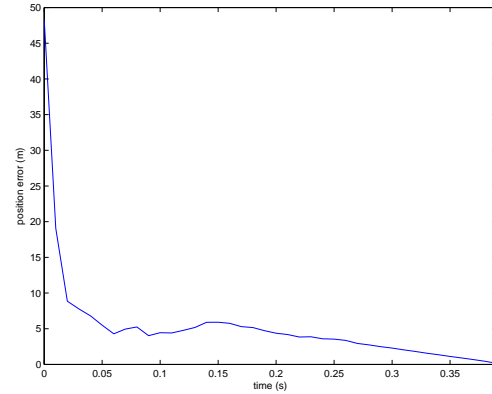
Figure 4.7: Unscented Kalman Filter Performance in Air-to-Air Missile Scoring Application with Continuous Velocity Dynamics Model (Target Aircraft Executing a Defensive Break Turn)

Table 4.7: Ensemble Mean Error Statistics for Missile States at Intercept using an Unscented Kalman Filter with Continuous Velocity Dynamics Model (Scenario 2)

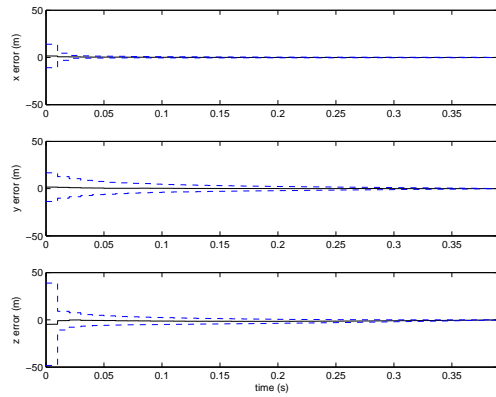
Missile State	Mean Error	Error Standard Deviation
$x$	-0.0005 m	0.0040 m
$y$	-0.0256 m	0.0310 m
$z$	0.0264 m	0.0317 m
$v_x$	1.1089 $\frac{\text{m}}{\text{s}}$	0.5608 $\frac{\text{m}}{\text{s}}$
$v_y$	2.6419 $\frac{\text{m}}{\text{s}}$	2.4432 $\frac{\text{m}}{\text{s}}$
$v_z$	-2.0683 $\frac{\text{m}}{\text{s}}$	2.5532 $\frac{\text{m}}{\text{s}}$



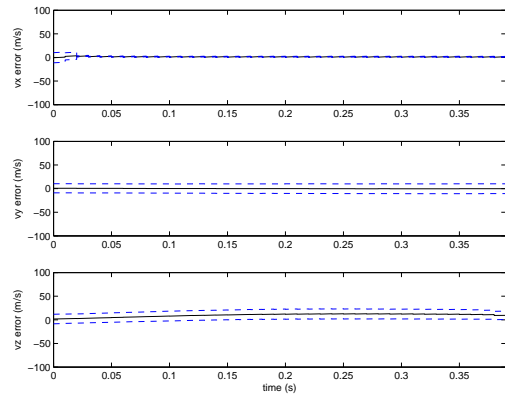
(a) 3D Aircraft and Missile Trajectory



(b) Root Sum Square Error in Missile Position Estimate (1 Run)



(c) Mean Error and Error Standard Deviation of Missile Position States (100 Runs)



(d) Mean Error and Error Standard Deviation of Missile Velocity States (100 Runs)

Figure 4.8: Unscented Kalman Filter Performance in Air-to-Air Missile Scoring Application with Continuous Velocity Dynamics Model (Target Aircraft Executing a Vertical Climb)

Table 4.8: Ensemble Mean Error Statistics for Missile States at Intercept using an Unscented Kalman Filter with Continuous Velocity Dynamics Model (Scenario 3)

Missile State	Mean Error	Error Standard Deviation
$x$	0.0068 m	0.0052 m
$y$	-0.0068 m	0.1091 m
$z$	-0.0634 m	0.0673 m
$v_x$	0.6113 $\frac{\text{m}}{\text{s}}$	0.5371 $\frac{\text{m}}{\text{s}}$
$v_y$	0.5280 $\frac{\text{m}}{\text{s}}$	8.4909 $\frac{\text{m}}{\text{s}}$
$v_z$	3.5622 $\frac{\text{m}}{\text{s}}$	3.6732 $\frac{\text{m}}{\text{s}}$

In all scenarios, the end-game mean position error is on the order of centimeters with a worst-case standard deviation of 0.1265 meters. Furthermore, the range resolution of the FMCW sensors is one of the primary limitations on position accuracy. Since range accuracy is advertised as 2.5 percent of range, sensor range measurement errors of 8.75 meters are expected at the scoring system's maximum range.

The improvement in estimation of velocity states is not quite as dramatic, especially in axes with limited observability based on geometry. However, the plots indicate that the error is constrained and the worst standard deviation at impact is only 3.5622 meters per second or, equivalently, 6.924 nautical miles per hour.

#### **4.8 Summary**

This chapter began by outlining the methods for performing Monte Carlo simulations to assess the performance of the missile scoring system. Three drone flight profiles were simulated to evaluate performance: non-maneuvering, 9G break-turn, and vertical climb. The simulation truth data for the three scenarios was generated using two 6DOF simulation software tools, *Profgen* and *Argos 3.0*. Next, this chapter describes the procedure for filter tuning, a key aspect of improving Kalman filter performance. The simulation methods were concluding by detailing the process for generating random noise to simulate GRDCS target handoff, noise corrupted radar measurements, and radar clutter.

The remainder of this chapter presented the results and analysis from the Monte Carlo simulations. The CV dynamics model and the UKF algorithm were determined to offer superior performance based on increased precision and reduced complexity. Finally, the simulated performance of the UKF with CV dynamics model was presented for each of the three scenarios. The mean error and error standard deviation was shown to be on the order of centimeters at impact. The next chapter further evaluates the proposed air-to-air missile scoring system through flight testing.

## V. Flight Test

The scoring system is evaluated through flight test by placing six automotive FMCW sensors at fixed locations on the ground to simulate installation on an F-16 drone. A series of passes in a Beechcraft C-12 aircraft are flown at low altitude over the sensor array to simulate an inbound air-to-air missile. The configuration of the sensors is adjusted between C-12 sorties to simulate different missile approach trajectories towards the F-16 drone. The range and range-rate measurements from the sensors are input into the UKF filter algorithm with a CV dynamics model to reconstruct the 3D position and velocity of the C-12 in a local ENU reference frame. The estimates of the aircraft navigation parameters are compared with data generated by a GPS system installed on the C-12. An error analysis is performed using the GPS data as truth to assess the performance of the scoring system estimation.

In the remainder of this chapter, Section 5.1 provides a detailed description of the scoring system implemented for testing. Section 5.2 contains a description of the C-12 aircraft. Section 5.3 explains the sources of truth data for the flight testing. Section 5.4 presents the flight profile flown to test the scoring system. Section 5.5 outlines the procedure for performing error analysis on the estimated aircraft position and velocity. Section 5.6 describes the process for reducing sensor measurement bias introduced by equipment limitations. Section 5.7 provides data on maximum sensor detection range. Finally, Sections 5.8-5.10 compare simulation predictions with the actual scoring system performance in reconstructing the trajectory of the C12 during flight test.

### *5.1 Scoring System Description*

Constructing the missile scoring system on the ground utilizes six COTS automotive FMCW sensors, two electronic control units (ECU), a laptop computer, controller-area network (CAN) bus cables, a DC power supply, and three tower platforms for mounting the sensors. The three towers are placed in a geometric configuration to simulate the planform of the F-16 drone as illustrated in Figure 5.1. The

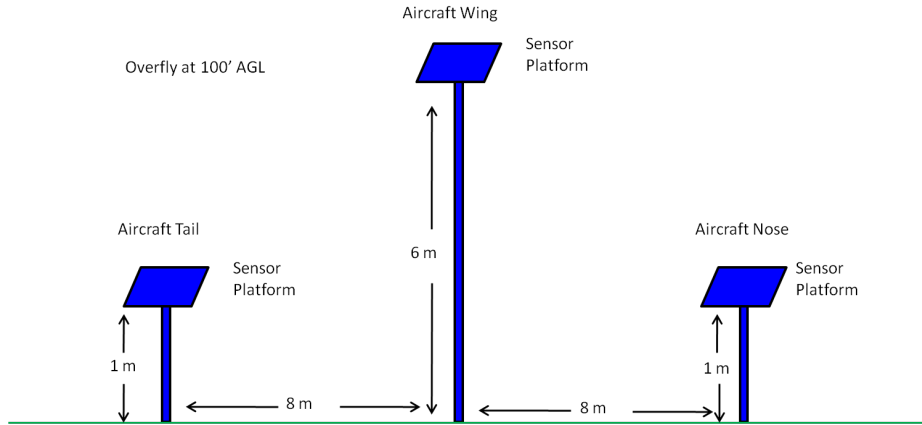


Figure 5.1: Sensor Platform Configuration (Simulates Installation Geometry on an F-16 Drone)

sensors on the towers represent the tail sensor, left wing sensor, and nose sensor as installed on the F-16 drone. The spacing between the towers and the height of the towers is precisely controlled to generate the appropriate geometry.

Two one meter jack stands and a six meter B-2 stand provide the necessary sensor platforms. These stands, as configured for testing, are shown in Figure 5.2. The heights of all three platforms are adjustable to obtain the desired vertical spacing.



Figure 5.2: Actual Sensor Platforms Used in Testing

The FMCW sensors mounted on the platforms operate at a center frequency of 24 gigahertz with a bandwidth of 250 megahertz. These sensors have an adjustable peak transmit power from 6 to 22 decibel milliwatts equivalent isotropically radiated power. Their update rate is 30 milliseconds with resolution as described in Section 3.1. Two different sensor types, Type 29 and Type 30, are utilized to improve coverage. The Type 29 sensor has an azimuth and elevation FOV of  $\pm 12$  and  $\pm 18$  degrees, respectively. The advertised maximum range for this sensor against a truck sized target is 240 meters. The Type 30 sensor has expanded azimuth and elevation coverage of  $\pm 15$  and  $\pm 35$  degrees, respectively. However, maximum range is reduced to 160 meters versus a truck sized target. One of each sensor type is placed on each tower platform. [32]

The sensors are attached to the towers via custom designed mounting brackets as shown in Figure 5.3. The brackets provide independently adjustable azimuth and elevation tilt for each sensor.



Figure 5.3: Sensor Mounting Brackets

The ECUs and CAN bus cables are used to connect the six FMCW sensors to the laptop computer for data output. Figure 5.4 depicts the electrical setup. As shown in this figure, three sensors are connected to each ECU. The two ECUs connect to the laptop computer via a dual channel CAN Personal Computer Memory Card International Association (PCMCIA) Card. All equipment is powered by a diesel generator through a 12 volt DC power supply. More detailed information on the sensors and ECU is available in [32].

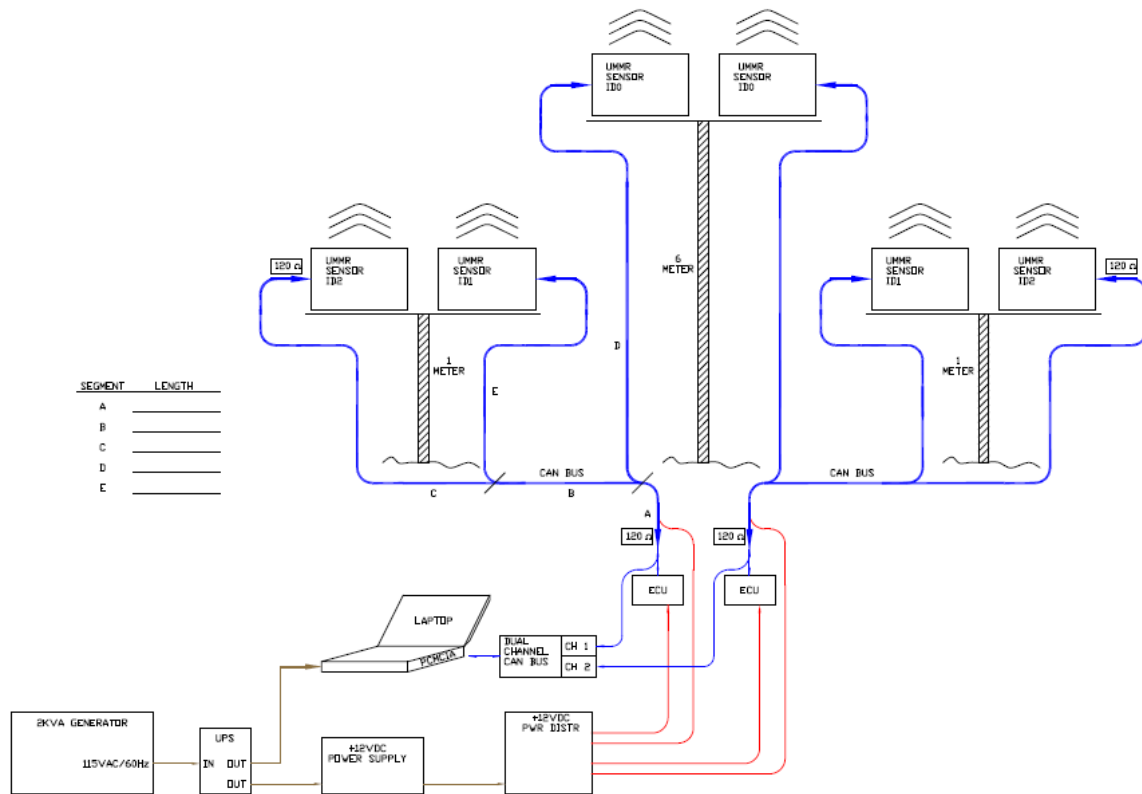


Figure 5.4: Sensor Electrical Wiring Setup

## 5.2 Surrogate Missile

A C-12 aircraft is used to simulate an inbound air-to-air missile relative to the ground based sensor suite. The C-12, shown in Figure 5.5, is a twin-engine turboprop transport built by Beechcraft with a wingspan of 54.5 feet [11]. The aircraft is powered by two Pratt and Whitney PT6A-41 engines which each turn an 8.2 foot diameter three bladed constant speed propeller. The aircraft large RCS and relatively low speed makes it compatible with the limitations of the COTS sensors used in testing. Furthermore, without a software modification, the COTS sensors are limited to detecting targets below 70 meters per second. Therefore, smaller and faster fighter-type aircraft are eliminated as options for the surrogate missile.

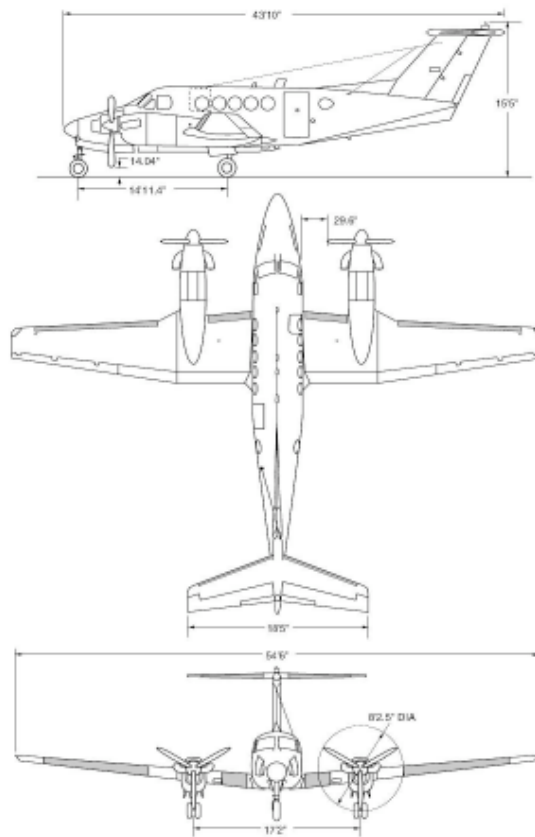


Figure 5.5: Beechcraft C-12C (Surrogate Missile)

### 5.3 Truth Data

The Beechcraft C-12 used in testing is equipped with a GPS Aided Inertial Navigation Reference (GAINR) Lite (GLite) system [2]. The GLite system records real-time position measurements using a highly accurate blended GPS and inertial measurement unit (IMU) navigation solution. The expected position and velocity accuracy of the system is 1.5 feet and 0.02 feet per second, respectively. Data is output at a rate of 50 hertz. The output from the GLite provides the C-12 truth data for performing an error analysis.

The sensor ground locations are surveyed and marked by the National Geospatial Intelligence-Agency to provide accuracy of 0.25 meters relative to WGS 84. There are a total of nine surveyed sensor points as illustrated in Figure 5.6. Although, only three sensor locations are used during any test flight, the additional survey locations allow for the simulation of different missile approach azimuths towards the F-16 drone. This is discussed further in Section 5.4.

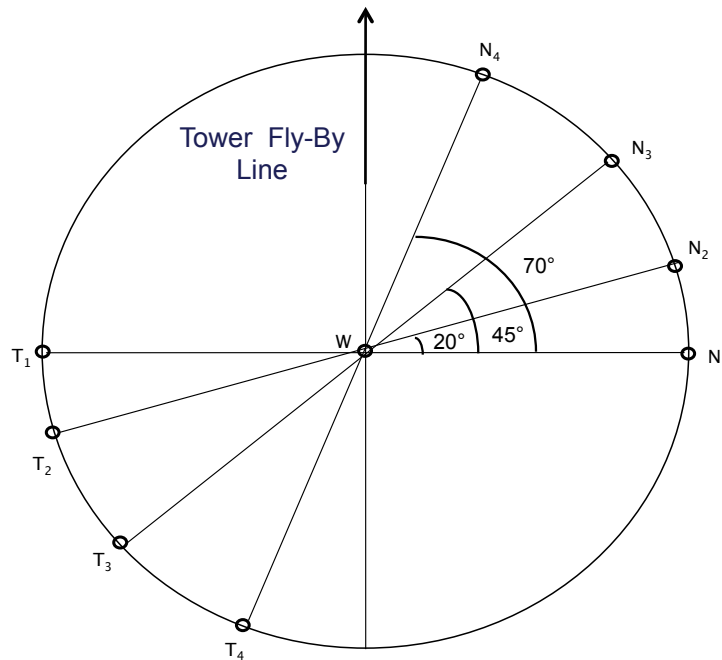


Figure 5.6: Surveyed Sensor Locations

Additionally, all the surveyed points on the outer ring have an accuracy of 0.01 meters relative to the center sensor reference location. A laser range finder is utilized to accurately set the tower height for the desired sensor geometry. The surveyed coordinates in conjunction with the laser range finder measurements provide the truth data for the sensor locations.

The truth data for the C-12 and the sensor locations are defined in a local ENU coordinate frame. The origin of the reference frame is defined at ground level underneath the center sensor. All error calculations are performed in this ENU reference frame.

#### ***5.4 Test Execution***

In order to simulate an inbound missile using the C-12, low-altitude flybys are performed over the sensor array as shown in Figure 5.7. The flybys are executed at 100 feet above ground level (AGL) with a minimum altitude of 70 feet AGL for safety. Since the center sensor platform is approximately 20 feet tall, the minimum altitude provides 50 feet of clearance when flying over the tower.



Figure 5.7: C-12 Performing Low-Altitude Flyby Over Sensor Array

The airspeed for all low-altitude passes is approximately 115 knots indicated airspeed (KIAS) with flaps set to 40 percent. This airspeed provides an acceptable safety margin for the C-12 aircrew by keeping them above 1.3 times the aircraft stall speed. Additionally, the low airspeed maintains the aircraft within the sensors' maximum range-rate for detection.

All of the low-altitude passes are performed along the tower flyby line at Edwards AFB depicted in Figure 5.8 [1]. The aircraft always flies towards the sensor array on the same heading along the tower flyby line. This ensures test repeatability by enabling the test team to control the surrogate missile approach azimuth relative to the simulated F-16 drone. Additionally, the COTS sensors have a narrow FOV and must be pointed in the direction of the incoming aircraft to maximize detection. Therefore, the tower fly line provides an excellent reference for aiming the sensors. Furthermore, the Type 29 and 30 sensors are set to an elevation tilt of 20 and 25 degrees up, respectively, using an inclinometer. Since the C-12 flies over the sensor array, the elevation tilt increases the time the aircraft remains within the sensor FOV.

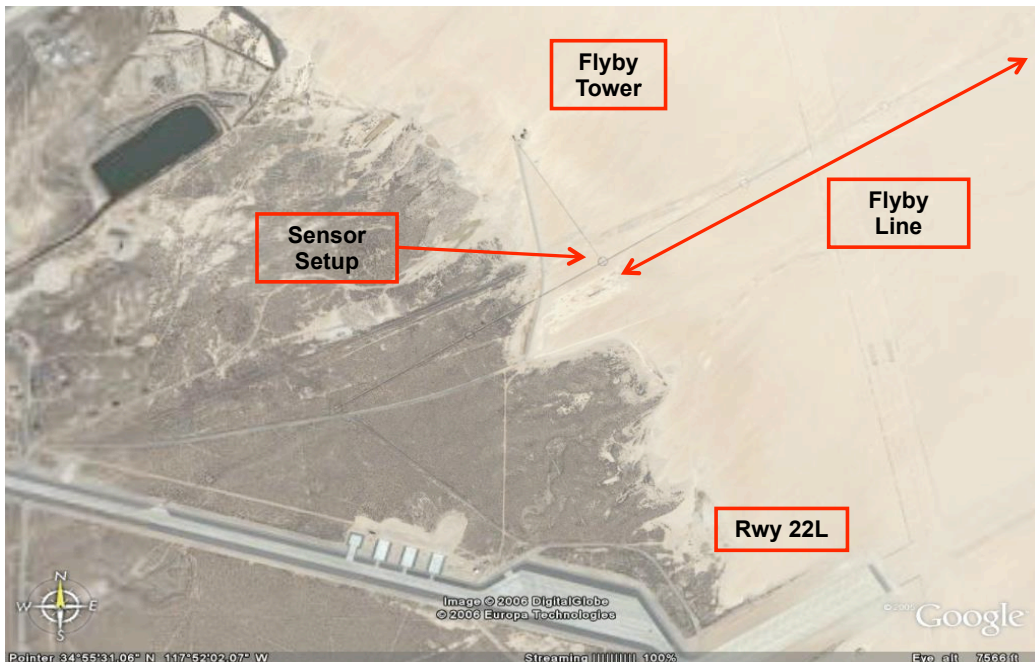


Figure 5.8: Tower Flyby Line at Edwards AFB, CA

In order to evaluate the system performance against different simulated missile approach trajectories, the sensors are maneuvered to different positions on the ground. Figure 5.6 illustrates the possible sensor locations. The left wing sensor is always located at point W on the center tower. However, the nose and tail sensors are adjusted between points N1-N4 and T1-T4, respectively. The location of the nose and tail sensors must be consistent to replicate the geometry on the F-16 drone. For example, if the nose sensor is placed at location N3, the tail sensor must be at location T3. Since the surrogate missile always approaches the sensor array along the same heading, adjusting the location of the nose and tail sensor effectively changes the aspect angle of the F-16 drone as viewed from the approaching missile. When the sensors are at positions N1, W, and T1 the drone aspect angle (AA) is 90 degrees. As explained in Section 2.6, this geometry is most favorable for estimating the surrogate missile navigation parameters because the angular spacing between the sensors relative to the missile (C-12) is maximized. When the nose and tail sensors are rotated to the remaining positions, F-16 drone aspect angles of 70, 45 and 20 degrees are simulated. Each of these aspect angles represents progressively worse missile trajectories for accurately estimating missile navigation parameters. The worst case geometry is a missile approach path directly off the tail (0 degree AA) or nose (180 degrees AA) of the F-16 drone.

Fifteen runs are performed at 90 and 45 degrees AA. Due to time constraints and maintenance limitations, only one run is conducted at 70 degrees AA and five runs are conducted at 20 degrees AA.

### ***5.5 Error Calculations***

An error analysis is performed by comparing the missile scoring software estimates of the C-12 position and velocity with the GLite provided truth data. Since simulations demonstrated the superior performance of the UKF with a CV dynamics model, this is the only Kalman filter and dynamics model combination considered

during flight test. Figure 5.9 illustrates the general process for performing the error analysis.

The UKF is initialized according to the process previously described in Section 3.4. The inputs to the UKF include the fixed sensor locations and the time stamped sensor measurements of range and range-rate. Based on this information, the Kalman filter estimates the C-12 position and velocity in the local ENU coordinate frame. Finally, this estimate is compared to GLite time space position information (TSPI) to determine error.

The average position and velocity error is reporting by calculating the RSS error for each run and then averaging across all runs at the same AA. The RSS position error is calculated using

$$P_{error} = \sqrt{(x_{test} - x_{TSPI})^2 + (y_{test} - y_{TSPI})^2 + (z_{test} - z_{TSPI})^2} \quad (5.1)$$

The subscript *test* refers to the UKF estimates and the subscript *TSPI* specifies GLite data.

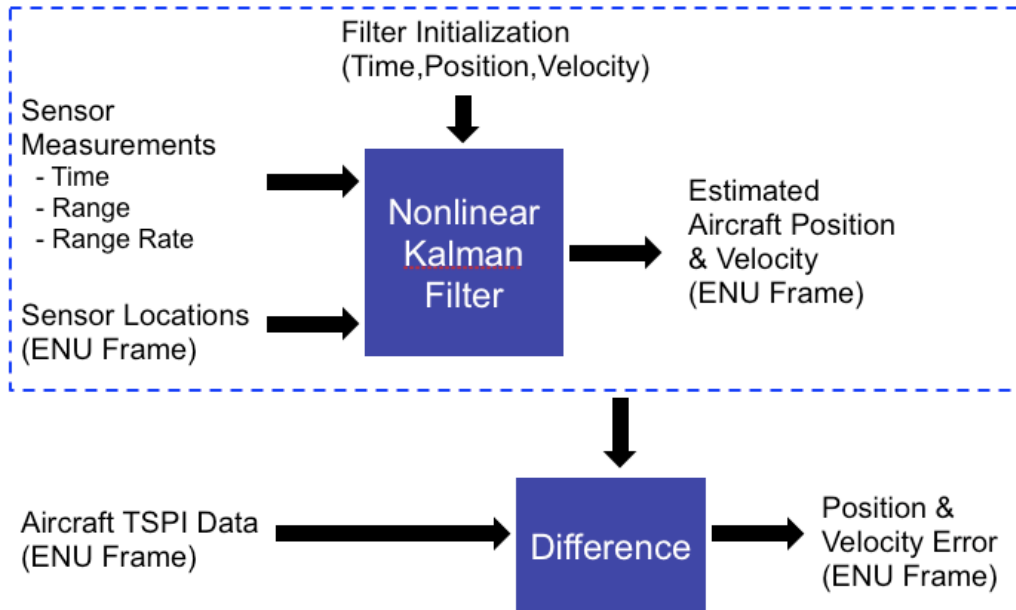


Figure 5.9: Data Flow for Flight Test Error Analysis

Similarly, the RSS velocity error is determined from the equation

$$V_{error} = \sqrt{(v_{x_{test}} - v_{x_{TSPI}})^2 + (v_{y_{test}} - v_{y_{TSPI}})^2 + (v_{z_{test}} - v_{z_{TSPI}})^2} \quad (5.2)$$

The position and velocity errors change with the decrease in slant range between the surrogate missile and ground based sensors. Ideally, the UKF will continue to reduce both position and velocity errors as the C-12 closes on the sensors since more measurements are available to improve state estimation. Additionally, as the aircraft closes on the sensor array, the changing sensor geometry relative to the C-12 will impact the accuracy of state estimates. Therefore, the average RSS position and velocity errors are reported within slant range bins. As detailed below in Section 5.7, maximum sensor range demonstrated in testing against the C-12 is approximately 120 meters. Additionally, there are some runs where the sensors don't detect the target until inside of 100 meters. Therefore, slant range bins of 10 meters are selected starting with 100 meters. The error reporting bins are recorded in Table 5.1. The error calculated at the center of each bin is reported for the entire bin. The Initial bin refers to the error after the first measurement update is received. The Final bin specifies the error after the last measurement update is received.

Table 5.1: Slant Range Bins for Error Reporting

Slant Range Bins (m)
Initial
> 90 - ≤ 100
> 80 - ≤ 90
> 70 - ≤ 80
> 60 - ≤ 70
> 50 - ≤ 60
> 40 - ≤ 50
Final

## 5.6 Bias Reduction

As discussed in Section 2.4, the Kalman filter algorithm assumes that measurement noise is accurately represented by a zero-mean Gaussian pdf. However, there are several test constraints that introduce some measurement bias. The two primary sources of measurement bias include imprecise time synchronization and the inability to determine the exact location on the C-12 where each sensor measurement occurs.

The COTS sensors have separate internal clocks not synced to GPS. Power is applied simultaneously to the clocks in an attempt to initialize them at the same time. At the time of initialization, GPS time is recorded to provide a rough estimate of the offset between the sensor clocks and GPS time. However, the sensor clocks still require precise alignment with GPS time for a valid error analysis since the truth source is synced to GPS. Moreover, the TSPI data obtained from the truth source is based on the location of the GLite on the aircraft. Yet, the majority of the sensor measurements will probably occur along the leading of the C-12, offset significantly from the GLite. Figure 5.10 illustrates this predicament.

In order to remove these biases, the actual slant range is calculated from the center sensor to the surrogate missile using the TSPI data. This TSPI slant range is

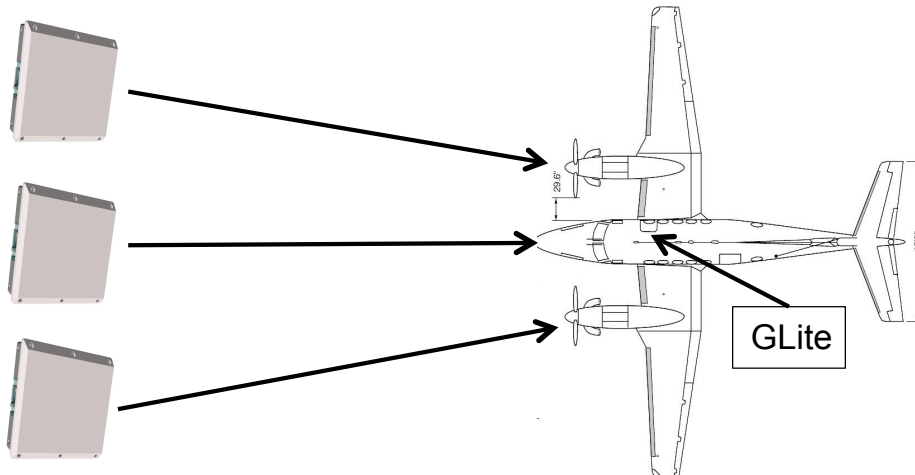


Figure 5.10: Radar Sensor Measurement Bias Caused by Aircraft Size and GLite Location

then plotted versus time and overlaid with the radar slant range measurement from the sensors on the center tower. A time shift is applied to visually align the TSPI slant range with the observed slant range measurements from the sensors on the center tower. This is done manually for each run and the resulting time shift is applied to data from all sensors.

If all six sensor clocks are perfectly synchronized and all sensors take measurements off the exact same location on the C-12, this technique completely removes any measurement bias. However, in reality there may be some initial offset between sensor clocks as well as different clock drift rates throughout the course of testing. Furthermore, the size and shape of the C-12 will result in varied return locations.

### 5.7 *Sensor Maximum Range*

Based on the assumption that the RCS of a C-12 is similar to a truck, the expected maximum detection range for the long range sensors is 240 meters. Nevertheless, flight tests demonstrated a significantly shorter maximum detection range. Table 5.2 records the average maximum detection range, standard deviation, and 95% confidence interval for the test runs. For each run, the maximum detection range is defined as the distance where all three long range sensors detect the target. The reduced detection range will adversely impact the accuracy and precision of Kalman filter state estimates since less observations are available to the filter.

Table 5.2: Maximum Range of COTS Frequency Modulated Continuous Wave Radar Sensors Versus a C-12

Average Maximum Detection Range (m)	Standard Deviation (m)	95% Confidence Interval (m)	Number of Samples
121.2	14.3	$121.2 \pm 4.9$	35

### 5.8 *Flight Test Predictions*

Due to real-world test conditions, the analysis in Chapter IV is not directly applicable. Prior to flight testing, Monte Carlo simulations similar to those described in

Chapter IV are performed under conditions which better represent the flight test conditions. In each simulation, the drone remains stationary and the missile approaches the drone along a constant heading at an airspeed of 120 knots to replicate the C-12 profile. Furthermore, to accurately represent the flight test scenario, the missile approaches the drone from above and then misses the drone by 35 meters horizontally as measured from the wingtip sensor. This simulates C-12 overflight of the sensor array by 100 feet AGL. In addition, only the three sensors included in the flight test are modeled in the simulation: nose, tail, and one wing. After completing the flight tests, all simulations are adjusted to account for the shorter maximum sensor detection range discussed in Section 5.7. UKF initialization and generation of noisy sensor measurements and false targets is performed according to the process outlined in Section 4.4. To facilitate comparison between the flight test predictions and results, the randomly generated initialization noise is saved and used in the flight test runs. As a result, the simulations and flight tests start with the same initial error.

Four simulations of 30 Monte Carlo runs are performed to model each of the different sensor configurations: 90, 70, 45, and 20 degrees AA. The RSS position and velocity error of the UKF estimates are calculated and categorized into the slant range bins discussed in Table 5.1. Additionally, the average RSS error and 95% confidence interval is determined from the simulations. Executing 30 Monte Carlo runs ensures the 95% confidence interval for the average RSS position error in the final slant range bin converges to less than two meters. The results from the flight test predictions are presented along with the flight test results in the next two sections.

### ***5.9 C-12 Position Estimate Error***

The flight test results presented in this section demonstrate that the proposed missile scoring system successfully reduces error in estimates of the C-12 position. Although the scoring performance is less than predicted through simulations, flight test constraints are the probable culprit. This section identifies several factors associated with flight test limitations contributing to the increased error.

Figure 5.11 depicts the average RSS position error in each slant range bin for the 15 flight test runs at 90 degrees AA. The brackets around each data point represent the 95% confidence interval for the true average RSS position error. In addition, the figure includes the predictions from the Monte Carlo simulation for comparison. The actual data values are recorded in Table 5.3.

The figure illustrates several important aspects from the flight test results. First, there is a decreasing trend in average RSS position error from initialization to the final sensor observation at approximately 35 meters of slant range. From the flight test data, the initial average RSS position error is 40 meters and the final average RSS position error is 14.9 meters as shown in Table 5.3. This suggests the error in the UKF estimates are converging as expected. Secondly, the simulation predictions show significantly less RSS position error than demonstrated in flight test. In fact, there is no overlap between the 95% confidence intervals for the true average RSS position error determined from flight test and simulations. Therefore, with 95% confidence, the actual scoring system RSS position error is greater than predicted. Finally, the flight test data shows an unexpected increase in average RSS position error from 45 meters slant range to sensor overflight. The predictions suggest the minimum position error will occur when the final sensor measurement is received. The expected final average RSS position error for this sensor configuration is 1.44 meters with a 95% confidence interval of 0.7 to 2.18 meters.

There are several probable factors contributing to the performance mismatch between the flight test results and predictions. First, as discussed in Section 5.6, there are several test constraints that introduce bias into sensor measurements. Post flight data analysis minimized this bias, but did not eliminate it. The two main sources of bias are imprecise time synchronization and the inability to determine the exact location on the C-12 where each sensor measurement is taken. In future testing, the bias issue can be mitigated by selecting a smaller test aircraft to emulate the missile and syncing all sensor measurements with GPS time.

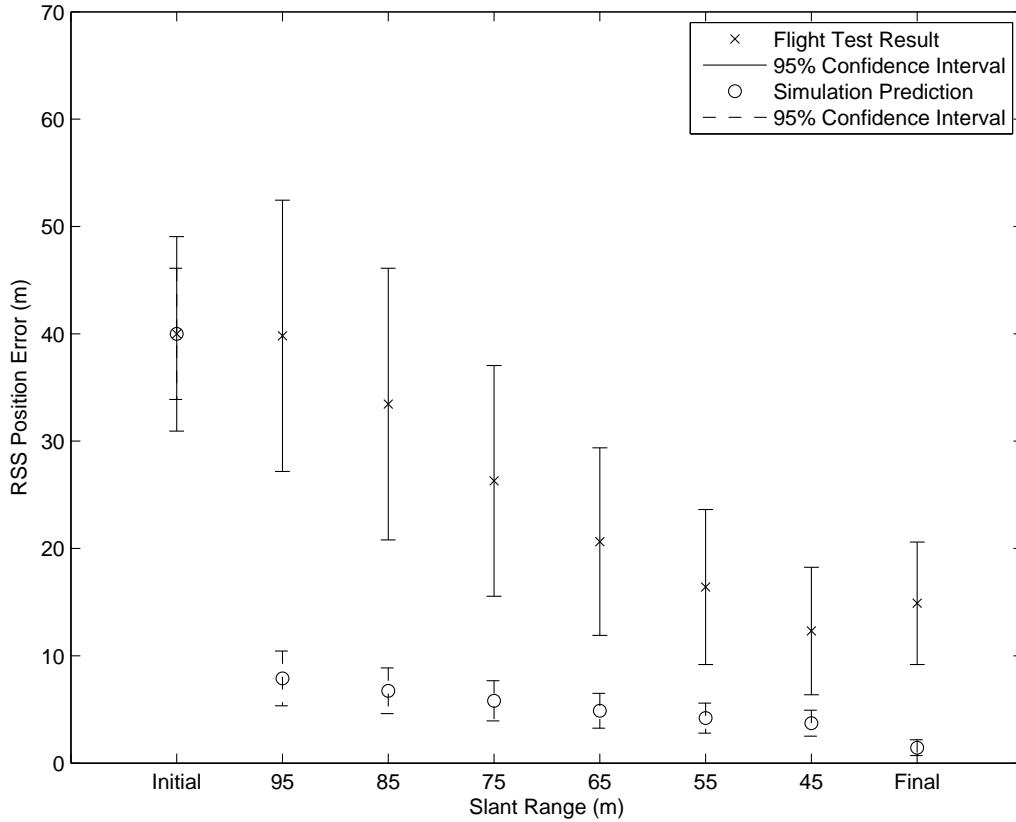
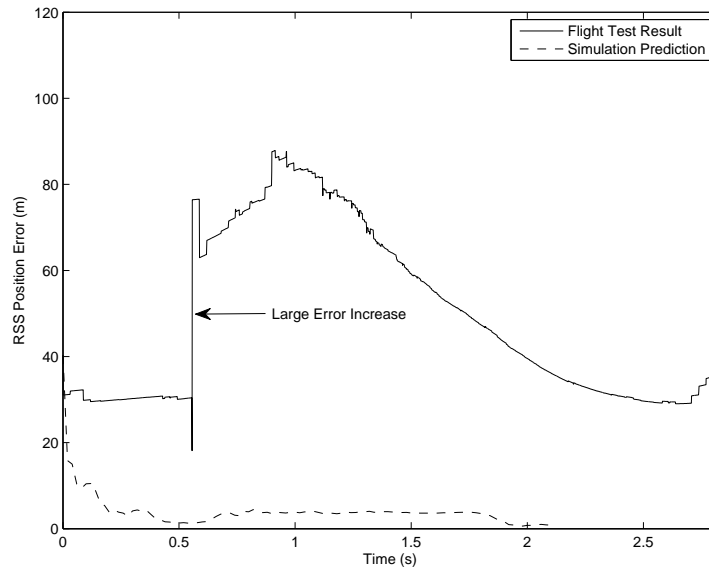


Figure 5.11: Comparison of Flight Test Results and Simulation Predictions for Average Root Sum Square Error in Unscented Kalman Filter Estimates of C-12 Position (90° Drone Aspect Angle)

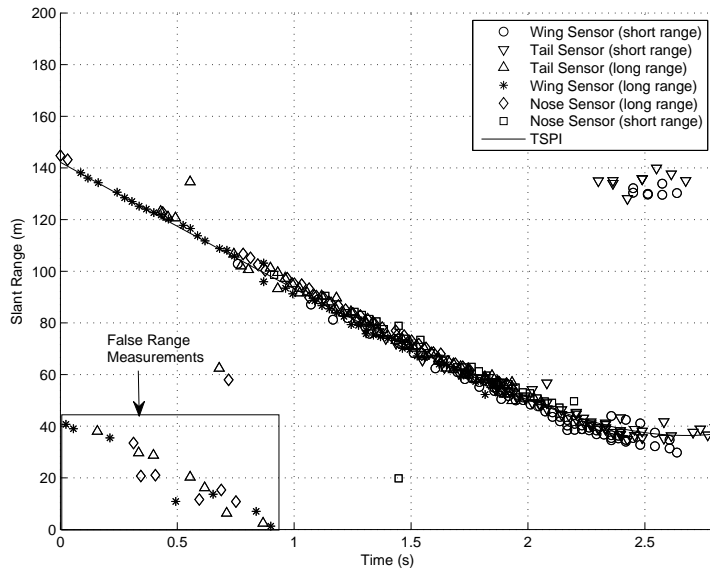
Table 5.3: C-12 Position Estimate Error per Slant Range Bin using an Unscented Kalman Filter with Continuous Velocity Dynamics Model (90° Drone Aspect Angle)

Range Bin (m)	Average RSS Position Error (m)	Standard Deviation (m)	95% Confidence Interval (m)
Initial	40.00	16.36	40.00 ± 9.06
> 90 - ≤ 100	39.81	22.82	39.81 ± 12.64
> 80 - ≤ 90	33.45	22.85	33.45 ± 12.66
> 70 - ≤ 80	26.30	19.41	26.30 ± 10.75
> 60 - ≤ 70	20.63	15.78	20.63 ± 8.74
> 50 - ≤ 60	16.41	13.04	16.41 ± 7.22
> 40 - ≤ 50	12.31	10.72	12.31 ± 5.93
Final	14.90	10.30	14.90 ± 5.70

Secondly, in simulations the gating and data association algorithms described in Section 3.3 demonstrated great effectiveness in eliminating false targets. In contrast, numerous flight test runs show corruption in UKF estimates caused by false targets. Figure 5.12 illustrates the issue with false targets. Initially, the UKF gates out all measurements and shows a relatively constant RSS position error of approximately



(a) Predicted and Actual Root Sum Square Position Error



(b) Radar Sensors Slant Range Measurements

Figure 5.12: Illustration of False Target Impact on Errors in Unscented Kalman Filter Position Estimates (Data from Run 11 at 90° Drone Aspect Angle)

30 meters. In Figure 5.12(a), from approximately 0.6 to 0.9 seconds the RSS position error increases dramatically as the UKF updates the C-12 position estimate using false sensor measurements. Figure 5.12(b) shows the raw range measurements from the sensors. There is a significant grouping of false range measurements between 0 and 0.9 seconds.

The gating algorithm relies on the assumption that random false targets will not exhibit both range and velocity comparable to the true target. However, the false range measurements in Figure 5.12(b) are also associated with realistic sensor speed measurements as shown in Figure 5.13. The probable source of these realistic false targets is multipath off of the C-12 surfaces and propellor effects. Reducing the gate size does not solve this issue because it eliminates the true target measurements along with the false targets. Fortunately, the presence of such realistic false targets is not anticipated during air-to-air missile scoring. Testing with a smaller target vehicle would validate this assumption.

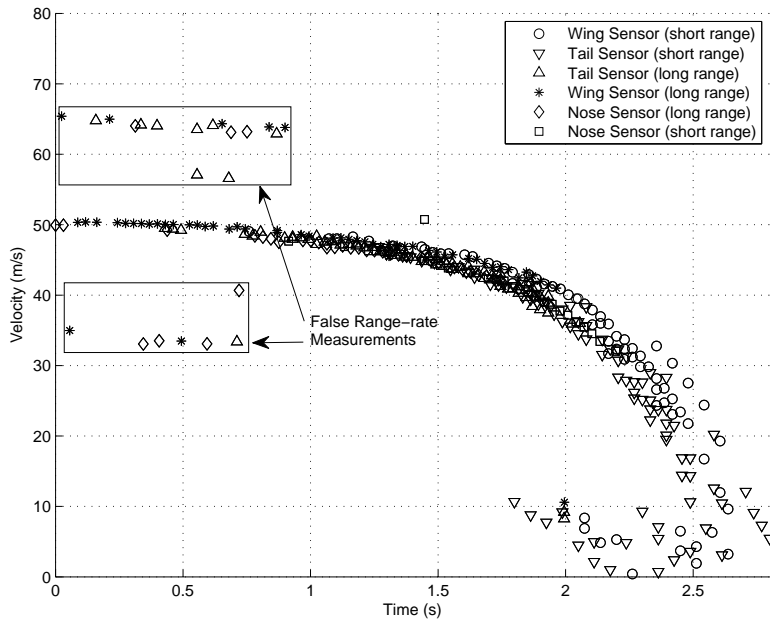


Figure 5.13: Illustration of False Target Speed Measurements (Data from Run 11 at 90° Drone Aspect Angle)

Appendix B includes a comprehensive library of plots from all flight test runs. There are four plots saved for each run. Two of the plots show the raw range and speed measurements for all six sensors. The remaining two plots depict the calculated RSS position and velocity error. These plots also include simulation predictions for RSS position and velocity error for comparison.

Figure 5.14 illustrates the average RSS position error with the sensor configuration adjusted to represent a drone aspect angle of 45 degrees. This geometry is less favorable for estimating C-12 navigation states because the angular spacing of the sensors is reduced as viewed from the incoming aircraft. The simulations predict a final RSS position error of 2.86 meters, compared to 1.44 meters when the sensors are configured for 90 degrees AA. Once again the position errors determined during flight testing are higher than the simulation predictions. There is no overlap between the confidence intervals so the true average RSS position error of the flight tests are higher than the prediction at 95% confidence .

The flight test data from 15 runs at 45 degrees AA are summarized in Table 5.4. The average RSS position error is actually lower at 45 degrees AA than 90 degrees AA in seven of the eight slant range bins. However, this is easily explained by the large overlapping confidence intervals between the results at the two different aspect angles. More runs are required to illustrate the improvement in state estimate accuracy based on sensor geometry.

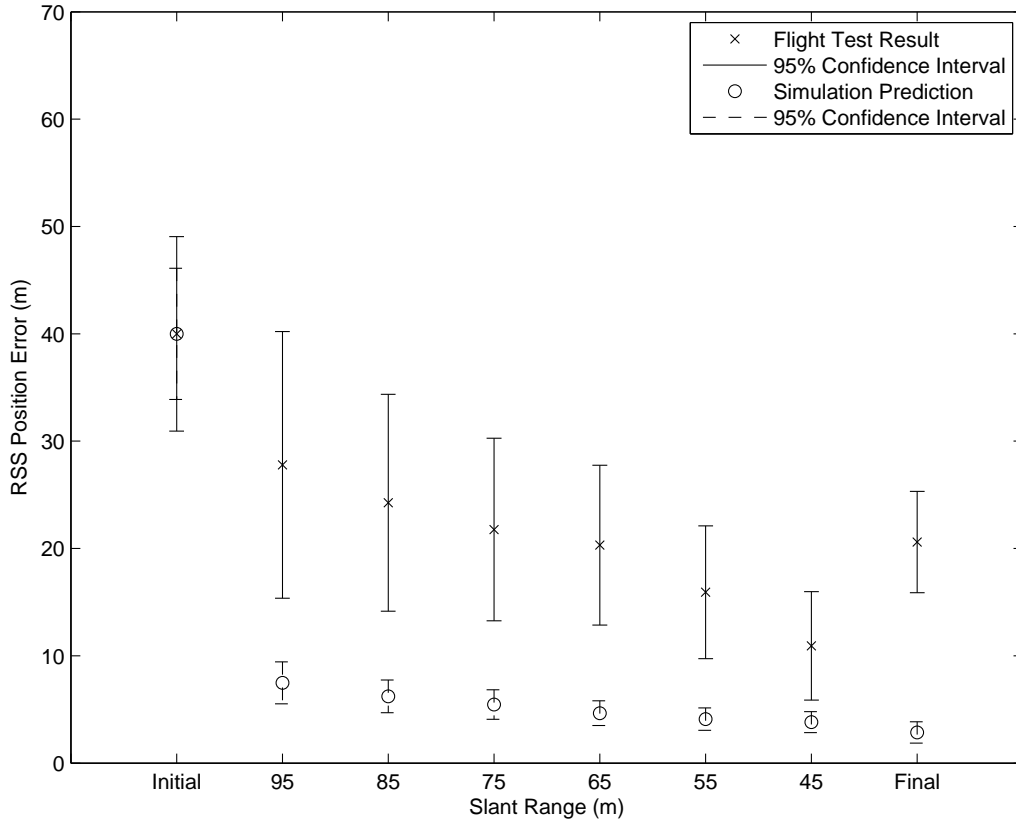
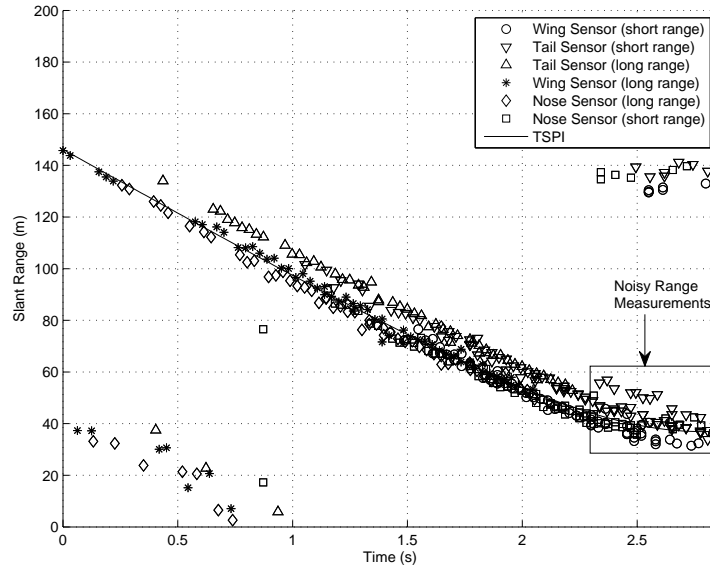


Figure 5.14: Comparison of Flight Test Results and Simulation Predictions for Average Root Sum Square Error in Unscented Kalman Filter Estimates of C-12 Position (45° Drone Aspect Angle)

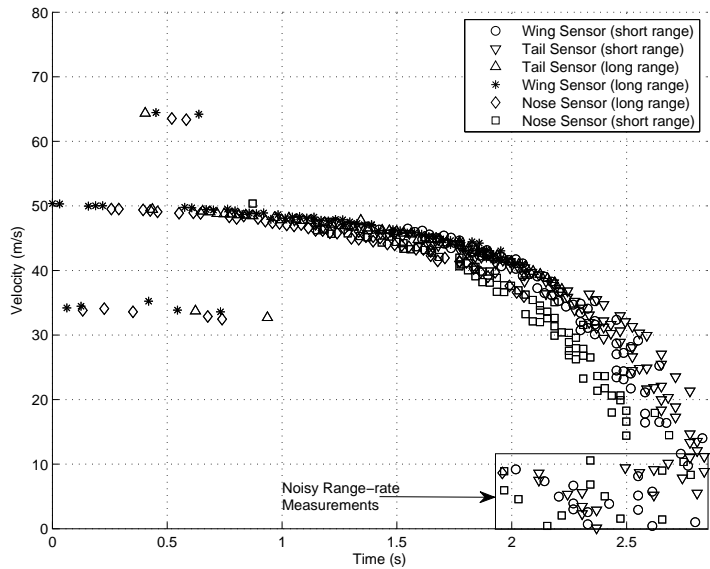
Table 5.4: C-12 Position Estimate Error per Slant Range Bins using an Unscented Kalman Filter with Continuous Velocity Dynamics Model (45° Drone Aspect Angle)

Range Bin (m)	Average RSS Position Error (m)	Standard Deviation (m)	95% Confidence Interval (m)
Initial	40.00	16.36	40.00 ± 9.06
> 90 - ≤ 100	27.79	22.44	27.79 ± 12.43
> 80 - ≤ 90	24.26	18.25	24.26 ± 10.10
> 70 - ≤ 80	21.76	15.36	21.76 ± 8.50
> 60 - ≤ 70	20.31	13.44	20.31 ± 7.44
> 50 - ≤ 60	15.92	11.18	15.921 ± 6.19
> 40 - ≤ 50	10.93	9.13	10.93 ± 5.06
Final	20.60	8.51	20.60 ± 4.71

There is a substantial increase in average RSS position error between 45 meters slant range and the final observation. This unexpected error increase is also present in the test runs at 90 degrees AA. The large error increase is the result of noisier measurements as the C-12 overflies the sensor array as shown in Figure 5.15.



(a) Radar Sensors Slant Range Measurements



(b) Radar Sensors Speed Measurements

Figure 5.15: Illustration of Increase in Sensor Measurement Noise as C-12 Approaches Sensor Overflight (Data from Run 1 at 45° Drone Aspect Angle)

As the C-12 approaches radar overflight, the aircraft presents greater planform to the stationary ground sensors. The increased cross sectional area viewed by the sensors results in numerous measurements off of widely varying parts of the aircraft. In contrast, at greater distances the majority of the sensor measurements stem from the leading edge of the aircraft.

Figure 5.16 depicts the results from four flight test runs executed with a sensor geometry of 20 degrees AA. Due to the limited number of test runs, the average RSS position error exhibits large 95% confidence intervals which partially overlap with the predictions. The overall data trend is consistent with the previous runs at 90 and 45 degrees aspect angle. The data results are summarized in Table 5.5.

For completeness the simulation prediction and result from a single run performed at 70 degrees aspect angle is included in Figure 5.17. Since the data is from a single run, no confidence interval are presented.

Overall, the demonstrated performance of the system in estimating C-12 position is encouraging. Although the accuracy did not match simulation predictions, there are substantial limitations present in the flight testing which will not exist in the actual system. The limitations are primarily driven by cost and safety in executing the flight test. Implementing the proposed system using customized FMCW sensors designed for the missile scoring application will eliminate the bias present due to absence of time syncing. Furthermore, sensors with a higher update rate and better range resolution will further improve accuracy of position estimates. Finally, the estimates of missile position improve significantly when the missile is flown to impact with the drone due to advantageous alignment of the sensors relative to the missile. This is confirmed by the difference between simulated system performance in Chapter IV and flight test predictions. Chapter IV simulations demonstrated final accuracy on the order of centimeters because the missile continued to impact. In contrast, flight test predictions only anticipated accuracy on the order of meters since the missile never got closer to the drone than approximately 30 meters.

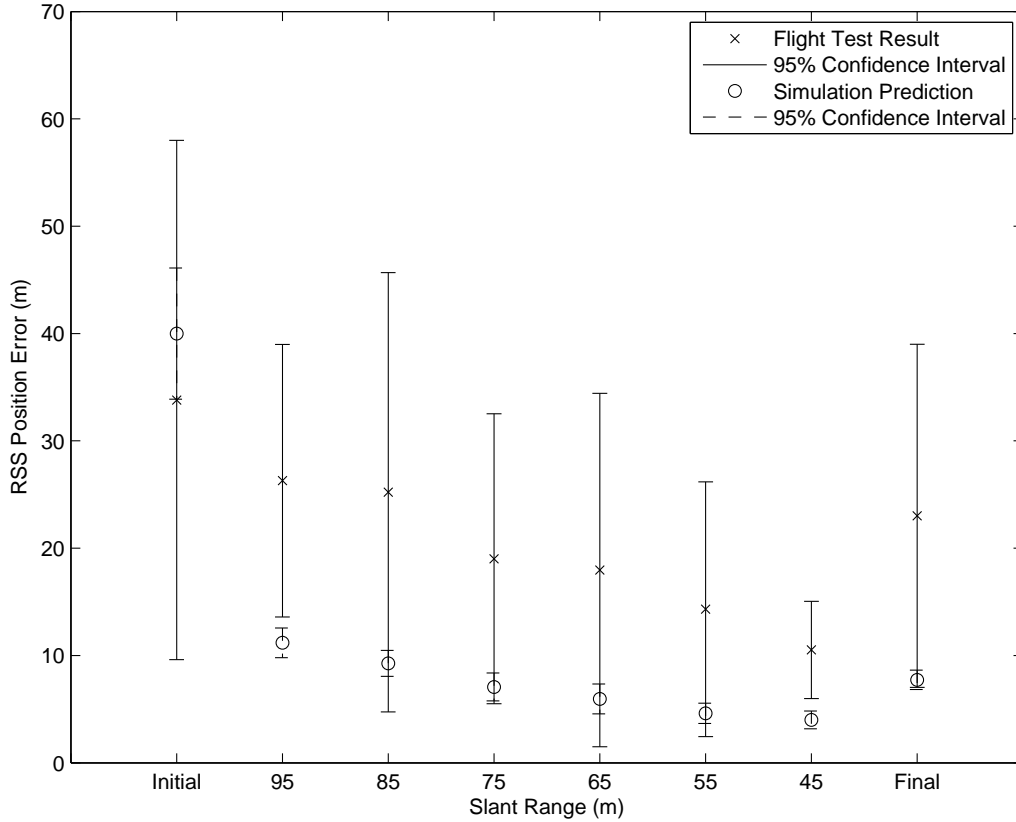


Figure 5.16: Comparison of Flight Test Results and Simulation Predictions for Average Root Sum Square Error in Unscented Kalman Filter Estimates of C-12 Position (20° Drone Aspect Angle)

Table 5.5: C-12 Position Estimate Error per Slant Range Bin using an Unscented Kalman Filter with Continuous Velocity Dynamics Model (20° Drone Aspect Angle)

Range Bin (m)	Average RSS Position Error (m)	Standard Deviation (m)	95% Confidence Interval (m)
Initial	33.80	15.21	$33.80 \pm 24.20$
> 90 - $\leq$ 100	26.29	7.98	$26.29 \pm 12.70$
> 80 - $\leq$ 90	25.22	12.86	$25.22 \pm 20.46$
> 70 - $\leq$ 80	19.01	8.49	$19.01 \pm 13.51$
> 60 - $\leq$ 70	17.96	10.35	$17.96 \pm 16.46$
> 50 - $\leq$ 60	14.31	7.46	$14.31 \pm 11.87$
> 40 - $\leq$ 50	10.52	2.85	$10.52 \pm 4.54$
Final	23.01	10.05	$23.01 \pm 15.98$

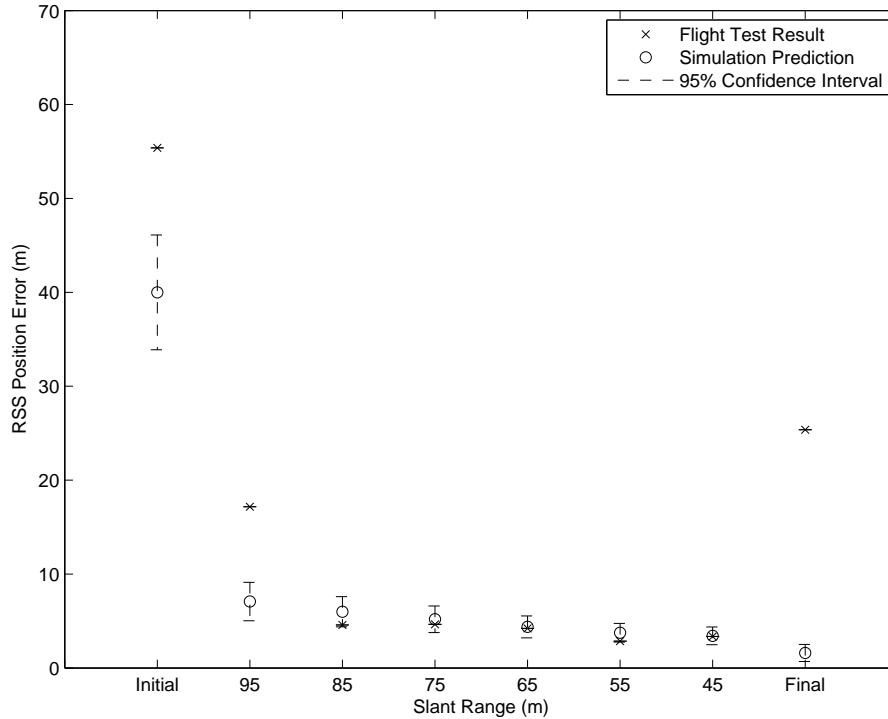


Figure 5.17: Comparison of Flight Test Results and Simulation Predictions for Average Root Sum Square Error in Unscented Kalman Filter Estimates of C-12 Position (70° Drone Aspect Angle)

### 5.10 C-12 Velocity Estimate Error

The flight test results in this section indicate the UKF software prevents the velocity error from diverging, but overall RSS velocity error does not improve after filter initialization. Figure 5.18 illustrates the predicted and actual average RSS velocity error at 90 degrees AA. According to the predictions, the average RSS velocity error will quickly converge to approximately three to six meters per second and then remain constant as the missile tracks inbound to the target. However, flight testing on the C-12 demonstrated an increase in average RSS velocity error after target initialization. The 95% confidence interval for the average RSS velocity error remains relatively constant between 10 to 25 meters per second across the slant range bins. Table 5.6 summarizes the data from the figure.

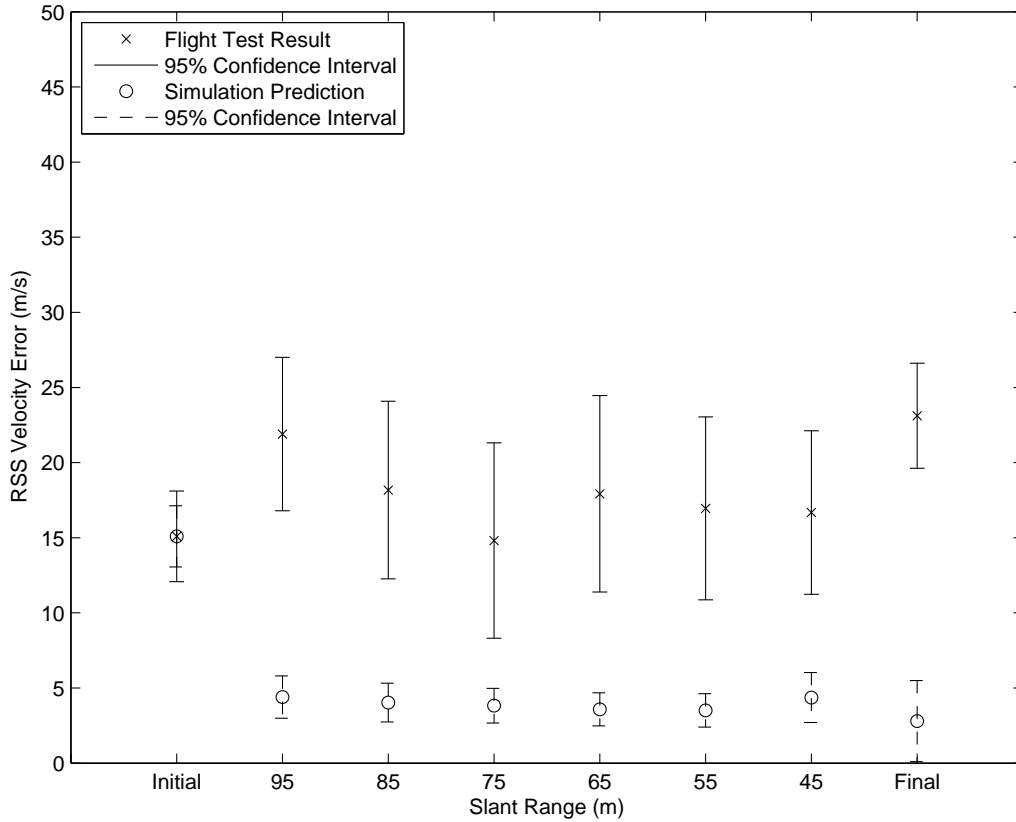


Figure 5.18: Comparison of Flight Test Results and Simulation Predictions for Average Root Sum Square Error in Unscented Kalman Filter Estimates of C-12 Velocity (90° Drone Aspect Angle)

Table 5.6: C-12 Velocity Estimate Error per Slant Range Bin using an Unscented Kalman Filter with Continuous Velocity Dynamics Model (90° Drone Aspect Angle)

Range Bin (m)	Average RSS Velocity Error ( $\frac{m}{s}$ )	Standard Deviation ( $\frac{m}{s}$ )	95% Confidence Interval ( $\frac{m}{s}$ )
Initial	15.09	5.45	$15.09 \pm 3.02$
> 90 - $\leq$ 100	21.90	9.22	$21.90 \pm 5.11$
> 80 - $\leq$ 90	18.17	10.68	$18.17 \pm 5.91$
> 70 - $\leq$ 80	14.81	11.74	$14.81 \pm 6.50$
> 60 - $\leq$ 70	17.92	11.81	$17.92 \pm 6.54$
> 50 - $\leq$ 60	16.95	10.99	$16.95 \pm 6.08$
> 40 - $\leq$ 50	16.68	9.83	$16.68 \pm 5.44$
Final	23.12	6.31	$23.12 \pm 3.49$

Since there is no overlap in the confidence intervals, the true average RSS velocity error is greater than the prediction with 95% confidence. These results are expected since the velocity state estimate error is highly correlated with the position error. As illustrated in Section 2.7, velocity vector calculations from speed measurements depend on knowledge of the sensor and target position. Therefore, since actual RSS position errors presented in the previous section are greater than predicted it is anticipated that velocity errors will also be higher. All of the factors driving the position error higher, such as measurement bias and inadequate gating of false targets, also explains the higher velocity error.

Figure 5.19 and Table 5.7 record the velocity error when the sensor configuration is changed to 45 degrees aspect angle. The errors are comparable to the runs performed at 90 degrees aspect. Based on the large standard deviations and confidence intervals for calculations of RSS velocity error, there are insufficient runs to show the superior performance of the first sensor geometry.

The results in Figure 5.19 emphasize the significant increase in RSS velocity error between 45 meters slant range and the final sensor measurement. As explained in Section 5.9, this is the result of noisier measurements just prior to overflight based on sensor LOS to C-12 platform.

Figures 5.20 and 5.21 and Table 5.8 show the results from the final two sensor configurations of 20 and 70 degrees aspect angle. Due to the small number of runs at 20 degrees AA, the standard deviation and 95% confidence interval for the RSS velocity error is much larger than the previous geometries.

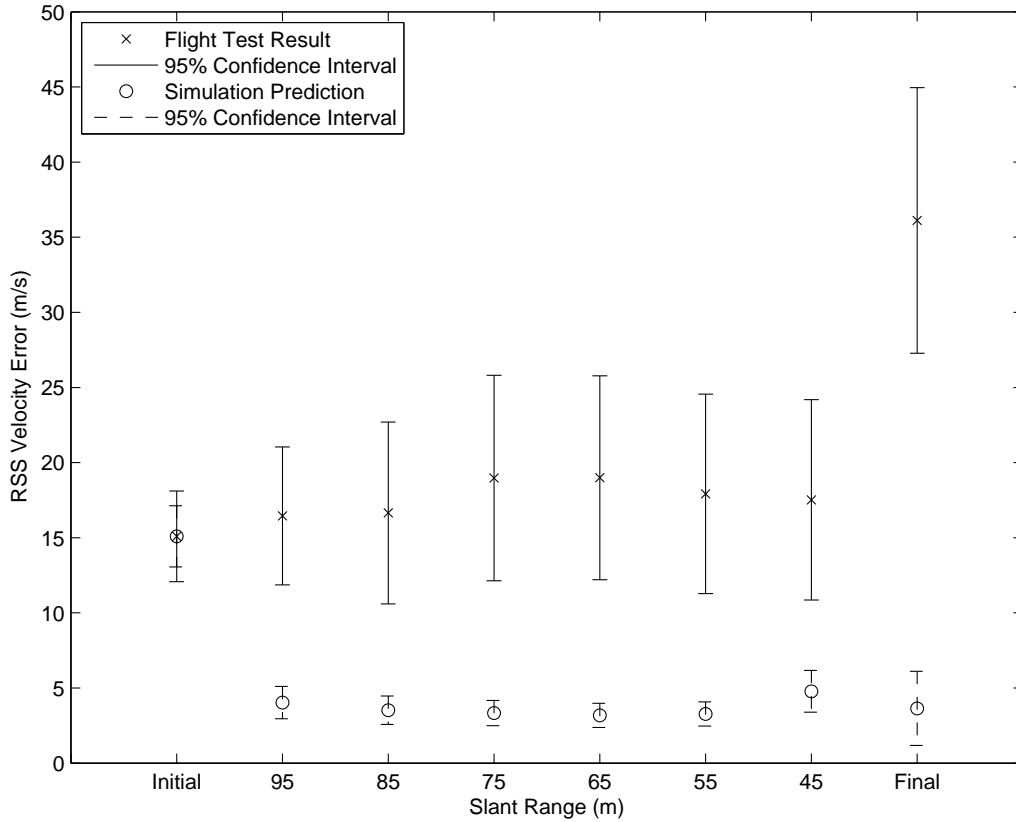


Figure 5.19: Comparison of Flight Test Results and Simulation Predictions for Average Root Sum Square Error in Unscented Kalman Filter Estimates of C-12 Velocity (45° Drone Aspect Angle)

Table 5.7: C-12 Velocity Estimate Error per Slant Range Bin using an Unscented Kalman Filter with Continuous Velocity Dynamics Model (45° Drone Aspect Angle)

Range Bin (m)	Average RSS Velocity Error ( $\frac{m}{s}$ )	Standard Deviation ( $\frac{m}{s}$ )	95% Confidence Interval ( $\frac{m}{s}$ )
Initial	15.09	5.45	$15.09 \pm 3.02$
$> 90 - \leq 100$	16.45	8.30	$16.45 \pm 4.59$
$> 80 - \leq 90$	16.65	10.93	$16.65 \pm 6.05$
$> 70 - \leq 80$	18.97	12.35	$18.97 \pm 6.84$
$> 60 - \leq 70$	18.99	12.26	$18.99 \pm 6.79$
$> 50 - \leq 60$	17.92	11.99	$17.92 \pm 6.64$
$> 40 - \leq 50$	17.52	12.04	$17.52 \pm 6.67$
Final	36.12	15.96	$36.12 \pm 8.84$

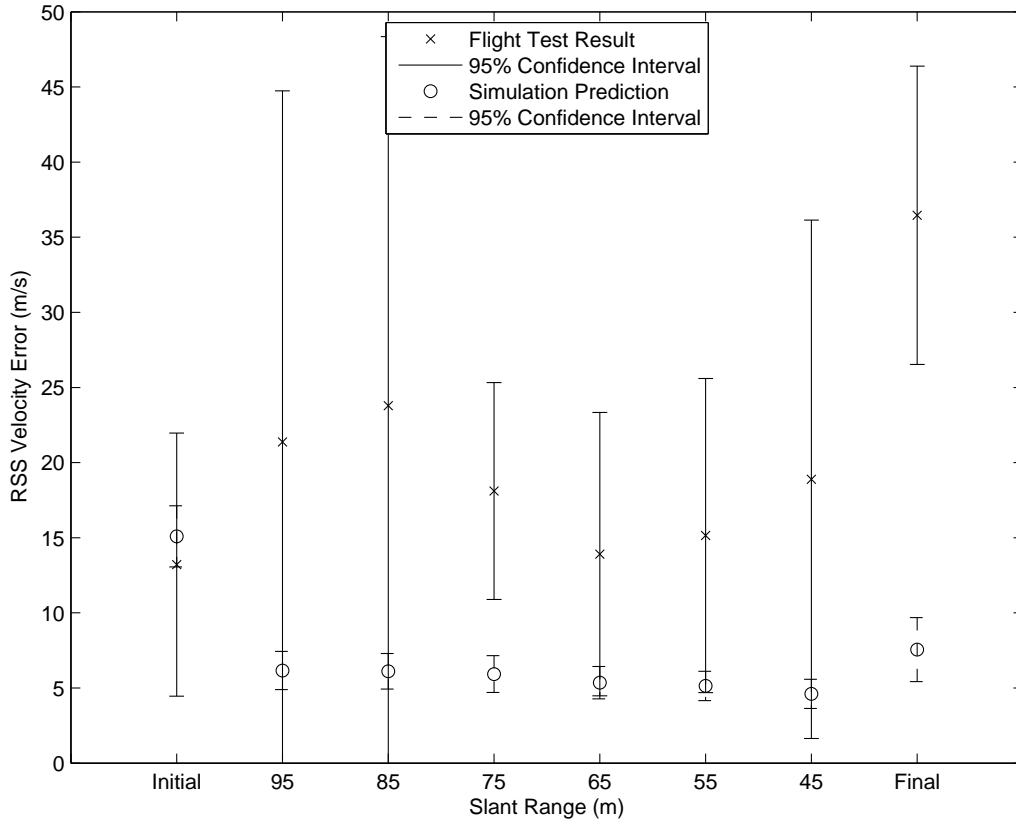


Figure 5.20: Comparison of Flight Test Results and Simulation Predictions for Average Root Sum Square Error in Unscented Kalman Filter Estimates of C-12 Velocity (20° Drone Aspect Angle)

Table 5.8: C-12 Velocity Estimate Error per Slant Range Bin using an Unscented Kalman Filter with Continuous Velocity Dynamics Model (20° Drone Aspect Angle)

Range Bin (m)	Average RSS Velocity Error ( $\frac{m}{s}$ )	Standard Deviation ( $\frac{m}{s}$ )	95% Confidence Interval ( $\frac{m}{s}$ )
Initial	13.21	5.50	$13.21 \pm 8.76$
> 90 - $\leq$ 100	21.37	14.69	$21.37 \pm 23.37$
> 80 - $\leq$ 90	23.78	15.44	$23.78 \pm 24.56$
> 70 - $\leq$ 80	18.11	4.54	$18.11 \pm 7.22$
> 60 - $\leq$ 70	13.91	5.92	$13.91 \pm 9.43$
> 50 - $\leq$ 60	15.15	6.57	$15.15 \pm 10.45$
> 40 - $\leq$ 50	18.89	10.84	$18.89 \pm 17.25$
Final	36.46	6.24	$36.46 \pm 9.93$

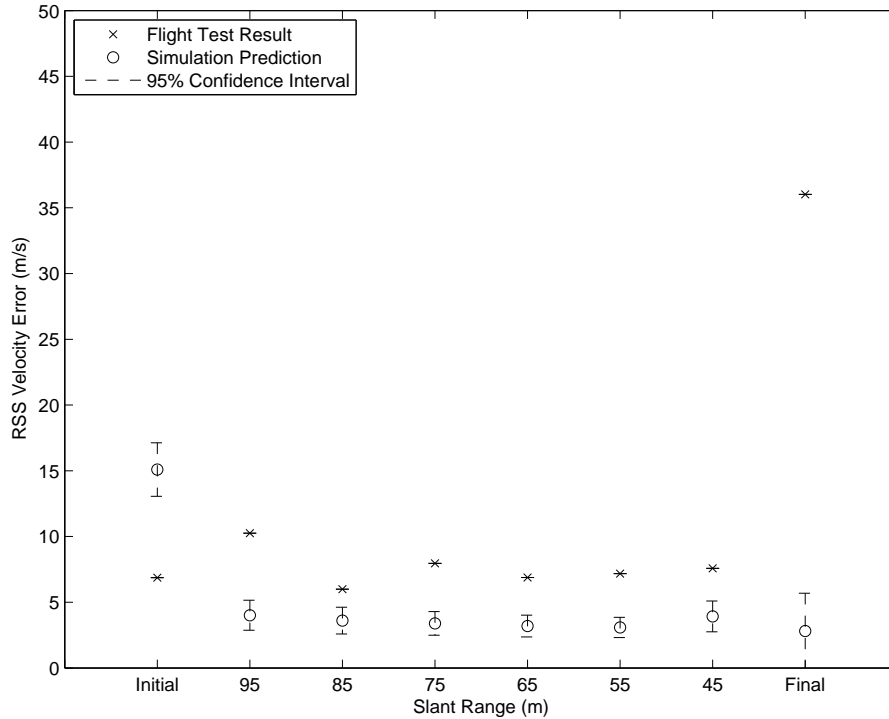


Figure 5.21: Comparison of Flight Test Results and Simulation Predictions for Average Root Sum Square Error in Unscented Kalman Filter Estimates of C-12 Velocity (70° Drone Aspect Angle)

### 5.11 Summary

This chapter presented the methods, results, and analysis for conducting flight testing on the proposed air-to-air missile scoring system. First, a detailed description of the flight tested scoring system and C-12 surrogate missile was provided. Secondly, the source of truth data for the sensor positions and the surrogate missile position and velocity was described. Next, the test execution procedures were explained to repeatably produce the desired trajectory. Additionally, this chapter described the process for calculating position and velocity error to include removal of sensor measurement bias. Finally, the test results were presented and analyzed to include average maximum sensor range and missile estimate RSS position and velocity error at each drone aspect angle. The successful implementation of the air-to-air scoring system demonstrates the potential for future application in flight test and evaluation. The

next and final chapter of this research provides a summary of relevant results and proposes future research for missile scoring.

## VI. Conclusions and Recommendations

This research demonstrated the potential for a low-cost, short-range, radar based air-to-air missile scoring system for installation on drone aircraft. The system presented utilized seven FMCW radar sensors strategically placed on the drone to provide 360 degrees spherical coverage around the aircraft. The sensors measure range and range-rate to the missile in-flight out to a distance of approximately 350 meters. A Kalman filter software algorithm fuses the sensor measurements with a missile dynamics model to estimate kinematic parameters of the missile in flight. Basic gating and data association was implemented in the software algorithm to deal with potential radar clutter. Missile position and velocity were the key parameters of interest in missile flight path reconstruction.

### *6.1 Summary of Results*

Based on the scoring strategy pursued in this research, the optimal drone configuration consists of placing sensors on the nose, tail, and both wing tips of the aircraft. In order to minimize aircraft masking, radar sensor locations were selected on both the upper and lower surface of the nose and wing tips such that four sensors maintain LOS to a missile approaching from above or below the aircraft. Since the scoring system relies on the concept of trilateration, the most accurate estimates of missile kinematic parameters require sensor placement to maximize angular separation as viewed from the incoming missile.

This research evaluated three missile dynamics model for Kalman filter implementation: constant velocity, constant acceleration, and 3D coordinated turn. The comparison was conducted by performing 100-run Monte Carlo simulations using three realistic missile trajectory scenarios. The constant dynamics model demonstrated greater precision in estimating missile position and velocity at impact. Additionally, the constant velocity dynamics model is simpler and computationally cheaper, since it only tracks missile position and velocity, while the other dynamics models also estimate missile acceleration.

This research also compared the performance of three popular nonlinear Kalman filters for this missile scoring application: an extended Kalman filter, unscented Kalman filter, and particle filter. Once again, the evaluation was conducted by executing three 100 run Monte Carlo simulations. The unscented Kalman filter demonstrated a clear advantage in precision of missile position and velocity states at impact. Furthermore, the extended Kalman filter required cumbersome calculations of numerous partial derivatives for implementation. The particle filter suffered from extreme vulnerability to particle starvation. Overcoming this limitation required large particle numbers and constant resampling which grossly increased computer processing requirements. Based on these simulation results, the unscented Kalman filter was the best choice for this air-to-air missile scoring application.

Simulation results from three scenarios demonstrated overall position accuracy and precision of the proposed scoring system on the order of centimeters. The simulated scenarios included a drone flying straight and level, executing a high-g break turn, and performing an aggressive vertical climb. Over the three scenarios, the greatest error in a position state estimate at impact by the unscented Kalman filter with a continuous velocity dynamics model was just 6.34 centimeters. Similarly, the worst-case precision at impact was characterized by a standard deviation of 12.65 centimeters. Furthermore, results were based on commercially available automotive sensors not optimized for this application. Improvement in sensor range resolution offers one method for further improving end-game position accuracy and precision.

Simulation results showed slightly greater error in estimating missile velocity at impact. Using an unscented Kalman filter with continuous velocity dynamics model, the worst-case mean error in any of the velocity states at impact was 3.5622 meters per second. Additionally, the greatest standard deviation in any velocity state was 8.4909 meters per second. Velocity estimation also suffered from observability issues, since sensors could only measure range-rate along their LOS to the missile. Therefore, the worst precision in velocity estimation occurred in the velocity components nearly

orthogonal to all sensors' LOS with the incoming missile. Despite these limitations, the velocity errors at impact were small relative to the speed of a missile.

Flight testing presented in this research supports the feasibility of employing this air-to-air missile scoring system. Using commercially available equipment, the proposed drone sensor configuration was reconstructed on the ground. A C-12 aircraft was flown at low-altitude over the sensor array to simulate a missile missing the target. Using the sensor measurements of the C-12 during overflight, the Kalman filter software successfully reconstructed the missile trajectory, reducing root sum square position error from initialization to overflight. Although error in position estimates were worse than predicted in simulations, the data suggests flight test limitations and not scoring system shortfalls were the primary cause of the reduction in performance. The inability to sync sensor measurements with GPS time and the large size of the surrogate missile (i.e., C-12) introduced significant bias into sensor measurements. Additionally, raw sensor data showed unrealistic false targets in the immediate vicinity of the C-12, probably caused by multipath or propeller effects. The software gating algorithms were only partially effective in eliminating this clutter due to its proximity to the real target.

## ***6.2 Future Work***

There are several areas in which additional research has the potential to significantly improve the usefulness of the system. First, software or hardware adjustments which improve the accuracy and/or precision of the system estimates are worth exploring. Secondly, follow on research should increase the autonomy of the system by removing the scoring system's dependence on an external system for target initialization. Finally, additional flight testing is necessary to verify system performance. The remainder of this chapter will explore each of these in greater detail.

The proposed missile scoring system is intended for missile test and evaluation; therefore, there is no requirement for real-time reconstruction of the missile trajectory. As a result, the Kalman filter software algorithm may be adjusted to

incorporate smoothing techniques. When reconstructing the missile trajectory during post-mission processing, all sensor measurements during the missile intercept are available to the Kalman filter. A Kalman filter smoother takes advantage of this knowledge when performing state estimation. At any given time in the missile trajectory, the Kalman filter smoother determines an optimal estimate of the missile position and velocity based on past and future measurements. The ability to consider future measurements allows the Kalman filter to improve estimate precision and accuracy. There are several different algorithms available for performing smoothing. Maybeck provides an in-depth discussion on the topic of Kalman filter smoothing [19].

Incorporating variable filter tuning in the Kalman filter algorithm is another option to improve system performance. As discussed in Section 4.3, two key filter tuning parameters include the dynamics noise strength,  $\mathbf{Q}$ , and the observation noise strength matrix,  $\mathbf{R}$ . The ratio of these two matrices tells the Kalman filter how much to weight the missile dynamics model versus the sensor measurements. However, the range resolution of the commercial sensors used in this research are specified as a percentage of slant range to the target. Therefore, the sensors provide more accurate measurements as the missile gets closer to the drone. Intuitively, this suggests the best estimate of missile kinematics will occur if the  $\mathbf{Q}$ -to- $\mathbf{R}$  ratio is varied according to the distance from the drone aircraft. Additional research in this area should experiment with different methods for adjusting the  $\mathbf{Q}$ -to- $\mathbf{R}$  ratio and characterize the degree of performance improvement.

The sensor specifications necessary to achieve a desired scoring performance is not directly addressed in this research. The automotive FMCW sensors considered in this research are not adequate for actual implementation for several different reasons. First, they lack the required sensitivity to detect a small RCS target like a missile, especially at a range of 350 meters. Secondly, the speed of a missile is outside their capability for range-rate measurements. Thirdly, the sensors have a narrow FOV and would not provide spherical coverage around a drone aircraft. Finally, their slow update rate and inability to sync to a GPS clock is undesirable for this application. So

presumably, implementation of this scoring system requires some careful consideration as to the design of an appropriate sensor. Future research could characterize the precision and accuracy in state estimation provided by different sensor resolutions and update rates. This knowledge would enable a customer to select or design a sensor with the minimum required specifications for the missile scoring application. This is critical to reduce cost since these sensors will be destroyed along with the drone aircraft during missile testing.

One limitation of the proposed system is the reliance on an external initialization system such as the GRDCS. With the current software, the scoring system requires this aide. Fortunately, the GRDCS is a range safety system so high reliability is expected. However, with adjustments to the missile scoring software it is possible to initialize the target solely using sensor measurements. As discussed in Section 2.6, simultaneous observations from four sensors provide enough information to uniquely identify the 3D position of the missile. However, the challenge stems from the possibility of false measurements. If four sensors simultaneously receive three range measurements for possible targets, the actual number of potential targets formed using multilateration is  $4^3$  or 64. Therefore, in the presence of radar clutter, the software scoring algorithm must include some form of track scoring or hypothesis testing [5] and [4]. In track scoring each potential target is identified as a track and additional measurements compatible with the track increase the track score. Eventually with sufficient updates the track transitions into a target. In contrast, tracks that do not receive reasonable sensor updates are discarded as clutter. Obviously, in a high clutter environment, the number of tracks can increase rapidly becoming computationally burdensome. Fortunately, limited clutter is anticipated in this end-game missile scoring application; therefore, false sensor measurements are expected rarely. Nevertheless, significant changes to the missile scoring system software are required to enable autonomous target initialization.

An additional benefit of modifying the software to incorporate track scoring is the expansion into the realm of scoring multiple missiles. There are numerous possible

scenarios in which testers may desire to evaluate multiple missile launches against a single target. Track scoring is one method to allow for multiple targets without any modifications to the scoring system hardware.

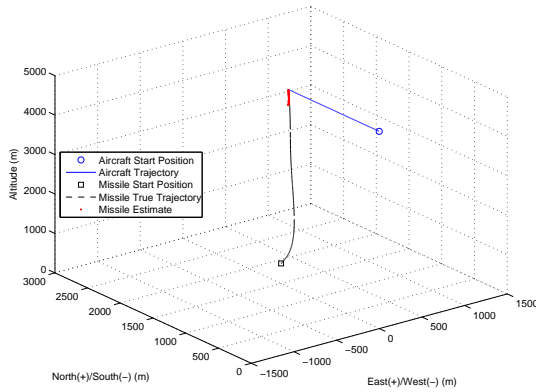
Lastly, further work on the proposed air-to-air scoring system should include additional flight testing to verify anticipated performance. The flight testing executed as part of this research demonstrated proof-of-concept, but test limitations prevented verification of actual system performance. Future flight testing should address the GPS syncing of sensors and modify the sensor firmware to allow for a higher speed target more representative of a missile. Removal of the target speed restrictions would also enable testing to proceed with a fighter-sized target as the surrogate missile thereby minimizing issues with multipath and reducing bias in sensor measurements.

### ***6.3 Summary***

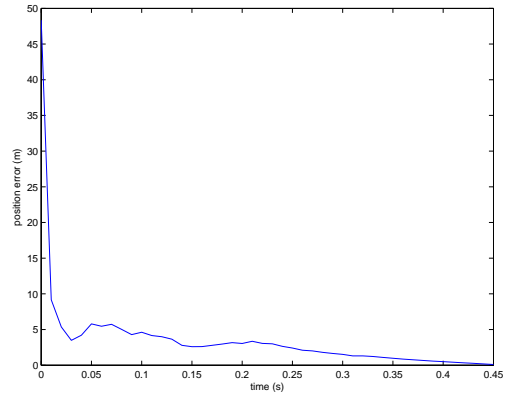
In summary, this research successfully designed, implemented, and compared several estimation techniques for air-to-air missile vector scoring. Exhaustive simulations were performed, and actual flight tests were executed. While comparison between simulations and flight tests showed some discrepancies, this research shows promise for actual implementation with modifications and opens the door to exciting follow-on work.

## Appendix A. Simulation Results

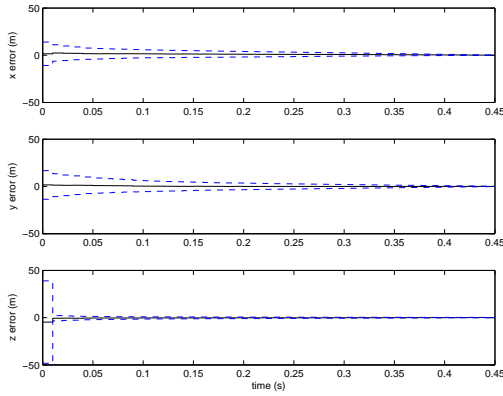
### A.1 Extended Kalman Filter Simulations



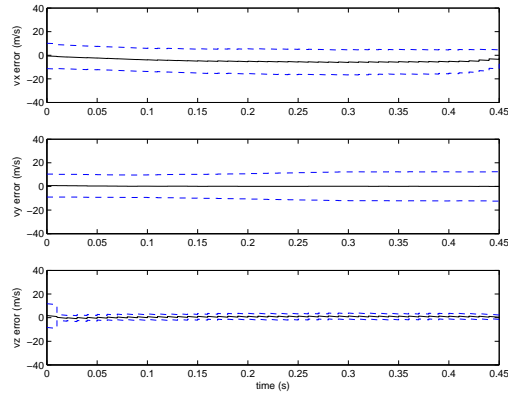
(a) 3D Aircraft and Missile Trajectory



(b) Root Sum Square Error in Missile Position Estimate (1 Run)

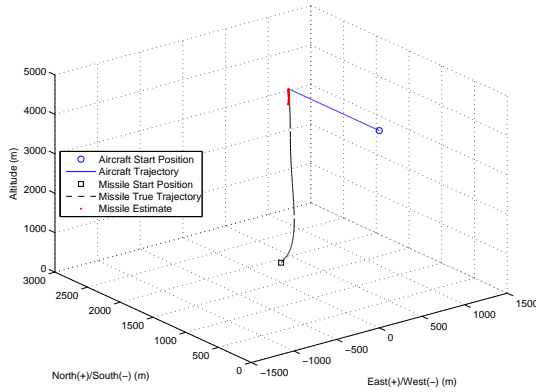


(c) Mean Error and Error Standard Deviation of Missile Position States (100 Runs)

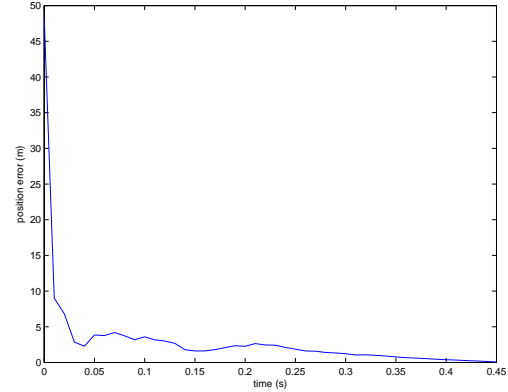


(d) Mean Error and Error Standard Deviation of Missile Velocity States (100 Runs)

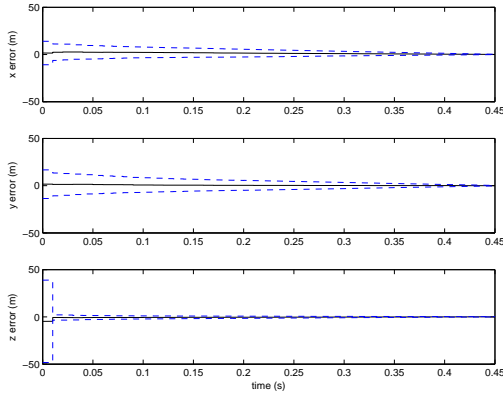
Figure A.1: Extended Kalman Filter Performance in Air-to-Air Missile Scoring Application with Continuous Velocity Dynamics Model (Target Aircraft Non-maneuvering)



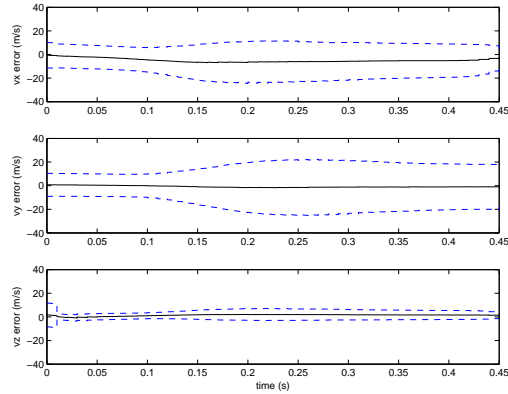
(a) 3D Aircraft and Missile Trajectory



(b) Root Sum Square Error in Missile Position Estimate (1 Run)

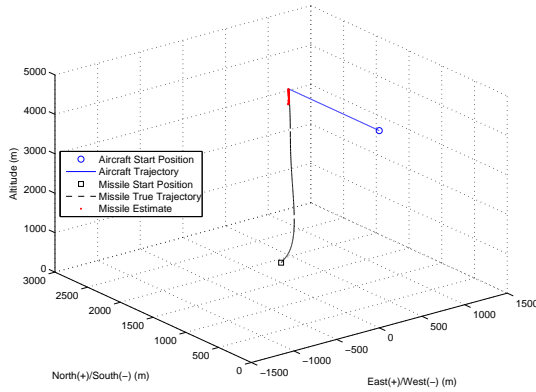


(c) Mean Error and Error Standard Deviation of Missile Position States (100 Runs)

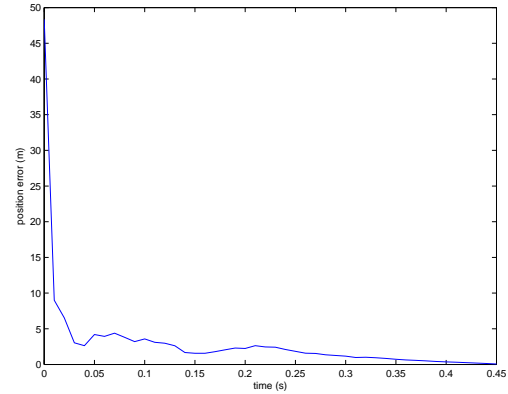


(d) Mean Error and Error Standard Deviation of Missile Velocity States (100 Runs)

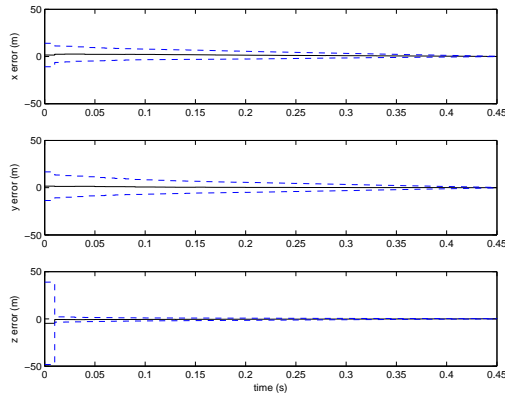
Figure A.2: Extended Kalman Filter Performance in Air-to-Air Missile Scoring Application with Continuous Acceleration Dynamics Model (Target Aircraft Non-maneuvering)



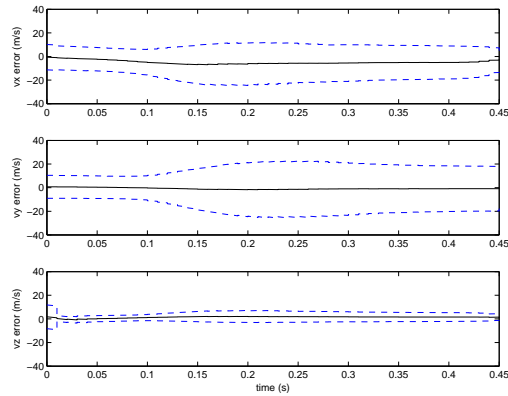
(a) 3D Aircraft and Missile Trajectory



(b) Root Sum Square Error in Missile Position Estimate (1 Run)



(c) Mean Error and Error Standard Deviation of Missile Position States (100 Runs)



(d) Mean Error and Error Standard Deviation of Missile Velocity States (100 Runs)

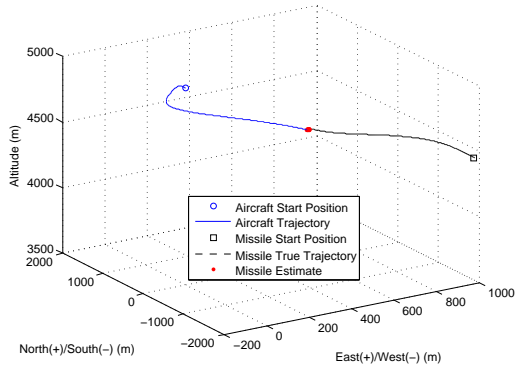
Figure A.3: Extended Kalman Filter Performance in Air-to-Air Missile Scoring Application with 3D Coordinated Turn Dynamics Model (Target Aircraft Non-maneuvering)

Table A.1: Comparison of Missile State Estimate Mean Error at Impact for Different Dynamics Models using an Extended Kalman Filter (Scenario 1)

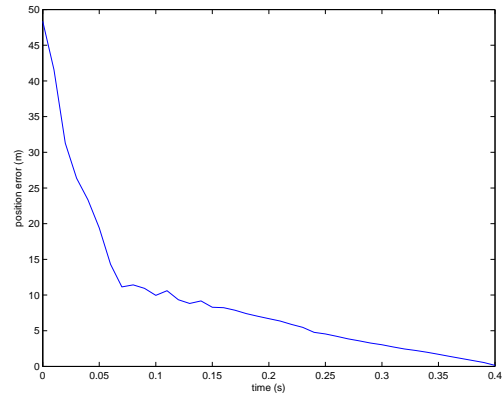
Missile State	CV Model Mean Error	CA Model Mean Error	CT Model Mean Error
$x$	0.0189 m	0.0250 m	0.0240 m
$y$	0.0126 m	0.0134 m	0.0136 m
$z$	-0.0074 m	-0.0025 m	-0.0016 m
$v_x$	-0.9687 $\frac{\text{m}}{\text{s}}$	-1.2647 $\frac{\text{m}}{\text{s}}$	-1.2212 $\frac{\text{m}}{\text{s}}$
$v_y$	-0.7961 $\frac{\text{m}}{\text{s}}$	-0.8471 $\frac{\text{m}}{\text{s}}$	-0.8617 $\frac{\text{m}}{\text{s}}$
$v_z$	0.2494 $\frac{\text{m}}{\text{s}}$	0.5409 $\frac{\text{m}}{\text{s}}$	0.5680 $\frac{\text{m}}{\text{s}}$

Table A.2: Comparison of Missile State Estimate Error Standard Deviation at Impact for Different Dynamics Models using an Extended Kalman Filter (Scenario 1)

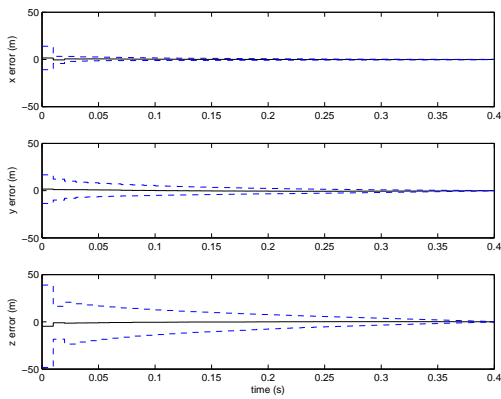
Missile State	CV Model Error Standard Deviation	CA Model Error Standard Deviation	CT Model Error Standard Deviation
$x$	0.0151 m	0.1270 m	0.1296 m
$y$	0.1503 m	0.1812 m	0.1874 m
$z$	0.0354 m	0.0294 m	0.0311 m
$v_x$	5.3800 $\frac{\text{m}}{\text{s}}$	6.0434 $\frac{\text{m}}{\text{s}}$	6.1386 $\frac{\text{m}}{\text{s}}$
$v_y$	9.4838 $\frac{\text{m}}{\text{s}}$	11.4375 $\frac{\text{m}}{\text{s}}$	11.8132 $\frac{\text{m}}{\text{s}}$
$v_z$	1.3355 $\frac{\text{m}}{\text{s}}$	1.5862 $\frac{\text{m}}{\text{s}}$	1.6022 $\frac{\text{m}}{\text{s}}$



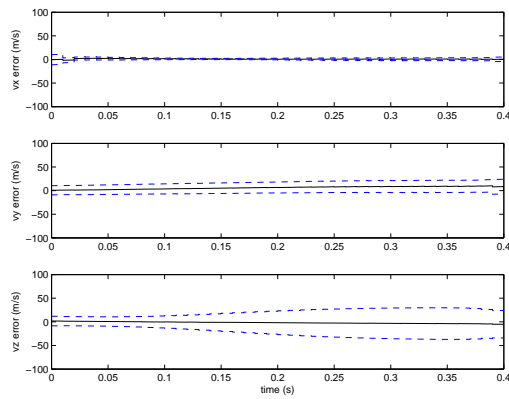
(a) 3D Aircraft and Missile Trajectory



(b) Root Sum Square Error in Missile Position Estimate (1 Run)

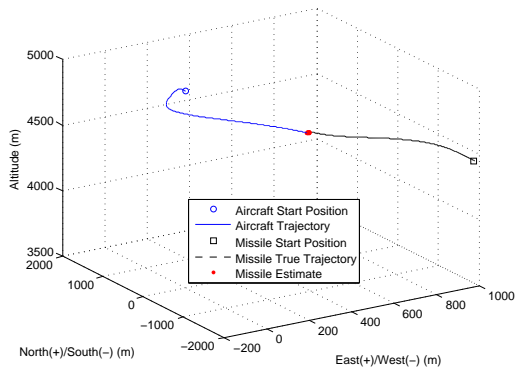


(c) Mean Error and Error Standard Deviation of Missile Position States (100 Runs)

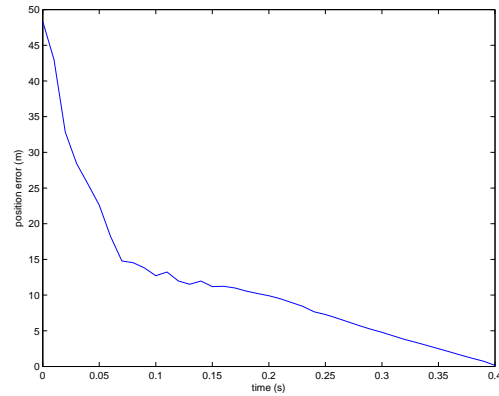


(d) Mean Error and Error Standard Deviation of Missile Velocity States (100 Runs)

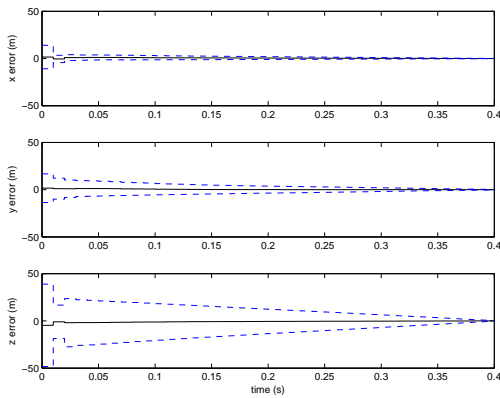
Figure A.4: Extended Kalman Filter Performance in Air-to-Air Missile Scoring Application with Continuous Velocity Dynamics Model (Target Aircraft Executing a Defensive Break Turn)



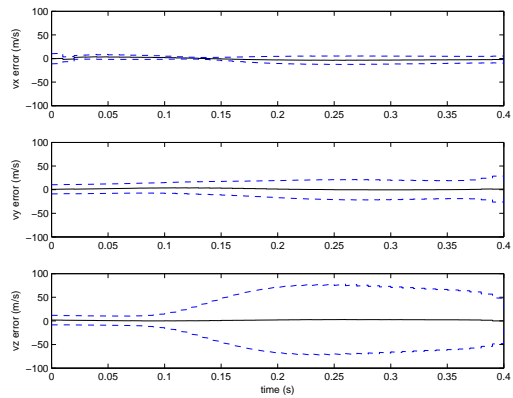
(a) 3D Aircraft and Missile Trajectory



(b) Root Sum Square Error in Missile Position Estimate (1 Run)

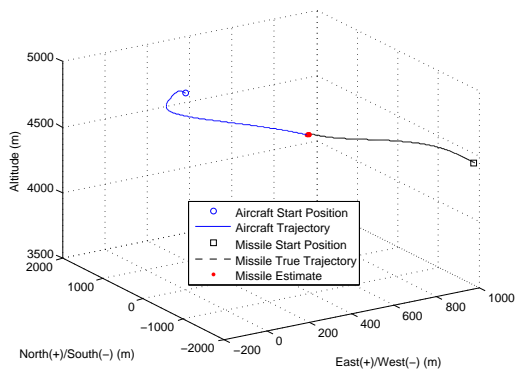


(c) Mean Error and Error Standard Deviation of Missile Position States (100 Runs)

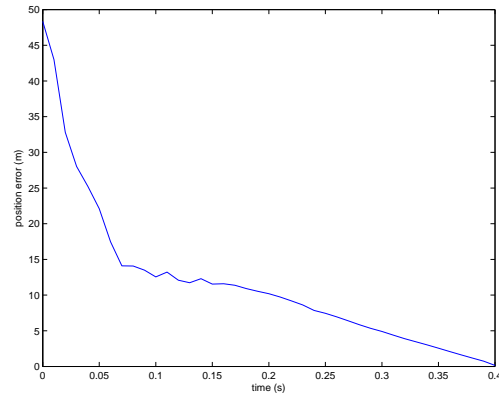


(d) Mean Error and Error Standard Deviation of Missile Velocity States (100 Runs)

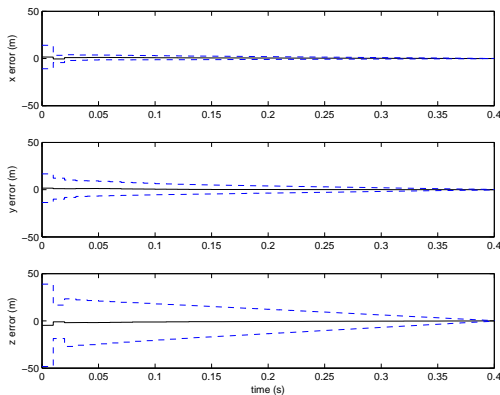
Figure A.5: Extended Kalman Filter Performance in Air-to-Air Missile Scoring Application with Continuous Acceleration Dynamics Model (Target Aircraft Executing a Defensive Break Turn)



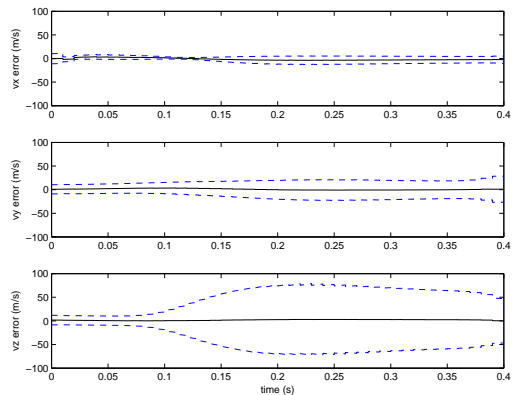
(a) 3D Aircraft and Missile Trajectory



(b) Root Sum Square Error in Missile Position Estimate (1 Run)



(c) Mean Error and Error Standard Deviation of Missile Position States (100 Runs)



(d) Mean Error and Error Standard Deviation of Missile Velocity States (100 Runs)

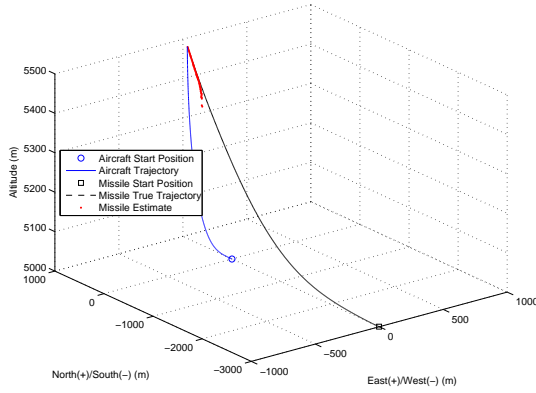
Figure A.6: Extended Kalman Filter Performance in Air-to-Air Missile Scoring Application with 3D Coordinated Turn Dynamics Model (Target Aircraft Executing a Defensive Break Turn)

Table A.3: Comparison of Missile State Estimate Mean Error at Impact for Different Dynamics Models using an Extended Kalman Filter (Scenario 2)

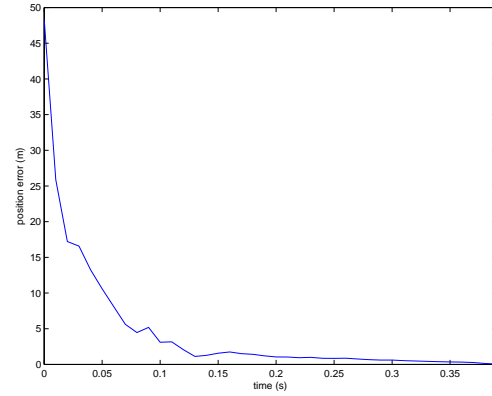
Missile State	CV Model Mean Error	CA Model Mean Error	CT Model Mean Error
$x$	0.0034 m	0.0000 m	-0.0012 m
$y$	-0.0199 m	-0.0153 m	-0.0120 m
$z$	0.0256 m	0.0250 m	0.0186 m
$v_x$	0.9924 $\frac{\text{m}}{\text{s}}$	0.6511 $\frac{\text{m}}{\text{s}}$	0.7266 $\frac{\text{m}}{\text{s}}$
$v_y$	2.2057 $\frac{\text{m}}{\text{s}}$	1.9207 $\frac{\text{m}}{\text{s}}$	1.2400 $\frac{\text{m}}{\text{s}}$
$v_z$	-1.9546 $\frac{\text{m}}{\text{s}}$	-2.4550 $\frac{\text{m}}{\text{s}}$	-1.2838 $\frac{\text{m}}{\text{s}}$

Table A.4: Comparison of Missile State Estimate Error Standard Deviation at Impact for Different Dynamics Models using an Extended Kalman Filter (Scenario 2)

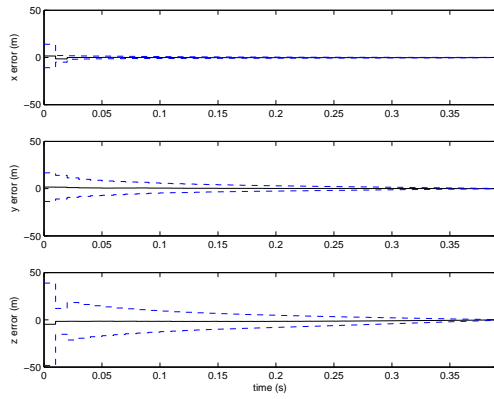
Missile State	CV Model Error Standard Deviation	CA Model Error Standard Deviation	CT Model Error Standard Deviation
$x$	0.0194 m	0.0224 m	0.0231 m
$y$	0.0762 m	0.1210 m	0.1099 m
$z$	0.1130 m	0.1983 m	0.1671 m
$v_x$	0.9391 $\frac{\text{m}}{\text{s}}$	1.9879 $\frac{\text{m}}{\text{s}}$	2.3412 $\frac{\text{m}}{\text{s}}$
$v_y$	6.2837 $\frac{\text{m}}{\text{s}}$	12.9057 $\frac{\text{m}}{\text{s}}$	9.1882 $\frac{\text{m}}{\text{s}}$
$v_z$	8.5262 $\frac{\text{m}}{\text{s}}$	19.7077 $\frac{\text{m}}{\text{s}}$	12.0386 $\frac{\text{m}}{\text{s}}$



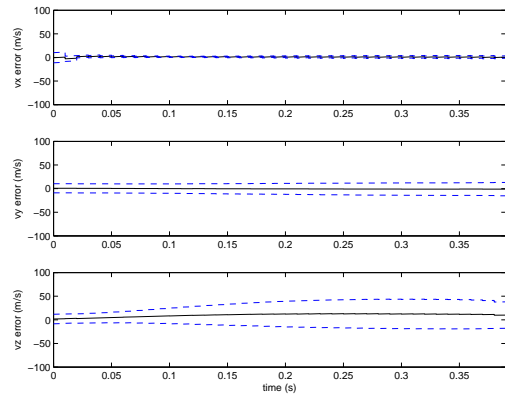
(a) 3D Aircraft and Missile Trajectory



(b) Root Sum Square Error in Missile Position Estimate (1 Run)

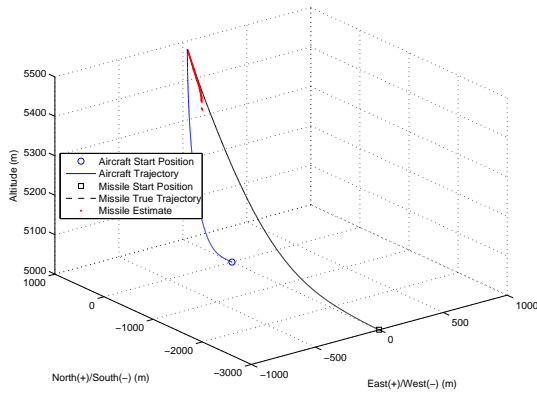


(c) Mean Error and Error Standard Deviation of Missile Position States (100 Runs)

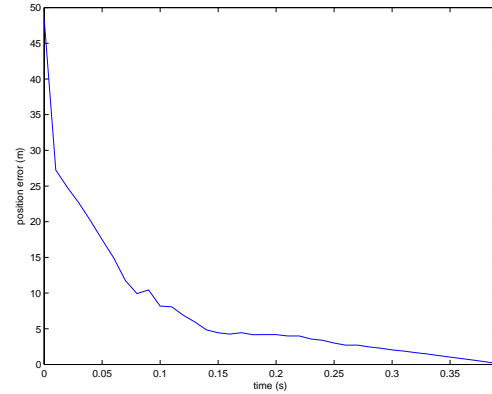


(d) Mean Error and Error Standard Deviation of Missile Velocity States (100 Runs)

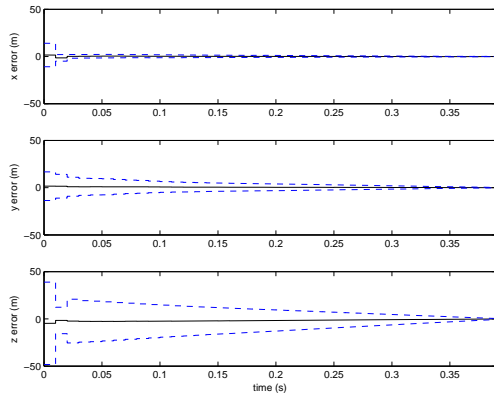
Figure A.7: Extended Kalman Filter Performance in Air-to-Air Missile Scoring Application with Continuous Velocity Dynamics Model (Target Aircraft Executing a Vertical Climb)



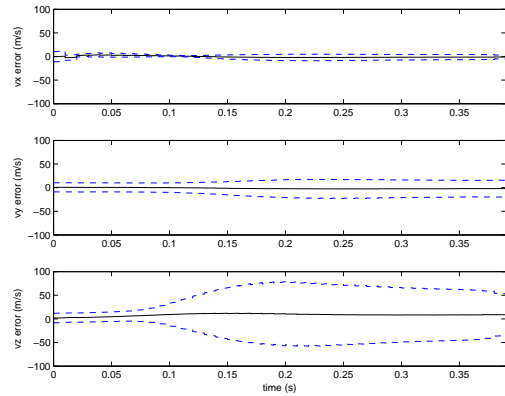
(a) 3D Aircraft and Missile Trajectory



(b) Root Sum Square Error in Missile Position Estimate (1 Run)

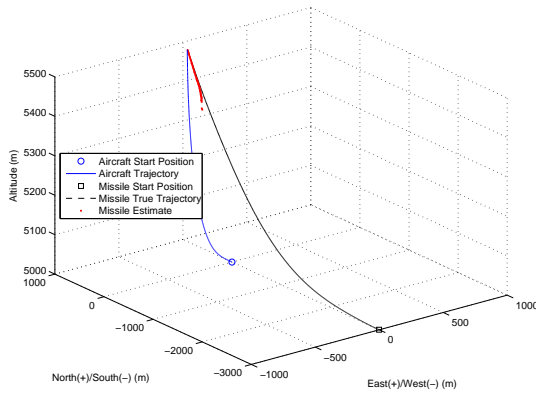


(c) Mean Error and Error Standard Deviation of Missile Position States (100 Runs)

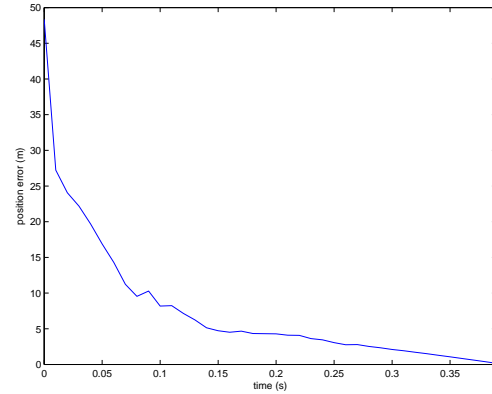


(d) Mean Error and Error Standard Deviation of Missile Velocity States (100 Runs)

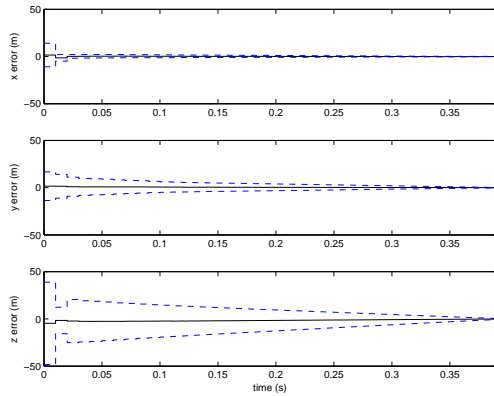
Figure A.8: Extended Kalman Filter Performance in Air-to-Air Missile Scoring Application with Continuous Acceleration Dynamics Model (Target Aircraft Executing a Vertical Climb)



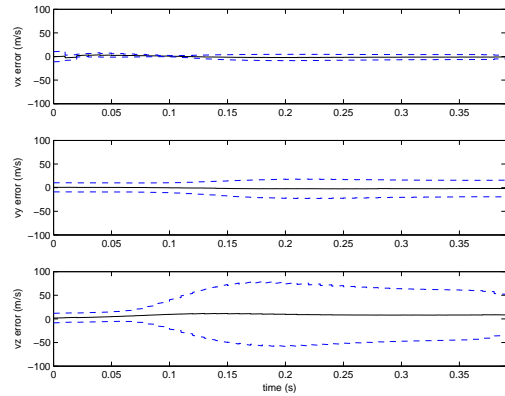
(a) 3D Aircraft and Missile Trajectory



(b) Root Sum Square Error in Missile Position Estimate (1 Run)



(c) Mean Error and Error Standard Deviation of Missile Position States (100 Runs)



(d) Mean Error and Error Standard Deviation of Missile Velocity States (100 Runs)

Figure A.9: Extended Kalman Filter Performance in Air-to-Air Missile Scoring Application with 3D Coordinated Turn Dynamics Model (Target Aircraft Executing a Vertical Climb)

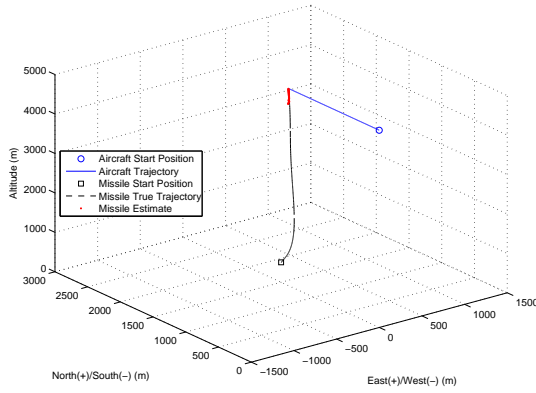
Table A.5: Comparison of Missile State Estimate Mean Error at Impact for Different Dynamics Models using an Extended Kalman Filter (Scenario 3)

Missile State	CV Model Mean Error	CA Model Mean Error	CT Model Mean Error
$x$	0.0088 m	-0.0017 m	-0.0026 m
$y$	0.0050 m	0.0219 m	0.0226 m
$z$	-0.0724 m	-0.0793 m	-0.0787 m
$v_x$	0.7081 $\frac{\text{m}}{\text{s}}$	0.0991 $\frac{\text{m}}{\text{s}}$	0.0299 $\frac{\text{m}}{\text{s}}$
$v_y$	-0.3869 $\frac{\text{m}}{\text{s}}$	-1.7269 $\frac{\text{m}}{\text{s}}$	-1.7766 $\frac{\text{m}}{\text{s}}$
$v_z$	3.9596 $\frac{\text{m}}{\text{s}}$	4.6376 $\frac{\text{m}}{\text{s}}$	4.6444 $\frac{\text{m}}{\text{s}}$

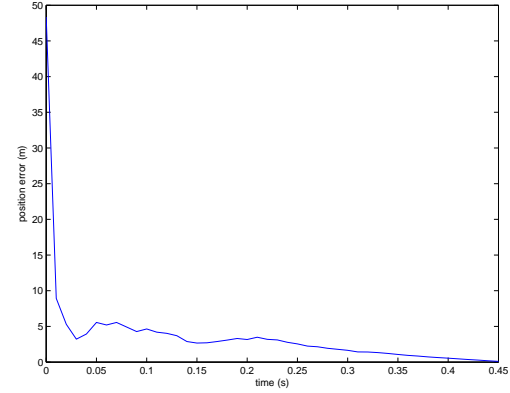
Table A.6: Comparison of Missile State Estimate Error Standard Deviation at Impact for Different Dynamics Models using an Extended Kalman Filter (Scenario 3)

Missile State	CV Model Error Standard Deviation	CA Model Error Standard Deviation	CT Model Error Standard Deviation
$x$	0.0150 m	0.0711 m	0.0684 m
$y$	0.1521 m	0.1934 m	0.1933 m
$z$	0.2529 m	0.4379 m	0.4440 m
$v_x$	1.7028 $\frac{\text{m}}{\text{s}}$	2.1058 $\frac{\text{m}}{\text{s}}$	2.1245 $\frac{\text{m}}{\text{s}}$
$v_y$	11.8460 $\frac{\text{m}}{\text{s}}$	15.1679 $\frac{\text{m}}{\text{s}}$	15.1300 $\frac{\text{m}}{\text{s}}$
$v_z$	13.7464 $\frac{\text{m}}{\text{s}}$	26.2245 $\frac{\text{m}}{\text{s}}$	26.2736 $\frac{\text{m}}{\text{s}}$

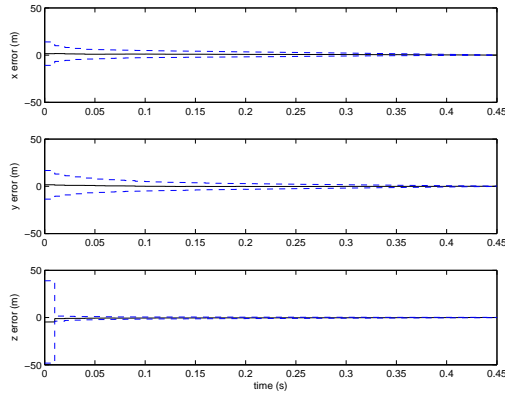
## A.2 Unscented Kalman Filter Simulations



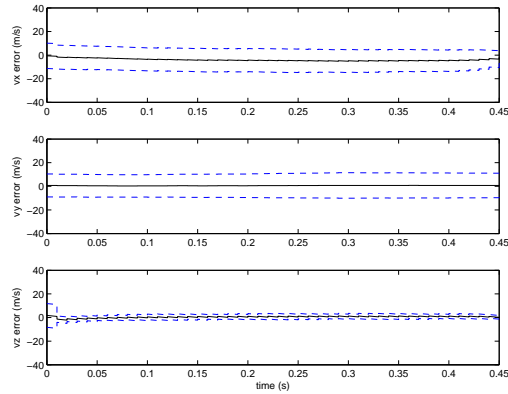
(a) 3D Aircraft and Missile Trajectory



(b) Root Sum Square Error in Missile Position Estimate (1 Run)

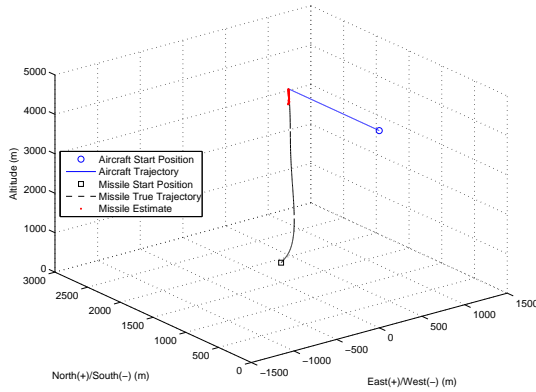


(c) Mean Error and Error Standard Deviation of Missile Position States (100 Runs)

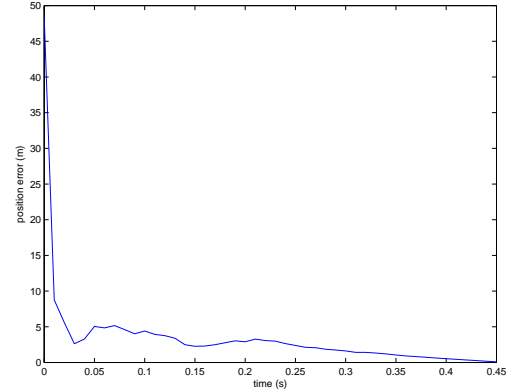


(d) Mean Error and Error Standard Deviation of Missile Velocity States (100 Runs)

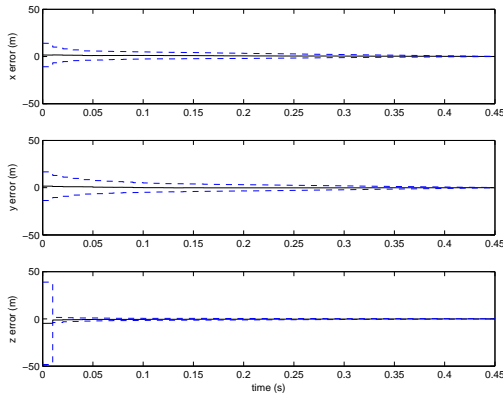
Figure A.10: Unscented Kalman Filter Performance in Air-to-Air Missile Scoring Application with Continuous Velocity Dynamics Model (Target Aircraft Non-maneuvering)



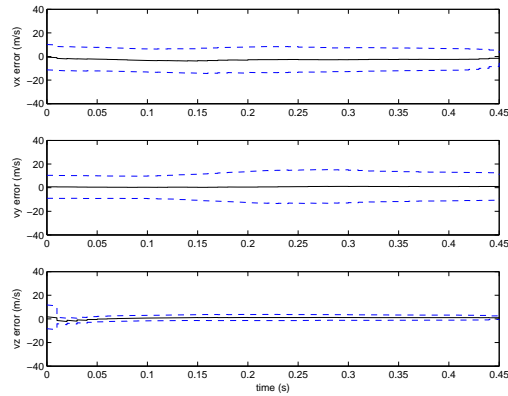
(a) 3D Aircraft and Missile Trajectory



(b) Root Sum Square Error in Missile Position Estimate (1 Run)

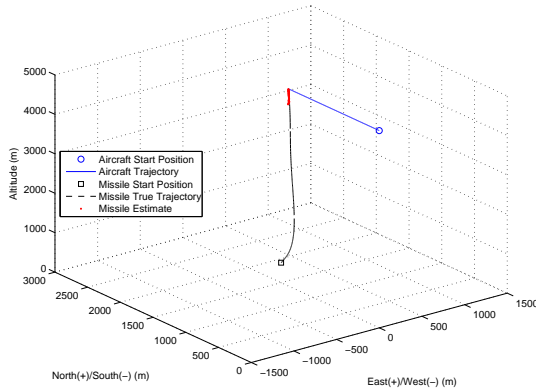


(c) Mean Error and Error Standard Deviation of Missile Position States (100 Runs)

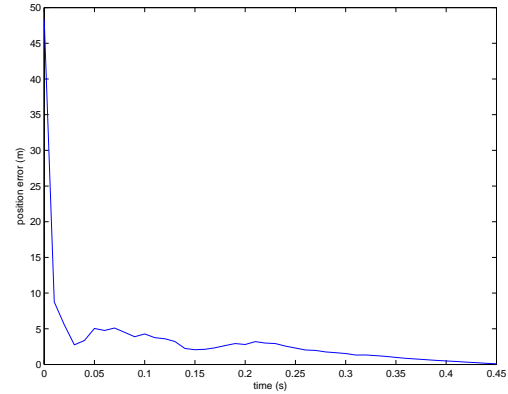


(d) Mean Error and Error Standard Deviation of Missile Velocity States (100 Runs)

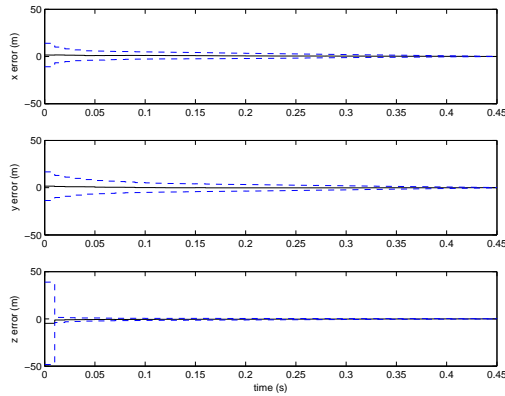
Figure A.11: Unscented Kalman Filter Performance in Air-to-Air Missile Scoring Application with Continuous Acceleration Dynamics Model (Target Aircraft Non-maneuvering)



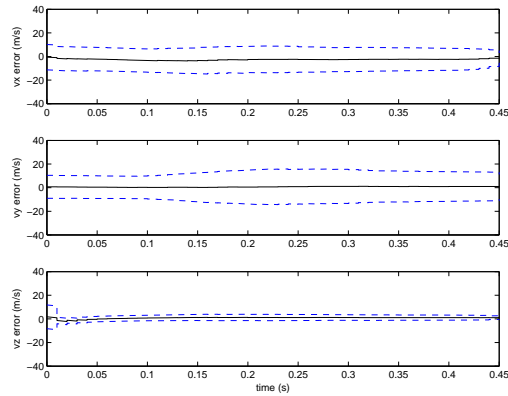
(a) 3D Aircraft and Missile Trajectory



(b) Root Sum Square Error in Missile Position Estimate (1 Run)



(c) Mean Error and Error Standard Deviation of Missile Position States (100 Runs)



(d) Mean Error and Error Standard Deviation of Missile Velocity States (100 Runs)

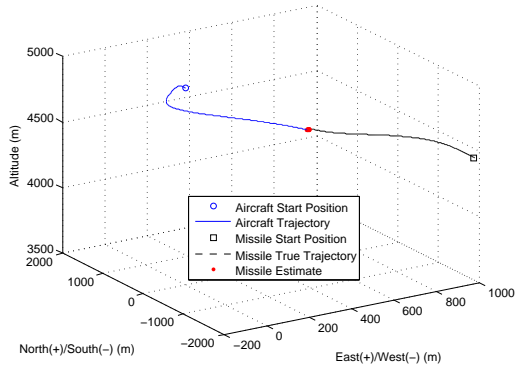
Figure A.12: Unscented Kalman Filter Performance in Air-to-Air Missile Scoring Application with 3D Coordinated Turn Dynamics Model (Target Aircraft Non-maneuvering)

Table A.7: Comparison of Missile State Estimate Mean Error at Impact for Different Dynamics Models using an Unscented Kalman Filter (Scenario 1)

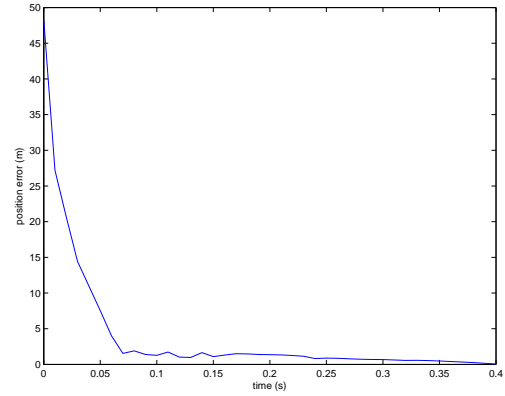
Missile State	CV Model Mean Error	CA Model Mean Error	CT Model Mean Error
$x$	0.0188 m	0.0100 m	0.0089 m
$y$	0.0093 m	0.0094 m	0.0097 m
$z$	-0.0166 m	-0.0012 m	-0.0005 m
$v_x$	-0.8801 $\frac{\text{m}}{\text{s}}$	-0.5274 $\frac{\text{m}}{\text{s}}$	-0.4853 $\frac{\text{m}}{\text{s}}$
$v_y$	-0.5921 $\frac{\text{m}}{\text{s}}$	-0.5948 $\frac{\text{m}}{\text{s}}$	-0.6142 $\frac{\text{m}}{\text{s}}$
$v_z$	0.1685 $\frac{\text{m}}{\text{s}}$	0.5865 $\frac{\text{m}}{\text{s}}$	0.6152 $\frac{\text{m}}{\text{s}}$

Table A.8: Comparison of Missile State Estimate Error Standard Deviation at Impact for Different Dynamics Models using an Unscented Kalman Filter (Scenario 1)

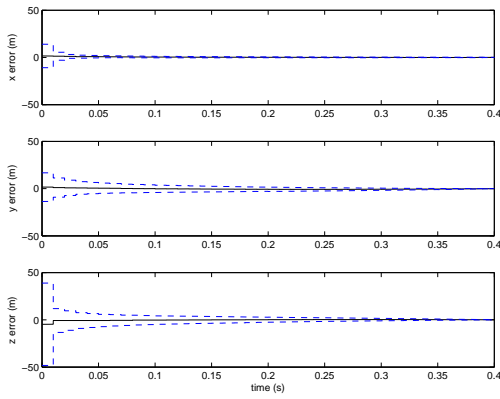
Missile State	CV Model Error Standard Deviation	CA Model Error Standard Deviation	CT Model Error Standard Deviation
$x$	0.1005 m	0.0923 m	0.0959 m
$y$	0.1265 m	0.1385 m	0.1460 m
$z$	0.0323 m	0.0222 m	0.0243 m
$v_x$	4.7050 $\frac{\text{m}}{\text{s}}$	4.3789 $\frac{\text{m}}{\text{s}}$	4.5283 $\frac{\text{m}}{\text{s}}$
$v_y$	8.0019 $\frac{\text{m}}{\text{s}}$	8.7537 $\frac{\text{m}}{\text{s}}$	9.2122 $\frac{\text{m}}{\text{s}}$
$v_z$	1.1521 $\frac{\text{m}}{\text{s}}$	1.1013 $\frac{\text{m}}{\text{s}}$	1.1356 $\frac{\text{m}}{\text{s}}$



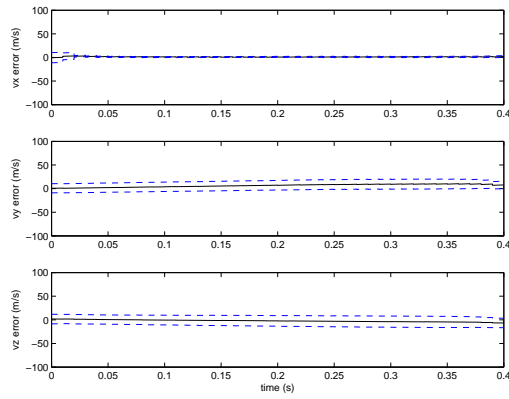
(a) 3D Aircraft and Missile Trajectory



(b) Root Sum Square Error in Missile Position Estimate (1 Run)

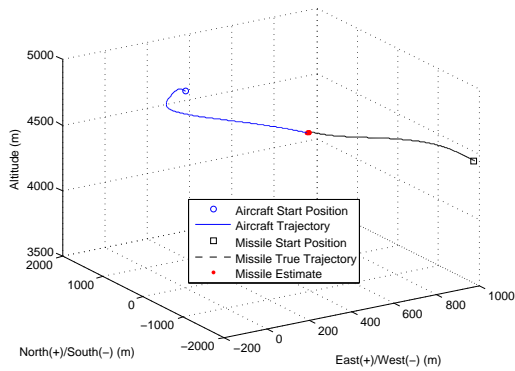


(c) Mean Error and Error Standard Deviation of Missile Position States (100 Runs)

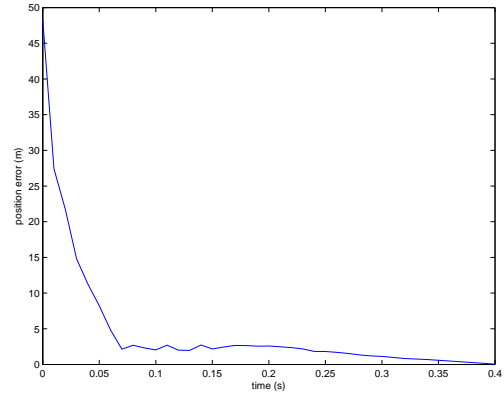


(d) Mean Error and Error Standard Deviation of Missile Velocity States (100 Runs)

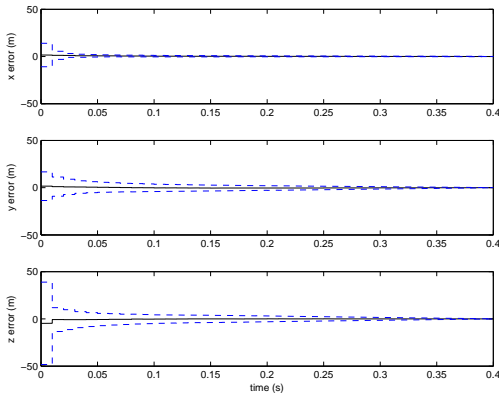
Figure A.13: Unscented Kalman Filter Performance in Air-to-Air Missile Scoring Application with Continuous Velocity Dynamics Model (Target Aircraft Executing a Defensive Break Turn)



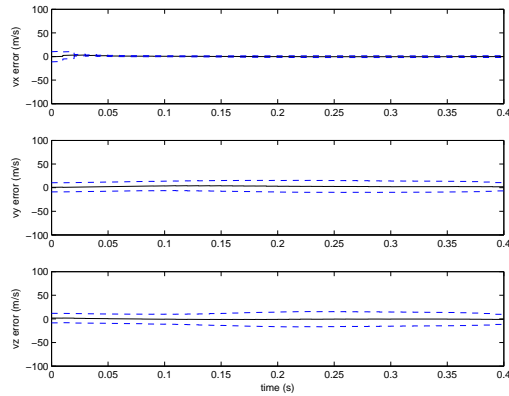
(a) 3D Aircraft and Missile Trajectory



(b) Root Sum Square Error in Missile Position Estimate (1 Run)

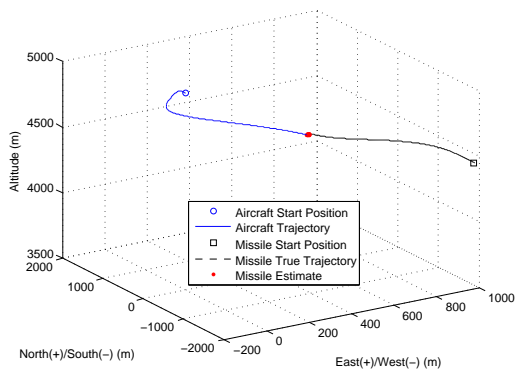


(c) Mean Error and Error Standard Deviation of Missile Position States (100 Runs)

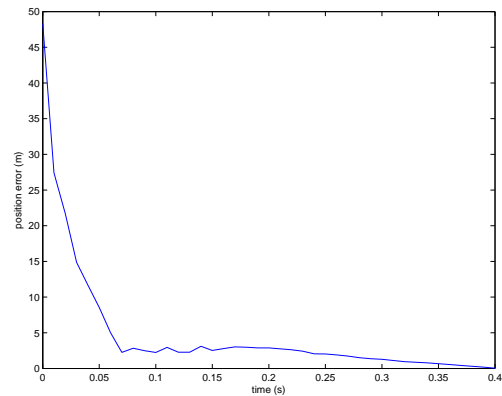


(d) Mean Error and Error Standard Deviation of Missile Velocity States (100 Runs)

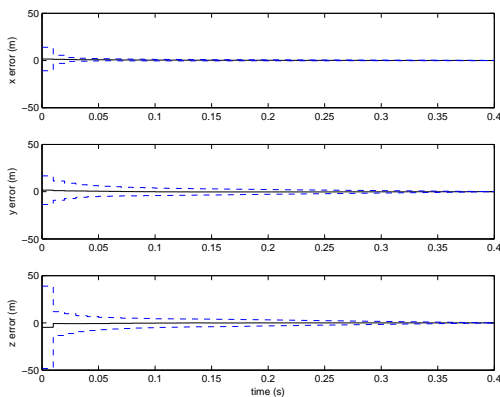
Figure A.14: Unscented Kalman Filter Performance in Air-to-Air Missile Scoring Application with Continuous Acceleration Dynamics Model (Target Aircraft Executing a Defensive Break Turn)



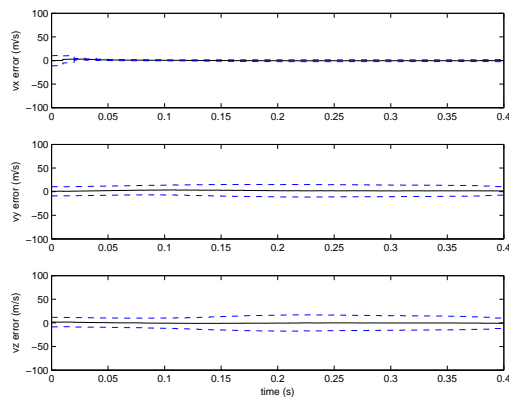
(a) 3D Aircraft and Missile Trajectory



(b) Root Sum Square Error in Missile Position Estimate (1 Run)



(c) Mean Error and Error Standard Deviation of Missile Position States (100 Runs)



(d) Mean Error and Error Standard Deviation of Missile Velocity States (100 Runs)

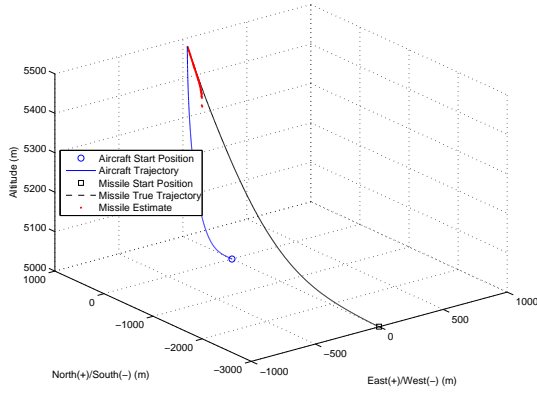
Figure A.15: Unscented Kalman Filter Performance in Air-to-Air Missile Scoring Application with 3D Coordinated Turn Dynamics Model (Target Aircraft Executing a Defensive Break Turn)

Table A.9: Comparison of Missile State Estimate Mean Error at Impact for Different Dynamics Models using an Unscented Kalman Filter (Scenario 2)

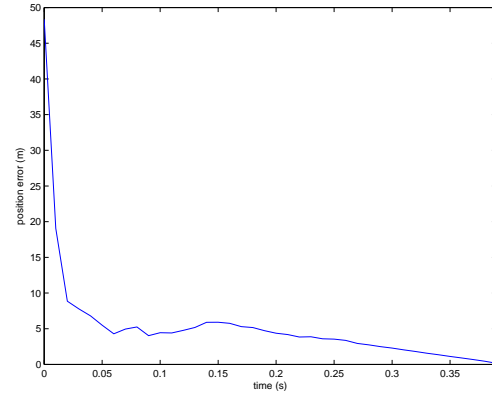
Missile State	CV Model Mean Error	CA Model Mean Error	CT Model Mean Error
$x$	-0.0005 m	-0.0015 m	-0.0017 m
$y$	-0.0256 m	-0.0097 m	-0.0095 m
$z$	0.0264 m	0.0123 m	0.0121 m
$v_x$	1.1089 $\frac{\text{m}}{\text{s}}$	-0.0420 $\frac{\text{m}}{\text{s}}$	-0.0551 $\frac{\text{m}}{\text{s}}$
$v_y$	2.6419 $\frac{\text{m}}{\text{s}}$	0.7519 $\frac{\text{m}}{\text{s}}$	0.7275 $\frac{\text{m}}{\text{s}}$
$v_z$	-2.0683 $\frac{\text{m}}{\text{s}}$	-0.9832 $\frac{\text{m}}{\text{s}}$	-0.9719 $\frac{\text{m}}{\text{s}}$

Table A.10: Comparison of Missile State Estimate Error Standard Deviation at Impact for Different Dynamics Models using an Unscented Kalman Filter (Scenario 2)

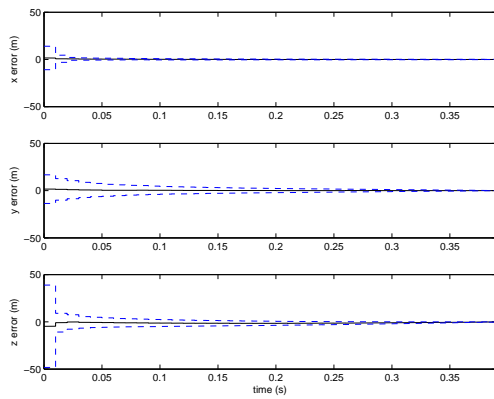
Missile State	CV Model Error Standard Deviation	CA Model Error Standard Deviation	CT Model Error Standard Deviation
$x$	0.0040 m	0.0027 m	0.0029 m
$y$	0.0310 m	0.0257 m	0.0265 m
$z$	0.0317 m	0.0262 m	0.0273 m
$v_x$	0.5608 $\frac{\text{m}}{\text{s}}$	0.4983 $\frac{\text{m}}{\text{s}}$	0.5138 $\frac{\text{m}}{\text{s}}$
$v_y$	2.4432 $\frac{\text{m}}{\text{s}}$	2.0602 $\frac{\text{m}}{\text{s}}$	2.1214 $\frac{\text{m}}{\text{s}}$
$v_z$	2.5532 $\frac{\text{m}}{\text{s}}$	2.0826 $\frac{\text{m}}{\text{s}}$	2.1590 $\frac{\text{m}}{\text{s}}$



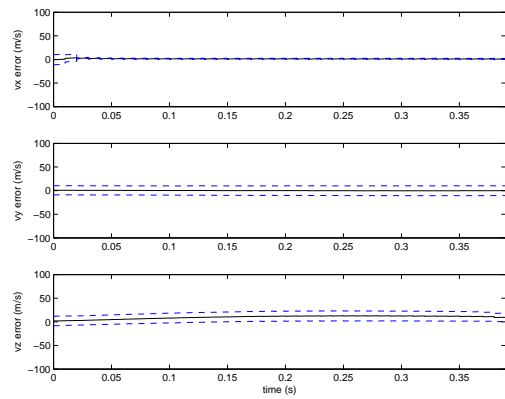
(a) 3D Aircraft and Missile Trajectory



(b) Root Sum Square Error in Missile Position Estimate (1 Run)

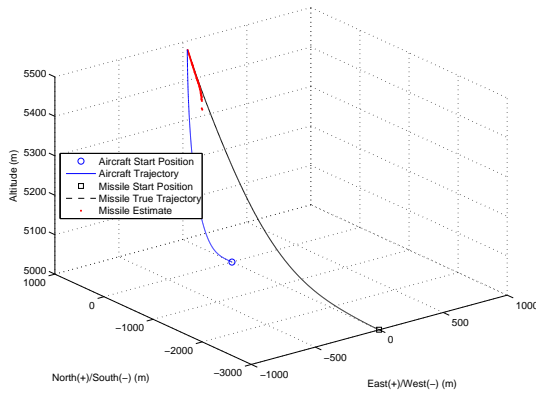


(c) Mean Error and Error Standard Deviation of Missile Position States (100 Runs)

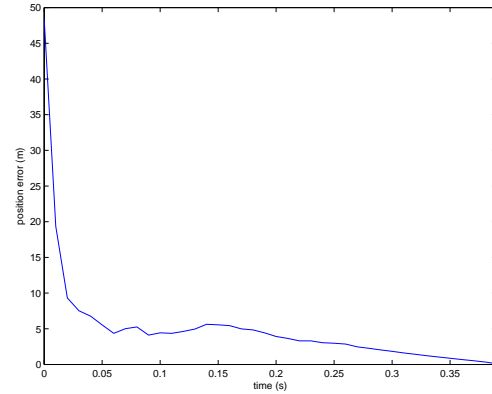


(d) Mean Error and Error Standard Deviation of Missile Velocity States (100 Runs)

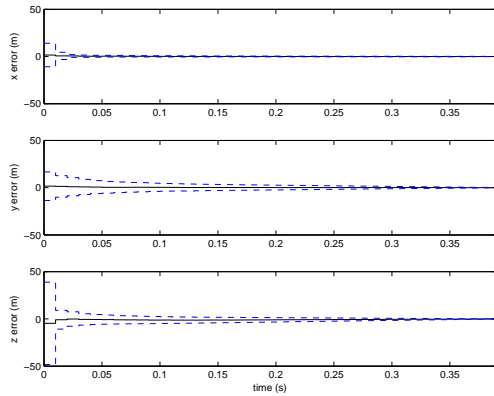
Figure A.16: Unscented Kalman Filter Performance in Air-to-Air Missile Scoring Application with Continuous Velocity Dynamics Model (Target Aircraft Executing a Vertical Climb)



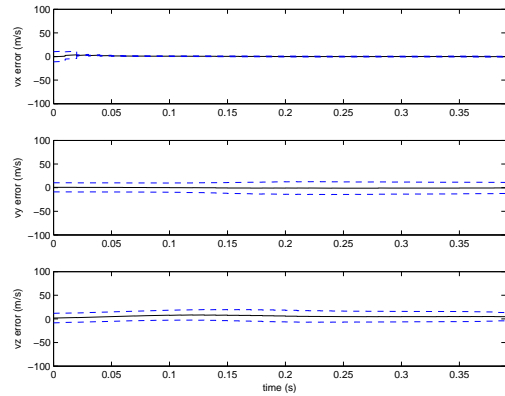
(a) 3D Aircraft and Missile Trajectory



(b) Root Sum Square Error in Missile Position Estimate (1 Run)

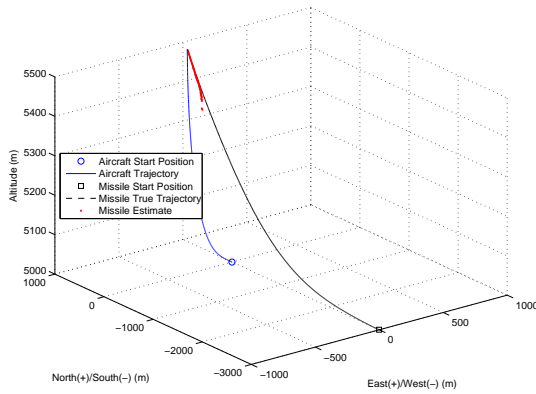


(c) Mean Error and Error Standard Deviation of Missile Position States (100 Runs)

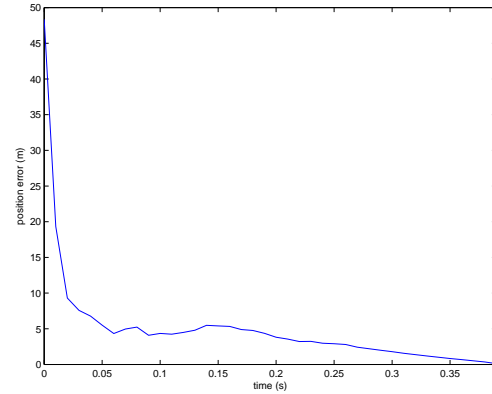


(d) Mean Error and Error Standard Deviation of Missile Velocity States (100 Runs)

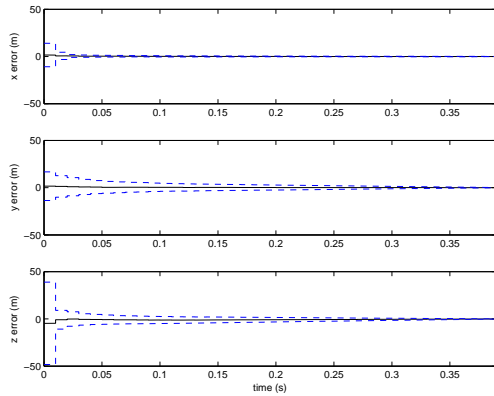
Figure A.17: Unscented Kalman Filter Performance in Air-to-Air Missile Scoring Application with Continuous Acceleration Dynamics Model (Target Aircraft Executing a Vertical Climb)



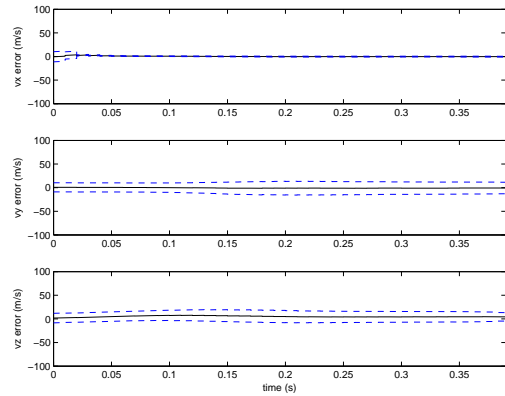
(a) 3D Aircraft and Missile Trajectory



(b) Root Sum Square Error in Missile Position Estimate (1 Run)



(c) Mean Error and Error Standard Deviation of Missile Position States (100 Runs)



(d) Mean Error and Error Standard Deviation of Missile Velocity States (100 Runs)

Figure A.18: Unscented Kalman Filter Performance in Air-to-Air Missile Scoring Application with 3D Coordinated Turn Dynamics Model (Target Aircraft Executing a Vertical Climb)

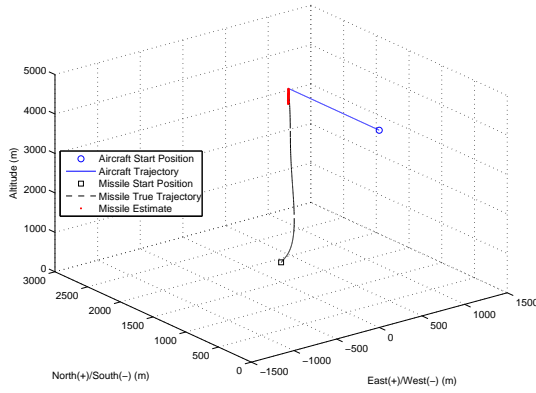
Table A.11: Comparison of Missile State Estimate Mean Error at Impact for Different Dynamics Models using an Unscented Kalman Filter (Scenario 3)

Missile State	CV Model Mean Error	CA Model Mean Error	CT Model Mean Error
$x$	0.0068 m	-0.0007 m	-0.0004 m
$y$	-0.0068 m	-0.0036 m	-0.0026 m
$z$	-0.0634 m	-0.0328 m	-0.0302 m
$v_x$	0.6113 $\frac{\text{m}}{\text{s}}$	-0.2165 $\frac{\text{m}}{\text{s}}$	-0.2599 $\frac{\text{m}}{\text{s}}$
$v_y$	0.5280 $\frac{\text{m}}{\text{s}}$	0.2801 $\frac{\text{m}}{\text{s}}$	0.2017 $\frac{\text{m}}{\text{s}}$
$v_z$	3.5622 $\frac{\text{m}}{\text{s}}$	1.7507 $\frac{\text{m}}{\text{s}}$	1.6033 $\frac{\text{m}}{\text{s}}$

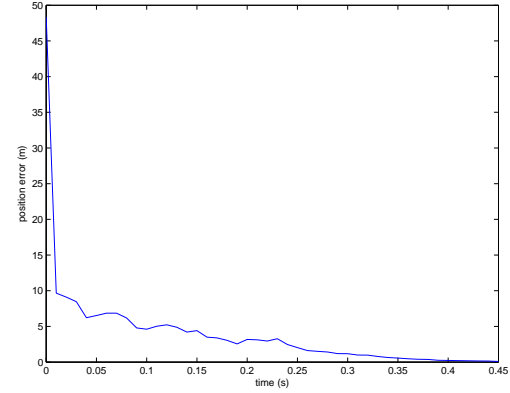
Table A.12: Comparison of Missile State Estimate Error Standard Deviation at Impact for Different Dynamics Models using an Unscented Kalman Filter (Scenario 3)

Missile State	CV Model Error Standard Deviation	CA Model Error Standard Deviation	CT Model Error Standard Deviation
$x$	0.0052 m	0.0037 m	0.0041 m
$y$	0.1091 m	0.1116 m	0.1167 m
$z$	0.0673 m	0.0553 m	0.0591 m
$v_x$	0.5371 $\frac{\text{m}}{\text{s}}$	0.4069 $\frac{\text{m}}{\text{s}}$	0.4345 $\frac{\text{m}}{\text{s}}$
$v_y$	8.4909 $\frac{\text{m}}{\text{s}}$	8.6923 $\frac{\text{m}}{\text{s}}$	9.0832 $\frac{\text{m}}{\text{s}}$
$v_z$	3.6732 $\frac{\text{m}}{\text{s}}$	3.0559 $\frac{\text{m}}{\text{s}}$	3.2494 $\frac{\text{m}}{\text{s}}$

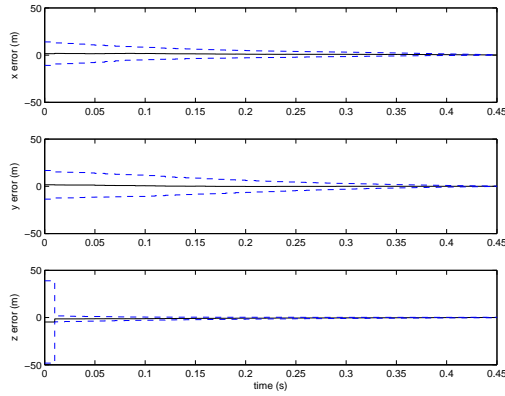
### A.3 Particle Filter Simulations



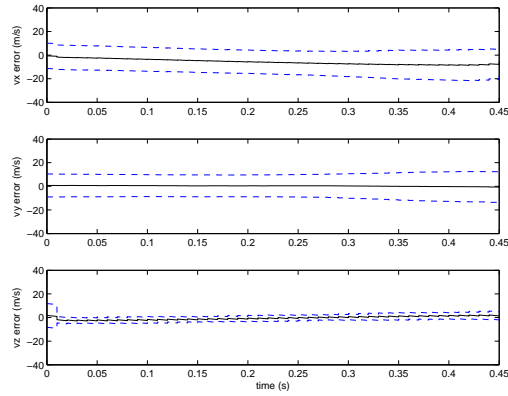
(a) 3D Aircraft and Missile Trajectory



(b) Root Sum Square Error in Missile Position Estimate (1 Run)

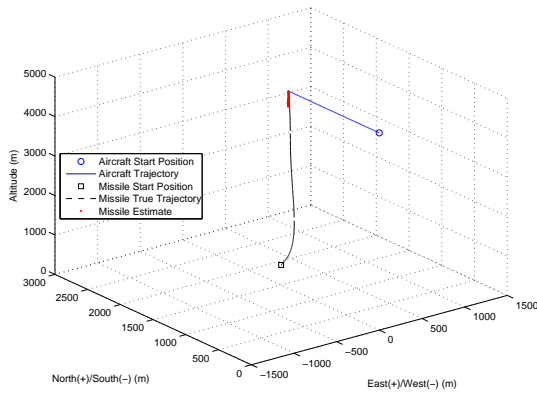


(c) Mean Error and Error Standard Deviation of Missile Position States (100 Runs)

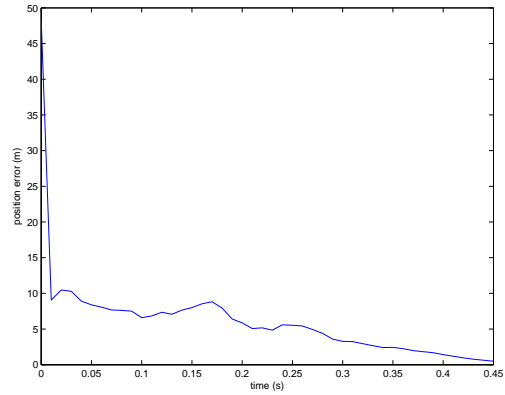


(d) Mean Error and Error Standard Deviation of Missile Velocity States (100 Runs)

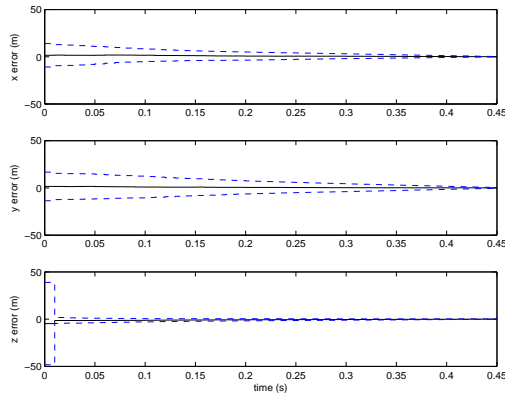
Figure A.19: Particle Filter Performance in Air-to-Air Missile Scoring Application with Continuous Velocity Dynamics Model (Target Aircraft Non-maneuvering)



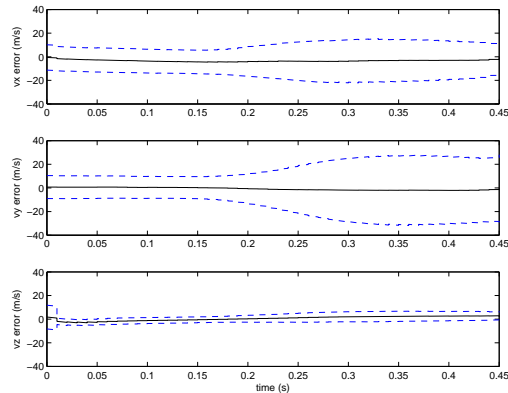
(a) 3D Aircraft and Missile Trajectory



(b) Root Sum Square Error in Missile Position Estimate (1 Run)

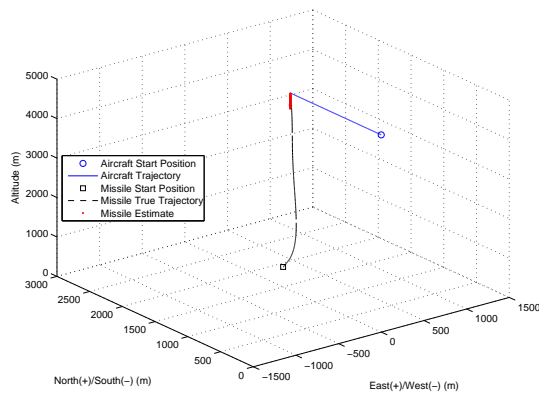


(c) Mean Error and Error Standard Deviation of Missile Position States (100 Runs)

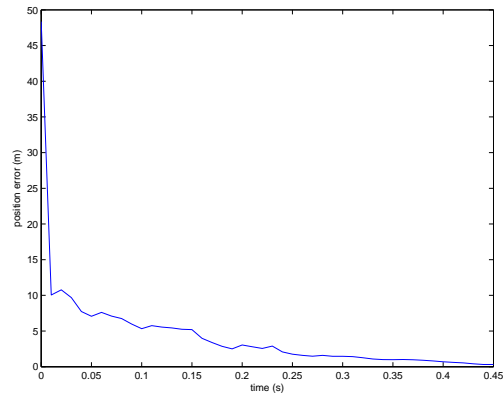


(d) Mean Error and Error Standard Deviation of Missile Velocity States (100 Runs)

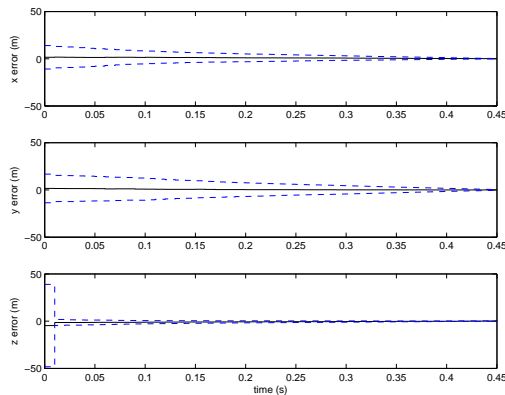
Figure A.20: Particle Filter Performance in Air-to-Air Missile Scoring Application with Continuous Acceleration Dynamics Model (Target Aircraft Non-maneuvering)



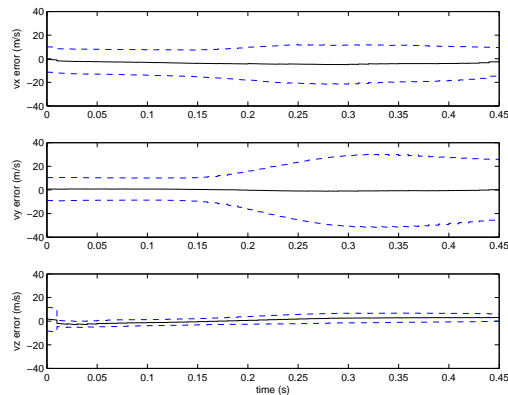
(a) 3D Aircraft and Missile Trajectory



(b) Root Sum Square Error in Missile Position Estimate (1 Run)



(c) Mean Error and Error Standard Deviation of Missile Position States (100 Runs)



(d) Mean Error and Error Standard Deviation of Missile Velocity States (100 Runs)

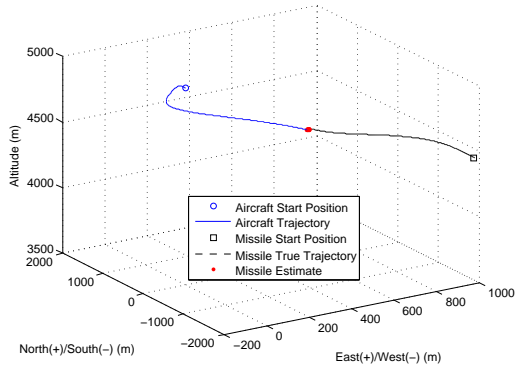
Figure A.21: Particle Filter Performance in Air-to-Air Missile Scoring Application with 3D Coordinated Turn Dynamics Model (Target Aircraft Non-maneuvering)

Table A.13: Comparison of Missile State Estimate Mean Error at Impact for Different Dynamics Models using a Particle Filter (Scenario 1)

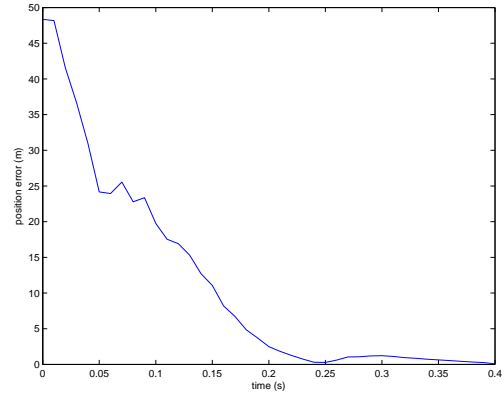
Missile State	CV Model Mean Error	CA Model Mean Error	CT Model Mean Error
$x$	0.0086 m	0.0106 m	-0.0135 m
$y$	0.0054 m	0.0103 m	-0.0017 m
$z$	0.0276 m	-0.0024 m	-0.0090 m
$v_x$	-0.9277 $\frac{\text{m}}{\text{s}}$	-0.8760 $\frac{\text{m}}{\text{s}}$	0.4401 $\frac{\text{m}}{\text{s}}$
$v_y$	-0.3060 $\frac{\text{m}}{\text{s}}$	-0.6064 $\frac{\text{m}}{\text{s}}$	0.1163 $\frac{\text{m}}{\text{s}}$
$v_z$	2.5258 $\frac{\text{m}}{\text{s}}$	2.1899 $\frac{\text{m}}{\text{s}}$	1.6425 $\frac{\text{m}}{\text{s}}$

Table A.14: Comparison of Missile State Estimate Error Standard Deviation at Impact for Different Dynamics Models using a Particle Filter (Scenario 1)

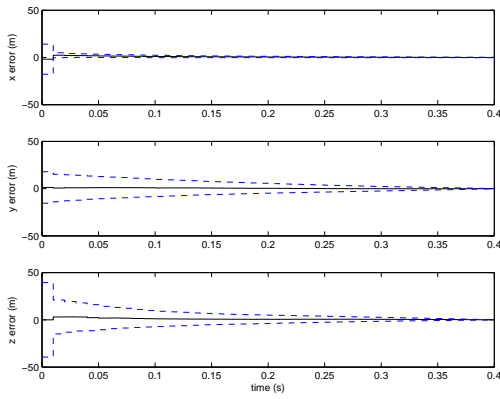
Missile State	CV Model Error Standard Deviation	CA Model Error Standard Deviation	CT Model Error Standard Deviation
$x$	0.2259 m	0.2818 m	0.2814 m
$y$	0.3086 m	0.4482 m	0.3769 m
$z$	0.0884 m	0.0811 m	0.0889 m
$v_x$	10.6083 $\frac{\text{m}}{\text{s}}$	13.8147 $\frac{\text{m}}{\text{s}}$	13.4921 $\frac{\text{m}}{\text{s}}$
$v_y$	19.3195 $\frac{\text{m}}{\text{s}}$	28.5924 $\frac{\text{m}}{\text{s}}$	24.0229 $\frac{\text{m}}{\text{s}}$
$v_z$	3.1860 $\frac{\text{m}}{\text{s}}$	3.7043 $\frac{\text{m}}{\text{s}}$	3.3387 $\frac{\text{m}}{\text{s}}$



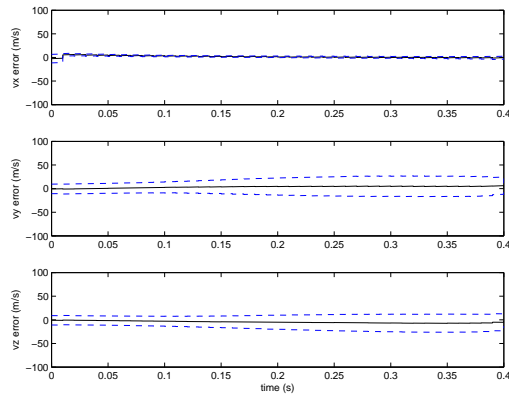
(a) 3D Aircraft and Missile Trajectory



(b) Root Sum Square Error in Missile Position Estimate (1 Run)

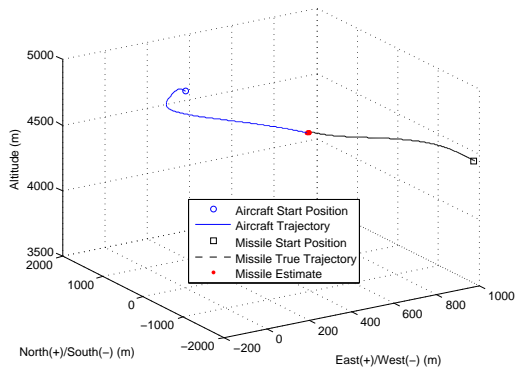


(c) Mean Error and Error Standard Deviation of Missile Position States (100 Runs)

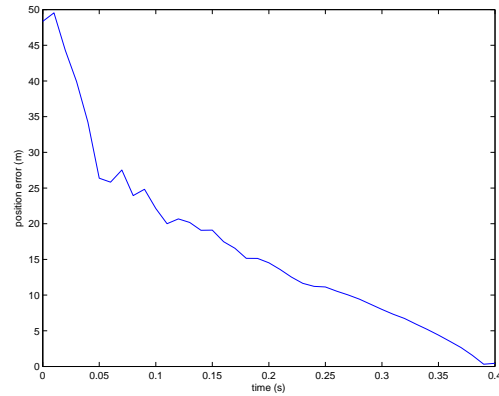


(d) Mean Error and Error Standard Deviation of Missile Velocity States (100 Runs)

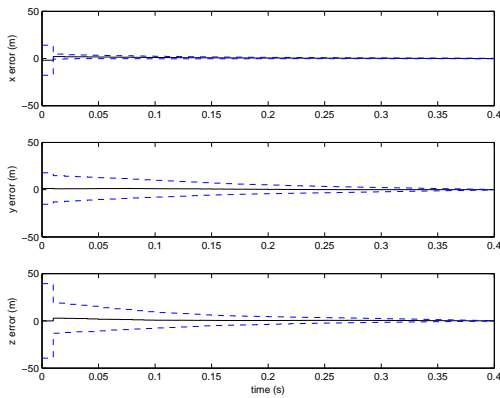
Figure A.22: Particle Filter Performance in Air-to-Air Missile Scoring Application with Continuous Velocity Dynamics Model (Target Aircraft Executing a Defensive Break Turn)



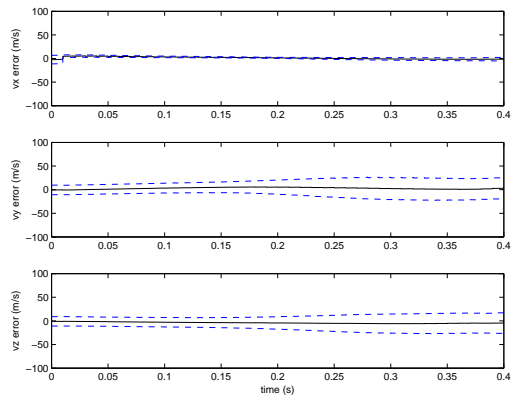
(a) 3D Aircraft and Missile Trajectory



(b) Root Sum Square Error in Missile Position Estimate (1 Run)

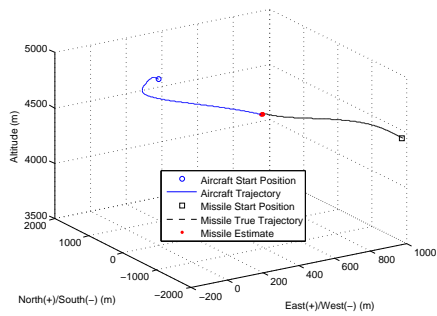


(c) Mean Error and Error Standard Deviation of Missile Position States (100 Runs)

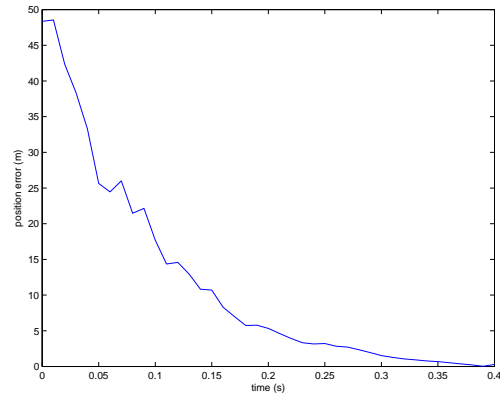


(d) Mean Error and Error Standard Deviation of Missile Velocity States (100 Runs)

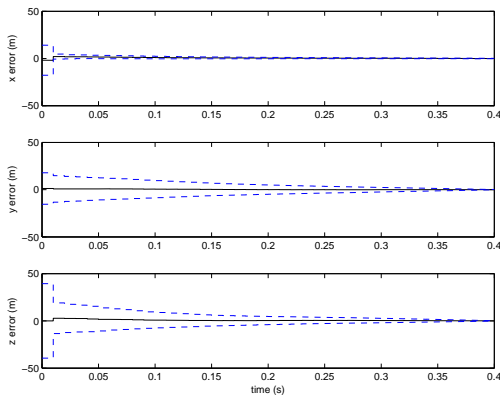
Figure A.23: Particle Filter Performance in Air-to-Air Missile Scoring Application with Continuous Acceleration Dynamics Model (Target Aircraft Executing a Defensive Break Turn)



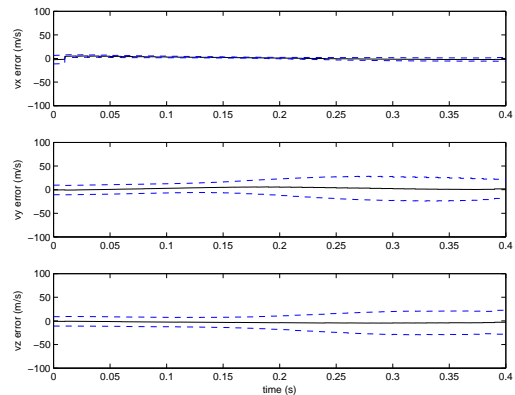
(a) 3D Aircraft and Missile Trajectory



(b) Root Sum Square Error in Missile Position Estimate (1 Run)



(c) Mean Error and Error Standard Deviation of Missile Position States (100 Runs)



(d) Mean Error and Error Standard Deviation of Missile Velocity States (100 Runs)

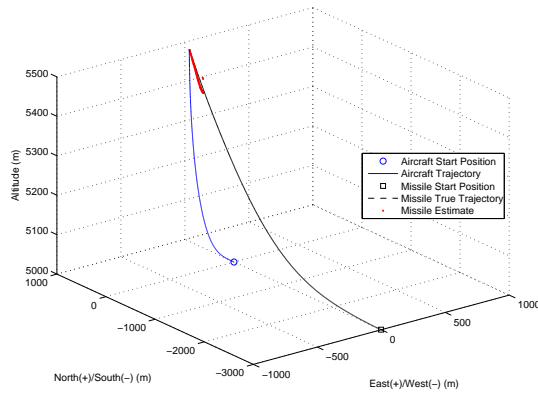
Figure A.24: Particle Filter Performance in Air-to-Air Missile Scoring Application with 3D Coordinated Turn Dynamics Model (Target Aircraft Executing a Defensive Break Turn)

Table A.15: Comparison of Missile State Estimate Mean Error at Impact for Different Dynamics Models using a Particle Filter (Scenario 2)

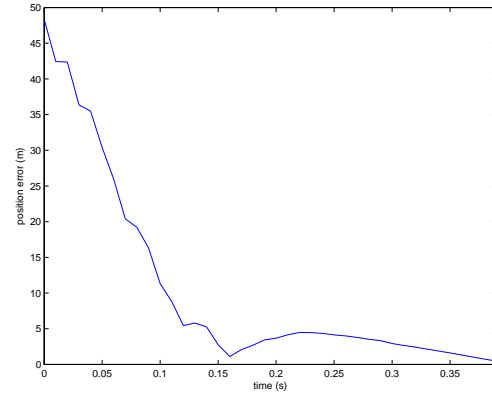
Missile State	CV Model Mean Error	CA Model Mean Error	CT Model Mean Error
$x$	0.0054 m	0.0133 m	0.0140 m
$y$	-0.0162 m	0.0153 m	0.0261 m
$z$	0.0358 m	0.0080 m	0.0064 m
$v_x$	0.0909 $\frac{\text{m}}{\text{s}}$	-0.6431 $\frac{\text{m}}{\text{s}}$	-0.7438 $\frac{\text{m}}{\text{s}}$
$v_y$	1.7767 $\frac{\text{m}}{\text{s}}$	-0.6020 $\frac{\text{m}}{\text{s}}$	-1.0024 $\frac{\text{m}}{\text{s}}$
$v_z$	-2.6757 $\frac{\text{m}}{\text{s}}$	-0.0664 $\frac{\text{m}}{\text{s}}$	-0.6370 $\frac{\text{m}}{\text{s}}$

Table A.16: Comparison of Missile State Estimate Error Standard Deviation at Impact for Different Dynamics Models using a Particle Filter (Scenario 2)

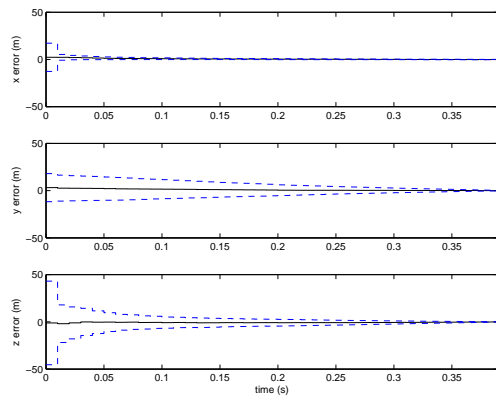
Missile State	CV Model Error Standard Deviation	CA Model Error Standard Deviation	CT Model Error Standard Deviation
$x$	0.0244 m	0.0548 m	0.0867 m
$y$	0.1261 m	0.2580 m	0.1949 m
$z$	0.1363 m	0.2705 m	0.2568 m
$v_x$	2.6605 $\frac{\text{m}}{\text{s}}$	4.8930 $\frac{\text{m}}{\text{s}}$	3.7204 $\frac{\text{m}}{\text{s}}$
$v_y$	9.4397 $\frac{\text{m}}{\text{s}}$	20.4866 $\frac{\text{m}}{\text{s}}$	16.6840 $\frac{\text{m}}{\text{s}}$
$v_z$	10.3529 $\frac{\text{m}}{\text{s}}$	22.7754 $\frac{\text{m}}{\text{s}}$	22.7241 $\frac{\text{m}}{\text{s}}$



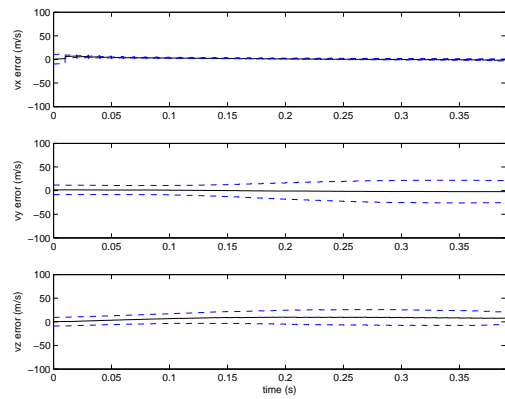
(a) 3D Aircraft and Missile Trajectory



(b) Root Sum Square Error in Missile Position Estimate (1 Run)

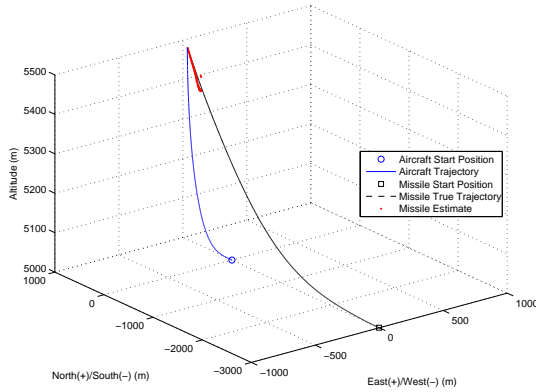


(c) Mean Error and Error Standard Deviation of Missile Position States (100 Runs)

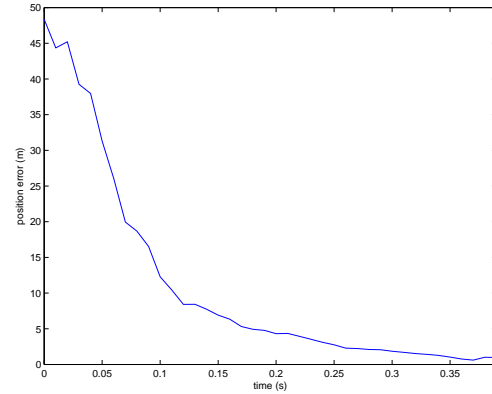


(d) Mean Error and Error Standard Deviation of Missile Velocity States (100 Runs)

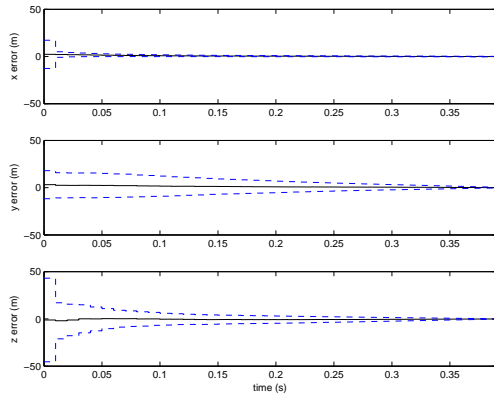
Figure A.25: Particle Filter Performance in Air-to-Air Missile Scoring Application with Continuous Velocity Dynamics Model (Target Aircraft Executing a Vertical Climb)



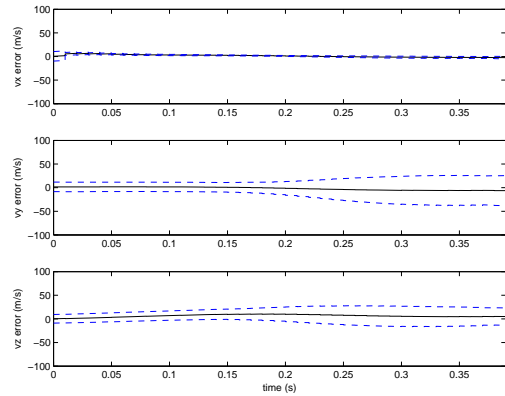
(a) 3D Aircraft and Missile Trajectory



(b) Root Sum Square Error in Missile Position Estimate (1 Run)

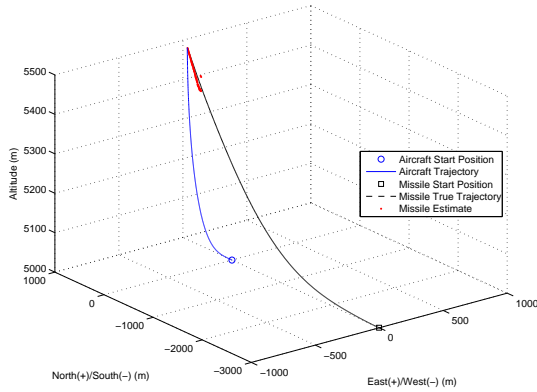


(c) Mean Error and Error Standard Deviation of Missile Position States (100 Runs)

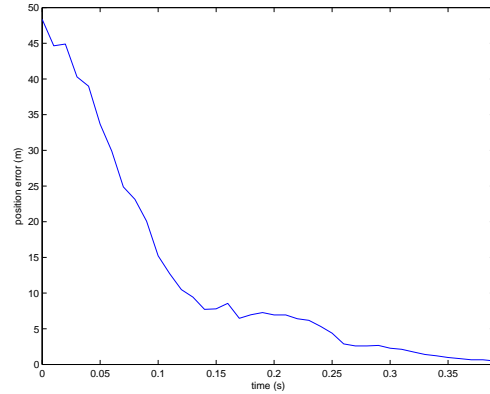


(d) Mean Error and Error Standard Deviation of Missile Velocity States (100 Runs)

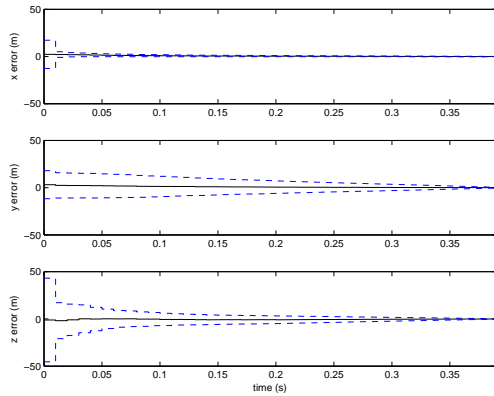
Figure A.26: Particle Filter Performance in Air-to-Air Missile Scoring Application with Continuous Acceleration Dynamics Model (Target Aircraft Executing a Vertical Climb)



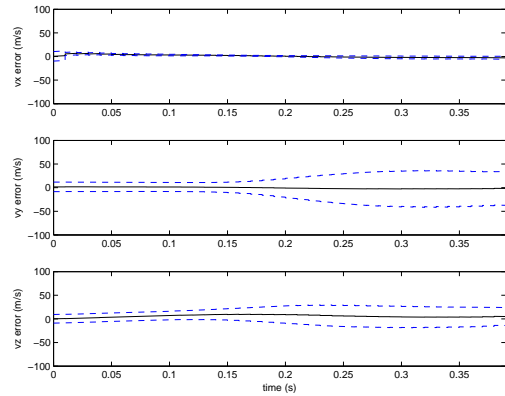
(a) 3D Aircraft and Missile Trajectory



(b) Root Sum Square Error in Missile Position Estimate (1 Run)



(c) Mean Error and Error Standard Deviation of Missile Position States (100 Runs)



(d) Mean Error and Error Standard Deviation of Missile Velocity States (100 Runs)

Figure A.27: Particle Filter Performance in Air-to-Air Missile Scoring Application with 3D Coordinated Turn Dynamics Model (Target Aircraft Executing a Vertical Climb)

Table A.17: Comparison of Missile State Estimate Mean Error at Impact for Different Dynamics Models using a Particle Filter (Scenario 3)

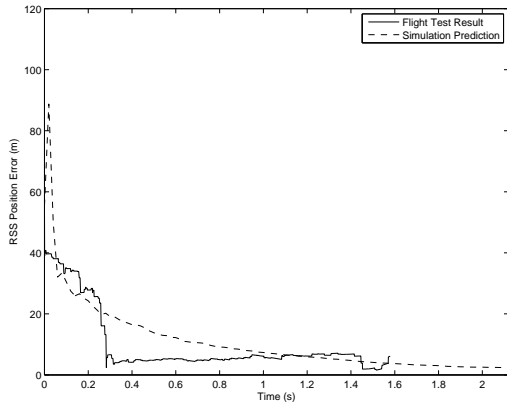
Missile State	CV Model Mean Error	CA Model Mean Error	CT Model Mean Error
$x$	0.0031 m	0.0202 m	0.0112 m
$y$	0.0260 m	0.0555 m	-0.0026 m
$z$	-0.0705 m	-0.0791 m	-0.0340 m
$v_x$	-1.1108 $\frac{\text{m}}{\text{s}}$	-1.3862 $\frac{\text{m}}{\text{s}}$	-1.9890 $\frac{\text{m}}{\text{s}}$
$v_y$	-2.0372 $\frac{\text{m}}{\text{s}}$	-4.2506 $\frac{\text{m}}{\text{s}}$	0.1984 $\frac{\text{m}}{\text{s}}$
$v_z$	3.6544 $\frac{\text{m}}{\text{s}}$	4.5102 $\frac{\text{m}}{\text{s}}$	1.5529 $\frac{\text{m}}{\text{s}}$

Table A.18: Comparison of Missile State Estimate Error Standard Deviation at Impact for Different Dynamics Models using a Particle Filter (Scenario 3)

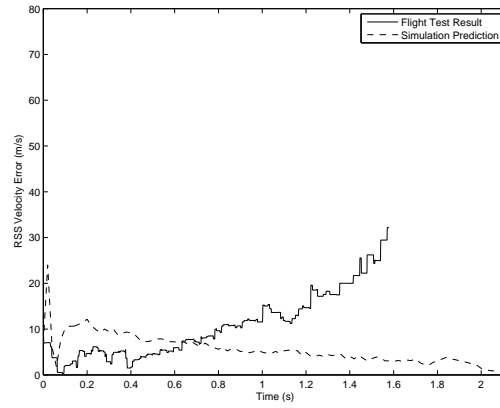
Missile State	CV Model Error Standard Deviation	CA Model Error Standard Deviation	CT Model Error Standard Deviation
$x$	0.0294 m	0.0742 m	0.0374 m
$y$	0.2684 m	0.4341 m	0.4629 m
$z$	0.1728 m	0.3194 m	0.3034 m
$v_x$	1.8390 $\frac{\text{m}}{\text{s}}$	2.9458 $\frac{\text{m}}{\text{s}}$	3.3191 $\frac{\text{m}}{\text{s}}$
$v_y$	20.8787 $\frac{\text{m}}{\text{s}}$	33.5605 $\frac{\text{m}}{\text{s}}$	36.3426 $\frac{\text{m}}{\text{s}}$
$v_z$	9.4543 $\frac{\text{m}}{\text{s}}$	19.3589 $\frac{\text{m}}{\text{s}}$	17.3036 $\frac{\text{m}}{\text{s}}$

## Appendix B. Flight Test Results

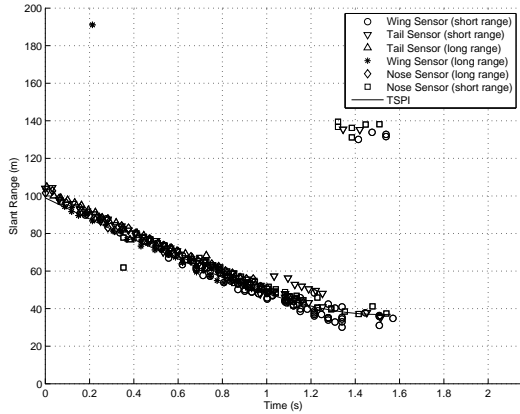
### B.1 Sensor Geometry: 90° Aspect Angle



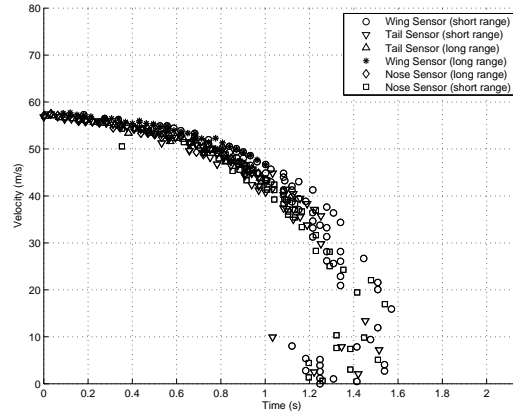
(a) Root Sum Square Error in Surrogate Missile Position Estimate



(b) Root Sum Square Error in Surrogate Missile Velocity Estimate

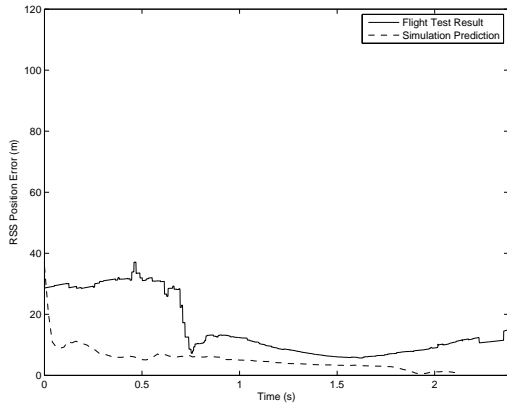


(c) Radar Sensors Slant Range Measurements

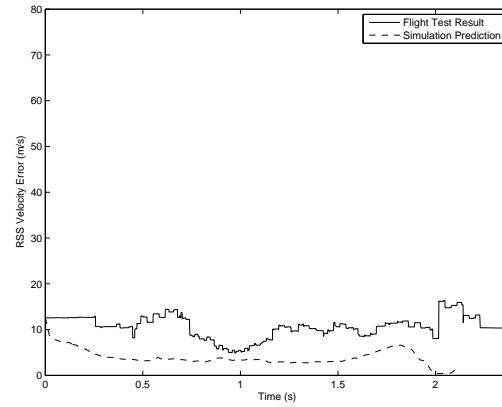


(d) Radar Sensors Speed Measurements

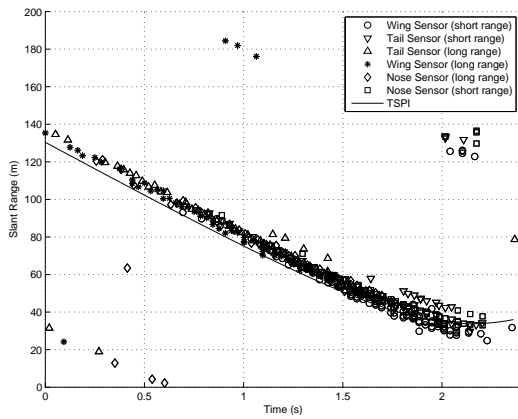
Figure B.1: Air-to-Air Missile Scoring System Performance in Scoring C-12 Surrogate Missile using an Unscented Kalman Filter with Continuous Dynamics Velocity Model (90° Drone Aspect Angle / Run 1)



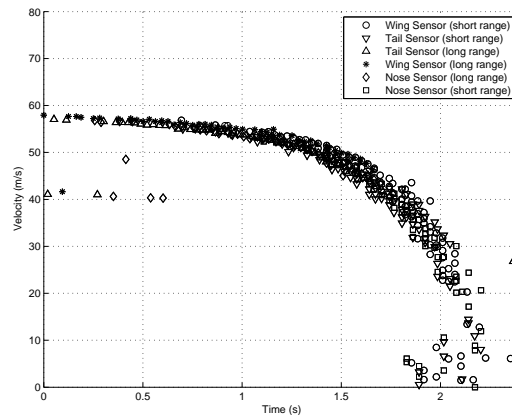
(a) Root Sum Square Error in Surrogate Missile Position Estimate



(b) Root Sum Square Error in Surrogate Missile Velocity Estimate

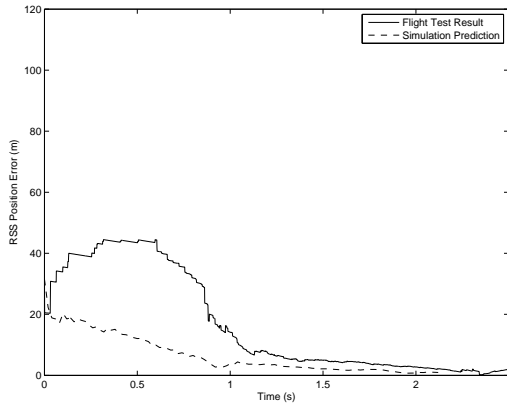


(c) Radar Sensors Slant Range Measurements

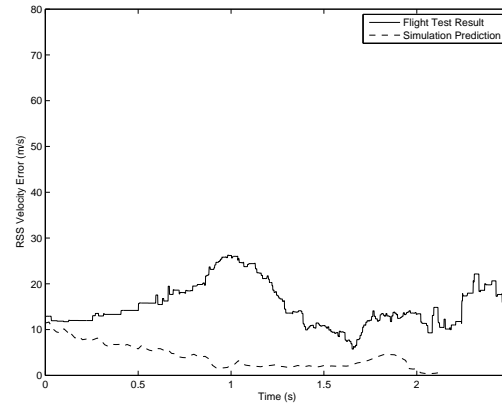


(d) Radar Sensors Speed Measurements

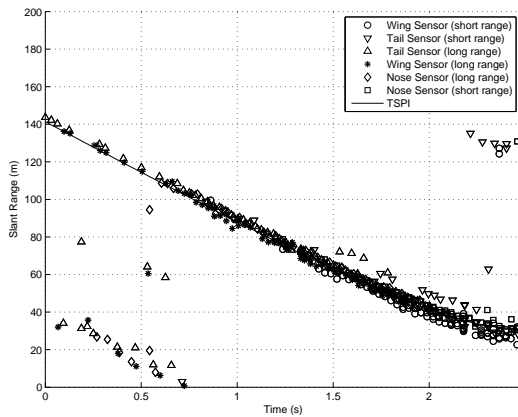
Figure B.2: Air-to-Air Missile Scoring System Performance in Scoring C-12 Surrogate Missile using an Unscented Kalman Filter with Continuous Dynamics Velocity Model (90° Drone Aspect Angle / Run 2)



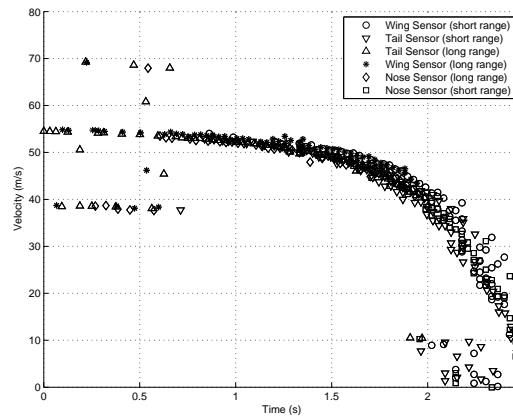
(a) Root Sum Square Error in Surrogate Missile Position Estimate



(b) Root Sum Square Error in Surrogate Missile Velocity Estimate

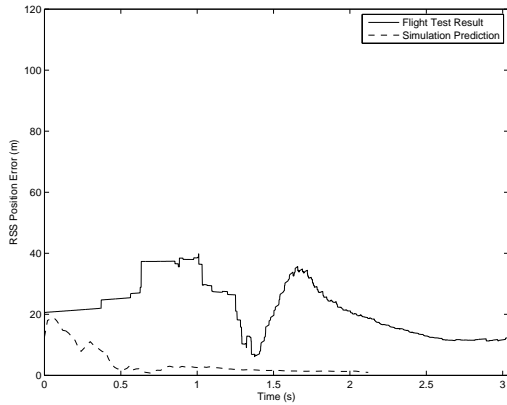


(c) Radar Sensors Slant Range Measurements

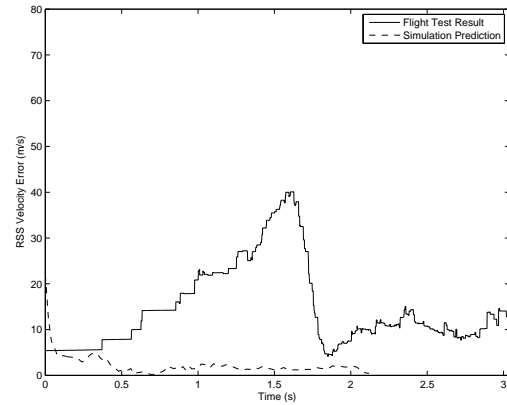


(d) Radar Sensors Speed Measurements

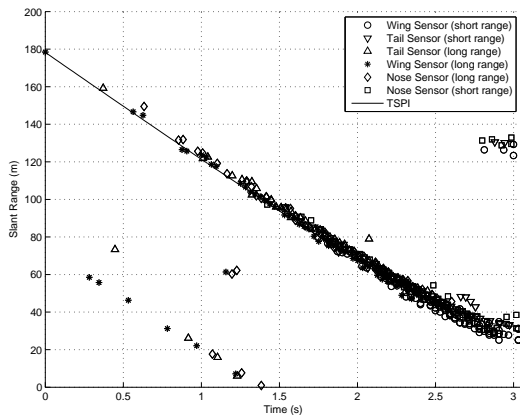
Figure B.3: Air-to-Air Missile Scoring System Performance in Scoring C-12 Surrogate Missile using an Unscented Kalman Filter with Continuous Dynamics Velocity Model (90° Drone Aspect Angle / Run 3)



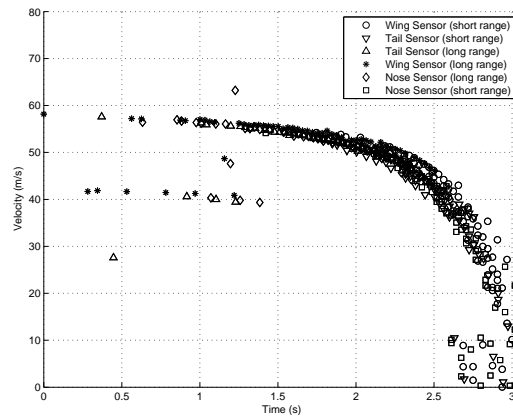
(a) Root Sum Square Error in Surrogate Missile Position Estimate



(b) Root Sum Square Error in Surrogate Missile Velocity Estimate

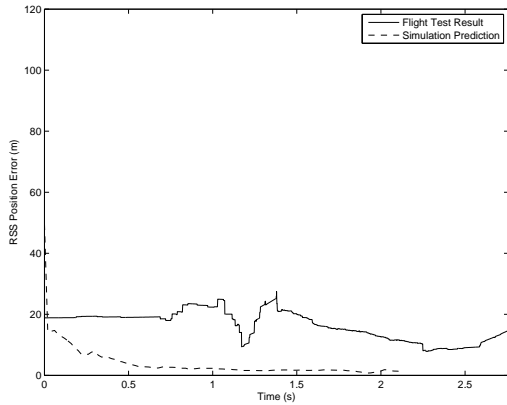


(c) Radar Sensors Slant Range Measurements

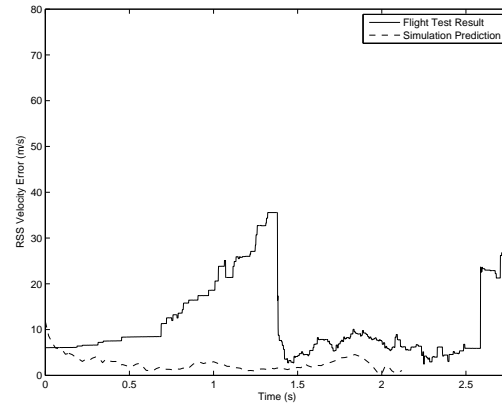


(d) Radar Sensors Speed Measurements

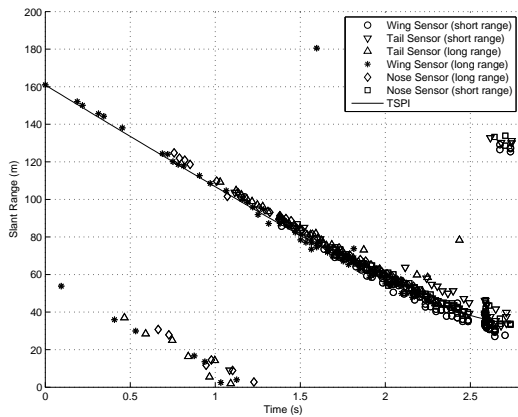
Figure B.4: Air-to-Air Missile Scoring System Performance in Scoring C-12 Surrogate Missile using an Unscented Kalman Filter with Continuous Dynamics Velocity Model (90° Drone Aspect Angle / Run 4)



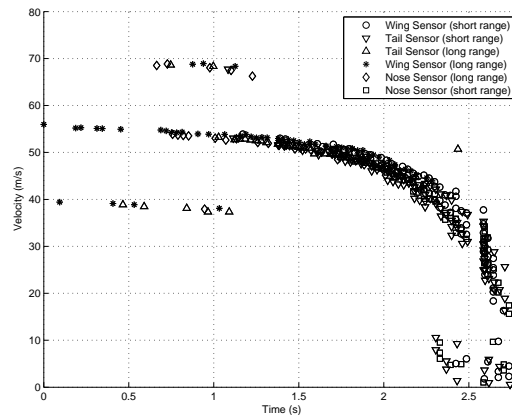
(a) Root Sum Square Error in Surrogate Missile Position Estimate



(b) Root Sum Square Error in Surrogate Missile Velocity Estimate

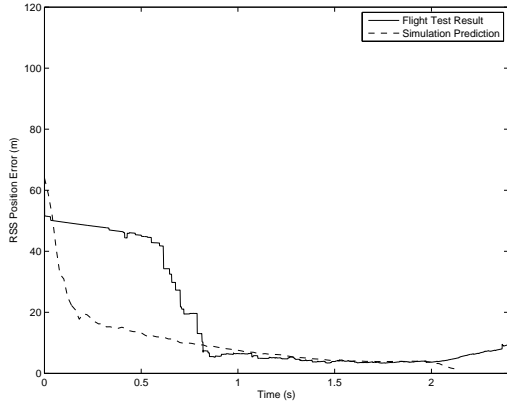


(c) Radar Sensors Slant Range Measurements

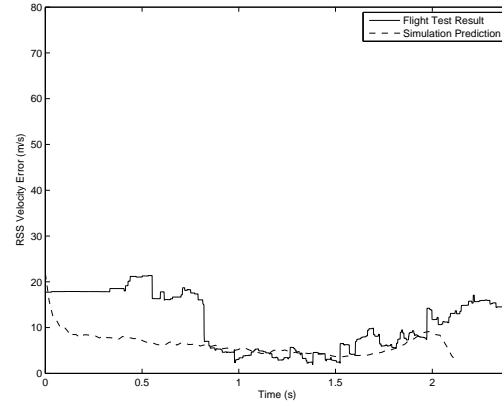


(d) Radar Sensors Speed Measurements

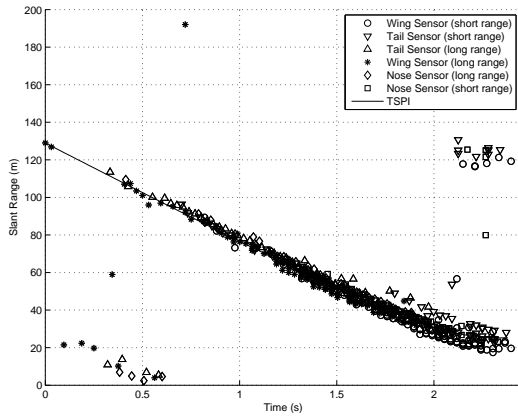
Figure B.5: Air-to-Air Missile Scoring System Performance in Scoring C-12 Surrogate Missile using an Unscented Kalman Filter with Continuous Dynamics Velocity Model (90° Drone Aspect Angle / Run 5)



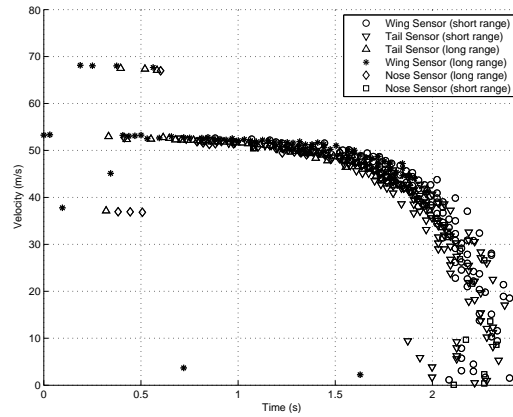
(a) Root Sum Square Error in Surrogate Missile Position Estimate



(b) Root Sum Square Error in Surrogate Missile Velocity Estimate

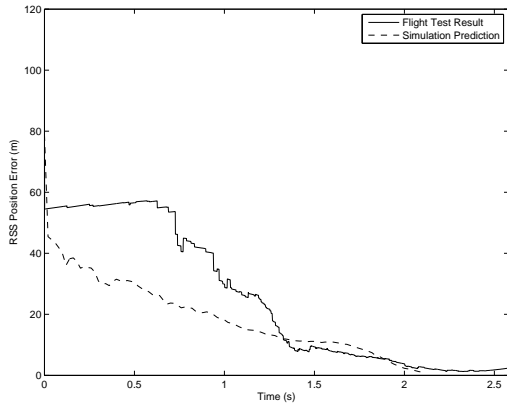


(c) Radar Sensors Slant Range Measurements

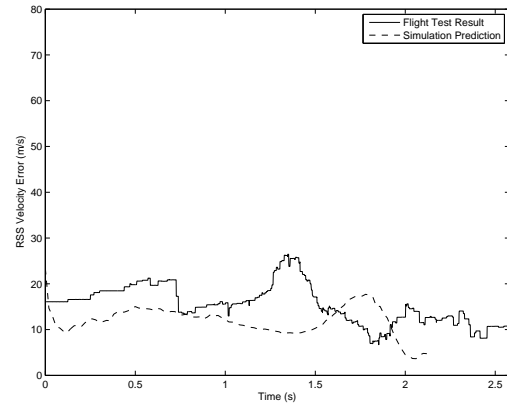


(d) Radar Sensors Speed Measurements

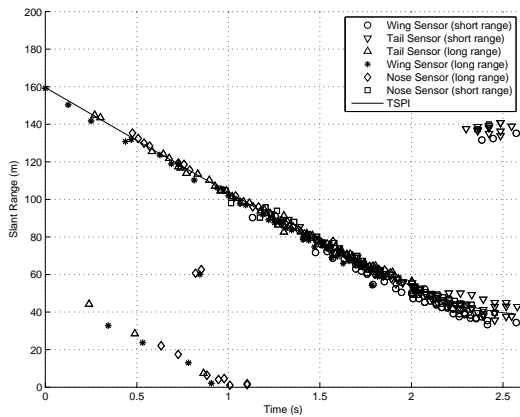
Figure B.6: Air-to-Air Missile Scoring System Performance in Scoring C-12 Surrogate Missile using an Unscented Kalman Filter with Continuous Dynamics Velocity Model (90° Drone Aspect Angle / Run 6)



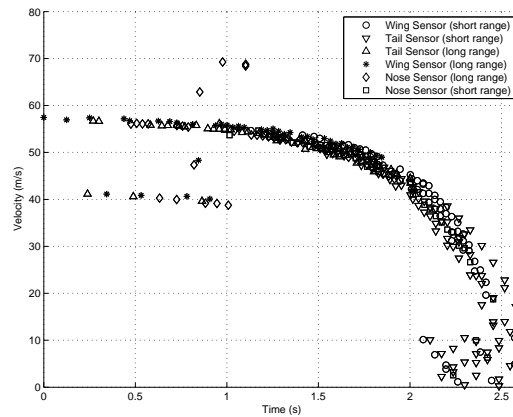
(a) Root Sum Square Error in Surrogate Missile Position Estimate



(b) Root Sum Square Error in Surrogate Missile Velocity Estimate

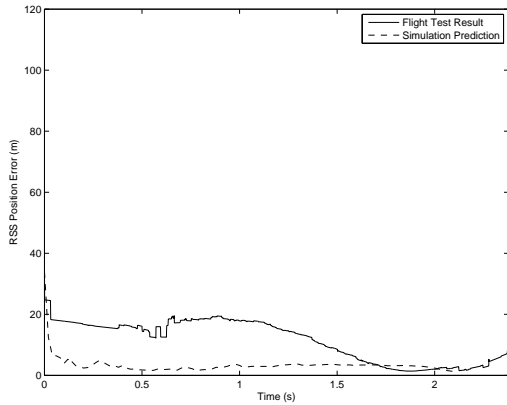


(c) Radar Sensors Slant Range Measurements

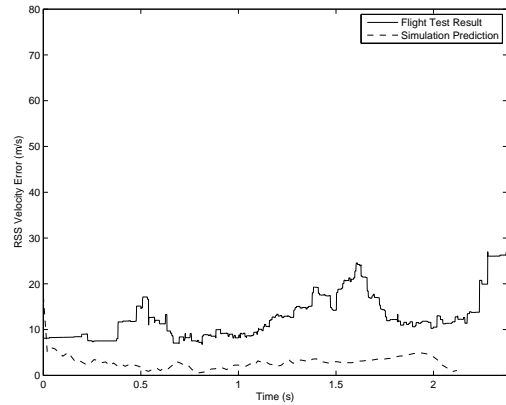


(d) Radar Sensors Speed Measurements

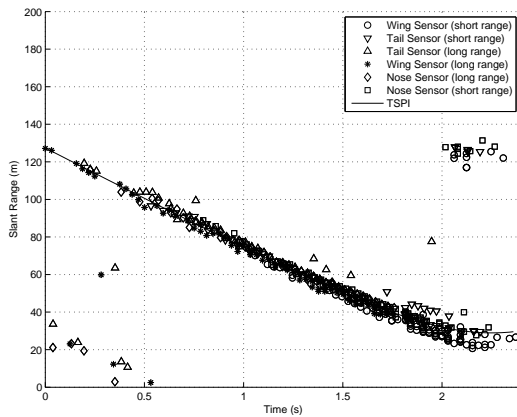
Figure B.7: Air-to-Air Missile Scoring System Performance in Scoring C-12 Surrogate Missile using an Unscented Kalman Filter with Continuous Dynamics Velocity Model (90° Drone Aspect Angle / Run 7)



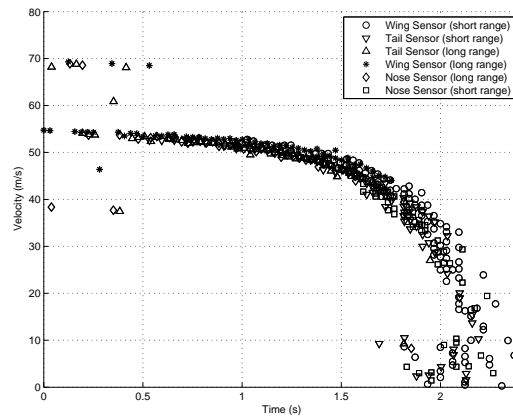
(a) Root Sum Square Error in Surrogate Missile Position Estimate



(b) Root Sum Square Error in Surrogate Missile Velocity Estimate

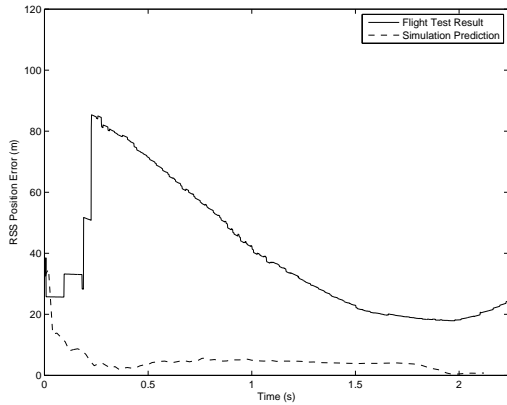


(c) Radar Sensors Slant Range Measurements

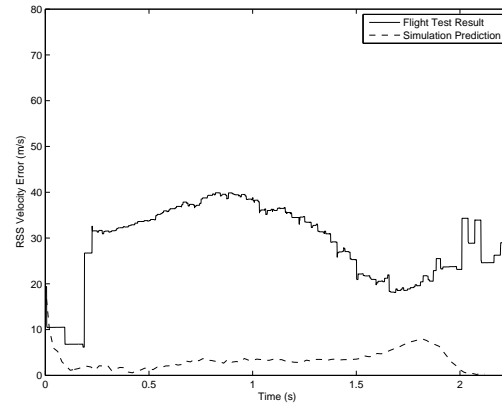


(d) Radar Sensors Speed Measurements

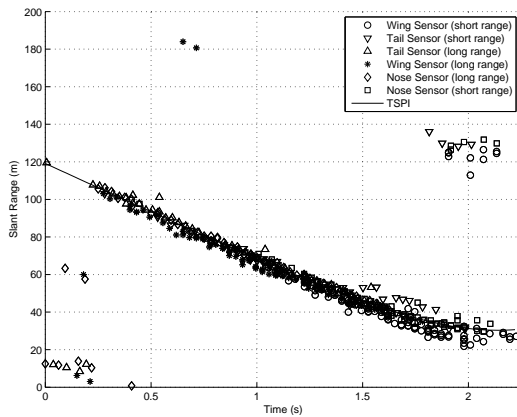
Figure B.8: Air-to-Air Missile Scoring System Performance in Scoring C-12 Surrogate Missile using an Unscented Kalman Filter with Continuous Dynamics Velocity Model (90° Drone Aspect Angle / Run 8)



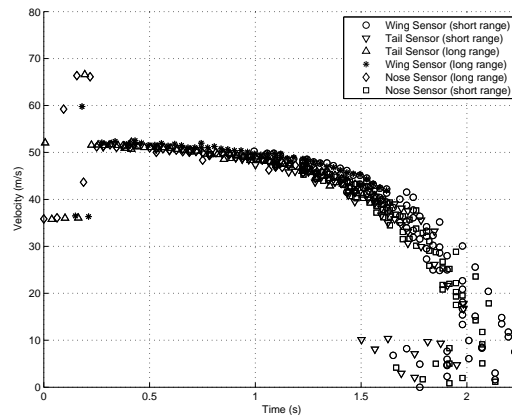
(a) Root Sum Square Error in Surrogate Missile Position Estimate



(b) Root Sum Square Error in Surrogate Missile Velocity Estimate

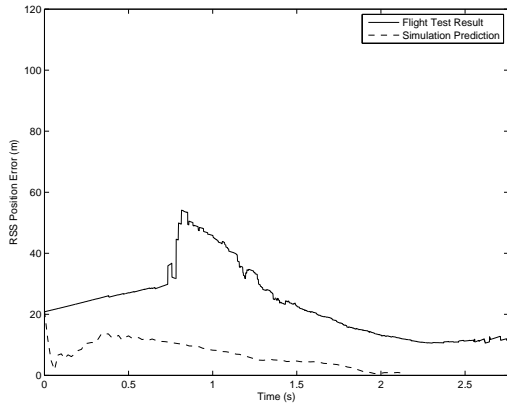


(c) Radar Sensors Slant Range Measurements

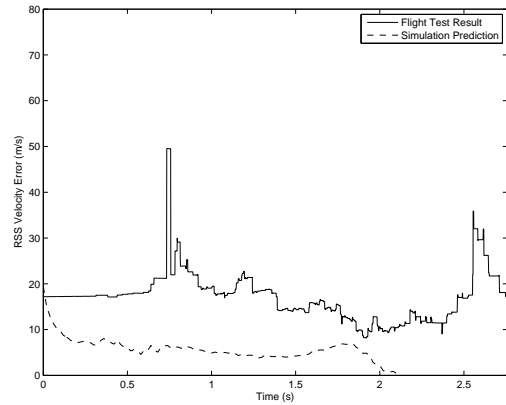


(d) Radar Sensors Speed Measurements

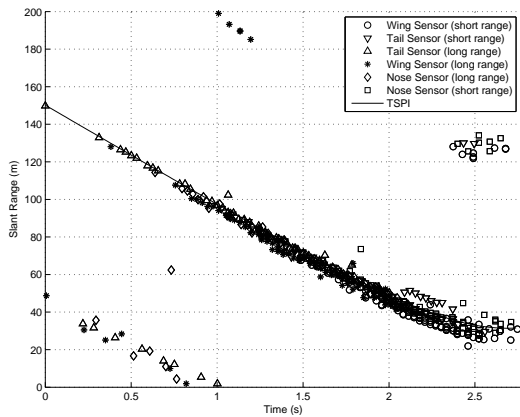
Figure B.9: Air-to-Air Missile Scoring System Performance in Scoring C-12 Surrogate Missile using an Unscented Kalman Filter with Continuous Dynamics Velocity Model (90° Drone Aspect Angle / Run 9)



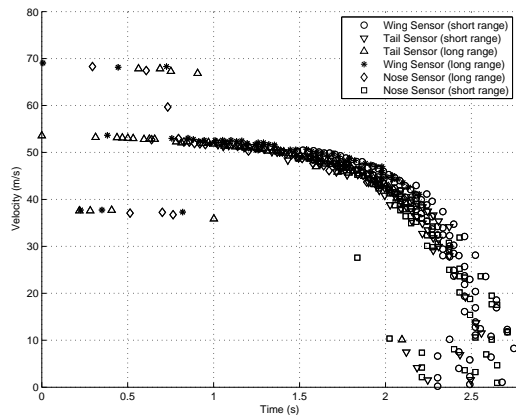
(a) Root Sum Square Error in Surrogate Missile Position Estimate



(b) Root Sum Square Error in Surrogate Missile Velocity Estimate

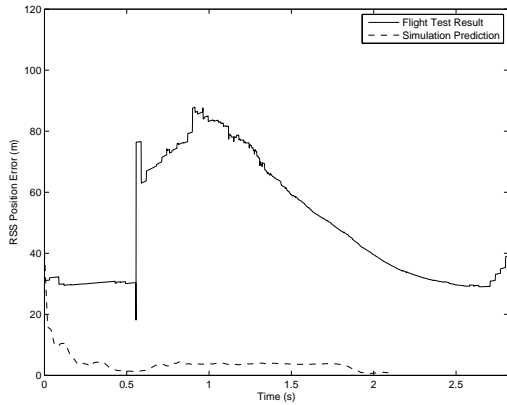


(c) Radar Sensors Slant Range Measurements

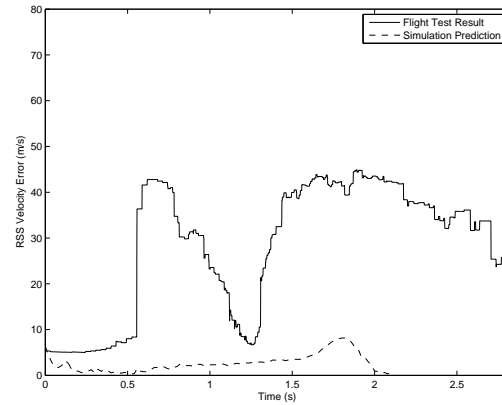


(d) Radar Sensors Speed Measurements

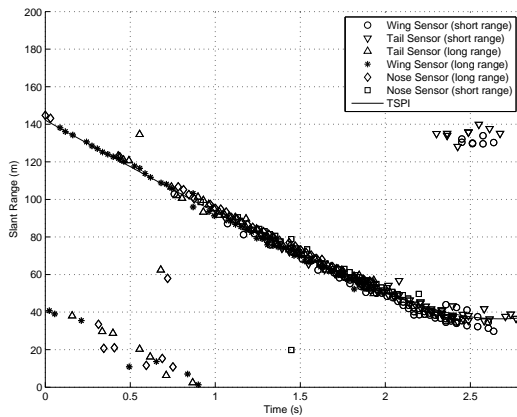
Figure B.10: Air-to-Air Missile Scoring System Performance in Scoring C-12 Surrogate Missile using an Unscented Kalman Filter with Continuous Dynamics Velocity Model (90° Drone Aspect Angle / Run 10)



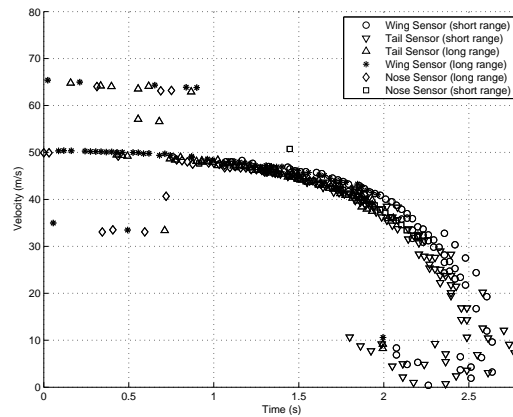
(a) Root Sum Square Error in Surrogate Missile Position Estimate



(b) Root Sum Square Error in Surrogate Missile Velocity Estimate

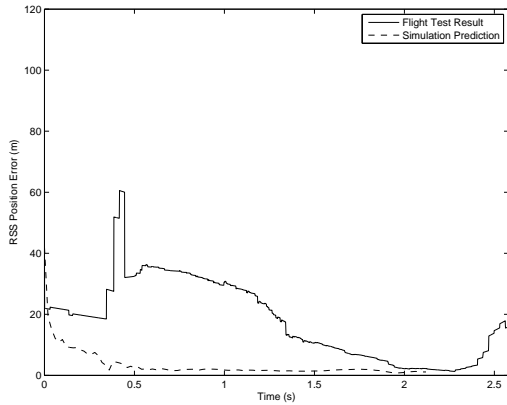


(c) Radar Sensors Slant Range Measurements

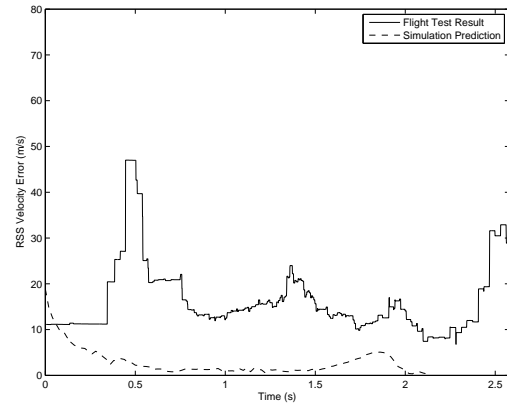


(d) Radar Sensors Speed Measurements

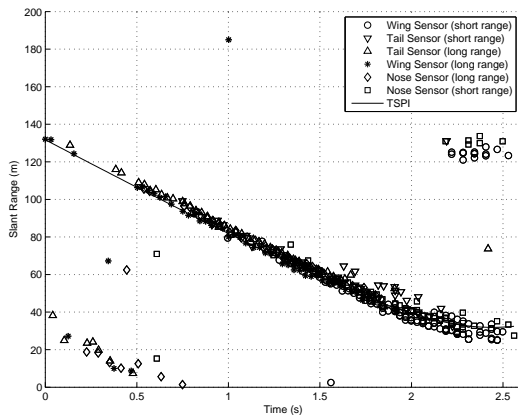
Figure B.11: Air-to-Air Missile Scoring System Performance in Scoring C-12 Surrogate Missile using an Unscented Kalman Filter with Continuous Dynamics Velocity Model (90° Drone Aspect Angle / Run 11)



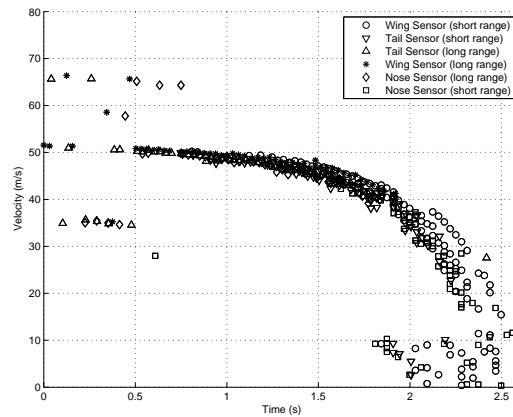
(a) Root Sum Square Error in Surrogate Missile Position Estimate



(b) Root Sum Square Error in Surrogate Missile Velocity Estimate

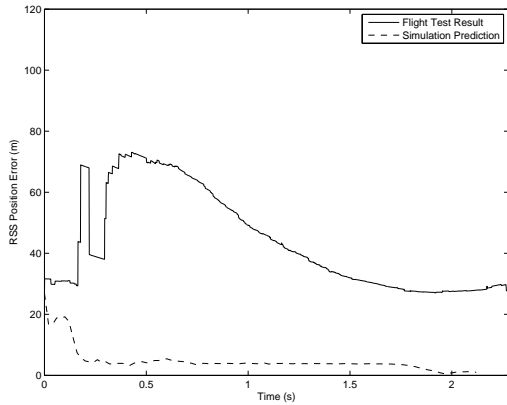


(c) Radar Sensors Slant Range Measurements

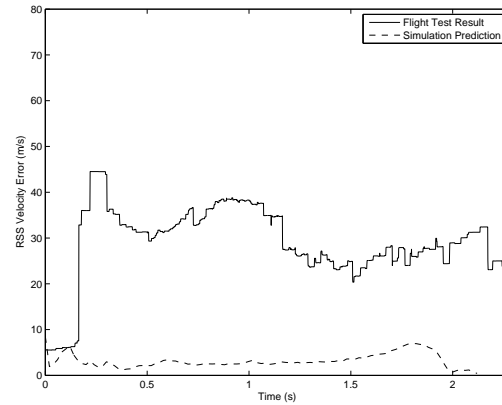


(d) Radar Sensors Speed Measurements

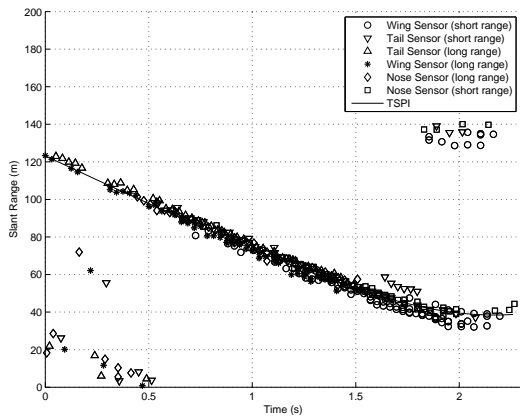
Figure B.12: Air-to-Air Missile Scoring System Performance in Scoring C-12 Surrogate Missile using an Unscented Kalman Filter with Continuous Dynamics Velocity Model (90° Drone Aspect Angle / Run 12)



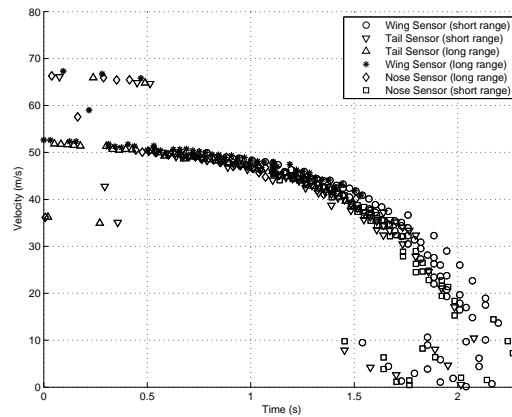
(a) Root Sum Square Error in Surrogate Missile Position Estimate



(b) Root Sum Square Error in Surrogate Missile Velocity Estimate

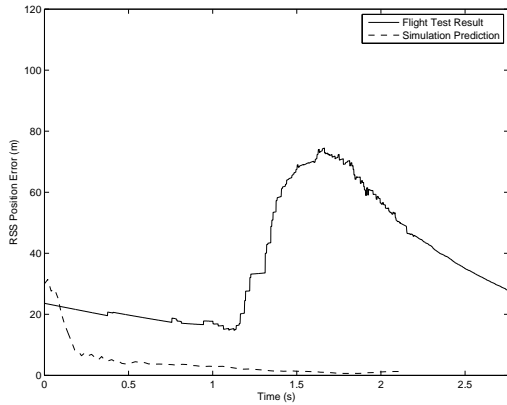


(c) Radar Sensors Slant Range Measurements

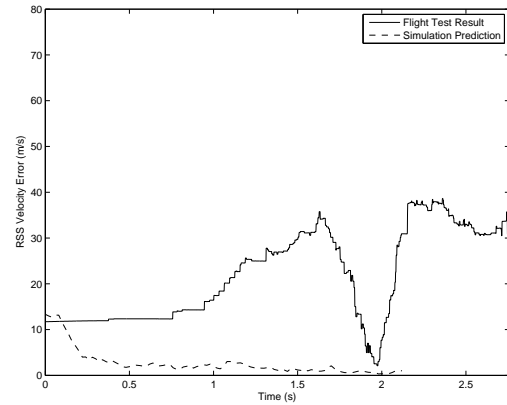


(d) Radar Sensors Speed Measurements

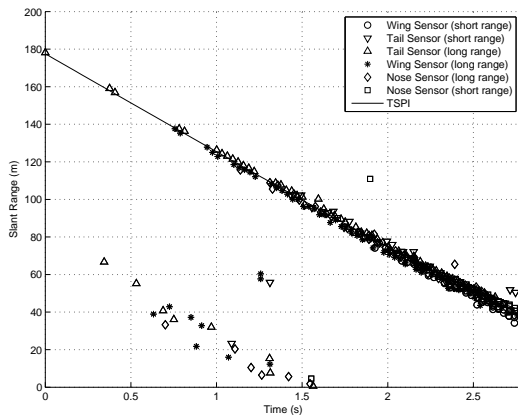
Figure B.13: Air-to-Air Missile Scoring System Performance in Scoring C-12 Surrogate Missile using an Unscented Kalman Filter with Continuous Dynamics Velocity Model (90° Drone Aspect Angle / Run 13)



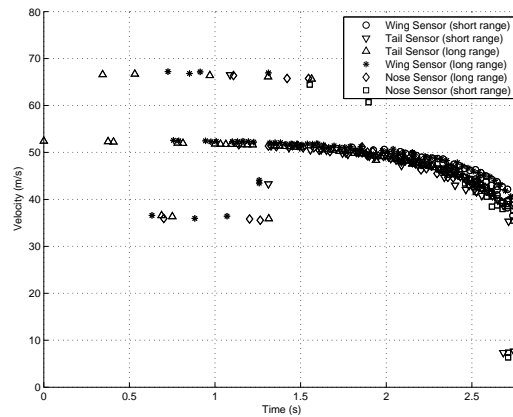
(a) Root Sum Square Error in Surrogate Missile Position Estimate



(b) Root Sum Square Error in Surrogate Missile Velocity Estimate

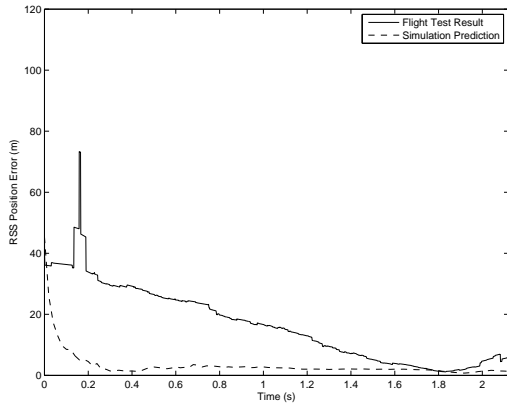


(c) Radar Sensors Slant Range Measurements

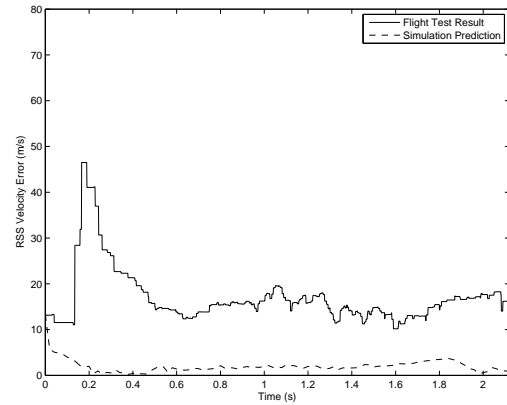


(d) Radar Sensors Speed Measurements

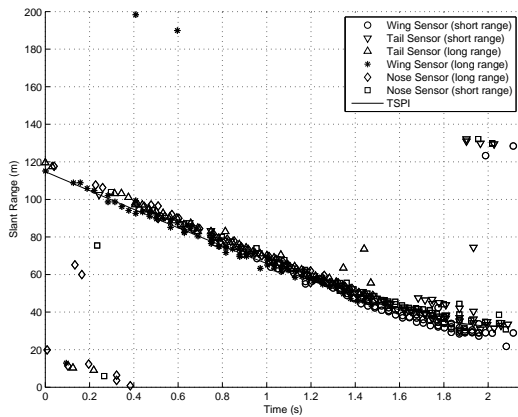
Figure B.14: Air-to-Air Missile Scoring System Performance in Scoring C-12 Surrogate Missile using an Unscented Kalman Filter with Continuous Dynamics Velocity Model (90° Drone Aspect Angle / Run 14)



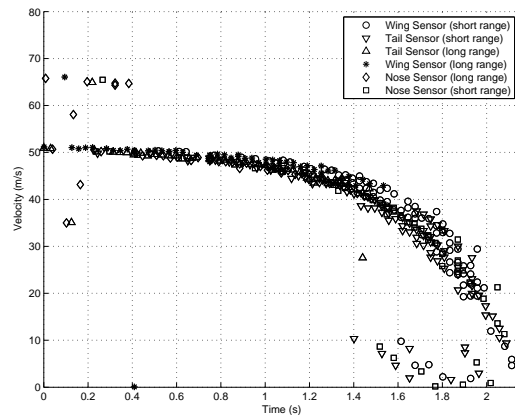
(a) Root Sum Square Error in Surrogate Missile Position Estimate



(b) Root Sum Square Error in Surrogate Missile Velocity Estimate



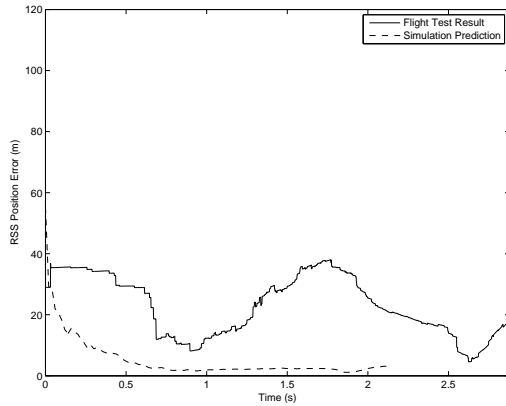
(c) Radar Sensors Slant Range Measurements



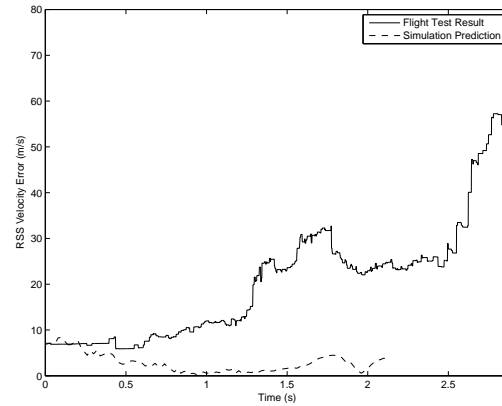
(d) Radar Sensors Speed Measurements

Figure B.15: Air-to-Air Missile Scoring System Performance in Scoring C-12 Surrogate Missile using an Unscented Kalman Filter with Continuous Dynamics Velocity Model (90° Drone Aspect Angle / Run 15)

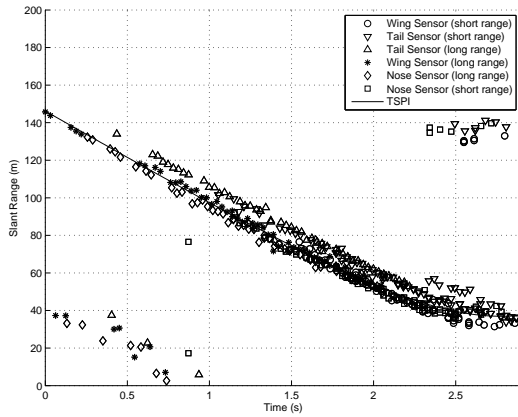
## B.2 Sensor Geometry: 45° Aspect Angle



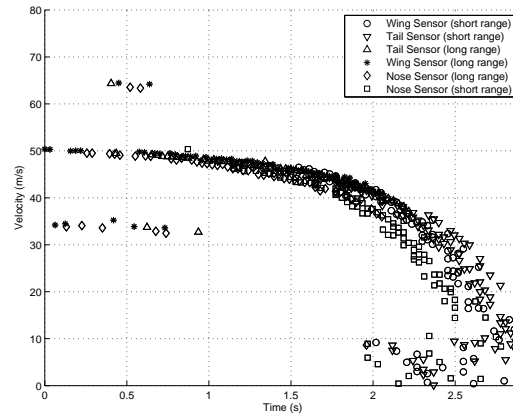
(a) Root Sum Square Error in Surrogate Missile Position Estimate



(b) Root Sum Square Error in Surrogate Missile Velocity Estimate

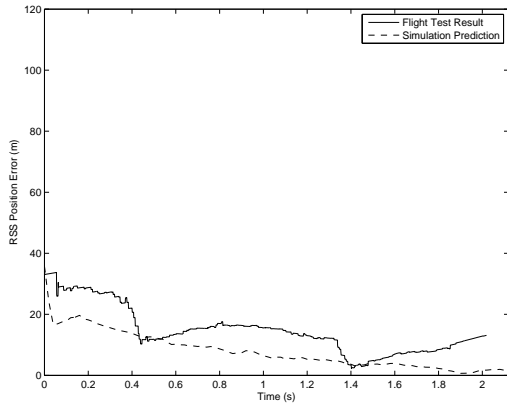


(c) Radar Sensors Slant Range Measurements

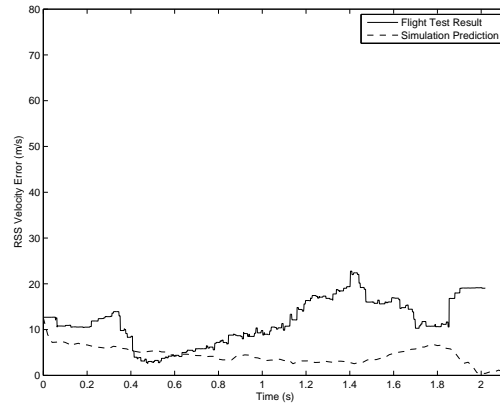


(d) Radar Sensors Speed Measurements

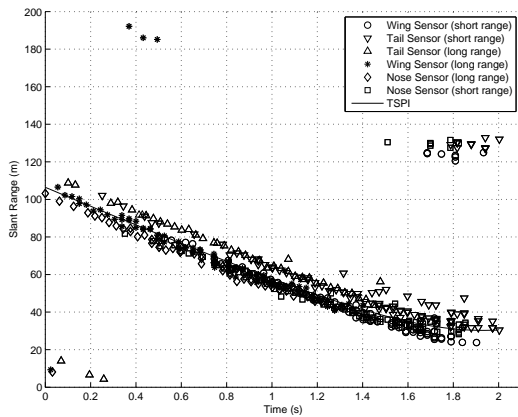
Figure B.16: Air-to-Air Missile Scoring System Performance in Scoring C-12 Surrogate Missile using an Unscented Kalman Filter with Continuous Dynamics Velocity Model (45° Drone Aspect Angle / Run 1)



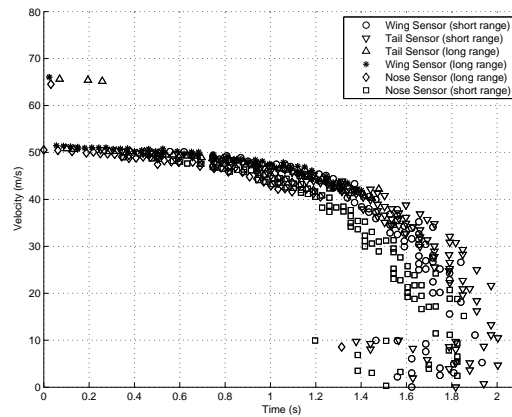
(a) Root Sum Square Error in Surrogate Missile Position Estimate



(b) Root Sum Square Error in Surrogate Missile Velocity Estimate

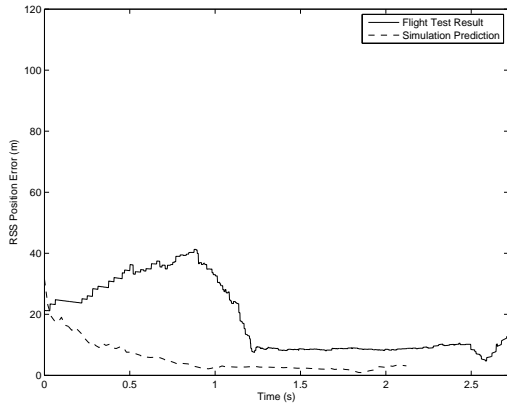


(c) Radar Sensors Slant Range Measurements

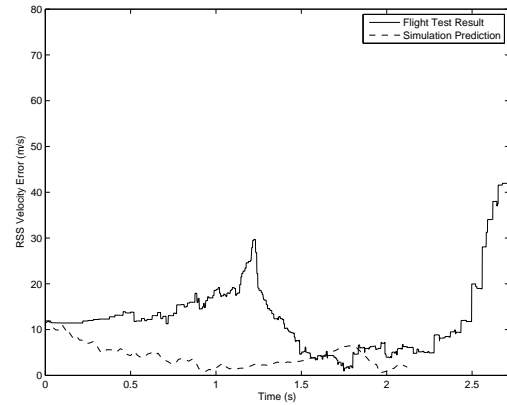


(d) Radar Sensors Speed Measurements

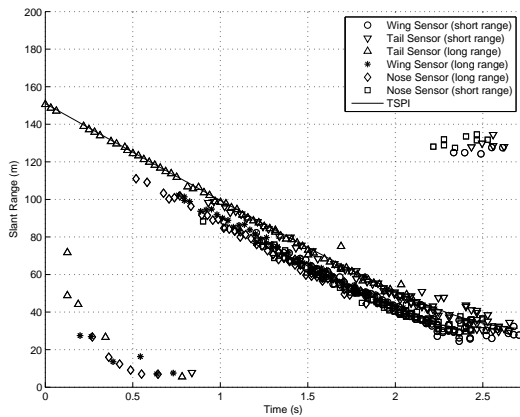
Figure B.17: Air-to-Air Missile Scoring System Performance in Scoring C-12 Surrogate Missile using an Unscented Kalman Filter with Continuous Dynamics Velocity Model (45° Drone Aspect Angle / Run 2)



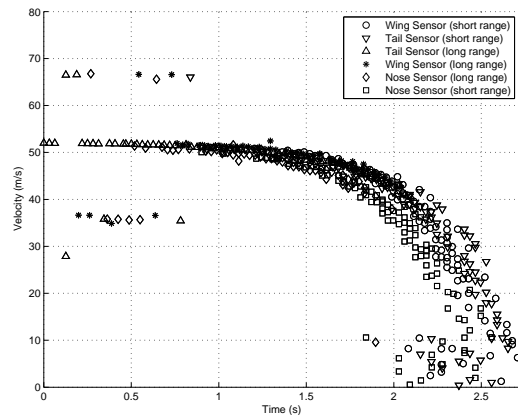
(a) Root Sum Square Error in Surrogate Missile Position Estimate



(b) Root Sum Square Error in Surrogate Missile Velocity Estimate

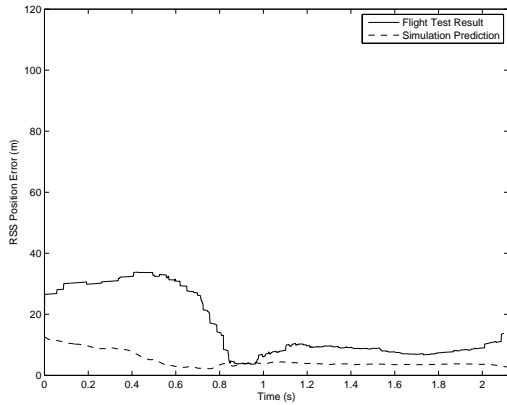


(c) Radar Sensors Slant Range Measurements

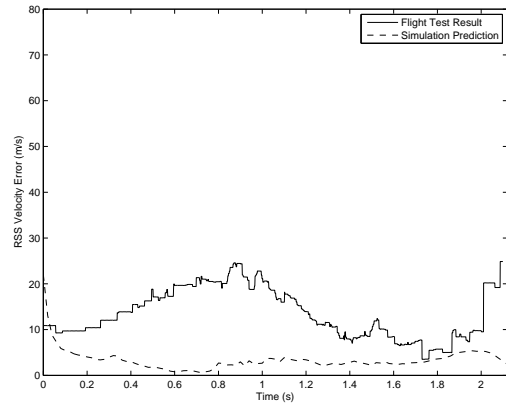


(d) Radar Sensors Speed Measurements

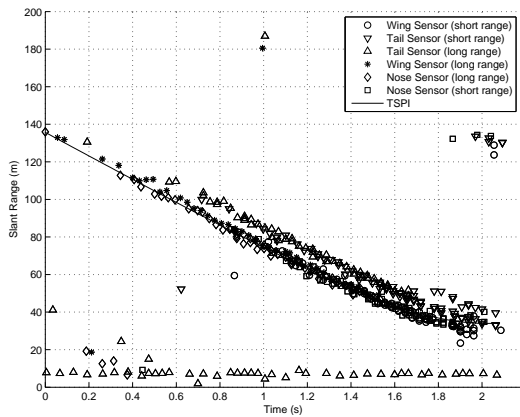
Figure B.18: Air-to-Air Missile Scoring System Performance in Scoring C-12 Surrogate Missile using an Unscented Kalman Filter with Continuous Dynamics Velocity Model (45° Drone Aspect Angle / Run 3)



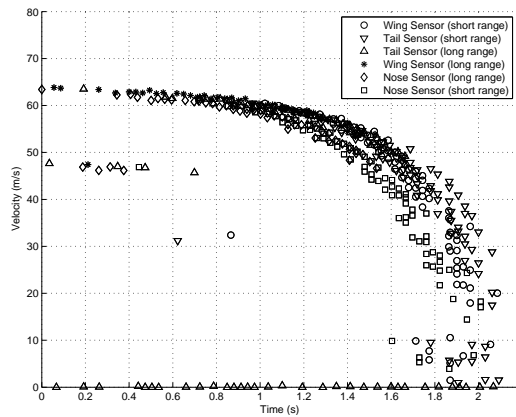
(a) Root Sum Square Error in Surrogate Missile Position Estimate



(b) Root Sum Square Error in Surrogate Missile Velocity Estimate

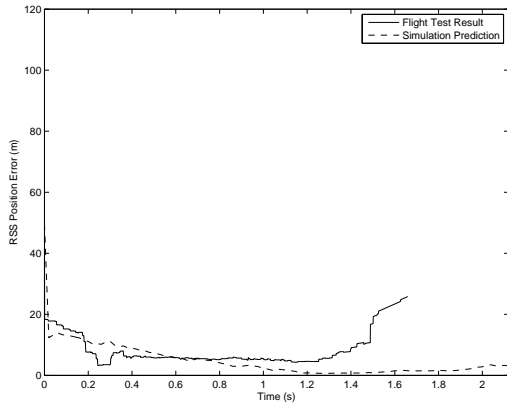


(c) Radar Sensors Slant Range Measurements

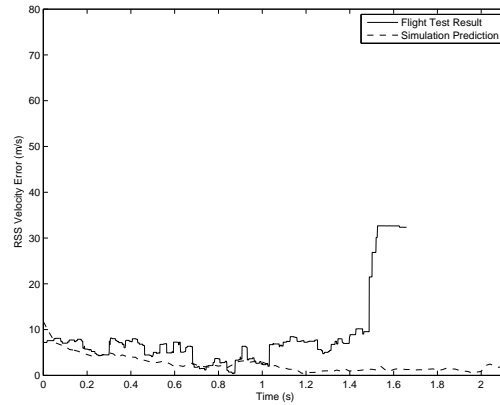


(d) Radar Sensors Speed Measurements

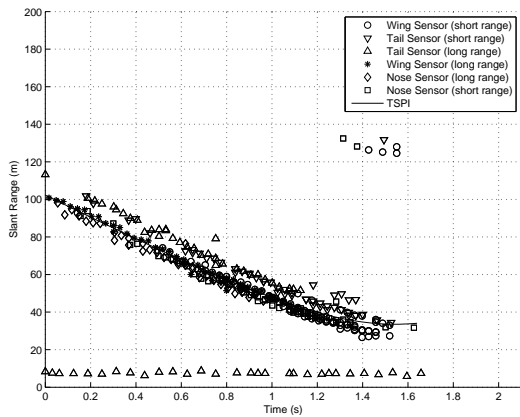
Figure B.19: Air-to-Air Missile Scoring System Performance in Scoring C-12 Surrogate Missile using an Unscented Kalman Filter with Continuous Dynamics Velocity Model (45° Drone Aspect Angle / Run 4)



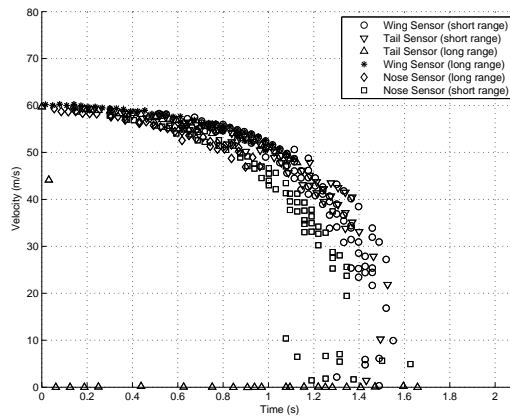
(a) Root Sum Square Error in Surrogate Missile Position Estimate



(b) Root Sum Square Error in Surrogate Missile Velocity Estimate

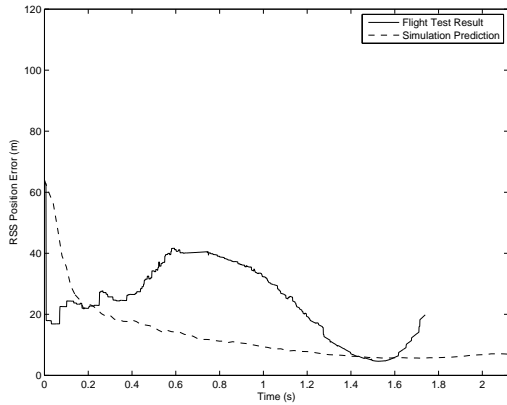


(c) Radar Sensors Slant Range Measurements

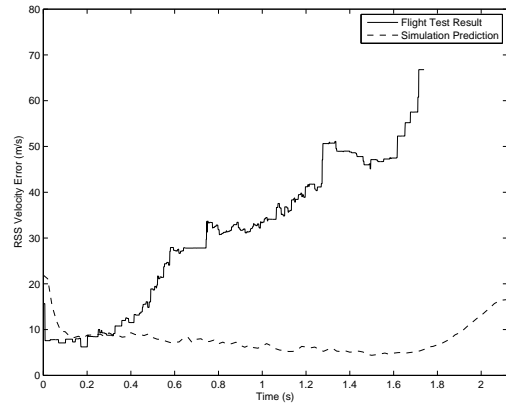


(d) Radar Sensors Speed Measurements

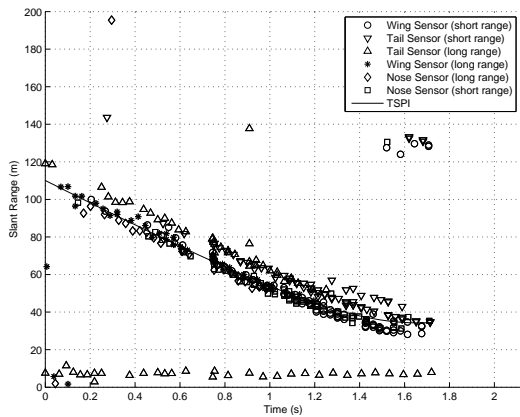
Figure B.20: Air-to-Air Missile Scoring System Performance in Scoring C-12 Surrogate Missile using an Unscented Kalman Filter with Continuous Dynamics Velocity Model (45° Drone Aspect Angle / Run 5)



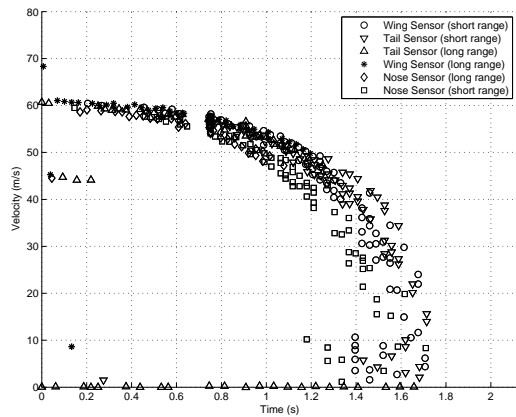
(a) Root Sum Square Error in Surrogate Missile Position Estimate



(b) Root Sum Square Error in Surrogate Missile Velocity Estimate

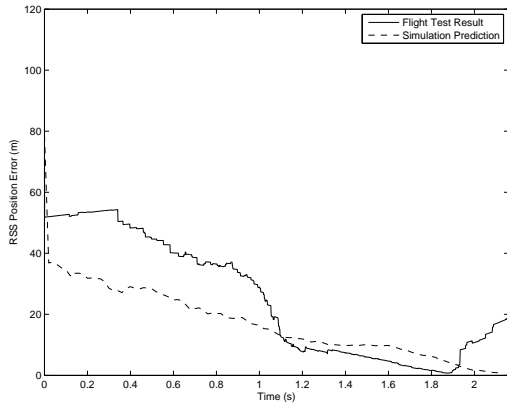


(c) Radar Sensors Slant Range Measurements

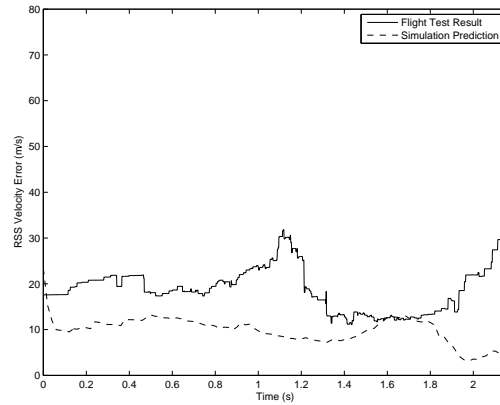


(d) Radar Sensors Speed Measurements

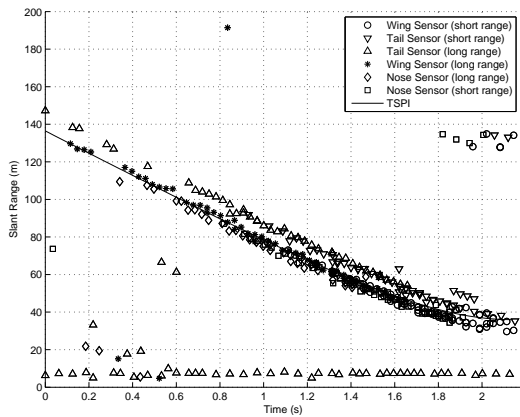
Figure B.21: Air-to-Air Missile Scoring System Performance in Scoring C-12 Surrogate Missile using an Unscented Kalman Filter with Continuous Dynamics Velocity Model (45° Drone Aspect Angle / Run 6)



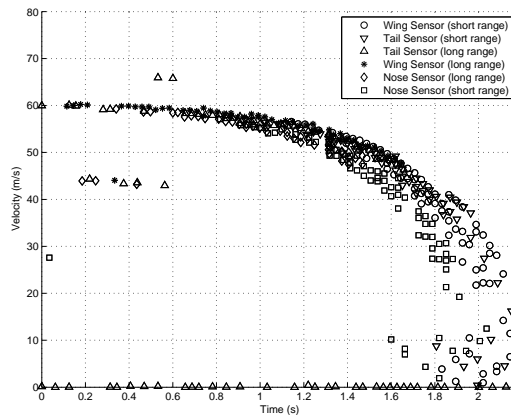
(a) Root Sum Square Error in Surrogate Missile Position Estimate



(b) Root Sum Square Error in Surrogate Missile Velocity Estimate

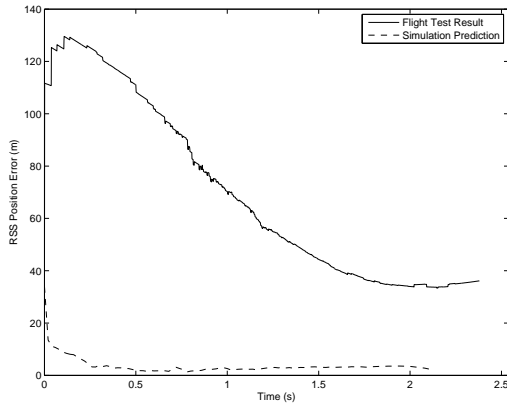


(c) Radar Sensors Slant Range Measurements

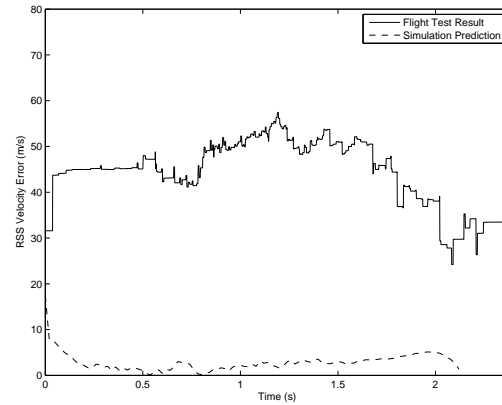


(d) Radar Sensors Speed Measurements

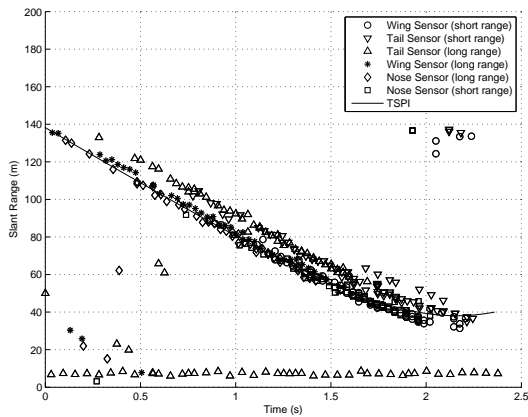
Figure B.22: Air-to-Air Missile Scoring System Performance in Scoring C-12 Surrogate Missile using an Unscented Kalman Filter with Continuous Dynamics Velocity Model (45° Drone Aspect Angle / Run 7)



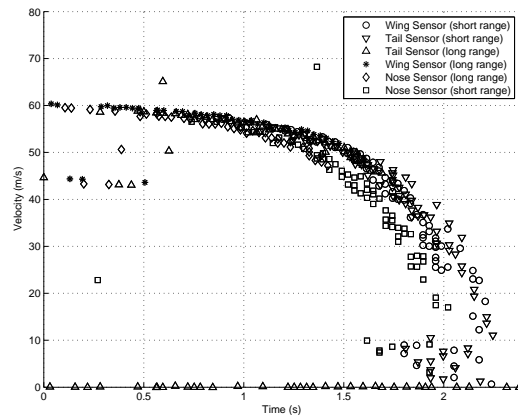
(a) Root Sum Square Error in Surrogate Missile Position Estimate



(b) Root Sum Square Error in Surrogate Missile Velocity Estimate

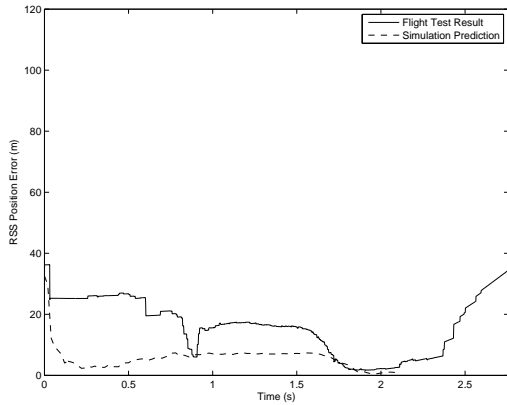


(c) Radar Sensors Slant Range Measurements

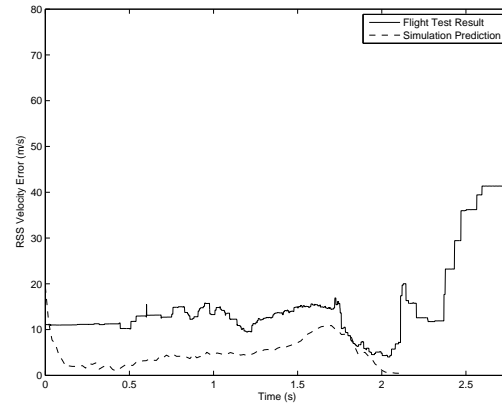


(d) Radar Sensors Speed Measurements

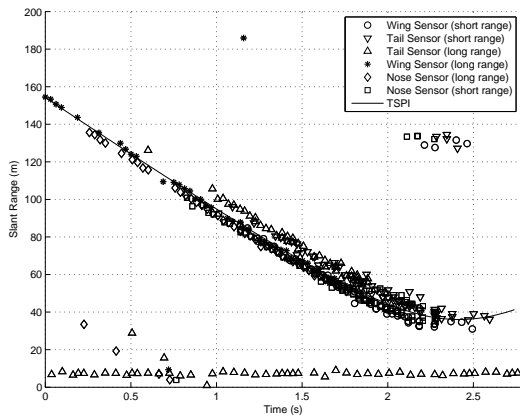
Figure B.23: Air-to-Air Missile Scoring System Performance in Scoring C-12 Surrogate Missile using an Unscented Kalman Filter with Continuous Dynamics Velocity Model (45° Drone Aspect Angle / Run 8)



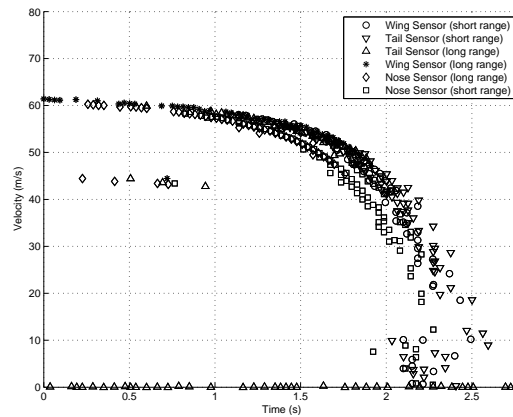
(a) Root Sum Square Error in Surrogate Missile Position Estimate



(b) Root Sum Square Error in Surrogate Missile Velocity Estimate

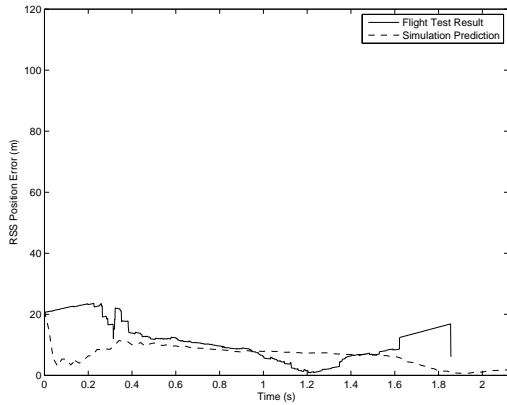


(c) Radar Sensors Slant Range Measurements

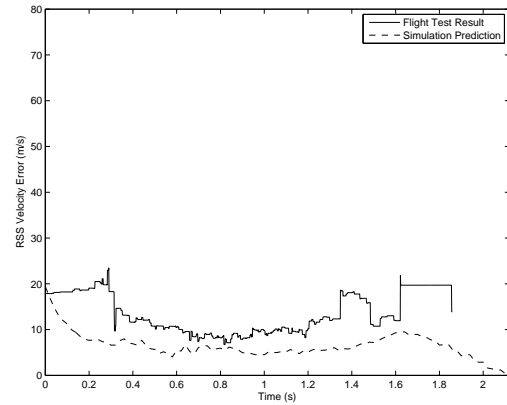


(d) Radar Sensors Speed Measurements

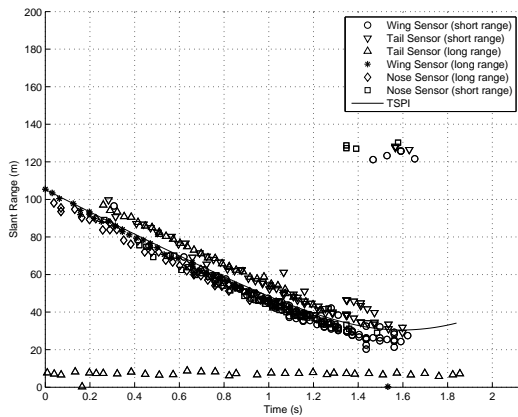
Figure B.24: Air-to-Air Missile Scoring System Performance in Scoring C-12 Surrogate Missile using an Unscented Kalman Filter with Continuous Dynamics Velocity Model (45° Drone Aspect Angle / Run 9)



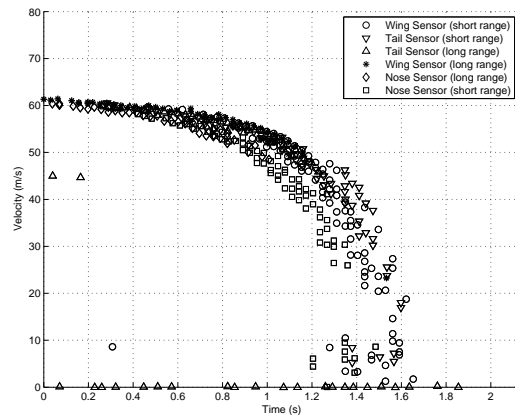
(a) Root Sum Square Error in Surrogate Missile Position Estimate



(b) Root Sum Square Error in Surrogate Missile Velocity Estimate

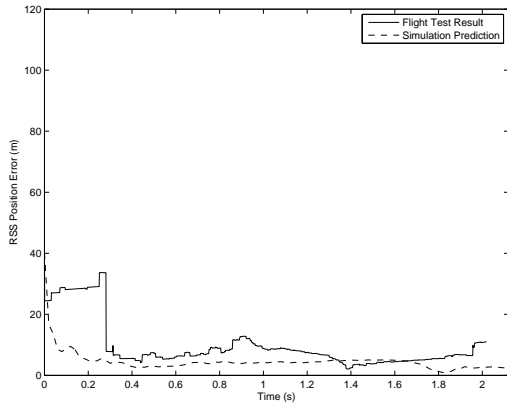


(c) Radar Sensors Slant Range Measurements

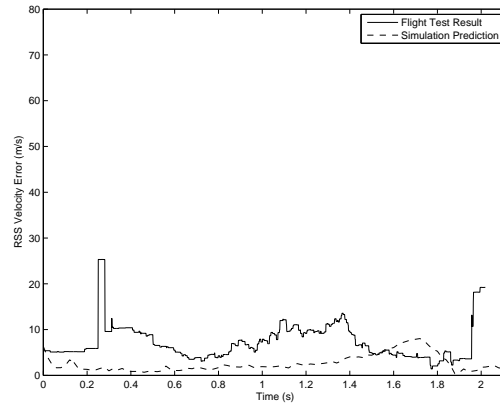


(d) Radar Sensors Speed Measurements

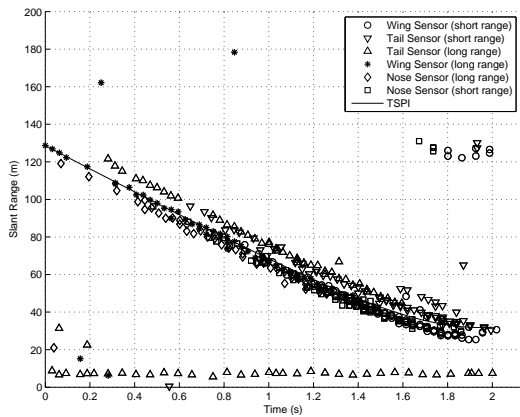
Figure B.25: Air-to-Air Missile Scoring System Performance in Scoring C-12 Surrogate Missile using an Unscented Kalman Filter with Continuous Dynamics Velocity Model ( $45^\circ$  Drone Aspect Angle / Run 10)



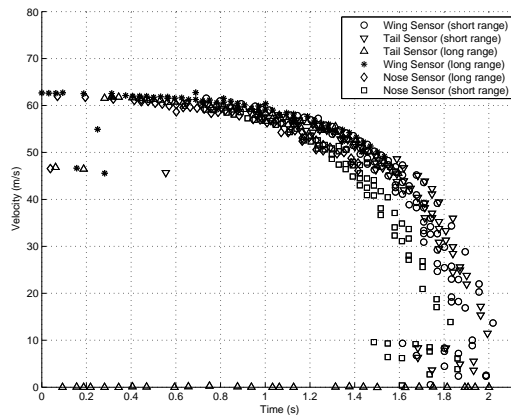
(a) Root Sum Square Error in Surrogate Missile Position Estimate



(b) Root Sum Square Error in Surrogate Missile Velocity Estimate

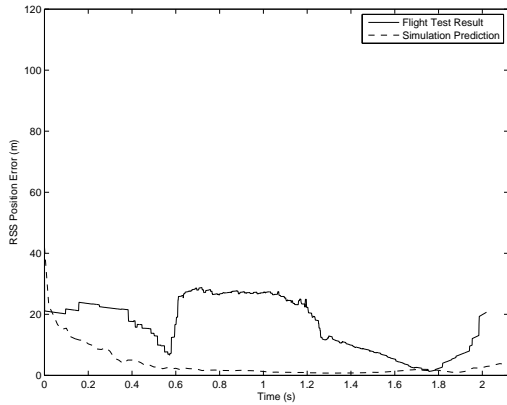


(c) Radar Sensors Slant Range Measurements

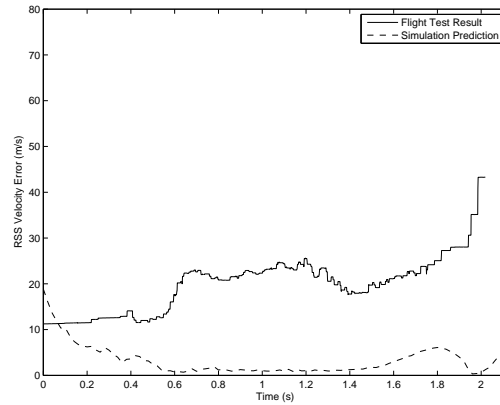


(d) Radar Sensors Speed Measurements

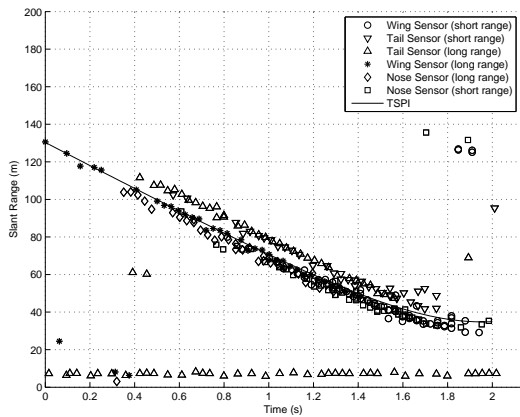
Figure B.26: Air-to-Air Missile Scoring System Performance in Scoring C-12 Surrogate Missile using an Unscented Kalman Filter with Continuous Dynamics Velocity Model (45° Drone Aspect Angle / Run 11)



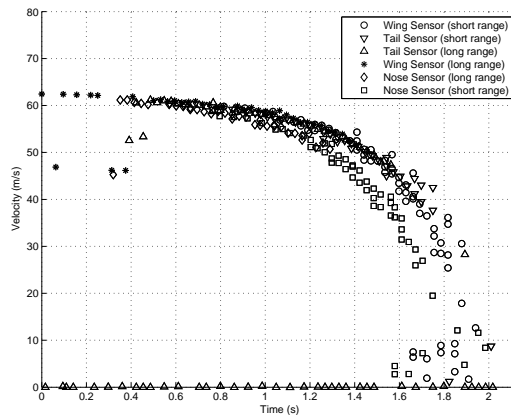
(a) Root Sum Square Error in Surrogate Missile Position Estimate



(b) Root Sum Square Error in Surrogate Missile Velocity Estimate

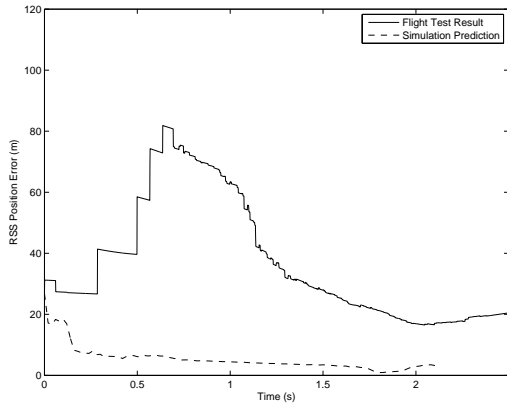


(c) Radar Sensors Slant Range Measurements

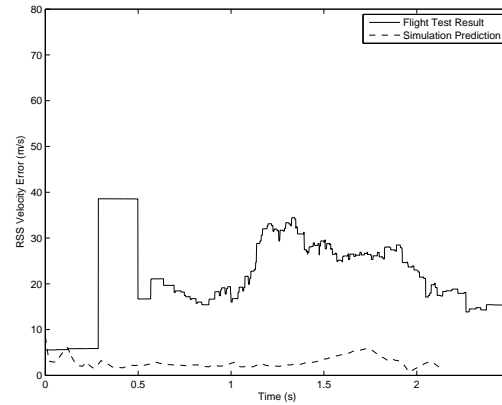


(d) Radar Sensors Speed Measurements

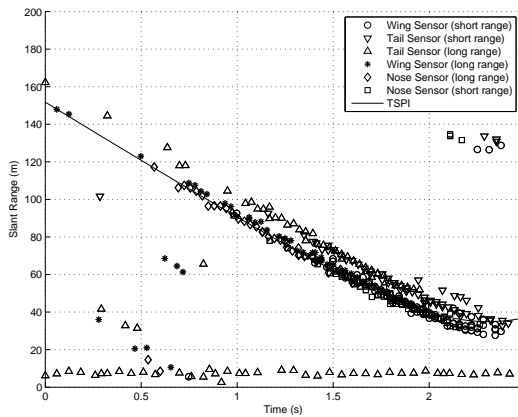
Figure B.27: Air-to-Air Missile Scoring System Performance in Scoring C-12 Surrogate Missile using an Unscented Kalman Filter with Continuous Dynamics Velocity Model (45° Drone Aspect Angle / Run 12)



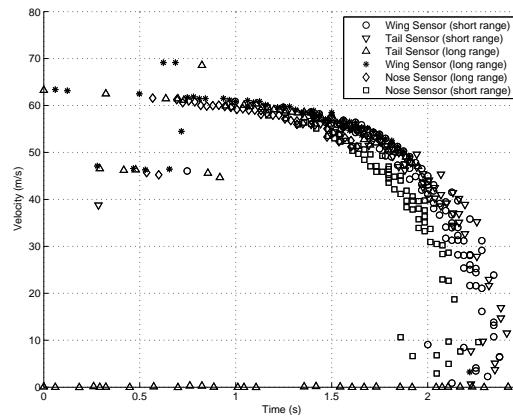
(a) Root Sum Square Error in Surrogate Missile Position Estimate



(b) Root Sum Square Error in Surrogate Missile Velocity Estimate

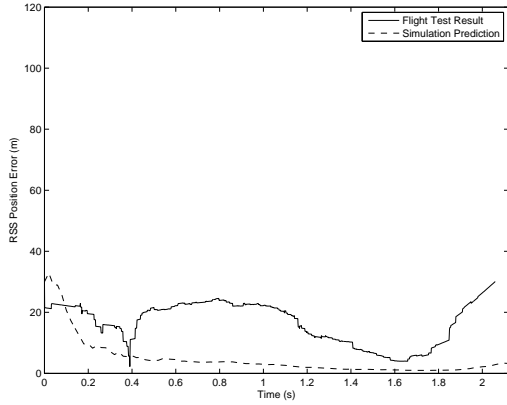


(c) Radar Sensors Slant Range Measurements

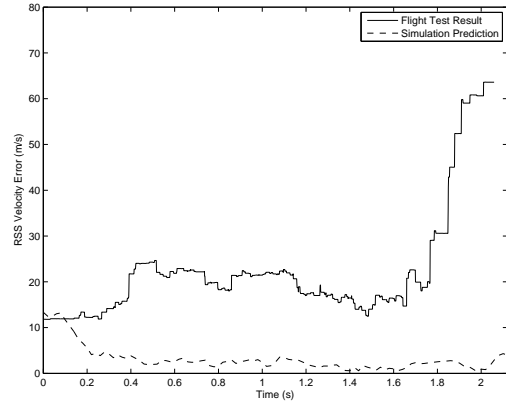


(d) Radar Sensors Speed Measurements

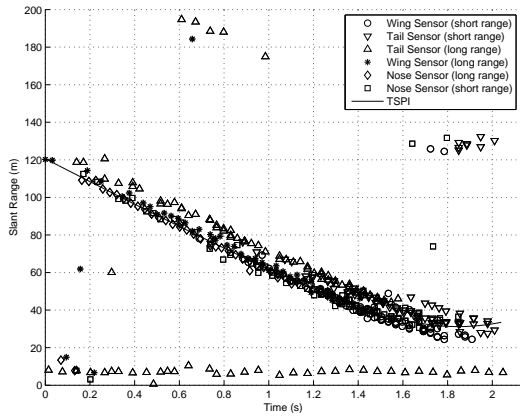
Figure B.28: Air-to-Air Missile Scoring System Performance in Scoring C-12 Surrogate Missile using an Unscented Kalman Filter with Continuous Dynamics Velocity Model (45° Drone Aspect Angle / Run 13)



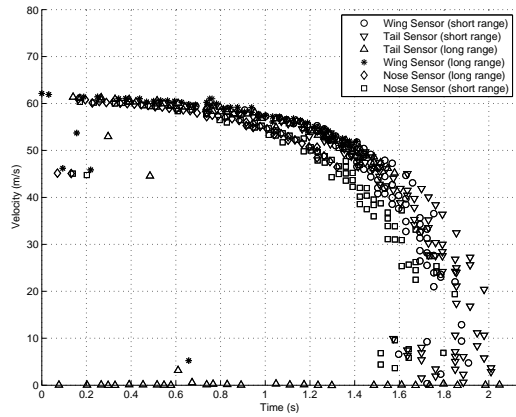
(a) Root Sum Square Error in Surrogate Missile Position Estimate



(b) Root Sum Square Error in Surrogate Missile Velocity Estimate

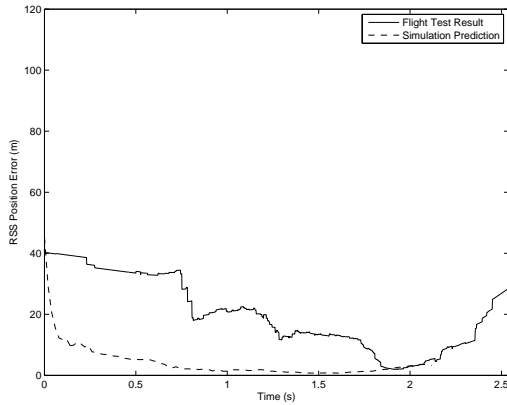


(c) Radar Sensors Slant Range Measurements

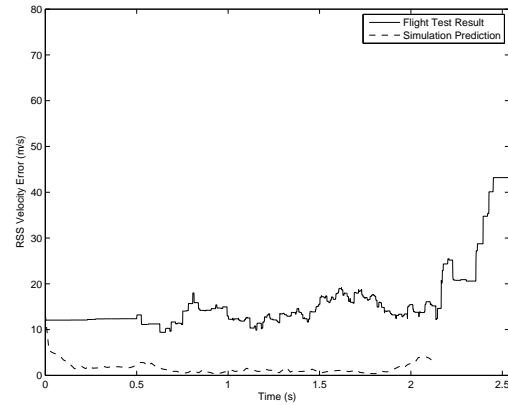


(d) Radar Sensors Speed Measurements

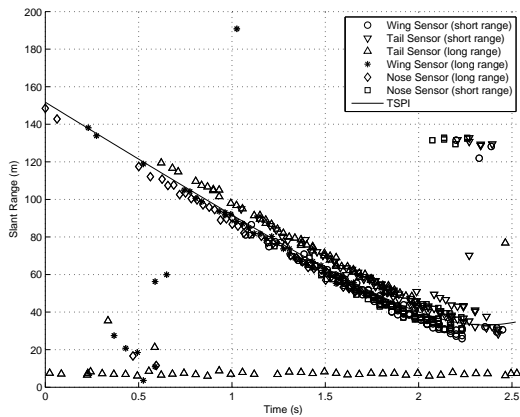
Figure B.29: Air-to-Air Missile Scoring System Performance in Scoring C-12 Surrogate Missile using an Unscented Kalman Filter with Continuous Dynamics Velocity Model (45° Drone Aspect Angle / Run 14)



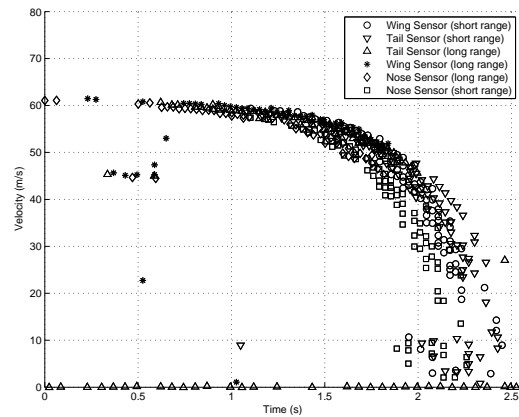
(a) Root Sum Square Error in Surrogate Missile Position Estimate



(b) Root Sum Square Error in Surrogate Missile Velocity Estimate



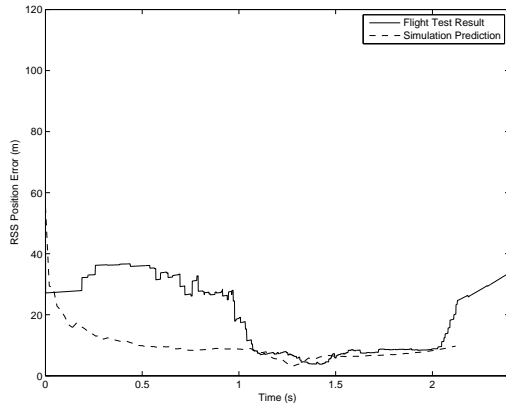
(c) Radar Sensors Slant Range Measurements



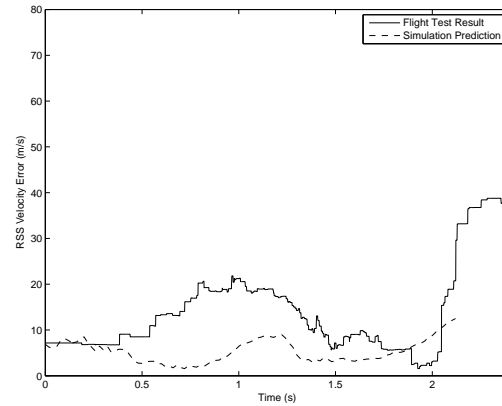
(d) Radar Sensors Speed Measurements

Figure B.30: Air-to-Air Missile Scoring System Performance in Scoring C-12 Surrogate Missile using an Unscented Kalman Filter with Continuous Dynamics Velocity Model (45° Drone Aspect Angle / Run 15)

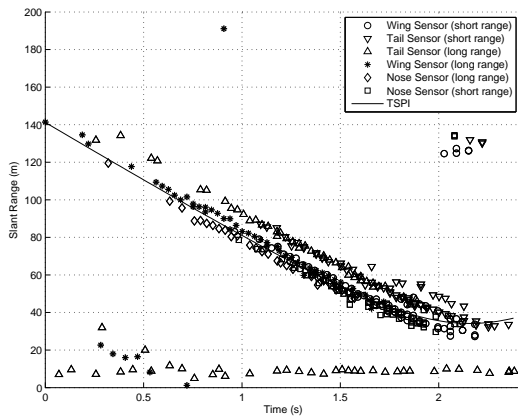
### B.3 Sensor Geometry: 20° Aspect Angle



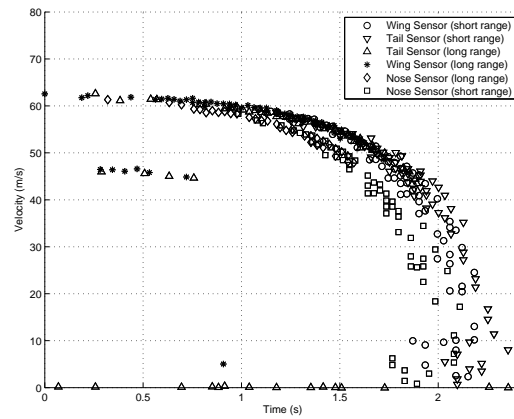
(a) Root Sum Square Error in Surrogate Missile Position Estimate



(b) Root Sum Square Error in Surrogate Missile Velocity Estimate

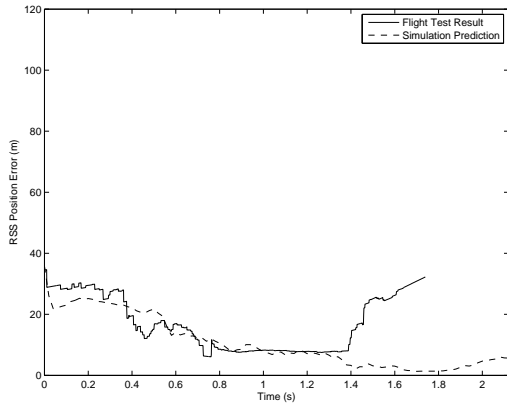


(c) Radar Sensors Slant Range Measurements

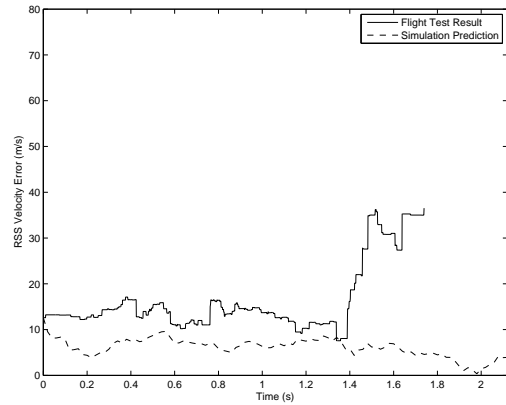


(d) Radar Sensors Speed Measurements

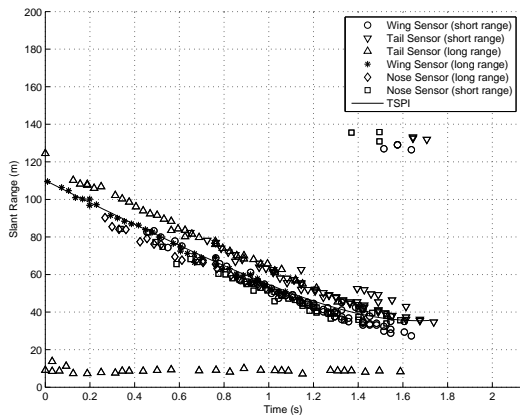
Figure B.31: Air-to-Air Missile Scoring System Performance in Scoring C-12 Surrogate Missile using an Unscented Kalman Filter with Continuous Dynamics Velocity Model (20° Drone Aspect Angle / Run 1)



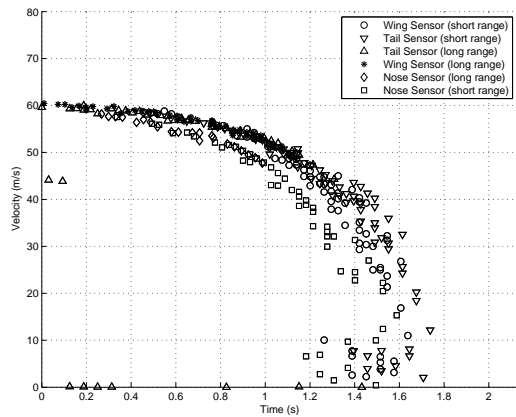
(a) Root Sum Square Error in Surrogate Missile Position Estimate



(b) Root Sum Square Error in Surrogate Missile Velocity Estimate

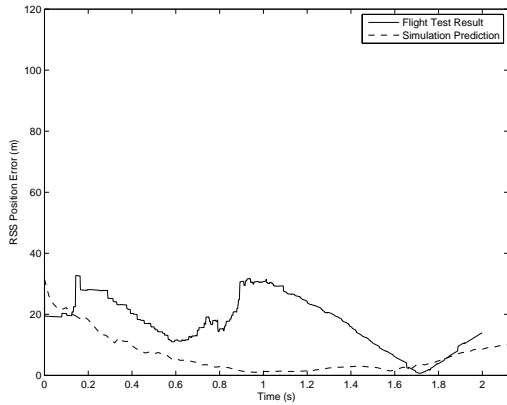


(c) Radar Sensors Slant Range Measurements

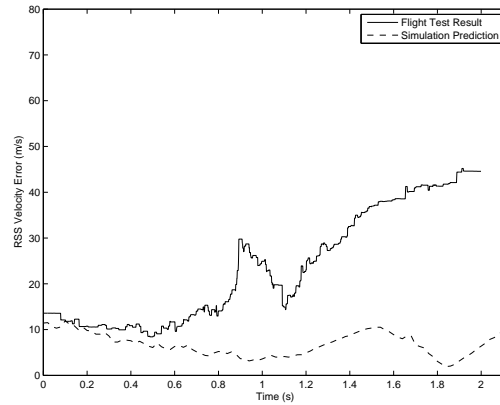


(d) Radar Sensors Speed Measurements

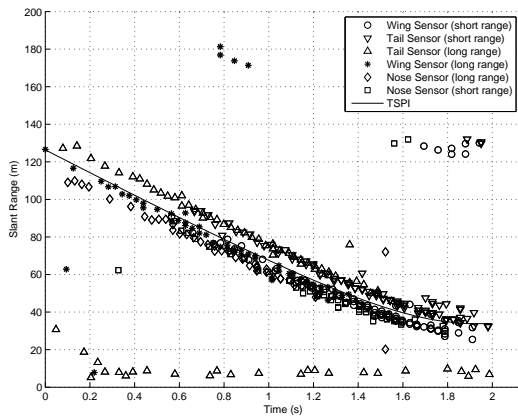
Figure B.32: Air-to-Air Missile Scoring System Performance in Scoring C-12 Surrogate Missile using an Unscented Kalman Filter with Continuous Dynamics Velocity Model (20° Drone Aspect Angle / Run 2)



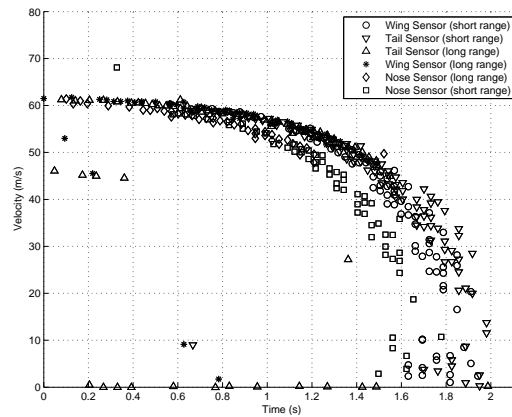
(a) Root Sum Square Error in Surrogate Missile Position Estimate



(b) Root Sum Square Error in Surrogate Missile Velocity Estimate

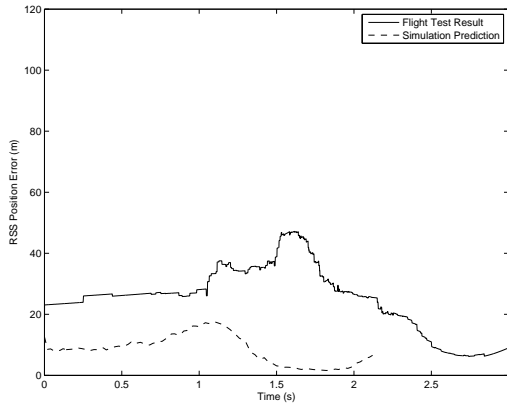


(c) Radar Sensors Slant Range Measurements

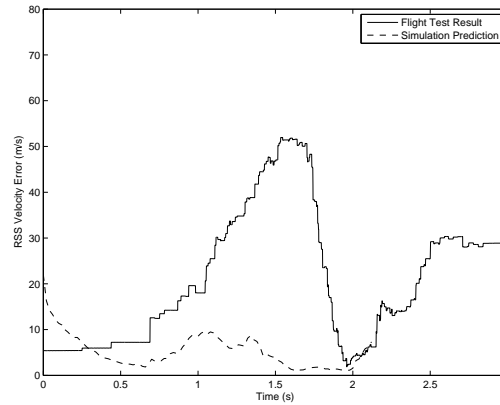


(d) Radar Sensors Speed Measurements

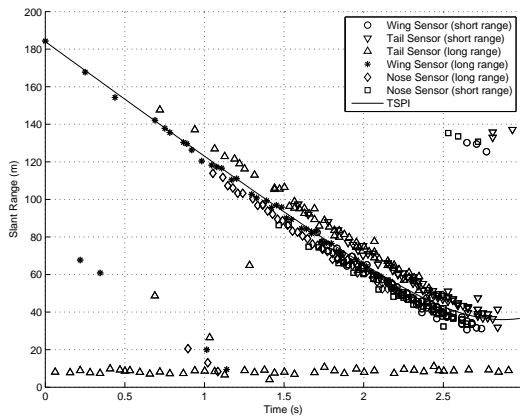
Figure B.33: Air-to-Air Missile Scoring System Performance in Scoring C-12 Surrogate Missile using an Unscented Kalman Filter with Continuous Dynamics Velocity Model (20° Drone Aspect Angle / Run 3)



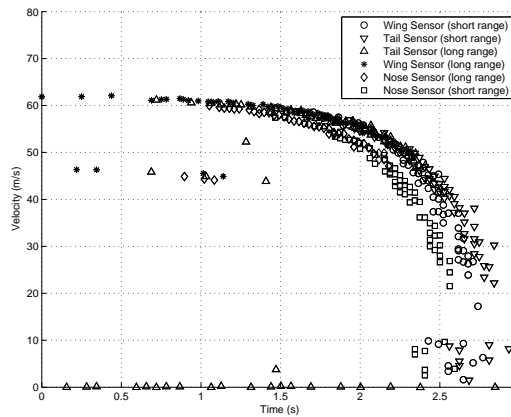
(a) Root Sum Square Error in Surrogate Missile Position Estimate



(b) Root Sum Square Error in Surrogate Missile Velocity Estimate



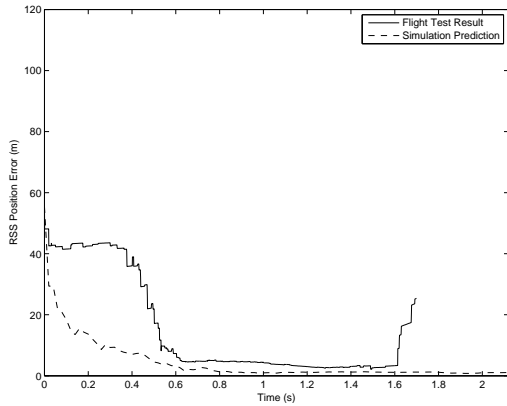
(c) Radar Sensors Slant Range Measurements



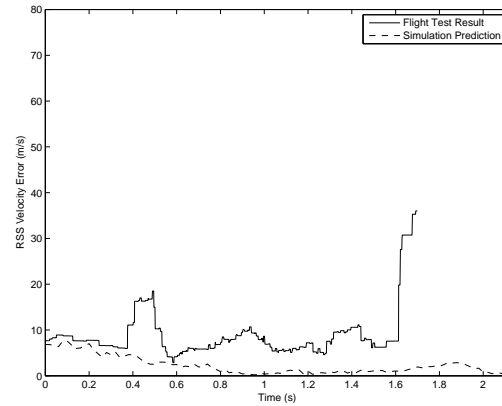
(d) Radar Sensors Speed Measurements

Figure B.34: Air-to-Air Missile Scoring System Performance in Scoring C-12 Surrogate Missile using an Unscented Kalman Filter with Continuous Dynamics Velocity Model (20° Drone Aspect Angle / Run 4)

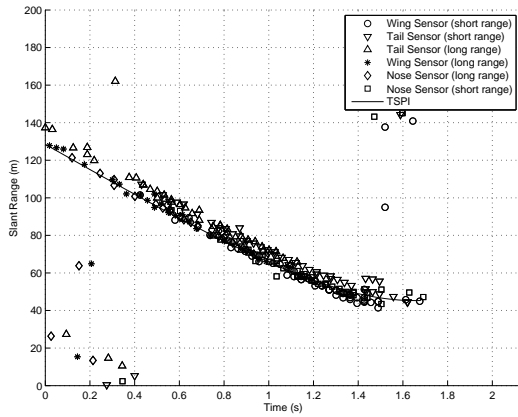
### B.4 Sensor Geometry: 70° Aspect Angle



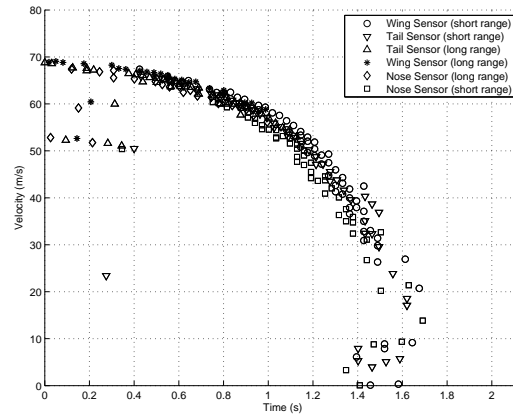
(a) Root Sum Square Error in Surrogate Missile Position Estimate



(b) Root Sum Square Error in Surrogate Missile Velocity Estimate



(c) Radar Sensors Slant Range Measurements



(d) Radar Sensors Speed Measurements

Figure B.35: Air-to-Air Missile Scoring System Performance in Scoring C-12 Surrogate Missile using an Unscented Kalman Filter with Continuous Dynamics Velocity Model (70° Drone Aspect Angle / Run 1)

## *Appendix C. Matlab Code*

### *C.1 Description of Software Programs*

- Extended Kalman Filter Main Program: Reconstructs an air-to-air missile trajectory relative to a drone aircraft using an EKF. The missile dynamics model is selectable and the observation model is based on seven range and range-rate sensors located on the drone.
- Unscented Kalman Filter Main Program: Reconstructs an air-to-air missile trajectory relative to a drone aircraft using an UKF. The missile dynamics model is selectable and the observation model is based on seven range and range-rate sensors located on the drone.
- Particle Filter Main Program: Reconstructs an air-to-air missile trajectory relative to a drone aircraft using a PF. The missile dynamics model is selectable and the observation model is based on seven range and range-rate sensors located on the drone.
- Constant Velocity Missile: Generates a discrete time dynamics model for a constant velocity missile.
- Constant Acceleration Missile: Generates a discrete time dynamics model for a constant acceleration missile.
- 3D Coordinated Turn Missile: Generates a discrete time dynamics model for a missile in a constant 3D coordinated turn.
- Generate Noise: Generates Kalman filter initialization noise and sensor measurement noise for all sensors and saves the data for seeding.
- Generate Measurements: Generates the noise corrupted sensor measurements using truth data and input noise. Also, produces random clutter measurements for each sensor.
- Coordinate Frame Converter: Transforms a vector from the body frame to a navigation frame.

- Nonlinear Transform Function: Transforms sigma points and particles into measurement space.

## C.2 Simulation Main Programs

Listing C.1: Extended Kalman Filter Main Program

```

1 %%%%%%%%%%%%%%%%%%%%%%%%%%%%%%%%%%%%%%%%%%%%%%%%%%%%%%%%%%%%%%%%%%%%%%%%%%
  % Title: Missile Air-to-Air Trajectory Reconstruction (Extended KF)
  % Author: Maj Nick Sweeney
  % Date: 5 Sep 2010
  %
6 % Description: This program reconstructs a missile air-to-air trajectory
  % relative to a target aircraft. The intent is to evaluate the missile's
  % performance in intercepting the aircraft. An Extended Kalman Filter
  % is used to perform the estimation. One of 3 missile dynamics model
  % is available for selection: constant velocity, constant acceleration
11 % and constant 3D coordinated turn. The observation model utilizes
  % 7 Frequency Modulated Continuous Wave (FMCW) radar sensors mounted on
  % the aircraft to provide range and range-rate of the target. The sensors
  % are distributed to provide spherical coverage around the aircraft with
16 % 2 sensors on the nose, 2 sensors on each wingtip and 1 sensor on the
  % tail.
  %
  % Inputs: truth_data_xxx.mat: (truth data file includes:)
  %         t: time vector
  %         dt: time step
21 %         x_true(6xt): missile true state vector (position & velocity)
  %         pos_acft(3xt): drone aircraft true position
  %         vel_acft(3xt): drone aircraft true velocity
  %         roll(1xt): drone aircraft roll in radians
  %         pitch(1xt): drone aircraft pitch in radians
26 %         yaw(1xt); drone aircraft yaw in radians (referenced to north)
  %
  % Outputs: x_out(6xtxRuns): missile's estimated state vector
  %          P_out(6x6xtxRuns): uncertainty in missile's state vector
  %          x_error(6xtxRuns): error in estimated missile state vector
31 %
  % Subprograms: gen_meas_seed: generates simulated sensor measurements
  %              along with clutter
  %              body_to_nav: translates sensor position from aircraft
  %                          body frame to navigation frame
36 %
  % User Selectable Parameters (in order):
  %   number of Monte Carlo runs (runs)
  %   dynamics noise parameter(q): uncertainty in dynamics model
  %   sensor range noise (r_dist): uncertainty in sensor range
41 %   sensor velocity noise (r_vel): uncertainty in sensor range-rate
  %   gate size (gamma)
  %   trajectory(traj): changes truth data file and configures plots
  %   dynamics model (model): constant_velocity, constant_acceleration,
  %                           constant_turn (all subprograms)
46 %   uncertainty in target handoff (x_sig, y_sig, z_sig, vel_sig)
  %
  % Notes: All inputs/outputs in local level Earth-centered navigation frame
  %        All units in metric (meters, meters/sec)
  %%%%%%%%%%%%%%%%%%%%%%%%%%%%%%%%%%%%%%%%%%%%%%%%%%%%%%%%%%%%%%%%%%%%%%%%%%
51 clf
  clear all

  %% SENSOR LOCATIONS
56 % Define Sensor Locations (body frame)
  % Sensor 1 - Aircraft Nose (top)
  p1 = [8; 0; -0.5];
  % Sensor 2 - Aircraft Nose (bottom)
61 p2 = [8; 0; 0.5];
  % Sensor 3 - Aircraft Left Wing (top)
  p3 = [0; -5; 0];

```

```

    % Sensor 4 – Aircraft Left Wing (bottom)
    p4 = [0; -5; 0.1];
66 % Sensor 5 – Aircraft Right Wing (top)
    p5 = [0; 5; 0];
    % Sensor 6 – Aircraft Right Wing (bottom)
    p6 = [0; 5; 0.1];
71 % Sensor 7 – Aircraft Tail (omni-directional)
    p7 = [-8; 0; -1];

%% USER SELECTIONS

76 % Determine Number of Monte Carlo Runs (USER SELECTION)
    runs = 100;

    % Define Gating and Tracks (USER SELECTION)
    NumTracks = 1; % only 1 target
81
    % Define Noise Strength and Gating (USER SELECTION/TUNING PARAMETER)
    q = 800000; % dynamics noise strength
    r.dist = 10; % sensor distance noise strength
    r.vel = 2; % sensor velocity noise strength
86 gamma = 20; % gate size

    % Select Trajectory (USER SELECTION)
    % Non-maneuver=1; Break-turn=2; Vertical=3;
    traj=3;
91
    % Load Truth Data for Program Test
    if traj==1
        profile = 'truth_data_below';
    elseif traj==2
96 profile = 'truth_data_ts';
    else
        profile = 'truth_data_vert';
    end
    load(['Users/Nick/Documents/MATLAB/Thesis/Simulation Software/Truth Data/'...
101 profile '.mat'])
    NT = length(x.true);

    % Choose Missile Dynamics Model (USER SELECTION)
    % Constant Velocity=1; Constant Acceleration=2; Constant Turn=3;
106 model=3;
    if model==1
        % Constant Velocity
        NS = 6; % number of states
        [phi,Qd,G] = constant_vel(dt,q); % constant velocity
111 elseif model==2
        % Constant Acceleration Model
        NS = 9; % number of states
        [phi,Qd,G] = constant_accel(dt,q); % constant acceleration
    else
116 % Constant Turn Model
        NS = 9; % number of states
    end

    % Initialize Track Variables
121 x_minus = zeros(NS,NT); % initialize state variable
    x_plus = zeros(NS,NT);
    P_minus = zeros(NS,NS,NT);
    P_plus = zeros(NS,NS,NT);
    x_out = zeros(NS,2*NT,runs);
126 P_out = zeros(NS,NS,2*NT,runs);
    x_error = zeros(6,2*NT,runs);
    dz = zeros(8,NT);

    % Set Track Initial Covariance Matrix
131 % Uncertainty in Target Handoff – 1 Sigma (USER SELECTION)
    x_sig = 15;
    y_sig = 15;
    z_sig = 45;
    vel_sig = 10;
136 if model==1
        % Constant Velocity Model
        Po = [x_sig^2 0 0 0 0 0;
141 0 y_sig^2 0 0 0 0;
            0 0 z_sig^2 0 0 0;
            0 0 0 vel_sig^2 0 0;
            0 0 0 0 0 0];

```

```

        0      0      0      0      vel_sig^2  0;
        0      0      0      0      0          vel_sig^2];
    else
        % Constant Accel/3d Coordinated Turn Model
146     Po = [x_sig^2  0      0      0      0      0      0      0  0  0;
            0      y_sig^2  0      0      0      0      0      0  0  0;
            0      0      z_sig^2  0      0      0      0      0  0  0;
            0      0      0      vel_sig^2  0      0      0      0  0  0;
            0      0      0      0      vel_sig^2  0      0      0  0  0;
151     0      0      0      0      0      vel_sig^2  0  0  0  0;
            0      0      0      0      0      0      10  0  0  0;
            0      0      0      0      0      0      0      10  0  0;
            0      0      0      0      0      0      0      0      10];
    end
156     P_minus(:,:,1) = Po;
        P_plus(:,:,1) = Po;

        %% SEED NOISE

161     % Load Default Noise
        if traj==1
            noise_file = 'DefaultNoise1';
        elseif traj==2
            noise_file = 'DefaultNoise2';
166     else
            noise_file = 'DefaultNoise3';
        end
        load(['/Users/Nick/Documents/MATLAB/Thesis/Simulation Software/Generate Measurements/' ...
            noise_file '.mat'])

171     %% INITIALIZE WAITBAR

        h = waitbar(0,sprintf('%i Runs',runs));

        %% MONTE CARLO RUN

176     tic % start timing
        for index=1:runs

            waitbar(index/runs,h);

181     % Initialize Target State Vector
            x_minus(1:6,1) = x_true(1:6,1)+([x_sig y_sig z_sig vel_sig vel_sig vel_sig]'.*...
                initial_noise(:,index));
            x_plus(:,1) = x_minus(:,1);

186     x_out(:,1,index) = x_minus(:,1);
            x_out(:,2,index) = x_plus(:,1);
            P_out(:,:,1,index) = P_minus(:,:,1);
            P_out(:,:,2,index) = P_plus(:,:,1);
            x_error(:,1,index) = x_out(1:6,1,index)-x_true(:,1);
191     x_error(:,2,index) = x_out(1:6,2,index)-x_true(:,1);

            % Time Loop
            for i=1:NT-1

196         for ii=1:NumTracks

                if model==3
                    % Choose Missile Dynamics Model (USER SELECTION)
                    [phi,Qd,G] = constant_turn(dt,q,x_plus(:,ii)); % constant turn model
201                 end

                % Time Propagation
                x_minus(:,i+1) = phi*x_plus(:,i);
                P_minus(:,:,i+1) = phi*P_plus(:,:,i)*phi'+Qd;
206

                x = x_minus(1,i+1); % shorthand
                y = x_minus(2,i+1);
                z = x_minus(3,i+1);
                vx = x_minus(4,i+1);
                vy = x_minus(5,i+1);
211                vz = x_minus(6,i+1);

                % Generate Measurements From True State Vector
                [z1,z2,z3,z4,z5,z6,z7,detect] = gen_meas_seed(x_true(1:6,i+1),pos_acft(:,i+1),...
                    vel_acft(:,i+1),roll(i+1),pitch(i+1),yaw(i+1),noise(:,i,index));
216

```

```

% Define Sensor Noise
R_gate = diag([r_dist; r_vel]);

% Clear/Initialize Variables
221 dz = []; % clear dz
H = []; % clear H
H_gate = zeros(2,NS); % initialize H_gate
P = P_minus(:, :, i+1); % abbreviate

226 % Predict Measurements and Calculate H Matrix
% Sensor 1
if detect(1)==1
    closest = 10000; % initialize closest to large number
    nearest_meas = []; % clear nearest measurement
231 % Convert Sensor Coordinates from Body Frame to Nav Frame
    [p1n] = body_to_nav(pos_acft(:, i+1), roll(i+1), pitch(i+1), yaw(i+1), p1);
% Nominal Distance and Speed Measurement
    dist = sqrt((x-p1n(1))^2+(y-p1n(2))^2+(z-p1n(3))^2);
    speed = -((vx-vel_acft(1, i+1))*(x-p1n(1))+(vy-vel_acft(2, i+1))*(y-p1n(2))+...
        vz-vel_acft(3, i+1))*(z-p1n(3)))/dist;
236 nom_meas = [dist; speed];
% Partial derivative with respect to x,y,z,vx,vy, and vz
H_gate(1,1) = (x-p1n(1))/dist;
H_gate(1,2) = (y-p1n(2))/dist;
H_gate(1,3) = (z-p1n(3))/dist;
241 H_gate(2,1) = (x-p1n(1))*-speed/dist^2-(vx-vel_acft(1, i+1))/dist;
H_gate(2,2) = (y-p1n(2))*-speed/dist^2-(vy-vel_acft(2, i+1))/dist;
H_gate(2,3) = (z-p1n(3))*-speed/dist^2-(vz-vel_acft(3, i+1))/dist;t;
H_gate(2,4) = -(x-p1n(1))/dist;
H_gate(2,5) = -(y-p1n(2))/dist;
246 H_gate(2,6) = -(z-p1n(3))/dist;
% Perform Gating
% Define Coarse Square Gate Size
S = H_gate*P*H_gate'+R_gate; % residual covariance
emax = sqrt(max(eig(gamma*S)));
251 num = size(z1,2); % size of sensor 1 measurement vector
% Loop For Number of Measurements
for j=1:num
    residual = (z1(:,j)-nom_meas); % measurement residual
% Apply Coarse Square Gate
256 if all(z1(:,j)>(nom_meas-emax) & z1(:,j)<(nom_meas+emax))
% Define Elliptical Gate Size
    d = residual'/S*residual; % residual norm
% Apply Elliptical Gate
    if d<gamma && d<closest
261 closest = d;
        nearest_meas = z1(:,j);
    end
end
end
266 % Determine if Any Measurement is Within Gate
if ~isempty(nearest_meas)
% Save Measurement and Update H Matrix
dz_update = nearest_meas-nom_meas;
dz = [dz; dz_update];
271 H = [H; H_gate];
end
end

% Sensor 2
276 if detect(2)==1
    closest = 10000; % initialize closest to large number
    nearest_meas = []; % clear nearest measurement
% Convert Sensor Coordinates from Body Frame to Nav Frame
    [p2n] = body_to_nav(pos_acft(:, i+1), roll(i+1), pitch(i+1), yaw(i+1), p2);
281 % Nominal Distance and Speed Measurement
    dist = sqrt((x-p2n(1))^2+(y-p2n(2))^2+(z-p2n(3))^2);
    speed = -((vx-vel_acft(1, i+1))*(x-p2n(1))+(vy-vel_acft(2, i+1))*(y-p2n(2))+...
        vz-vel_acft(3, i+1))*(z-p2n(3)))/dist;
    nom_meas = [dist; speed];
286 % Partial derivative with respect to x,y,z,vx,vy, and vz
H_gate(1,1) = (x-p2n(1))/dist;
H_gate(1,2) = (y-p2n(2))/dist;
H_gate(1,3) = (z-p2n(3))/dist;
H_gate(2,1) = (x-p2n(1))*-speed/dist^2-(vx-vel_acft(1, i+1))/dist;
H_gate(2,2) = (y-p2n(2))*-speed/dist^2-(vy-vel_acft(2, i+1))/dist;
291 H_gate(2,3) = (z-p2n(3))*-speed/dist^2-(vz-vel_acft(3, i+1))/dist;
H_gate(2,4) = -(x-p2n(1))/dist;

```

```

    H_gate(2,5) = -(y-p2n(2))/dist;
    H_gate(2,6) = -(z-p2n(3))/dist;
296 % Perform Gating
    % Define Coarse Square Gate Size
    S = H_gate*P*H_gate'+R_gate; % residual covariance
    emax = sqrt(max(eig(gamma*S)));
    num = size(z2,2); % size of sensor 2 measurement vector
    % Loop For Number of Measurements
301 for j=1:num
        residual = (z2(:,j)-nom.meas); % measurement residual
        % Apply Coarse Square Gate
        if all(z2(:,j)>(nom.meas-emax) & z2(:,j)<(nom.meas+emax))
306 % Define Elliptical Gate Size
            d = residual'/S*residual; % residual norm
            % Apply Elliptical Gate
            if d<gamma && d<closest
                closest = d;
                nearest.meas = z2(:,j);
311 end
        end
    end
    % Determine if Any Measurement is Within Gate
316 if ~isempty(nearest.meas)
        % Save Measurement and Update H Matrix
        dz_update = nearest.meas-nom.meas;
        dz = [dz; dz_update];
        H = [H; H_gate];
    end
321 end

% Sensor 3
if detect(3)==1
326 closest = 10000; % initialize closest to large number
    nearest.meas = []; % clear nearest measurement
    % Convert Sensor Coordinates from Body Frame to Nav Frame
    [p3n] = body_to_nav(pos.acft(:,i+1),roll(i+1),pitch(i+1),yaw(i+1),p3);
    % Nominal Distance and Speed Measurement
331 dist = sqrt((x-p3n(1))^2+(y-p3n(2))^2+(z-p3n(3))^2);
    speed = -((vx-vel.acft(1,i+1))*(x-p3n(1))+(vy-vel.acft(2,i+1))*(y-p3n(2))+(...
        vz-vel.acft(3,i+1))*(z-p3n(3)))/dist;
    nom.meas = [dist; speed];
    % Partial derivative with respect to x,y,z,vx,vy, and vz
    H_gate(1,1) = (x-p3n(1))/dist;
    H_gate(1,2) = (y-p3n(2))/dist;
336 H_gate(1,3) = (z-p3n(3))/dist;
    H_gate(2,1) = (x-p3n(1))*-speed/dist^2-(vx-vel.acft(1,i+1))/dist;
    H_gate(2,2) = (y-p3n(2))*-speed/dist^2-(vy-vel.acft(2,i+1))/dist;
    H_gate(2,3) = (z-p3n(3))*-speed/dist^2-(vz-vel.acft(3,i+1))/dist;
341 H_gate(2,4) = -(x-p3n(1))/dist;
    H_gate(2,5) = -(y-p3n(2))/dist;
    H_gate(2,6) = -(z-p3n(3))/dist;
    % Perform Gating
    % Define Coarse Square Gate Size
346 S = H_gate*P*H_gate'+R_gate; % residual covariance
    emax = sqrt(max(eig(gamma*S)));
    num = size(z3,2); % size of sensor 3 measurement vector
    % Loop For Number of Measurements
    for j=1:num
351 residual = (z3(:,j)-nom.meas); % measurement residual
        % Apply Coarse Square Gate
        if all(z3(:,j)>(nom.meas-emax) & z3(:,j)<(nom.meas+emax))
            % Define Elliptical Gate Size
            d = residual'/S*residual; % residual norm
            % Apply Elliptical Gate
356 if d<gamma && d<closest
                closest = d;
                nearest.meas = z3(:,j);
            end
        end
    end
361 end
    % Determine if Any Measurement is Within Gate
    if ~isempty(nearest.meas)
        % Save Measurement and Update H Matrix
366 dz_update = nearest.meas-nom.meas;
        dz = [dz; dz_update];
        H = [H; H_gate];
    end
end
end

```

```

371 % Sensor 4
    if detect(4)==1
        closest = 10000; % initialize closest to large number
        nearest_meas = []; % clear nearest measurement
        % Convert Sensor Coordinates from Body Frame to Nav Frame
376 [p4n] = body_to_nav(pos_acft(:,i+1),roll(i+1),pitch(i+1),yaw(i+1),p4);
        % Nominal Distance and Speed Measurement
        dist = sqrt((x-p4n(1))^2+(y-p4n(2))^2+(z-p4n(3))^2);
        speed = -((vx-vel_acft(1,i+1))*(x-p4n(1))+(vy-vel_acft(2,i+1))*(y-p4n(2))+...
            vz-vel_acft(3,i+1))*(z-p4n(3)))/dist;
        nom_meas = [dist; speed];
381 % Partial derivative with respect to x,y,z,vx,vy, and vz
        H_gate(1,1) = (x-p4n(1))/dist;
        H_gate(1,2) = (y-p4n(2))/dist;
        H_gate(1,3) = (z-p4n(3))/dist;
        H_gate(2,1) = (x-p4n(1))*-speed/dist^2-(vx-vel_acft(1,i+1))/dist;
386 H_gate(2,2) = (y-p4n(2))*-speed/dist^2-(vy-vel_acft(2,i+1))/dist;
        H_gate(2,3) = (z-p4n(3))*-speed/dist^2-(vz-vel_acft(3,i+1))/dist;
        H_gate(2,4) = -(x-p4n(1))/dist;
        H_gate(2,5) = -(y-p4n(2))/dist;
        H_gate(2,6) = -(z-p4n(3))/dist;
391 % Perform Gating
        % Define Coarse Square Gate Size
        S = H_gate*P*H_gate'+R_gate; % residual covariance
        emax = sqrt(max(eig(gamma*S)));
        num = size(z4,2); % size of sensor 4 measurement vector
396 % Loop For Number of Measurements
        for j=1:num
            residual = (z4(:,j)-nom_meas); % measurement residual
            % Apply Coarse Square Gate
            if all(z4(:,j)>(nom_meas-emax) & z4(:,j)<(nom_meas+emax))
401 % Define Elliptical Gate Size
                d = residual'/S*residual; % residual norm
                % Apply Elliptical Gate
                if d<gamma && d<closest
406 closest = d;
                    nearest_meas = z4(:,j);
                end
            end
        end
        % Determine if Any Measurement is Within Gate
411 if ~isempty(nearest_meas)
            % Save Measurement and Update H Matrix
            dz_update = nearest_meas-nom_meas;
            dz = [dz; dz_update];
            H = [H; H_gate];
416 end
    end

% Sensor 5
    if detect(5)==1
421 closest = 10000; % initialize closest to large number
        nearest_meas = []; % clear nearest measurement
        % Convert Sensor Coordinates from Body Frame to Nav Frame
        [p5n] = body_to_nav(pos_acft(:,i+1),roll(i+1),pitch(i+1),yaw(i+1),p5);
        % Nominal Distance and Speed Measurement
426 dist = sqrt((x-p5n(1))^2+(y-p5n(2))^2+(z-p5n(3))^2);
        speed = -((vx-vel_acft(1,i+1))*(x-p5n(1))+(vy-vel_acft(2,i+1))*(y-p5n(2))+...
            vz-vel_acft(3,i+1))*(z-p5n(3)))/dist;
        nom_meas = [dist; speed];
        % Partial derivative with respect to x,y,z,vx,vy, and vz
        H_gate(1,1) = (x-p5n(1))/dist;
431 H_gate(1,2) = (y-p5n(2))/dist;
        H_gate(1,3) = (z-p5n(3))/dist;
        H_gate(2,1) = (x-p5n(1))*-speed/dist^2-(vx-vel_acft(1,i+1))/dist;
        H_gate(2,2) = (y-p5n(2))*-speed/dist^2-(vy-vel_acft(2,i+1))/dist;
        H_gate(2,3) = (z-p5n(3))*-speed/dist^2-(vz-vel_acft(3,i+1))/dist;
436 H_gate(2,4) = -(x-p5n(1))/dist;
        H_gate(2,5) = -(y-p5n(2))/dist;
        H_gate(2,6) = -(z-p5n(3))/dist;
        % Perform Gating
        % Define Coarse Square Gate Size
441 S = H_gate*P*H_gate'+R_gate; % residual covariance
        emax = sqrt(max(eig(gamma*S)));
        num = size(z5,2); % size of sensor 5 measurement vector
        % Loop For Number of Measurements
        for j=1:num

```

```

446     residual = (z5(:,j)-nom_meas); % measurement residual
% Apply Coarse Square Gate
if all(z5(:,j)>(nom_meas-emax) & z5(:,j)<(nom_meas+emax))
    % Define Elliptical Gate Size
451     d = residual'/S*residual; % residual norm
% Apply Elliptical Gate
if d<gamma && d<closest
    closest = d;
    nearest_meas = z5(:,j);
end
456 end
end
% Determine if Any Measurement is Within Gate
if ~isempty(nearest_meas)
    % Save Measurement and Update H Matrix
461 dz_update = nearest_meas-nom_meas;
dz = [dz; dz_update];
H = [H; H_gate];
end
end
466 % Sensor 6
if detect(6)==1
    closest = 10000; % initialize closest to large number
    nearest_meas = []; % clear nearest measurement
471 % Convert Sensor Coordinates from Body Frame to Nav Frame
[p6n] = body_to_nav(pos_acft(:,i+1),roll(i+1),pitch(i+1),yaw(i+1),p6);
% Nominal Distance and Speed Measurement
dist = sqrt((x-p6n(1))^2+(y-p6n(2))^2+(z-p6n(3))^2);
speed = -((vx-vel_acft(1,i+1))*(x-p6n(1))+(vy-vel_acft(2,i+1))*(y-p6n(2))+(...
    vz-vel_acft(3,i+1))*(z-p6n(3)))/dist;
476 nom_meas = [dist; speed];
% Partial derivative with respect to x,y,z,vx,vy, and vz
H_gate(1,1) = (x-p6n(1))/dist;
H_gate(1,2) = (y-p6n(2))/dist;
H_gate(1,3) = (z-p6n(3))/dist;
481 H_gate(2,1) = (x-p6n(1))*-speed/dist^2-(vx-vel_acft(1,i+1))/dist;
H_gate(2,2) = (y-p6n(2))*-speed/dist^2-(vy-vel_acft(2,i+1))/dist;
H_gate(2,3) = (z-p6n(3))*-speed/dist^2-(vz-vel_acft(3,i+1))/dist;
H_gate(2,4) = -(x-p6n(1))/dist;
H_gate(2,5) = -(y-p6n(2))/dist;
486 H_gate(2,6) = -(z-p6n(3))/dist;
% Perform Gating
% Define Coarse Square Gate Size
S = H_gate*P*H_gate'+R_gate; % residual covariance
emax = sqrt(max(eig(gamma*S)));
491 num = size(z6,2); % size of sensor 6 measurement vector
% Loop For Number of Measurements
for j=1:num
    residual = (z6(:,j)-nom_meas); % measurement residual
% Apply Coarse Square Gate
496 if all(z6(:,j)>(nom_meas-emax) & z6(:,j)<(nom_meas+emax))
    % Define Elliptical Gate Size
d = residual'/S*residual; % residual norm
% Apply Elliptical Gate
if d<gamma && d<closest
501 closest = d;
nearest_meas = z6(:,j);
end
end
end
506 % Determine if Any Measurement is Within Gate
if ~isempty(nearest_meas)
    % Save Measurement and Update H Matrix
dz_update = nearest_meas-nom_meas;
dz = [dz; dz_update];
511 H = [H; H_gate];
end
end
% Sensor 7
516 if detect(7)==1
    closest = 10000; % initialize closest to large number
    nearest_meas = []; % clear nearest measurement
% Convert Sensor Coordinates from Body Frame to Nav Frame
[p7n] = body_to_nav(pos_acft(:,i+1),roll(i+1),pitch(i+1),yaw(i+1),p7);
521 % Nominal Distance and Speed Measurement
dist = sqrt((x-p7n(1))^2+(y-p7n(2))^2+(z-p7n(3))^2);

```

```

        speed = -((vx-vel_acft(1,i+1))*(x-p7n(1))+(vy-vel_acft(2,i+1))*(y-p7n(2))+(...
            vz-vel_acft(3,i+1))*(z-p7n(3)))/dist;
        nom_meas = [dist; speed];
526 % Partial derivative with respect to x,y,z,vx,vy, and vz
        H_gate(1,1) = (x-p7n(1))/dist;
        H_gate(1,2) = (y-p7n(2))/dist;
        H_gate(1,3) = (z-p7n(3))/dist;
        H_gate(2,1) = (x-p7n(1))*-speed/dist^2-(vx-vel_acft(1,i+1))/dist;
531 H_gate(2,2) = (y-p7n(2))*-speed/dist^2-(vy-vel_acft(2,i+1))/dist;
        H_gate(2,3) = (z-p7n(3))*-speed/dist^2-(vz-vel_acft(3,i+1))/dist;
        H_gate(2,4) = -(x-p7n(1))/dist;
        H_gate(2,5) = -(y-p7n(2))/dist;
        H_gate(2,6) = -(z-p7n(3))/dist;
536 % Perform Gating
        % Define Coarse Square Gate Size
        S = H_gate*P*H_gate'+R_gate; % residual covariance
        emax = sqrt(max(eig(gamma*S)));
        num = size(z7,2); % size of sensor 7 measurement vector
541 % Loop For Number of Measurements
        for j=1:num
            residual = (z7(:,j)-nom_meas); % measurement residual
            % Apply Coarse Square Gate
            if all(z7(:,j)>(nom_meas-emax) & z7(:,j)<(nom_meas+emax))
546 % Define Elliptical Gate Size
                d = residual'/S*residual; % residual norm
                % Apply Elliptical Gate
                if d<gamma && d<closest
                    closest = d;
                    nearest_meas = z7(:,j);
551                end
            end
            end
            % Determine if Any Measurement is Within Gate
556 if ~isempty(nearest_meas)
                % Save Measurement and Update H Matrix
                dz_update = nearest_meas-nom_meas;
                dz = [dz; dz_update];
                H = [H; H_gate];
            end
561 end
        if ~isempty(dz)
            % Sensor Noise
566 r = [];
            NM = size(dz,1);
            for iii=1:NM/2
                r = [r; r_dist; r_vel;];
            end
571 R = diag(r);
            K = P*H'/(H*P*H'+R); % kalman gain
            x_plus(:,i+1) = x_minus(:,i+1)+K*dz;
            P_plus(:, :, i+1) = P-K*H*P;
        else
576 x_plus(:,i+1) = x_minus(:,i+1);
            P_plus(:, :, i+1) = P;
        end
581 % Save Output Data
        x_out(:,2*i+1,index) = x_minus(:,i+1);
        x_out(:,2*i+2,index) = x_plus(:,i+1);
        P_out(:, :, 2*i+1,index) = P_minus(:, :, i+1);
        P_out(:, :, 2*i+2,index) = P_plus(:, :, i+1);
586 % Calculate Error
        x_error(:,2*i+1,index) = x_out(1:6,2*i+1,index)-x_true(:,i+1);
        x_error(:,2*i+2,index) = x_out(1:6,2*i+2,index)-x_true(:,i+1);
591 end
    end
    toc % stop timing
596 %% PLOT RESULTS
    % Define Output Time Vector
    t_out = zeros(2*NT,1);

```

```

t_out(1:2:2*NT) = t;
601 t_out(2:2:2*NT) = t;
t_final = max(t_out);

% Define Plot Axes
if traj==1 % non-maneuvering
606 traj_axis = [-1500 1500 0000 3000 0 5000];
pos_axis = [0 0.45 -50 50];
vel_axis = [0 0.45 -40 40];
RMS_axis = [0 0.45 0 50];
elseif traj==2 % break-turn
611 traj_axis = [-200 1000 -2000 2000 3500 5000];
pos_axis = [0 0.4 -50 50];
vel_axis = [0 0.4 -100 100];
RMS_axis = [0 0.4 0 50];
else % vertical man
616 traj_axis = [-1000 1000 -3000 1000 5000 5500];
pos_axis = [0 0.39 -50 50];
vel_axis = [0 0.39 -100 100];
RMS_axis = [0 0.39 0 50];
end
621 % Plot Sample 3D Trajectory
figure(1)
plot3(acft(2,1),acft(1,1),-acft(3,1),'bo')
hold on
626 plot3(acft(2,:),acft(1,:),-acft(3,:),'b')
plot3(x_msl(2,1),x_msl(1,2),-x_msl(3,3),'ks')
plot3(x_msl(2,:),x_msl(1,:),-x_msl(3,:),'k—')
plot3(x_out(2,:,1),x_out(1,:,1),-x_out(3,:,1),'r.')
ylabel('North(+)/South(-) (m)')
631 xlabel('East(+)/West(-) (m)')
zlabel('Altitude (m)')
legend('Aircraft Start Position','Aircraft Trajectory','Missile Start Position','...
Missile True Trajectory','Missile Estimate','Location','West')
axis(traj_axis)
grid on
636 hold off

% Plot Mean State Errors
x_error_mean = mean(x_error,3);
x_error_std = std(x_error,0,3);
641 % Position Error
sigma_plot = P_out(1,1,:,1);
figure(2)
subplot(3,1,1)
646 plot(t_out,x_error_mean(1,:),'k',t_out,x_error_mean(1,:)+x_error_std(1,:),'b—',...
t_out,x_error_mean(1,:)-x_error_std(1,:), 'b—')
% title(sprintf('Missile Mean Position Error and Standard Deviation(%i Runs)',runs))
ylabel('x error (m)')
axis(pos_axis)
651 subplot(3,1,2)
plot(t_out,x_error_mean(2,:),'k',t_out,x_error_mean(2,:)+x_error_std(2,:),'b—',...
t_out,x_error_mean(2,:)-x_error_std(2,:), 'b—');
ylabel('y error (m)')
axis(pos_axis)
656 subplot(3,1,3)
plot(t_out,x_error_mean(3,:),'k',t_out,x_error_mean(3,:)+x_error_std(3,:),'b—',...
t_out,x_error_mean(3,:)-x_error_std(3,:), 'b—');
ylabel('z error (m)')
xlabel('time (s)')
661 axis(pos_axis)

% Velocity Error
figure(3)
subplot(3,1,1)
666 plot(t_out,x_error_mean(4,:),'k',t_out,x_error_mean(4,:)+x_error_std(4,:),'b—',...
t_out,x_error_mean(4,:)-x_error_std(4,:), 'b—');
% title(sprintf('Missile Mean Velocity Error and Standard Deviation(%i Runs)',runs))
ylabel('vx error (m/s)')
axis(vel_axis)
671 subplot(3,1,2)
plot(t_out,x_error_mean(5,:),'k',t_out,x_error_mean(5,:)+x_error_std(5,:),'b—',...
t_out,x_error_mean(5,:)-x_error_std(5,:), 'b—');
ylabel('vy error (m/s)')
axis(vel_axis)
676 subplot(3,1,3)

```

```

plot(t_out,x_error_mean(6,:), 'k', t_out, x_error_mean(6, :)+x_error_std(6, :), 'b—', ...
     t_out, x_error_mean(6, :)-x_error_std(6, :), 'b—');
ylabel('vz error (m/s)')
xlabel('time (s)')
681 axis(vel-axis)

% Plot RMS Error
RMS_error = sqrt(sum((x_true(1:3, :)-x_plus(1:3, :)).^2, 1));
figure(4)
686 plot(t, RMS_error)
% title('Missile Position Root-Sum-Squared Error (1 Run)')
ylabel('position error (m)')
xlabel('time (s)')
axis(RMS-axis)
691

% Calculate Mean Error and Standard Deviation at Impact
final_error.mean = x_error.mean(:, 2*NT);
final_error.std = x_error.std(:, 2*NT);

696 % Categorize Filemanes by Model (CV, CA, CT)
if model==1
    name2 = '_CV';
elseif model==2
    name2 = '_CA';
701 else
    name2 = '_CT';
end

% Save Plots to Desired Directory
706 save([' /Users/Nick/Documents/LaTex/My.Thesis/Plots/' 'traj' num2str(traj) name2 '_EKF' ...
        '.mat'], 'final_error_mean', 'final_error_std')
print(1, '-dpdf', [' /Users/Nick/Documents/LaTex/My.Thesis/Plots/' 'traj' num2str(traj) ...
                 name2 '_EKF'])
print(2, '-dpdf', [' /Users/Nick/Documents/LaTex/My.Thesis/Plots/' 'pos' num2str(traj) ...
                 name2 '_EKF'])
print(3, '-dpdf', [' /Users/Nick/Documents/LaTex/My.Thesis/Plots/' 'vel' num2str(traj) ...
                 name2 '_EKF'])
print(4, '-dpdf', [' /Users/Nick/Documents/LaTex/My.Thesis/Plots/' 'rms' num2str(traj) ...
                 name2 '_EKF'])
711 close(h)

```

## Listing C.2: Unscented Kalman Filter Main Program

```

1 %%%%%%%%%%%%%%%%%%%%%%%%%%%%%%%%%%%%%%%%%%%%%%%%%%%%%%%%%%%%%%%%%%%%%%%%%
% Title: Missile Air-to-Air Trajectory Reconstruction (Unscented KF)
% Author: Maj Nick Sweeney
% Date: 5 Sep 2010
%
6 % Description: This program reconstructs a missile air-to-air trajectory
% relative to a target aircraft. The intent is to evaluate the missile's
% performance in intercepting the aircraft. An Unscented Kalman Filter
% is used to perform the estimation. One of 3 missile dynamics model
11 % is available for selection: constant velocity, constant acceleration
% and constant 3D coordinated turn. The observation model utilizes
% 7 Frequency Modulated Continuous Wave (FMCW) radar sensors mounted on
% the aircraft to provide range and range-rate of the target. The sensors
% are distributed to provide spherical coverage around the aircraft with
% 2 sensors on the nose, 2 sensors on each wingtip and 1 sensor on the
16 % tail.
%
% Inputs: truth_data_xxx.mat: (truth data file includes:)
%         t: time vector
%         dt: time step
21 %         x_true(6xt): missile true state vector (position & velocity)
%         pos_acft(3xt): drone aircraft true position
%         vel_acft(3xt): drone aircraft true velocity
%         roll(1xt): drone aircraft roll in radians
%         pitch(1xt): drone aircraft pitch in radians
26 %         yaw(1xt); drone aircraft yaw in radians (referenced to north)
%
% Outputs: x_out(6xtxRuns): missile's estimated state vector
%          P_out(6x6xtxRuns): uncertainty in missile's state vector
%          x_error(6xtxRuns): error in estimated missile state vector
31 %
% Subprograms: gen_meas_seed: generates simulated sensor measurements
%              along with clutter
%              body_to_nav: translates sensor position from aircraft
%              body frame to navigation frame
36 %              h_transform: transforms sigma points through nonlinear
%              observation function
%
% User Selectable Parameters (in order):
%   number of Monte Carlo runs (runs)
41 %   dynamics noise parameter(q): uncertainty in dynamics model
%   sensor range noise (r_dist): uncertainty in sensor range
%   sensor velocity noise (r_vel): uncertainty in sensor range-rate
%   gate size (gamma)
%   trajectory(traj): changes truth data file and configures plots
46 %   dynamics model (model): constant_velocity, constant acceleration,
%   constant_turn (all subprograms)
%   uncertainty in target handoff (x_sig, y_sig, z_sig, vel_sig)
%
% Notes: All inputs/outputs in local level Earth-centered navigation frame
51 %       All units in metric (meters, meters/sec)
%%%%%%%%%%%%%%%%%%%%%%%%%%%%%%%%%%%%%%%%%%%%%%%%%%%%%%%%%%%%%%%%%%%%%%%%

clf
clear all
56 %% SENSOR LOCATIONS

% Define Sensor Locations (body frame)
% Sensor 1 - Aircraft Nose (top)
61 p1 = [8; 0; -0.5];
% Sensor 2 - Aircraft Nose (bottom)
p2 = [8; 0; 0.5];
% Sensor 3 - Aircraft Left Wing (top)
p3 = [0; -5; 0];
66 % Sensor 4 - Aircraft Left Wing (bottom)
p4 = [0; -5; 0.1];
% Sensor 5 - Aircraft Right Wing (top)
p5 = [0; 5; 0];
% Sensor 6 - Aircraft Right Wing (bottom)
71 p6 = [0; 5; 0.1];
% Sensor 7 - Aircraft Tail (omni-directional)
p7 = [-8; 0; -1];

%% USER SELECTIONS
76 % Determine Number of Monte Carlo Runs (USER SELECTION)

```

```

runs = 100;

% Define Gating and Tracks (USER SELECTION)
81 NumTracks = 1; % only 1 target

% Define Noise Strength and Gating (USER SELECTION/TUNING PARAMETER)
q = 800000; % dynamics noise strength
r.dist = 10; % sensor distance noise strength
86 r.vel = 2; % sensor velocity noise strength
gamma = 20; % gate size

% Select Trajectory (USER SELECTION)
% Non-maneuver=1; Break-turn=2; Vertical=3;
91 traj=3;

% Load Truth Data for Program Test
if traj==1
    profile = 'truth_data_below';
96 elseif traj==2
    profile = 'truth_data_ts';
else
    profile = 'truth_data_vert';
end
101 load(['/Users/Nick/Documents/MATLAB/Thesis/Simulation Software/Truth Data/'...
    profile '.mat'])
NT = length(x_true);

% Choose Missile Dynamics Model (USER SELECTION)
106 % Constant Velocity=1; Constant Acceleration=2; Constant Turn=3;
model=3;
if model==1
    % Constant Velocity
    NS = 6; % number of states
111 [phi,Qd,G] = constant_vel(dt,q); % constant velocity
elseif model==2
    % Constant Acceleration Model
    NS = 9; % number of states
116 [phi,Qd,G] = constant_accel(dt,q); % constant acceleration
else
    % Constant Turn Model
    NS = 9; % number of states
end

121 % Initialize Track Variables
x.minus = zeros(NS,NT); % initialize state variable
x.plus = zeros(NS,NT);
P.minus = zeros(NS,NS,NT);
P.plus = zeros(NS,NS,NT);
126 x.out = zeros(NS,2*NT,runs);
P.out = zeros(NS,NS,2*NT,runs);
x.error = zeros(6,2*NT,runs);

% Set Track Initial Covariance Matrix
131 % Uncertainty in Target Handoff - 1 Sigma (USER SELECTION)
x.sig = 15;
y.sig = 15;
z.sig = 45;
vel.sig = 10;
136 if model==1
    % Constant Velocity Model
    Po = [x.sig^2 0 0 0 0 0;
          0 y.sig^2 0 0 0 0;
          0 0 z.sig^2 0 0 0;
141 0 0 0 vel.sig^2 0 0;
          0 0 0 0 vel.sig^2 0;
          0 0 0 0 0 vel.sig^2];
else
    % Constant Accel/3d Coordinated Turn Model
146 Po = [x.sig^2 0 0 0 0 0 0 0 0;
          0 y.sig^2 0 0 0 0 0 0 0;
          0 0 z.sig^2 0 0 0 0 0 0;
          0 0 0 vel.sig^2 0 0 0 0 0;
          0 0 0 0 vel.sig^2 0 0 0 0;
151 0 0 0 0 0 vel.sig^2 0 0 0 0;
          0 0 0 0 0 0 10 0 0;
          0 0 0 0 0 0 0 10 0;
          0 0 0 0 0 0 0 0 10];
end

```

```

156 P_minus(:, :, 1) = Po;
    P_plus(:, :, 1) = Po;

    %% SEED NOISE

161 % Load Default Noise
    if traj==1
        noise_file = 'DefaultNoise1';
    elseif traj==2
        noise_file = 'DefaultNoise2';
166 else
        noise_file = 'DefaultNoise3';
    end
    load(['/Users/Nick/Documents/MATLAB/Thesis/Simulation Software/Generate Measurements/' ...
        noise_file '.mat'])

171 %% SIGMA POINT PARAMETERS

    % Define Sigma Point Parameters
    alpha = 0.1; % changes spread of sigma points
    beta = 2; % tuning parameter (2 for Gaussian)
176 kappa = 0; % secondary tuning parameter (usually 0)
    lambda = alpha^2*(NS+kappa)-NS;
    scaling_value = lambda+NS;
    SP = 2*NS+1; % number of sigma points

181 % Calculate Sigma Point Weights
    % Mean Weights
    Wo_m = lambda/scaling_value;
    Wi_m = 1/(2*scaling_value);
    Wm = [Wo_m Wi_m*ones(1,2*NS)];
186 % Covariance Weights
    Wo_c = lambda/scaling_value+(1-alpha^2+beta);
    Wi_c = Wi_m;
    Wc = [Wo_c Wi_c*ones(1,2*NS)];

191 %% INITIALIZE WAITBAR

    h = waitbar(0, sprintf('%i Runs', runs));

    %% MONTE CARLO RUN

196 tic % start timing
    for index=1:runs

201 waitbar(index/runs, h);

    % Initialize Target State Vector
    x_minus(1:6, 1) = x_true(1:6, 1) + ([x_sig y_sig z_sig vel_sig vel_sig vel_sig]'.*...
        initial_noise(:, index));
    x_plus(:, 1) = x_minus(:, 1);

206 x_out(:, 1, index) = x_minus(:, 1);
    x_out(:, 2, index) = x_plus(:, 1);
    P_out(:, :, 1, index) = P_minus(:, :, 1);
    P_out(:, :, 2, index) = P_plus(:, :, 1);
    x_error(:, 1, index) = x_out(1:6, 1, index) - x_true(:, 1);
211 x_error(:, 2, index) = x_out(1:6, 2, index) - x_true(:, 1);

    % Time Loop
    for i=1:NT-1

216 for ii=1:NumTracks

        if model==3
            % Choose Missile Dynamics Model (USER SELECTION)
            [phi, Qd, G] = constant_turn(dt, q, x_plus(:, ii)); % constant turn model
221 end

        % Time Propagation
        x_minus(:, i+1) = phi*x_plus(:, i);
        P_minus(:, :, i+1) = phi*P_plus(:, :, i)*phi'+Qd;
226

        % Generate Measurements From True State Vector
        [z1, z2, z3, z4, z5, z6, z7, detect] = gen_meas_seed(x_true(1:6, i+1), pos_acft(:, i+1), ...
            vel_acft(:, i+1), roll(i+1), pitch(i+1), yaw(i+1), noise(:, i, index));

        % Define Sensor Noise

```

```

231     R_gate = diag([r_dist; r_vel]);

% Clear Variables
meas = [];
ZSigma = [];

236

% Calculate Sigma Point Locations
x_mean = x_minus(:,i+1);
P_chol = chol(P_minus(:, :, i+1));
XSigma0 = x_mean;
241     XSigmai = x_mean*ones(1,2*NS)+sqrt(scaling_value)*[P_chol -P_chol];
XSigma = [XSigma0 XSigmai];

% Calculate Transformed Sigma Points
% Sensor 1
246     if detect(1)==1
        closest = 10000; % initialize closest to large number
        nearest_meas = []; % clear nearest measurement
        % Convert Sensor 1 Coordinates from Body Frame to Nav Frame
        [p1n] = body_to_nav(pos_acft(:,i+1),roll(i+1),pitch(i+1),yaw(i+1),p1);
251     % Transform Sigma Points Through Nonlinear Function h[.]
        [Update_Sigma] = h.transform(XSigma(1:6,:),p1n,vel_acft(:,i+1));
        % Calculate Measurement Prediction and Residual Uncertainty
        zhat = Wm(1)*Update_Sigma(:,1)+sum(Wm(2)*Update_Sigma(:,2:SP),2);
        dZ = Update_Sigma-zhat*ones(1,SP);
256     P_gate = Wc(1)*dZ(:,1)*dZ(:,1)'+Wc(2)*dZ(:,2:SP)*dZ(:,2:SP)'+R_gate;
        % Perform Gating
        % Define Coarse Square Gate Size
        S = P_gate; % residual covariance
        emax = sqrt(max(eig(gamma*S)));
261     num = size(z1,2); % size of sensor 1 measurement vector
        % Loop For Number of Measurements
        for j=1:num
            residual = (z1(:,j)-zhat); % measurement residual
            % Apply Coarse Square Gate
266             if all(z1(:,j)>(zhat-emax) & z1(:,j)<(zhat+emax))
                % Define Elliptical Gate Size
                d = residual'/S*residual; % residual norm
                % Apply Elliptical Gate
                if d<gamma && d<closest
271                     closest = d;
                    nearest_meas = z1(:,j);
                end
            end
        end
276     % Determine if Any Measurement is Within Gate
        if isempty(nearest_meas)
            % Save Measurement and Update Sigma Points
            meas = [meas; nearest_meas];
            ZSigma = [ZSigma; Update_Sigma];
281     end
end

% Sensor 2
286     if detect(2)==1
        closest = 10000; % initialize closest to large number
        nearest_meas = []; % clear nearest measurement
        % Convert Sensor 2 Coordinates from Body Frame to Nav Frame
        [p2n] = body_to_nav(pos_acft(:,i+1),roll(i+1),pitch(i+1),yaw(i+1),p2);
291     % Transform Sigma Points Through Nonlinear Function h[.]
        [Update_Sigma] = h.transform(XSigma(1:6,:),p2n,vel_acft(:,i+1));
        % Calculate Measurement Prediction and Residual Uncertainty
        zhat = Wm(1)*Update_Sigma(:,1)+sum(Wm(2)*Update_Sigma(:,2:SP),2);
        dZ = Update_Sigma-zhat*ones(1,SP);
296     P_gate = Wc(1)*dZ(:,1)*dZ(:,1)'+Wc(2)*dZ(:,2:SP)*dZ(:,2:SP)'+R_gate;
        % Perform Gating
        % Define Coarse Square Gate Size
        S = P_gate; % residual covariance
        emax = sqrt(max(eig(gamma*S)));
301     num = size(z2,2); % size of sensor 2 measurement vector
        % Loop For Number of Measurements
        for j=1:num
            residual = (z2(:,j)-zhat); % measurement residual
            % Apply Coarse Square Gate
306             if all(z2(:,j)>(zhat-emax) & z2(:,j)<(zhat+emax))
                % Define Elliptical Gate Size
                d = residual'/S*residual; % residual norm
                % Apply Elliptical Gate

```

```

311         if d<gamma && d<closest
                closest = d;
                nearest_meas = z2(:,j);
            end
        end
    end
    % Determine if Any Measurement is Within Gate
316    if ~isempty(nearest_meas)
        % Save Measurement and Update Sigma Points
        meas = [meas; nearest_meas];
        ZSigma = [ZSigma; Update_Sigma];
    end
321    end

% Sensor 3
if detect(3)==1
326    closest = 10000; % initialize closest to large number
        nearest_meas = []; % clear nearest measurement
    % Convert Sensor 3 Coordinates from Body Frame to Nav Frame
    [p3n] = body_to_nav(pos_acft(:,i+1),roll(i+1),pitch(i+1),yaw(i+1),p3);
    % Transform Sigma Points Through Nonlinear Function h[.]
    [Update_Sigma] = h.transform(XSigma(1:6,:),p3n,vel_acft(:,i+1));
331    % Calculate Measurement Prediction and Residual Uncertainty
        zhat = Wm(1)*Update_Sigma(:,1)+sum(Wm(2)*Update_Sigma(:,2:SP),2);
        dZ = Update_Sigma-zhat*ones(1,SP);
        P_gate = Wc(1)*dZ(:,1)*dZ(:,1)'+Wc(2)*dZ(:,2:SP)*dZ(:,2:SP)'+R_gate;
    % Perform Gating
336    % Define Coarse Square Gate Size
        S = P_gate; % residual covariance
        emax = sqrt(max(eig(gamma*S)));
        num = size(z3,2); % size of sensor 3 measurement vector
    % Loop For Number of Measurements
341    for j=1:num
        residual = (z3(:,j)-zhat); % measurement residual
        % Apply Coarse Square Gate
        if all(z3(:,j)>(zhat-emax) & z3(:,j)<(zhat+emax))
            % Define Elliptical Gate Size
346            d = residual'/S*residual; % residual norm
            % Apply Elliptical Gate
            if d<gamma && d<closest
                closest = d;
                nearest_meas = z3(:,j);
351            end
        end
    end
    % Determine if Any Measurement is Within Gate
356    if ~isempty(nearest_meas)
        % Save Measurement and Update Sigma Points
        meas = [meas; nearest_meas];
        ZSigma = [ZSigma; Update_Sigma];
    end
361    end

% Sensor 4
if detect(4)==1
366    closest = 10000; % initialize closest to large number
        nearest_meas = []; % clear nearest measurement
    % Convert Sensor 4 Coordinates from Body Frame to Nav Frame
    [p4n] = body_to_nav(pos_acft(:,i+1),roll(i+1),pitch(i+1),yaw(i+1),p4);
    % Transform Sigma Points Through Nonlinear Function h[.]
    [Update_Sigma] = h.transform(XSigma(1:6,:),p4n,vel_acft(:,i+1));
371    % Calculate Measurement Prediction and Residual Uncertainty
        zhat = Wm(1)*Update_Sigma(:,1)+sum(Wm(2)*Update_Sigma(:,2:SP),2);
        dZ = Update_Sigma-zhat*ones(1,SP);
        P_gate = Wc(1)*dZ(:,1)*dZ(:,1)'+Wc(2)*dZ(:,2:SP)*dZ(:,2:SP)'+R_gate;
    % Perform Gating
376    % Define Coarse Square Gate Size
        S = P_gate; % residual covariance
        emax = sqrt(max(eig(gamma*S)));
        num = size(z4,2); % size of sensor 4 measurement vector
    % Loop For Number of Measurements
381    for j=1:num
        residual = (z4(:,j)-zhat); % measurement residual
        % Apply Coarse Square Gate
        if all(z4(:,j)>(zhat-emax) & z4(:,j)<(zhat+emax))
            % Define Elliptical Gate Size
386            d = residual'/S*residual; % residual norm
            % Apply Elliptical Gate

```

```

        if d<gamma && d<closest
            closest = d;
            nearest_meas = z4(:,j);
        end
    end
391 end
    % Determine if Any Measurement is Within Gate
    if isempty(nearest_meas)
        % Save Measurement and Update Sigma Points
396 meas = [meas; nearest_meas];
        ZSigma = [ZSigma; Update_Sigma];
    end
end

401 % Sensor 5
if detect(5)==1
    closest = 10000; % initialize closest to large number
    nearest_meas = []; % clear nearest measurement
    % Convert Sensor 5 Coordinates from Body Frame to Nav Frame
406 [p5n] = body_to_nav(pos_acft(:,i+1),roll(i+1),pitch(i+1),yaw(i+1),p5);
    % Transform Sigma Points Through Nonlinear Function h[.]
    [Update_Sigma] = h.transform(XSigma(1:6,:),p5n,vel_acft(:,i+1));
    % Calculate Measurement Prediction and Residual Uncertainty
    zhat = Wm(1)*Update_Sigma(:,1)+sum(Wm(2)*Update_Sigma(:,2:SP),2);
411 dZ = Update_Sigma-zhat*ones(1,SP);
    P_gate = Wc(1)*dZ(:,1)*dZ(:,1)'+Wc(2)*dZ(:,2:SP)*dZ(:,2:SP)'+R_gate;
    % Perform Gating
    % Define Coarse Square Gate Size
    S = P_gate; % residual covariance
416 emax = sqrt(max(eig(gamma*S)));
    num = size(z5,2); % size of sensor 5 measurement vector
    % Loop For Number of Measurements
    for j=1:num
        residual = (z5(:,j)-zhat); % measurement residual
421 % Apply Coarse Square Gate
        if all(z5(:,j)>(zhat-emax) & z5(:,j)<(zhat+emax))
            % Define Elliptical Gate Size
            d = residual'/S*residual; % residual norm
            % Apply Elliptical Gate
426 if d<gamma && d<closest
                closest = d;
                nearest_meas = z5(:,j);
            end
        end
    end
431 end
    % Determine if Any Measurement is Within Gate
    if isempty(nearest_meas)
        % Save Measurement and Update Sigma Points
436 meas = [meas; nearest_meas];
        ZSigma = [ZSigma; Update_Sigma];
    end
end

441 % Sensor 6
if detect(6)==1
    closest = 10000; % initialize closest to large number
    nearest_meas = []; % clear nearest measurement
    % Convert Sensor 6 Coordinates from Body Frame to Nav Frame
446 [p6n] = body_to_nav(pos_acft(:,i+1),roll(i+1),pitch(i+1),yaw(i+1),p6);
    % Transform Sigma Points Through Nonlinear Function h[.]
    [Update_Sigma] = h.transform(XSigma(1:6,:),p6n,vel_acft(:,i+1));
    % Calculate Measurement Prediction and Residual Uncertainty
    zhat = Wm(1)*Update_Sigma(:,1)+sum(Wm(2)*Update_Sigma(:,2:SP),2);
451 dZ = Update_Sigma-zhat*ones(1,SP);
    dX = XSigma-x.mean*ones(1,SP);
    P_gate = Wc(1)*dZ(:,1)*dZ(:,1)'+Wc(2)*dZ(:,2:SP)*dZ(:,2:SP)'+R_gate;
    % Perform Gating
    % Define Coarse Square Gate Size
    S = P_gate; % residual covariance
456 emax = sqrt(max(eig(gamma*S)));
    num = size(z6,2); % size of sensor 6 measurement vector
    % Loop For Number of Measurements
    for j=1:num
        residual = (z6(:,j)-zhat); % measurement residual
461 % Apply Coarse Square Gate
        if all(z6(:,j)>(zhat-emax) & z6(:,j)<(zhat+emax))
            % Define Elliptical Gate Size
            d = residual'/S*residual; % residual norm

```

```

466         % Apply Elliptical Gate
         if d<gamma && d<closest
             closest = d;
             nearest_meas = z6(:,j);
         end
     end
471 end
    % Determine if Any Measurement is Within Gate
    if ~isempty(nearest_meas)
        % Save Measurement and Update Sigma Points
476         meas = [meas; nearest_meas];
         ZSigma = [ZSigma; Update.Sigma];
    end
end

% Sensor 7
481 if detect(7)==1
    closest = 10000; % initialize closest to large number
    nearest_meas = []; % clear nearest measurement
    % Convert Sensor 7 Coordinates from Body Frame to Nav Frame
    [p7n] = body_to_nav(pos.acft(:,i+1),roll(i+1),pitch(i+1),yaw(i+1),p7);
486 % Transform Sigma Points Through Nonlinear Function h[.]
    [Update.Sigma] = h.transform(XSigma(1:6,:),p7n,vel.acft(:,i+1));
    % Calculate Measurement Prediction and Residual Uncertainty
    zhat = Wm(1)*Update.Sigma(:,1)+sum(Wm(2)*Update.Sigma(:,2:SP),2);
    dZ = Update.Sigma-zhat*ones(1,SP);
491 dX = XSigma-x.mean*ones(1,SP);
    P_gate = Wc(1)*dZ(:,1)*dZ(:,1)'+Wc(2)*dZ(:,2:SP)*dZ(:,2:SP)'+R_gate;
    % Perform Gating
    % Define Coarse Square Gate Size
496 S = P_gate; % residual covariance
    emax = sqrt(max(eig(gamma*S)));
    num = size(z7,2); % size of sensor 7 measurement vector
    % Loop For Number of Measurements
    for j=1:num
        residual = (z7(:,j)-zhat); % measurement residual
501 % Apply Coarse Square Gate
        if all(z7(:,j)>(zhat-emax) & z7(:,j)<(zhat+emax))
            % Define Elliptical Gate Size
            d = residual'/S*residual; % residual norm
            % Apply Elliptical Gate
506             if d<gamma && d<closest
                 closest = d;
                 nearest_meas = z7(:,j);
             end
        end
    end
511 end
    % Determine if Any Measurement is Within Gate
    if ~isempty(nearest_meas)
        % Save Measurement and Update Sigma Points
516         meas = [meas; nearest_meas];
         ZSigma = [ZSigma; Update.Sigma];
    end
end

if ~isempty(meas)
521 % Sensor Noise
    r = [];
    NM = size(ZSigma,1);
    for iii=1:NM/2
526         r = [r; r_dist; r_vel;];
    end
    R = diag(r);

    % Calculate Measurement Prediction and Residual Uncertainty
531 zhat = Wm(1)*ZSigma(:,1)+sum(Wm(2)*ZSigma(:,2:SP),2);
    dZ = ZSigma-zhat*ones(1,SP);
    dX = XSigma-x.mean*ones(1,SP);
    Pzz = Wc(1)*dZ(:,1)*dZ(:,1)'+Wc(2)*dZ(:,2:SP)*dZ(:,2:SP)'+R;
    Pxz = Wc(1)*dX(:,1)*dZ(:,1)'+Wc(2)*dX(:,2:SP)*dZ(:,2:SP)';

536 % Measurement Update
    K = Pxz/Pzz; % kalman gain
    x_plus(:,i+1) = x_minus(:,i+1)+K*(meas-zhat);
    P_plus(:,i+1) = P_minus(:,i+1)-K*Pzz*K';
541 else
    x_plus(:,i+1) = x_minus(:,i+1);
    P_plus(:,i+1) = P_minus(:,i+1);
end

```

```

        end

        % Save Output Data
546     x_out(:,2*i+1,index) = x_minus(:,i+1);
        x_out(:,2*i+2,index) = x_plus(:,i+1);
        P_out(:, :, 2*i+1,index) = P_minus(:, :, i+1);
        P_out(:, :, 2*i+2,index) = P_plus(:, :, i+1);

551     % Calculate Error
        x_error(:,2*i+1,index) = x_out(1:6,2*i+1,index)-x_true(:,i+1);
        x_error(:,2*i+2,index) = x_out(1:6,2*i+2,index)-x_true(:,i+1);

    end
556 end

    end
    toc % stop timing

561 %% PLOT RESULTS

    % Define Output Time Vector
    t_out = zeros(2*NT,1);
    t_out(1:2:2*NT) = t;
566 t_out(2:2:2*NT) = t;
    t_final = max(t_out);

    % Define Plot Axes and Save Filenames
    if traj==1 % non-maneuvering
571     traj_axis = [-1500 1500 0000 3000 0 5000];
        pos_axis = [0 0.45 -50 50];
        vel_axis = [0 0.45 -40 40];
        RMS_axis = [0 0.45 0 50];
    elseif traj==2 % break-turn
576     traj_axis = [-200 1000 -2000 2000 3500 5000];
        pos_axis = [0 0.4 -50 50];
        vel_axis = [0 0.4 -100 100];
        RMS_axis = [0 0.4 0 50];
    else % vertical man
581     traj_axis = [-1000 1000 -3000 1000 5000 5500];
        pos_axis = [0 0.39 -50 50];
        vel_axis = [0 0.39 -100 100];
        RMS_axis = [0 0.39 0 50];
    end

586 % Plot Sample 3D Trajectory
    figure(1)
    plot3(acft(2,1), acft(1,1), -acft(3,1), 'bo')
    hold on
591 plot3(acft(2,:), acft(1,:), -acft(3,:), 'b')
    plot3(x_msl(2,1), x_msl(1,2), -x_msl(3,3), 'ks')
    plot3(x_msl(2,:), x_msl(1,:), -x_msl(3,:), 'k-')
    plot3(x_out(2,:,1), x_out(1,:,1), -x_out(3,:,1), 'r.')
    ylabel('North(+)/South(-) (m)')
596 xlabel('East(+)/West(-) (m)')
    zlabel('Altitude (m)')
    legend('Aircraft Start Position', 'Aircraft Trajectory', 'Missile Start Position'...
        , 'Missile True Trajectory', 'Missile Estimate', 'Location', 'West')
    axis(traj_axis)
601 grid on
    hold off

    % Plot Mean State Errors
    x_error_mean = mean(x_error,3);
606 x_error_std = std(x_error,0,3);

    % Position Error
    sigma_plot = P_out(1,1,:,1);
    figure(2)
611 subplot(3,1,1)
    plot(t_out, x_error_mean(1,:), 'k', t_out, x_error_mean(1,:)+x_error_std(1,:), 'b-', ...
        t_out, x_error_mean(1,:)-x_error_std(1,:), 'b-')
    % title(sprintf('Missile Mean Position Error and Standard Deviation(%i Runs)', runs))
    ylabel('x error (m)')
616 axis(pos_axis)
    subplot(3,1,2)
    plot(t_out, x_error_mean(2,:), 'k', t_out, x_error_mean(2,:)+x_error_std(2,:), 'b-', ...
        t_out, x_error_mean(2,:)-x_error_std(2,:), 'b-');
    ylabel('y error (m)')

```

```

621 axis(pos_axis)
    subplot(3,1,3)
    plot(t_out,x_error_mean(3,:), 'k', t_out, x_error_mean(3,:)+x_error_std(3,:), 'b—', ...
         t_out, x_error_mean(3,:)-x_error_std(3,:), 'b—');
    ylabel('z error (m)')
626 xlabel('time (s)')
    axis(pos_axis)

    % Velocity Error
    figure(3)
631 subplot(3,1,1)
    plot(t_out,x_error_mean(4,:), 'k', t_out, x_error_mean(4,:)+x_error_std(4,:), 'b—', ...
         t_out, x_error_mean(4,:)-x_error_std(4,:), 'b—');
    % title(sprintf('Missile Mean Velocity Error and Standard Deviation(%i Runs)', runs))
    ylabel('vx error (m/s)')
636 axis(vel_axis)
    subplot(3,1,2)
    plot(t_out,x_error_mean(5,:), 'k', t_out, x_error_mean(5,:)+x_error_std(5,:), 'b—', ...
         t_out, x_error_mean(5,:)-x_error_std(5,:), 'b—');
    ylabel('vy error (m/s)')
641 axis(vel_axis)
    subplot(3,1,3)
    plot(t_out,x_error_mean(6,:), 'k', t_out, x_error_mean(6,:)+x_error_std(6,:), 'b—', ...
         t_out, x_error_mean(6,:)-x_error_std(6,:), 'b—');
    ylabel('vz error (m/s)')
646 xlabel('time (s)')
    axis(vel_axis)

    % Plot RMS Error
    RMS_error = sqrt(sum((x_true(1:3,:)-x_plus(1:3,:)).^2,1));
651 figure(4)
    plot(t,RMS_error)
    % title('Missile Position Root-Sum-Squared Error (1 Run)')
    ylabel('position error (m)')
    xlabel('time (s)')
656 axis(RMS_axis)

    % Calculate Mean Error and Standard Deviation at Impact
    final_error_mean = x_error_mean(:,2*NT);
    final_error_std = x_error_std(:,2*NT);

661 % Categorize Filemanes by Model (CV,CA,CT)
    if model==1
        name2 = '_CV';
    elseif model==2
666 name2 = '_CA';
    else
        name2 = '_CT';
    end

671 % Save Plots to Desired Directory
    save(['/Users/Nick/Documents/LaTex/My_Thesis/Plots/' 'traj' num2str(traj) name2 '_UKF' ...
         '.mat'],'final_error_mean','final_error_std')
    print(1, '-dpdf', ['/Users/Nick/Documents/LaTex/My_Thesis/Plots/' 'traj' num2str(traj) ...
                    name2 '_UKF'])
    print(2, '-dpdf', ['/Users/Nick/Documents/LaTex/My_Thesis/Plots/' 'pos' num2str(traj) ...
                    name2 '_UKF'])
    print(3, '-dpdf', ['/Users/Nick/Documents/LaTex/My_Thesis/Plots/' 'vel' num2str(traj) ...
                    name2 '_UKF'])
676 print(4, '-dpdf', ['/Users/Nick/Documents/LaTex/My_Thesis/Plots/' 'rms' num2str(traj) ...
                    name2 '_UKF'])

    close(h)

```

## Listing C.3: Particle Filter Main Program

```

%%%%%%%%%%%%%%%%%%%%%%%%%%%%%%%%%%%%%%%%%%%%%%%%%%%%%%%%%%%%%%%%%%%%%%%%
2 % Title: Missile Air-to-Air Trajectory Reconstruction (Particle Filter)
  % Author: Maj Nick Sweeney
  % Date: 5 Sep 2010
  %
7 % Description: This program reconstructs a missile air-to-air trajectory
  % relative to a target aircraft. The intent is to evaluate the missile's
  % performance in intercepting the aircraft. A Particle Filter
  % is used to perform the estimation. One of 3 missile dynamics model
  % is available for selection: constant velocity, constant acceleration
12 % and constant 3D coordinated turn. The observation model utilizes
  % 7 Frequency Modulated Continuous Wave (FMCW) radar sensors mounted on
  % the aircraft to provide range and range-rate of the target. The sensors
  % are distributed to provide spherical coverage around the aircraft with
  % 2 sensors on the nose, 2 sensors on each wingtip and 1 sensor on the
  % tail.
17 %
  % Inputs: truth_data_xxx.mat: (truth data file includes:)
  %         t: time vector
  %         dt: time step
  %         x_true(6xt): missile true state vector (position & velocity)
22 %         pos_acft(3xt): drone aircraft true position
  %         vel_acft(3xt): drone aircraft true velocity
  %         roll(1xt): drone aircraft roll in radians
  %         pitch(1xt): drone aircraft pitch in radians
  %         yaw(1xt); drone aircraft yaw in radians (referenced to north)
27 %
  % Outputs: x_out(6xtxRuns): missile's estimated state vector
  %          P_out(6x6xtxRuns): uncertainty in missile's state vector
  %          x_error(6xtxRuns): error in estimated missile state vector
  %
32 % Subprograms: gen_meas_seed: generates simulated sensor measurements
  %              along with clutter
  %              body_to_nav: translates sensor position from aircraft
  %              body frame to navigation frame
  %              h_transform: transforms particles through nonlinear
37 %              observation function
  %              resample_particles: performs particle resampling
  %
  % User Selectable Parameters (in order):
  % number of Monte Carlo runs (runs)
42 % number of particles (NP): determines particles used in filter
  % dynamics noise parameter(q): uncertainty in dynamics model
  % sensor range noise (r_dist): uncertainty in sensor range
  % sensor velocity noise (r_vel): uncertainty in sensor range-rate
  % gate size (gamma)
47 % trajectory(traj): changes truth data file and configures plots
  % dynamics model (model): constant_velocity, constant_acceleration,
  % constant_turn (all subprograms)
  % uncertainty in target handoff (x_sig, y_sig, z_sig, vel_sig)
  %
52 % Notes: All inputs/outputs in local level Earth-centered navigation frame
  %         All units in metric (meters, meters/sec)
  %
  % Documentation: Refereced Matlab code from Lt Col Veth's (AFIT/ENG)
  %                 EENG 766 Stochastics II Proj 3. Lines 487-500 taken
57 %                 from his algorithm.
%%%%%%%%%%%%%%%%%%%%%%%%%%%%%%%%%%%%%%%%%%%%%%%%%%%%%%%%%%%%%%%%%%%%%%%%

clf
clear all
62 %% SENSOR LOCATIONS

% Define Sensor Locations (body frame)
% Sensor 1 - Aircraft Nose (top)
67 p1 = [8; 0; -0.5];
% Sensor 2 - Aircraft Nose (bottom)
p2 = [8; 0; 0.5];
% Sensor 3 - Aircraft Left Wing (top)
p3 = [0; -5; 0];
72 % Sensor 4 - Aircraft Left Wing (bottom)
p4 = [0; -5; 0.1];
% Sensor 5 - Aircraft Right Wing (top)
p5 = [0; 5; 0];
% Sensor 6 - Aircraft Right Wing (bottom)
77 p6 = [0; 5; 0.1];

```

```

% Sensor 7 – Aircraft Tail (omni-directional)
p7 = [-8; 0; -1];

%% USER SELECTIONS
82 % Determine Number of Monte Carlo Runs (USER SELECTION)
runs = 100;

% Define Gating and Tracks (USER SELECTION)
87 NumTracks = 1; % only 1 target

% Choose Number of Particles (USER SELECTION)
NP = 50000;

92 % Define Noise Strength and Gating (USER SELECTION/TUNING PARAMETER)
q = 800000; % dynamics noise strength
r.dist = 20; % sensor distance noise strength
r.vel = 20; % sensor velocity noise strength
gamma = 20; % gate size

97 % Select Trajectory (USER SELECTION)
% Non-maneuver=1; Break-turn=2; Vertical=3;
traj=3;

102 % Load Truth Data for Program Test
if traj==1
    profile = 'truth.data_below';
elseif traj==2
    profile = 'truth.data_ts';
107 else
    profile = 'truth.data_vert';
end
load(['/Users/Nick/Documents/MATLAB/Thesis/Simulation Software/Truth Data/'...
    profile '.mat'])
112 NT = length(x_true);

% Choose Missile Dynamics Model (USER SELECTION)
% Constant Velocity=1; Constant Acceleration=2; Constant Turn=3;
model=3;
117 if model==1
    % Constant Velocity
    NS = 6; % number of states
    [phi,Qd,G] = constant_vel(dt,q); % constant velocity
elseif model==2
122 % Constant Acceleration Model
    NS = 9; % number of states
    [phi,Qd,G] = constant_accel(dt,q); % constant acceleration
else
    % Constant Turn Model
127 NS = 9; % number of states
end

% Initialize Track Variables
x_minus = zeros(NS,NT); % initialize state variable
132 x_plus = zeros(NS,NT);
P_minus = zeros(NS,NS,NT);
P_plus = zeros(NS,NS,NT);
x_out = zeros(NS,2*NT,runs);
P_out = zeros(NS,NS,2*NT,runs);
137 x_error = zeros(6,2*NT,runs);

% Set Track Initial Covariance Matrix
% Uncertainty in Target Handoff – 1 Sigma (USER SELECTION)
x_sig = 15;
142 y_sig = 15;
z_sig = 45;
vel_sig = 10;
if model==1
    % Constant Velocity Model
147 Po = [x_sig^2 0 0 0 0 0;
        0 y_sig^2 0 0 0 0;
        0 0 z_sig^2 0 0 0;
        0 0 0 vel_sig^2 0 0;
        0 0 0 0 vel_sig^2 0;
        0 0 0 0 0 vel_sig^2];
152 else
    % Constant Accel/3d Coordinated Turn Model
    Po = [x_sig^2 0 0 0 0 0 0 0 0;

```

```

0      y_sig^2 0      0      0      0      0      0 0 0;
157    0      0      z_sig^2 0      0      0      0      0 0 0;
0      0      0      vel_sig^2 0      0      0      0 0 0;
0      0      0      0      vel_sig^2 0      0      0 0 0;
0      0      0      0      0      vel_sig^2 0 0 0 0;
0      0      0      0      0      0      10 0 0;
162    0      0      0      0      0      0      0 10 0;
0      0      0      0      0      0      0 0 10];
end
P_minus(:,:,1) = Po;
P_plus(:,:,1) = Po;
167    %% SEED NOISE

% Load Default Noise
if traj==1
172    noise_file = 'DefaultNoise1';
elseif traj==2
    noise_file = 'DefaultNoise2';
else
    noise_file = 'DefaultNoise3';
177 end
load(['\Users\Nick\Documents\MATLAB\Thesis\Simulation Software\Generate Measurements/' ...
    noise_file '.mat'])

%% INITIALIZE WAITBAR
182 h = waitbar(0,sprintf('%i Runs',runs));

%% MONTE CARLO RUN

tic % start timing
187 for index=1:runs

    waitbar(index/runs,h);

% Initialize Target State Vector
192 % Uncertainty in Target Handoff
x_minus(1:6,1) = x_true(1:6,1)+([x_sig y_sig z_sig vel_sig vel_sig vel_sig]'.*...
    initial_noise(:,index));
x_plus(:,1) = x_minus(:,1);

x_out(:,1,index) = x_minus(:,1);
197 x_out(:,2,index) = x_plus(:,1);
P_out(:,:,1,index) = P_minus(:,:,1);
P_out(:,:,2,index) = P_plus(:,:,1);
x_error(:,1,index) = x_out(1:6,1,index)-x_true(:,1);
x_error(:,2,index) = x_out(1:6,2,index)-x_true(:,1);
202

% Define Initial Particle Location
x_mean = x_minus(:,1);
Po_sqrt = chol(Po);
XParticle_plus = x_mean*ones(1,NP)+Po_sqrt.*randn(NS,NP);
207

% Define Initial Particle Weights
W = (1/NP)*ones(1,NP);

% Time Loop
212 for i=1:NT-1

    for ii=1:NumTracks

        if model==3
17    % Choose Missile Dynamics Model (USER SELECTION)
            [phi,Qd,G] = constant_turn(dt,q,x_plus(:,i)); % constant turn model
        end

% Time Propagation
222 % Define Random Noise Kick (wk)
wk = chol(Qd).*randn(NS,NP);
% Determine apriori estimate and uncertainty
XParticle_minus = phi*XParticle_plus+wk;
W_matrix = ones(NS,1)*W;
227 x_minus(:,i+1) = sum(W_matrix.*XParticle_minus,2);
xhat_matrix = x_minus(:,i+1)*ones(1,NP);
P_minus(:,:,i+1) = particle_cov(XParticle_minus,W',x_minus(:,i+1));

% Generate Measurements From True State Vector

```

```

232     [z1,z2,z3,z4,z5,z6,z7,detect] = gen_meas_seed(x_true(1:6,i+1),pos_acft(:,i+1),...
        vel_acft(:,i+1),roll(i+1),pitch(i+1),yaw(i+1),noise(:,i,index));

% Define Sensor Noise
R_gate = diag([r_dist; r_vel]);

237 % Clear Variables
meas = [];
ZParticle = [];
P_gate = zeros(2,2);

242 % Calculate Transformed Particles
% Sensor 1
if detect(1)==1
    closest = 10000;           % initialize closest to large number
    nearest_meas = [];       % clear nearest measurement
247 % Convert Sensor 1 Coordinates from Body Frame to Nav Frame
    [p1n] = body_to_nav(pos_acft(:,i+1),roll(i+1),pitch(i+1),yaw(i+1),p1);
% Transform Particles Through Nonlinear Function h[.]
    [Update_Particle] = h_transform(XParticle_minus(1:6,:),p1n,vel_acft(:,i+1))...
        ;
% Calculate Measurement Prediction and Residual Uncertainty
252 W_matrix = ones(2,1)*W;
    zhat = sum(W_matrix.*Update_Particle,2);
    dZ = Update_Particle-zhat*ones(1,NP);
    P_gate = (W_matrix.*dZ)*dZ'+R_gate;
% Perform Gating
% Define Coarse Square Gate Size
S = P_gate;           % residual covariance
257 emax = sqrt(max(eig(gamma*S)));
    num = size(z1,2); % size of sensor 1 measurement vector
% Loop For Number of Measurements
262 for j=1:num
    residual = (z1(:,j)-zhat); % measurement residual
    % Apply Coarse Square Gate
    if all(z1(:,j)>(zhat-emax) & z1(:,j)<(zhat+emax))
        % Define Elliptical Gate Size
267 d = residual'/S*residual; % residual norm
        % Apply Elliptical Gate
        if d<gamma && d<closest
            closest = d;
            nearest_meas = z1(:,j);
272        end
    end
end
% Determine if Any Measurement is Within Gate
277 if ~isempty(nearest_meas)
    % Save Measurement and Update Particles
    meas = [meas; nearest_meas];
    ZParticle = [ZParticle; Update_Particle];
end
end

282 % Sensor 2
if detect(2)==1
    closest = 10000;           % initialize closest to large number
    nearest_meas = [];       % clear nearest measurement
287 % Convert Sensor 2 Coordinates from Body Frame to Nav Frame
    [p2n] = body_to_nav(pos_acft(:,i+1),roll(i+1),pitch(i+1),yaw(i+1),p2);
% Transform Particles Through Nonlinear Function h[.]
    [Update_Particle] = h_transform(XParticle_minus(1:6,:),p2n,vel_acft(:,i+1))...
        ;
% Calculate Measurement Prediction and Residual Uncertainty
292 W_matrix = ones(2,1)*W;
    zhat = sum(W_matrix.*Update_Particle,2);
    dZ = Update_Particle-zhat*ones(1,NP);
    P_gate = (W_matrix.*dZ)*dZ'+R_gate;
% Perform Gating
% Define Coarse Square Gate Size
S = P_gate;           % residual covariance
297 emax = sqrt(max(eig(gamma*S)));
    num = size(z2,2); % size of sensor 2 measurement vector
% Loop For Number of Measurements
302 for j=1:num
    residual = (z2(:,j)-zhat); % measurement residual
    % Apply Coarse Square Gate
    if all(z2(:,j)>(zhat-emax) & z2(:,j)<(zhat+emax))
        % Define Elliptical Gate Size

```

```

307         d = residual'/S*residual; % residual norm
           % Apply Elliptical Gate
           if d<gamma && d<closest
312             closest = d;
             nearest_meas = z2(:,j);
           end
         end
       end
       % Determine if Any Measurement is Within Gate
       if ~isempty(nearest_meas)
317         % Save Measurement and Update Particles
           meas = [meas; nearest_meas];
           ZParticle = [ZParticle; Update_Particle];
       end
     end
322   end

   % Sensor 3
   if detect(3)==1
327     closest = 10000; % initialize closest to large number
     nearest_meas = []; % clear nearest measurement
     % Convert Sensor 3 Coordinates from Body Frame to Nav Frame
     [p3n] = body_to_nav(pos_acft(:,i+1),roll(i+1),pitch(i+1),yaw(i+1),p3);
     % Transform Particles Through Nonlinear Function h[.]
     [Update_Particle] = h_transform(XParticle_minus(1:6,:),p3n,vel_acft(:,i+1))...
       ;
332     % Calculate Measurement Prediction and Residual Uncertainty
     W_matrix = ones(2,1)*W;
     zhat = sum(W_matrix.*Update_Particle,2);
     dZ = Update_Particle-zhat*ones(1,NP);
     P_gate = (W_matrix.*dZ)*dZ'+R_gate;
337     % Perform Gating
     % Define Coarse Square Gate Size
     S = P_gate; % residual covariance
     emax = sqrt(max(eig(gamma*S)));
     num = size(z3,2); % size of sensor 3 measurement vector
     % Loop For Number of Measurements
342     for j=1:num
         residual = (z3(:,j)-zhat); % measurement residual
         % Apply Coarse Square Gate
         if all(z3(:,j)>(zhat-emax) & z3(:,j)<(zhat+emax))
347             % Define Elliptical Gate Size
                 d = residual'/S*residual; % residual norm
                 % Apply Elliptical Gate
                 if d<gamma && d<closest
352                     closest = d;
                     nearest_meas = z3(:,j);
                 end
             end
         end
       end
       % Determine if Any Measurement is Within Gate
       if ~isempty(nearest_meas)
357         % Save Measurement and Update Particles
           meas = [meas; nearest_meas];
           ZParticle = [ZParticle; Update_Particle];
       end
     end
362   end

   % Sensor 4
   if detect(4)==1
367     closest = 10000; % initialize closest to large number
     nearest_meas = []; % clear nearest measurement
     % Convert Sensor 4 Coordinates from Body Frame to Nav Frame
     [p4n] = body_to_nav(pos_acft(:,i+1),roll(i+1),pitch(i+1),yaw(i+1),p4);
     % Transform Particles Through Nonlinear Function h[.]
     [Update_Particle] = h_transform(XParticle_minus(1:6,:),p4n,vel_acft(:,i+1))...
       ;
372     % Calculate Measurement Prediction and Residual Uncertainty
     W_matrix = ones(2,1)*W;
     zhat = sum(W_matrix.*Update_Particle,2);
     dZ = Update_Particle-zhat*ones(1,NP);
     P_gate = (W_matrix.*dZ)*dZ'+R_gate;
377     % Perform Gating
     % Define Coarse Square Gate Size
     S = P_gate; % residual covariance
     emax = sqrt(max(eig(gamma*S)));
     num = size(z4,2); % size of sensor 4 measurement vector
     % Loop For Number of Measurements
382     for j=1:num

```

```

    residual = (z4(:,j)-zhat); % measurement residual
    % Apply Coarse Square Gate
    if all(z4(:,j)>(zhat-emax) & z4(:,j)<(zhat+emax))
    % Define Elliptical Gate Size
387     d = residual'/S*residual; % residual norm
    % Apply Elliptical Gate
    if d<gamma && d<closest
        closest = d;
        nearest_meas = z4(:,j);
392     end
    end
end
% Determine if Any Measurement is Within Gate
397 if ~isempty(nearest_meas)
    % Save Measurement and Update Particles
    meas = [meas; nearest_meas];
    ZParticle = [ZParticle; Update.Particle];
end
end
402 % Sensor 5
if detect(5)==1
    closest = 10000; % initialize closest to large number
    nearest_meas = []; % clear nearest measurement
407 % Convert Sensor 5 Coordinates from Body Frame to Nav Frame
    [p5n] = body_to_nav(pos_acft(:,i+1),roll(i+1),pitch(i+1),yaw(i+1),p5);
    % Transform Particles Through Nonlinear Function h[.]
    [Update.Particle] = h.transform(XParticle_minus(1:6,:),p5n,vel_acft(:,i+1))...
    ;
    % Calculate Measurement Prediction and Residual Uncertainty
412 W_matrix = ones(2,1)*W;
    zhat = sum(W_matrix.*Update.Particle,2);
    dZ = Update.Particle-zhat*ones(1,NP);
    P_gate = (W_matrix.*dZ)*dZ'+R_gate;
417 % Perform Gating
    % Define Coarse Square Gate Size
    S = P_gate; % residual covariance
    emax = sqrt(max(eig(gamma*S)));
    num = size(z5,2); % size of sensor 5 measurement vector
    % Loop For Number of Measurements
422 for j=1:num
        residual = (z5(:,j)-zhat); % measurement residual
        % Apply Coarse Square Gate
        if all(z5(:,j)>(zhat-emax) & z5(:,j)<(zhat+emax))
        % Define Elliptical Gate Size
427     d = residual'/S*residual; % residual norm
        % Apply Elliptical Gate
        if d<gamma && d<closest
            closest = d;
            nearest_meas = z5(:,j);
432     end
        end
    end
end
% Determine if Any Measurement is Within Gate
437 if ~isempty(nearest_meas)
    % Save Measurement and Update Particles
    meas = [meas; nearest_meas];
    ZParticle = [ZParticle; Update.Particle];
end
end
442 % Sensor 6
if detect(6)==1
    closest = 10000; % initialize closest to large number
    nearest_meas = []; % clear nearest measurement
447 % Convert Sensor 6 Coordinates from Body Frame to Nav Frame
    [p6n] = body_to_nav(pos_acft(:,i+1),roll(i+1),pitch(i+1),yaw(i+1),p6);
    % Transform Particles Through Nonlinear Function h[.]
    [Update.Particle] = h.transform(XParticle_minus(1:6,:),p6n,vel_acft(:,i+1))...
    ;
    % Calculate Measurement Prediction and Residual Uncertainty
452 W_matrix = ones(2,1)*W;
    zhat = sum(W_matrix.*Update.Particle,2);
    dZ = Update.Particle-zhat*ones(1,NP);
    P_gate = (W_matrix.*dZ)*dZ'+R_gate;
457 % Perform Gating
    % Define Coarse Square Gate Size
    S = P_gate; % residual covariance

```

```

    emax = sqrt(max(eig(gamma*S)));
    num = size(z6,2); % size of sensor 6 measurement vector
    % Loop For Number of Measurements
462 for j=1:num
        residual = (z6(:,j)-zhat); % measurement residual
        % Apply Coarse Square Gate
        if all(z6(:,j)>(zhat-emax) & z6(:,j)<(zhat+emax))
            % Define Elliptical Gate Size
467         d = residual'/S*residual; % residual norm
            % Apply Elliptical Gate
            if d<gamma && d<closest
                closest = d;
                nearest_meas = z6(:,j);
472         end
            end
        end
    end
    % Determine if Any Measurement is Within Gate
    if ~isempty(nearest_meas)
477     % Save Measurement and Update Particles
        meas = [meas; nearest_meas];
        ZParticle = [ZParticle; Update.Particle];
    end
end
482
% Sensor 7
if detect(7)==1
    closest = 10000; % initialize closest to large number
    nearest_meas = []; % clear nearest measurement
487 % Convert Sensor 7 Coordinates from Body Frame to Nav Frame
    [p7n] = body_to_nav(pos_acft(:,i+1),roll(i+1),pitch(i+1),yaw(i+1),p7);
    % Transform Particles Through Nonlinear Function h[.]
    [Update.Particle] = h_transform(XParticle_minus(1:6,:),p7n,vel_acft(:,i+1))...
    ;
    % Calculate Measurement Prediction and Residual Uncertainty
492 W_matrix = ones(2,1)*W;
    zhat = sum(W_matrix.*Update.Particle,2);
    dZ = Update.Particle-zhat*ones(1,NP);
    P_gate = (W_matrix.*dZ)*dZ'+R_gate;
    % Perform Gating
497 % Define Coarse Square Gate Size
    S = P_gate; % residual covariance
    emax = sqrt(max(eig(gamma*S)));
    num = size(z7,2); % size of sensor 7 measurement vector
    % Loop For Number of Measurements
502 for j=1:num
        residual = (z7(:,j)-zhat); % measurement residual
        % Apply Coarse Square Gate
        if all(z7(:,j)>(zhat-emax) & z7(:,j)<(zhat+emax))
            % Define Elliptical Gate Size
507         d = residual'/S*residual; % residual norm
            % Apply Elliptical Gate
            if d<gamma && d<closest
                closest = d;
                nearest_meas = z7(:,j);
512         end
            end
        end
    end
    % Determine if Any Measurement is Within Gate
    if ~isempty(nearest_meas)
517     % Save Measurement and Update Particles
        meas = [meas; nearest_meas];
        ZParticle = [ZParticle; Update.Particle];
    end
end
522
if ~isempty(meas)
    % Sensor Noise
    r = [];
    NM = size(ZParticle,1);
527 for iii=1:NM/2
        r = [r; r_dist; r_vel;];
    end
    R = diag(r);
532
    % Calculate Residual of Each Particle
    residual_p = meas*ones(1,NP)-ZParticle;

    % Calculate Likelihood of the Residual

```

```

Rinv = inv(R);
537 T = chol(Rinv); % build a transform to diagonalize measurement covar
rT = T*residual.p;% transform the measurement residuals
% Sum the likelihood from each measurement
D = zeros(NP,1);
542 for jj=1:NM
D = D + (rT(jj,:)).^2;
end
Likelihood = exp(-.5*D)';

% Update Weights Based on Particle Likelihood
547 W = W.*Likelihood;
W = W/sum(W); % normalize

% Update Particles
552 XParticle_plus = XParticle_minus;

% Resampling
[XParticle_plus,W]=resample_particles(XParticle_plus,W');
W = W';

557 % Measurement Update
% Determine aposteriori estimate and uncertainty
W_matrix = ones(NS,1)*W;
x_plus(:,i+1) = sum(W_matrix.*XParticle_plus,2);
xhat_matrix = x_minus(:,i+1)*ones(1,NP);
562 P_plus(:, :, i+1) = particle_cov(XParticle_plus,W', x_plus(:,i+1));
else
x_plus(:,i+1) = x_minus(:,i+1);
P_plus(:, :, i+1) = P_minus(:, :, i+1);
567 end

% Save Output Data
x_out(:,2*i+1,index) = x_minus(:,i+1);
x_out(:,2*i+2,index) = x_plus(:,i+1);
P_out(:, :, 2*i+1,index) = P_minus(:, :, i+1);
572 P_out(:, :, 2*i+2,index) = P_plus(:, :, i+1);

% Calculate Error
x_error(:,2*i+1,index) = x_out(1:6,2*i+1,index)-x_true(:,i+1);
x_error(:,2*i+2,index) = x_out(1:6,2*i+2,index)-x_true(:,i+1);
577 end
end
end
582 toc % stop timing

%% PLOT RESULTS

% Define Output Time Vector
587 t_out = zeros(2*NT,1);
t_out(1:2:2*NT) = t;
t_out(2:2:2*NT) = t;
t_final = max(t_out);

592 % Define Plot Axes and Save Filenames
if traj==1 % non-maneuvering
traj_axis = [-1500 1500 0000 3000 0 5000];
pos_axis = [0 0.45 -50 50];
597 vel_axis = [0 0.45 -40 40];
RMS_axis = [0 0.45 0 50];
elseif traj==2 % break turn
traj_axis = [-200 1000 -2000 2000 3500 5000];
pos_axis = [0 0.4 -50 50];
602 vel_axis = [0 0.4 -100 100];
RMS_axis = [0 0.4 0 50];
else % vertical man
traj_axis = [-1000 1000 -3000 1000 5000 5500];
pos_axis = [0 0.39 -50 50];
607 vel_axis = [0 0.39 -100 100];
RMS_axis = [0 0.39 0 50];
end

% Plot Sample 3D Trajectory
figure(1)
612 plot3(acft(2,1),acft(1,1),-acft(3,1),'bo')
hold on

```

```

plot3(acft(2,:),acft(1,:),-acft(3,:), 'b')
plot3(x_msl(2,1),x_msl(1,2),-x_msl(3,3), 'ks')
plot3(x_msl(2,:),x_msl(1,:),-x_msl(3,:), 'k—')
617 plot3(x_out(2,:),1,x_out(1,:),1,-x_out(3,:),1), 'r.')
    ylabel('North(+)/South(-) (m)')
    xlabel('East(+)/West(-) (m)')
    zlabel('Altitude (m)')
    legend('Aircraft Start Position','Aircraft Trajectory','Missile Start Position'...
622     , 'Missile True Trajectory','Missile Estimate','Location','West')
    axis(traj_axis)
    grid on
    hold off

627 % Plot Mean State Errors
    x_error_mean = mean(x_error,3);
    x_error_std = std(x_error,0,3);

    % Position Error
632 sigma_plot = P_out(1,1,:,1);
    figure(2)
    subplot(3,1,1)
    plot(t_out,x_error_mean(1,:), 'k',t_out,x_error_mean(1,:)+x_error_std(1,:), 'b—', ...
         t_out,x_error_mean(1,:)-x_error_std(1,:), 'b—')
637 % title(sprintf('Missile Mean Position Error and Standard Deviation(%i Runs)',runs))
    ylabel('x error (m)')
    axis(pos_axis)
    subplot(3,1,2)
    plot(t_out,x_error_mean(2,:), 'k',t_out,x_error_mean(2,:)+x_error_std(2,:), 'b—', ...
         t_out,x_error_mean(2,:)-x_error_std(2,:), 'b—');
642 ylabel('y error (m)')
    axis(pos_axis)
    subplot(3,1,3)
    plot(t_out,x_error_mean(3,:), 'k',t_out,x_error_mean(3,:)+x_error_std(3,:), 'b—', ...
         t_out,x_error_mean(3,:)-x_error_std(3,:), 'b—');
647 ylabel('z error (m)')
    xlabel('time (s)')
    axis(pos_axis)

652 % Velocity Error
    figure(3)
    subplot(3,1,1)
    plot(t_out,x_error_mean(4,:), 'k',t_out,x_error_mean(4,:)+x_error_std(4,:), 'b—', ...
         t_out,x_error_mean(4,:)-x_error_std(4,:), 'b—');
657 % title(sprintf('Missile Mean Velocity Error and Standard Deviation(%i Runs)',runs))
    ylabel('vx error (m/s)')
    axis(vel_axis)
    subplot(3,1,2)
    plot(t_out,x_error_mean(5,:), 'k',t_out,x_error_mean(5,:)+x_error_std(5,:), 'b—', ...
         t_out,x_error_mean(5,:)-x_error_std(5,:), 'b—');
662 ylabel('vy error (m/s)')
    axis(vel_axis)
    subplot(3,1,3)
    plot(t_out,x_error_mean(6,:), 'k',t_out,x_error_mean(6,:)+x_error_std(6,:), 'b—', ...
         t_out,x_error_mean(6,:)-x_error_std(6,:), 'b—');
667 ylabel('vz error (m/s)')
    xlabel('time (s)')
    axis(vel_axis)

672 % Plot RMS Error
    RMS_error = sqrt(sum((x_true(1:3,:)-x_plus(1:3,:)).^2,1));
    figure(4)
    plot(t,RMS_error)
    % title('Missile Position Root-Sum-Squared Error (1 Run)')
677 ylabel('position error (m)')
    xlabel('time (s)')
    axis(RMS_axis)

    % Calculate Mean Error and Standard Deviation at Impact
682 final_error_mean = x_error.mean(:,2*NT);
    final_error_std = x_error_std(:,2*NT);

    % Categorize Filemanes by Model (CV,CA,CT)
    if model==1
687     name2 = '_CV';
    elseif model==2
        name2 = '_CA';
    else
        name2 = '_CT';
    end

```

```
692 end

% Save Plots to Desired Directory
save(['/Users/Nick/Documents/LaTeX/My-Thesis/Plots/' 'traj' num2str(traj) name2 '_PF' '...
.mat'], 'final_error_mean', 'final_error_std')
print(1, '-dpdf', ['/Users/Nick/Documents/LaTeX/My-Thesis/Plots/' 'traj' num2str(traj) ...
name2 '_PF'])
697 print(2, '-dpdf', ['/Users/Nick/Documents/LaTeX/My-Thesis/Plots/' 'pos' num2str(traj) ...
name2 '_PF'])
print(3, '-dpdf', ['/Users/Nick/Documents/LaTeX/My-Thesis/Plots/' 'vel' num2str(traj) ...
name2 '_PF'])
print(4, '-dpdf', ['/Users/Nick/Documents/LaTeX/My-Thesis/Plots/' 'rms' num2str(traj) ...
name2 '_PF'])

%close(h)
```

### C.3 Simulation Subprograms

Listing C.4: Constant Velocity Missile

```

function [phi,Qd,G] = constant_vel(dt,q)
%%%%%%%%%%%%%%%%%%%%%%%%%%%%%%%%%%%%%%%%%%%%%%%%%%%%%%%%%%%%%%%%%%%%%%%%
% Title: Constant Velocity Missile Model
4 % Author: Maj Nick Sweeney
% Date: 23 June 2010
%
% Description: This program generates a discrete time dynamics model for a
% constant velocity missile. The states include position and velocity in
9 % cartesian coordinates: x=[x,y,z,vx,vy,vz]'. The model represents the
% missile acceleration in each axis by a white, independent, zero-mean,
% Gaussian noise source.
%
% Inputs:  dt:      Sampling Rate (sec)
14 %        q:      Noise Strength i.e. variance (tuning parameter)
%
% Outputs: phi:    State Transition Matrix
%           Qd:    Discrete Noise Matrix
%           G:     Noise Influence Matrix
19 %
%%%%%%%%%%%%%%%%%%%%%%%%%%%%%%%%%%%%%%%%%%%%%%%%%%%%%%%%%%%%%%%%%%%%%%%%

%% Continous Time Dynamics Model

24 % Dynamics Matrix
F=[0 0 0 1 0 0;
   0 0 0 0 1 0;
   0 0 0 0 0 1;
   0 0 0 0 0 0;
29  0 0 0 0 0 0;
   0 0 0 0 0 0];

% Number of States
NS=length(F);

34 % Deterministic Input Matrix
B=zeros(NS,1);

% Noise Matrix
39 G=[zeros(3,3);
     eye(3,3)];

% Noise Strength Matrix
44 Q=[q 0 0;
     0 q 0;
     0 0 q];

%% Discrete Time Dynamics Model
49 % State Transition Matrix
[phi,Bd] = c2d(F,B,dt);

% Calculate Qd (Van Loan Method)
54 V1=[-F          G*Q*G';
      zeros(NS,NS) F'];

V2=expm(V1*dt);

59 % Discrete Noise Strength Matrix
Qd=V2(NS+1:2*NS,NS+1:2*NS)'*V2(1:NS,NS+1:2*NS);

% Insure Qd is Symmetric
64 Qd=(Qd+Qd')/2;

end

```

## Listing C.5: Constant Acceleration Missile

```

function [phi,Qd,G] = constant_accel(dt,q)
%%%%%%%%%%%%%%%%%%%%%%%%%%%%%%%%%%%%%%%%%%%%%%%%%%%%%%%%%%%%%%%%%%%%%%%%
% Title: Constant Acceleration Missile Model
4 % Author: Maj Nick Sweeney
% Date: 22 June 2010
%
% Description: This program generates a discrete time dynamics model for a
% constant acceleration missile. The states include position, velocity
9 % and acceleration in cartesian coordinates: x=[x,y,z,vx,vy,vz,ax,ay,az]'.
% The model represents the missile jerk (acceleration rate-of-change) in
% each axis by a white, independent, zero-mean, Gaussian noise source.
%
14 % Inputs: dt: Sampling Rate (sec)
% q: Noise Strength i.e. variance (tuning parameter)
%
% Outputs: phi: State Transition Matrix
% Qd: Discrete Noise Matrix
% G: Noise Influence Matrix
19 %
%%%%%%%%%%%%%%%%%%%%%%%%%%%%%%%%%%%%%%%%%%%%%%%%%%%%%%%%%%%%%%%%%%%%%%%%

%% Continous Time Dynamics Model

24 % Dynamics Matrix
F=[0 0 0 1 0 0 0 0 0;
  0 0 0 0 1 0 0 0 0;
  0 0 0 0 0 1 0 0 0;
  0 0 0 0 0 0 1 0 0;
29 0 0 0 0 0 0 0 1 0;
  0 0 0 0 0 0 0 0 1;
  0 0 0 0 0 0 0 0 0;
  0 0 0 0 0 0 0 0 0;
  0 0 0 0 0 0 0 0 0];
34
% Number of States
NS=length(F);

% Deterministic Input Matrix
39 B=zeros(9,1);

% Noise Matrix
G=[zeros(6,3);
  eye(3,3)];
44

% Noise Strength Matrix
Q=[q 0 0;
  0 q 0;
49 0 0 q];

%% Discrete Time Dynamics Model

54 % State Transition Matrix
[phi,Bd] = c2d(F,B,dt);

% Calculate Qd (Van Loan Method)
V1=[-F G*Q*G';
59 zeros(NS,NS) F'];

V2=expm(V1*dt);

% Discrete Noise Strength Matrix
64 Qd=V2(NS+1:2*NS,NS+1:2*NS)'*V2(1:NS,NS+1:2*NS);

% Insure Qd is Symmetric
Qd=(Qd+Qd')/2;

69 end
end

```

## Listing C.6: 3D Coordinated Turn Missile

```

function [phi,Qd,G] = constant_turn(dt,q,x_plus)
%%%%%%%%%%%%%%%%%%%%%%%%%%%%%%%%%%%%%%%%%%%%%%%%%%%%%%%%%%%%%%%%%%%%%%%%
% Title: 3D Coordinated Turn Missile Model
4 % Author: Maj Nick Sweeney
% Date: 27 July 2010
%
% Description: This program generates a discrete time dynamics model for a
% 3D coordinated turn missile. The states include position, velocity
9 % and acceleration in cartesian coordinates: x=[x,y,z,vx,vy,vz,ax,ay,az]'.
% The model represents the missile jerk (acceleration rate-of-change) in
% each axis with the equation a_dot=-omega^2*v+w where omega is the turn
% rate given by omega = |v x a|/v^2 and w is a white, independent,
% zero-mean, Gaussian noise source.
14 %
% Inputs: dt: Sampling Rate (sec)
% q: Noise Strength i.e. variance (tuning parameter)
% x_plus: Current State Vector
% x_plus=[x,y,z,vx,vy,vz,ax,ay,az]
19 %
% Outputs: phi: State Transition Matrix
% Qd: Discrete Noise Matrix
% G: Noise Influence Matrix
%
24 %%%%%%%%%%%%%%%%%%%%%%%%%%%%%%%%%%%%%%%%%%%%%%%%%%%%%%%%%%%%%%%%%%%%%%%%%
%% Continuous Time Dynamics Model

v = x_plus(4:6);
29 a = x_plus(7:9);

% Calculate Turn Rate (w)
w = norm(cross(v,a))/norm(v)^2;

34 % Dynamics Matrix
F=[0 0 0 1 0 0 0 0 0;
  0 0 0 0 1 0 0 0 0;
  0 0 0 0 0 1 0 0 0;
39 0 0 0 0 0 0 1 0 0;
  0 0 0 0 0 0 0 0 1 0;
  0 0 0 0 0 0 0 0 0 1;
  0 0 0 -w^2 0 0 0 0 0 0;
44 0 0 0 0 -w^2 0 0 0 0 0;
  0 0 0 0 0 -w^2 0 0 0 0];

% Number of States
NS=length(F);

49 % Deterministic Input Matrix
B=zeros(9,1);

% Noise Matrix
G=[zeros(6,3);
54 eye(3,3)];

% Noise Strength Matrix
59 Q=[q 0 0;
  0 q 0;
  0 0 q];

%% Discrete Time Dynamics Model
64 % State Transition Matrix
[phi,Bd] = c2d(F,B,dt);

69 % Calculate Qd (Van Loan Method)
[m,n]=size(F);
V1=[-F G*Q*G';
  zeros(m,n) F'];
74 V2=expm(V1*dt);

% Discrete Noise Strength Matrix
Qd=V2(m+1:2*m,n+1:2*n)'*V2(1:m,n+1:2*n);

```

```
79 % Insure Qd is Symmetric
   Qd=(Qd+Qd')/2;
end
```

## Listing C.7: Generate Noise

```

%%%%%%%%%%%%%%%%%%%%%%%%%%%%%%%%%%%%%%%%%%%%%%%%%%%%%%%%%%%%%%%%%%%%%%%%
2 % Title: Generate Noise
  % Author: Maj Nick Sweeney
  % Date: 27 July 2010
  %
  % Description: This program generates noise for Kalman Filter
7 % initialization and 4 sensor measurements for 100 Monte Carlo runs.
  % This data is saved for seeding across 3 Kalman Filters and 3 different
  % dynamics models (9 combinations in total).
  %
  % Inputs: truth_data_xxx.mat: (truth data file includes:)
12 %     t: time vector
  %     dt: time step
  %     x_true(6xt): missile true state vector (position & velocity)
  %     pos_acft(3xt): drone aircraft true position
  %     vel_acft(3xt): drone aircraft true velocity
17 %     roll(1xt): drone aircraft roll in radians
  %     pitch(1xt): drone aircraft pitch in radians
  %     yaw(1xt); drone aircraft yaw in radians (referenced to north)
  %
  % Outputs: DefaultNoiseX.mat (noise file data includes:)
22 %     initial_noise(6xruns): Kalman filter initialization noise
  %     noise(8xtxruns): noise for 4 sensor measurements (range &
  %     range-rate)
  %
  %%%%%%%%%%%%%%%%%%%%%%%%%%%%%%%%%%%%%%%%%%%%%%%%%%%%%%%%%%%%%%%%%%%%%%%%%
27 runs = 100; % Number of Monte Carlo runs

  % Define Scenario Filenames
  profile1 = 'truth_data_below';
32 profile2 = 'truth_data_ts';
  profile3 = 'truth_data_vert';

  % Generate Initial Kalman Filter Noise
  initial_noise = randn(6,runs);
37

  % Scenario 1
  % Load Truth Data
  load(['/Users/Nick/Documents/MATLAB/Thesis/Simulation Software/Truth Data/'...
  profile1 '.mat'])
42 NT = length(x_true);

  % Generate Random Noise for 4 Sensors
  noise = randn(8,NT,runs);

47 % Save Noise
  save(['/Users/Nick/Documents/MATLAB/Thesis/Simulation Software/Generate Measurements/...
  DefaultNoise1'],'noise','initial_noise');

  % Scenario 2
  % Load Truth Data
52 load(['/Users/Nick/Documents/MATLAB/Thesis/Simulation Software/Truth Data/'...
  profile2 '.mat'])
  NT = length(x_true);

  % Generate Random Noise for 4 Sensors
57 noise = randn(8,NT,runs);

  % Save Noise
  save(['/Users/Nick/Documents/MATLAB/Thesis/Simulation Software/Generate Measurements/...
  DefaultNoise2'],'noise','initial_noise');

62 % Scenario 3
  % Load Truth Data
  load(['/Users/Nick/Documents/MATLAB/Thesis/Simulation Software/Truth Data/'...
  profile3 '.mat'])
  NT = length(x_true);
67

  % Generate Random Noise for 4 Sensors
  noise = randn(8,NT,runs);

  % Save Noise
72 save(['/Users/Nick/Documents/MATLAB/Thesis/Simulation Software/Generate Measurements/...
  DefaultNoise3'],'noise','initial_noise');

```

## Listing C.8: Generate Measurements

```

function [z1,z2,z3,z4,z5,z6,z7,detect] = gen_meas_seed(x_true,pos_acft,vel_acft,roll,...
    pitch,yaw,noise)
%%%%%%%%%%%%%%%%%%%%%%%%%%%%%%%%%%%%%%%%%%%%%%%%%%%%%%%%%%%%%%%%%%%%%%%%
3 % Title: Generate Measurements
% Author: Maj Nick Sweeney
% Date: 27 July 2010
%
% Description: This program generates noise corrupted measurements of
8 % missile distance and velocity using seven sensors located on an
% aircraft. It also produces a random number of clutter measurements.
%
% Inputs:   x_true: 6x1 true state vector for missile
%          pos_acft: 3x1 true position vector for drone aircraft
13 %          vel_acft: 3x1 true velocity vector for drone aircraft
%          roll: current roll of aircraft in radians
%          pitch: current pitch of aircraft in radians
%          yaw: current yaw (referenced to north) of acft in radians
%
18 % Outputs: detect: 7x1 vector indicating which sensors observed a target
%          z1-z7: 2xN vector of sensor range and range-rate measurements
%
% Note: Inputs are all in local-level Earth-centered navigation frame
%%%%%%%%%%%%%%%%%%%%%%%%%%%%%%%%%%%%%%%%%%%%%%%%%%%%%%%%%%%%%%%%%%%%%%%%
23 % Define Sensor Locations (meters)
% Sensor 1 - Aircraft Nose (top)
px1 = 8;
py1 = 0;
28 pz1 = -0.5;
% Sensor 2 - Aircraft Nose (bottom)
px2 = 8;
py2 = 0;
pz2 = 0.5;
33 % Sensor 3 - Aircraft Left Wing (top)
px3 = 0;
py3 = -5;
pz3 = 0;
% Sensor 4 - Aircraft Left Wing (bottom)
38 px4 = 0;
py4 = -5;
pz4 = 0.1;
% Sensor 5 - Aircraft Right Wing (top)
43 px5 = 0;
py5 = 5;
pz5 = 0;
% Sensor 6 - Aircraft Right Wing (bottom)
px6 = 0;
py6 = 5;
48 pz6 = 0.1;
% Sensor 7 - Aircraft Tail (omni-directional)
px7 = -8;
py7 = 0;
pz7 = -1;
53 % Convert Missile LL Nav Earth-centered Coordinates to Body Frame
% Nav to Body Rotation
C1 = [cos(yaw) sin(yaw) 0;          % rotation about z-axis
      -sin(yaw) cos(yaw) 0;
      0          0          1];
58
C2 = [cos(pitch) 0 -sin(pitch);    % rotation about y-axis
      0          1  0;
      sin(pitch) 0  cos(pitch)];
63
C3 = [1 0 0;                       % rotation about x-axis
      0 cos(roll) sin(roll);
      0 -sin(roll) cos(roll)];
68 Cnb = C3*C2*C1;
% Missile True Position in Body Frame
pos_true_b = Cnb*(x_true(1:3)-pos_acft);
73 % Missile True Velocity in Body Frame
vel_true_b = Cnb*(x_true(4:6)-vel_acft);
% Define Position and Velocity Variables

```

```

x = pos.true_b(1);
78 y = pos.true_b(2);
z = pos.true_b(3);
vx = vel.true_b(1);
vy = vel.true_b(2);
vz = vel.true_b(3);
83
% Define Sensor Noise
% Sensor Range Accuracy is Better than 2.5% of Range (used 2.5% for 2 sigma)
sigma_dist = 0.025/2;
% Sensor Velocity Accuracy is Better than 0.25 km/hr (used 0.25 m/s for 2 sigma)
88 sigma_vel = 0.25/2;

% Randomly Determine Number of Clutter Measurements on each Sensor
NC = randi(3,4,1); % generates 1-3 ghost targets with equal probability

93 if z>0 % missile is below aircraft

    detect = [0; 1; 0; 1; 0; 1; 1];

    % Sensors 1,3,5 (no measurements)
98    z1 = [];
    z3 = [];
    z5 = [];

    % Sensor 2
    % True Measurements
103    dist = sqrt((x-px2)^2+(y-py2)^2+(z-pz2)^2);
    speed = -(vx*(x-px2)+vy*(y-py2)+vz*(z-pz2))/dist;
    z2(1,1) = dist+sigma_dist*dist*noise(1);
    z2(2,1) = speed+sigma_vel*noise(2);
108    % Clutter Measurements (uniformly distributed)
    z2(1,2:NC(1)+1) = 350*rand(1,NC(1));
    z2(2,2:NC(1)+1) = 650*rand(1,NC(1));

    % Sensor 4
113    % True Measurements
    dist = sqrt((x-px4)^2+(y-py4)^2+(z-pz4)^2);
    speed = -(vx*(x-px4)+vy*(y-py4)+vz*(z-pz4))/dist;
    z4(1,1) = dist+sigma_dist*dist*noise(3);
    z4(2,1) = speed+sigma_vel*noise(4);
118    % Clutter Measurements (uniformly distributed)
    z4(1,2:NC(2)+1) = 350*rand(1,NC(2));
    z4(2,2:NC(2)+1) = 650*rand(1,NC(2));

    % Sensor 6
123    % True Measurements
    dist = sqrt((x-px6)^2+(y-py6)^2+(z-pz6)^2);
    speed = -(vx*(x-px6)+vy*(y-py6)+vz*(z-pz6))/dist;
    z6(1,1) = dist+sigma_dist*dist*noise(5);
    z6(2,1) = speed+sigma_vel*noise(6);
128    % Clutter Measurements (uniformly distributed)
    z6(1,2:NC(3)+1) = 350*rand(1,NC(3));
    z6(2,2:NC(3)+1) = 650*rand(1,NC(3));

    % Sensor 7
133    % True Measurements
    dist = sqrt((x-px7)^2+(y-py7)^2+(z-pz7)^2);
    speed = -(vx*(x-px7)+vy*(y-py7)+vz*(z-pz7))/dist;
    z7(1,1) = dist+sigma_dist*dist*noise(7);
    z7(2,1) = speed+sigma_vel*noise(8);
138    % Clutter Measurements (uniformly distributed)
    z7(1,2:NC(4)+1) = 350*rand(1,NC(4));
    z7(2,2:NC(4)+1) = 650*rand(1,NC(4));

else % missile is above aircraft
143    detect = [1; 0; 1; 0; 1; 0; 1];

    % Sensors 2,4,6 (no measurements)
148    z2 = [];
    z4 = [];
    z6 = [];

    % Sensor 1
    % True Measurements
153    dist = sqrt((x-px1)^2+(y-py1)^2+(z-pz1)^2);
    speed = -(vx*(x-px1)+vy*(y-py1)+vz*(z-pz1))/dist;

```

```

z1(1,1) = dist+sigma_dist*dist*noise(1);
z1(2,1) = speed+sigma_vel*noise(2);
% Clutter Measurements (uniformly distributed)
158 z1(1,2:NC(1)+1) = 350*rand(1,NC(1));
z1(2,2:NC(1)+1) = 650*rand(1,NC(1));

% Sensor 3
% True Measurements
163 dist = sqrt((x-px3)^2+(y-py3)^2+(z-pz3)^2);
speed = -(vx*(x-px3)+vy*(y-py3)+vz*(z-pz3))/dist;
z3(1,1) = dist+sigma_dist*dist*noise(3);
z3(2,1) = speed+sigma_vel*noise(4);
% Clutter Measurements (uniformly distributed)
168 z3(1,2:NC(2)+1) = 350*rand(1,NC(2));
z3(2,2:NC(2)+1) = 650*rand(1,NC(2));

% Sensor 5
% True Measurements
173 dist = sqrt((x-px5)^2+(y-py5)^2+(z-pz5)^2);
speed = -(vx*(x-px5)+vy*(y-py5)+vz*(z-pz5))/dist;
z5(1,1) = dist+sigma_dist*dist*noise(5);
z5(2,1) = speed+sigma_vel*noise(6);
% Clutter Measurements (uniformly distributed)
178 z5(1,2:NC(3)+1) = 350*rand(1,NC(3));
z5(2,2:NC(3)+1) = 650*rand(1,NC(3));

% Sensor 7
% True Measurements
183 dist = sqrt((x-px7)^2+(y-py7)^2+(z-pz7)^2);
speed = -(vx*(x-px7)+vy*(y-py7)+vz*(z-pz7))/dist;
z7(1,1) = dist+sigma_dist*dist*noise(7);
z7(2,1) = speed+sigma_vel*noise(8);
% Clutter Measurements (uniformly distributed)
188 z7(1,2:NC(4)+1) = 350*rand(1,NC(4));
z7(2,2:NC(4)+1) = 650*rand(1,NC(4));

end
193 end

```

## Listing C.9: Coordinate Converter

```

1 function [x_nav] = body_to_nav(pos_acft,roll,pitch,yaw,x_body)
   %%%%%%%%%%%%%%%%%%%%%%%%%%%%%%%%%%%%%%%%%%%%%%%%%%%%%%%%%%%%%%%%%%%%%%%%%
   % Title: Coordinate Frame Converter (Acft Body to LL Nav Frame)
   % Author: Maj Nick Sweeney
   % Date: 6 July 2010
6  %
   % Description: This program takes a position vector in the aircraft body
   % coordinate frame and converts it into a LL Earth-centered navigation frame.
   %
   % Input:      pos_acft: 3x1 acft position vector
11 %            pitch:  Acft pitch from local level (rad)
   %            roll:   Acft roll (rad)
   %            yaw:    Acft heading from north (rad)
   %            x_body: 3x1 position vector in body frame
   %
16 % Output:     x_cart: 3x1 position vector in nav frame
   %
   % Notes: All inputs/outputs in local level Earth-centered navigation frame
   %        All units in metric (meters, meters/sec)
   %%%%%%%%%%%%%%%%%%%%%%%%%%%%%%%%%%%%%%%%%%%%%%%%%%%%%%%%%%%%%%%%%%%%%%%%%
21 % Calculate Direction Cosine Matrix (DCM)
   % Body to Nav Rotation

   C1 = [cos(yaw) sin(yaw) 0;          % rotation about z-axis
26     -sin(yaw) cos(yaw) 0;
         0         0         1];

   C2 = [cos(pitch) 0 -sin(pitch);    % rotation about y-axis
31     0             1  0;
         sin(pitch) 0  cos(pitch)];

   C3 = [1 0          0;              % rotation about x-axis
36     0 cos(roll)   sin(roll);
         0 -sin(roll) cos(roll)];

   Cbn = C1'*C2'*C3';

   % Calculate Missile Position and Velocity (ECF Frame)
41 x_nav = Cbn*x_body+pos_acft;
end

```

## Listing C.10: Nonlinear Transform Function

```

function [ZSigma] = h_transform(XSigma,p_n,v_n)
2 %%%%%%%%%%%%%%%%%%%%%%%%%%%%%%%%%%%%%%%%%%%%%%%%%%%%%%%%%%%%%%%%%%%%%%%%%
% Title: Nonlinear Distance Function
% Author: Maj Nick Sweeney
% Date: 5 August 2010
%
7 % Description: This program takes a set of sigma points from an unscented
% Kalman filter or a set of particles from a particle filter and transforms
% them through a nonlinear observation function.
%
% Inputs:   XSigma:   UKF Sigma Points or PF Particles
12 %        p_n:      Sensor Position in Earth-centered LL Nav Frame
%        v_n:      Sensor Velocity in Earth-centered LL Nav Frame
%
% Outputs:  ZSigma:   Sigma Points or Particles Transformed through
17 %              Distance and Velocity Functions
%
%%%%%%%%%%%%%%%%%%%%%%%%%%%%%%%%%%%%%%%%%%%%%%%%%%%%%%%%%%%%%%%%%%%%%%%%

N = length(XSigma);
p_matrix = p_n*ones(1,N);
22 v_matrix = v_n*ones(1,N);

% Distance Transform
ZSigma(1,:) = sqrt((XSigma(1,)-p_matrix(1,)).^2+(XSigma(2,)-p_matrix(2,)).^2+(...
    XSigma(3,)-p_matrix(3,)).^2);

27 % Velocity Transform
ZSigma(2,:) = -((XSigma(4,)-v_matrix(1,)).*(XSigma(1,)-p_matrix(1,))+XSigma(5,)-...
    v_matrix(2,)).*(XSigma(2,)-p_matrix(2,))+XSigma(6,)-v_matrix(3,)).*(XSigma...
    (3,)-p_matrix(3,))./ZSigma(1,);

end

```

## Bibliography

1. 412th Operational Support Squadron. *Air Force Flight Test Center Instruction 11-1*, January 2004.
2. 412th Range Squadron. *Glite System Version 3*, January 2011.
3. Barton, David A. *Paired Layering: The Argo Way of Simulation Construction*. National Air and Space Intelligence Center, December 2005.
4. Blackman, Samuel. "Multiple Hypothesis Tracking for Multiple Target Tracking". *IEEE Aerospace and Electronic Systems Magazine*, 19:5–18, 2004.
5. Blackman, Samuel and Robert Popoli. *Modern Tracking Systems*. Artech House, 1999.
6. Bradley, Joseph. *Miss Distance Vector Scoring System*. United States Patent Number 5614910, 1997.
7. Brown, Robert G. and Patrick Y. C. Hwang. *Introduction to Random Signals and Applied Kalman Filtering*. John Wiley and Sons, 3rd edition, 1997.
8. DiFilippo, David and Lori Campbell. "Design and Implementation of a Tracking Algorithm for Active Missile Approach Warning Systems". *Canadian Conf. on Electrical and Computer Engineering*, volume 2, 756–759. 1995.
9. Farrell, William. "Interacting multiple model filter for tactical ballistic missile tracking". *IEEE Transactions on Aerospace and Electronic Systems*, volume 44, 418–426. 2008.
10. Folster, Florian, Hermann Rohling, and Urs Lubbert. "An Automotive Radar Network Based on 77GHz FMCW Sensors". *IEEE Int. Radar Conf.* 2005.
11. Incorporated, Hebc. *USAF Series C-12C/D Technical Order 1C-12A-1*, October 2010.
12. Kalandros, Michael K., Lidija Trailovic, Lucy Y. Pao, and Yaakov Bar-Shalom. "Tutorial on Multisensor Management and Fusion Algorithms for Target Tracking". *American Control Conf.* 2004.
13. Kikic, Goran and Branko Kovacevic. "Target Tracking with Passive IR sensors". *Int. Conf. on Telecommunications in Modern Satellite, Cable and Broadcasting Service*, volume 2, 745–748. 2001.
14. Kim, Brian. *Evaluating the Correlation Characteristics of Arbitrary AM and FM Radio Signals for the Purpose of Navigation*. Master's thesis, Air Force Institute of Technology, 2006.
15. Klotz, Michael. *An Automotive Short Range High Resolution Pulse Radar Network*. Ph.D. thesis, Technische Univ. Hamburg-Hamburg, 2002.

16. Mahmood, Sultan, Jane Colee, Jim Luse, Dwight Payne, Joseph Taylor, and Samuel Burkett. "Gulf Range Target Control Using Rajpo GPS Equipment, Test Results and an Alternate Concept". *Position Location and Navigation Symposium*, 306–313. 1992.
17. Maybeck, Peter, James Negro, Salvatore Cusumano, and Manuel De Ponte. "A New Tracker for Air-to-Air Missile Targets". *IEEE Transactions on Automatic Control*, 900–905. 1979.
18. Maybeck, Peter S. *Stochastic Models, Estimation and Control*, volume 1. Navtech Book and Software Store, 1994.
19. Maybeck, Peter S. *Stochastic Models, Estimation and Control*, volume 2. Navtech Book and Software Store, 1994.
20. van der Merwe, Rudolph, Arnaud Doucet, Nando de Freitas, and Eric Wan. *The Unscented Particle Filter*. Technical report, Cambridge University Engineering Department, 2000.
21. Miah, M. Suruz and Wail Gueaieb. "A Stochastic Approach of Mobil Robot Navigation Using Customized RFID Systems". *Int. Conf. on Signals, Circuits and Systems*. 2009.
22. Minor, Roy and David Rowe. "Utilization of GPS/MEMS-IMU for Measurement of Dynamics for Range Testing of Missiles and Rockets". *IEEE Position Location and Navigation Symposium*, 602-607. 1998.
23. Minvielle, Pierre. "Decades of improvements in re-entry ballistic vehicle tracking". *IEEE Aerospace and Electronic Systems Magazine*, 20:1–14, 2005.
24. Misra, Pratap and Per Enge. *Global Positioning System Signals, Measurements and Performance*. Ganga-Jamuna Press, 2nd edition, 2006.
25. Musick, Stanton H. *User's Guide for Profgen, A Trajectory Generator*. Air Force Research Laboratory, December 2004.
26. Pastorelli, A., G. Torricelli, M. Scabia, E. Biagi, and L. Masotti. "A Real-Time 2-D Vector Doppler System for Clinical Experimentation". *IEEE Transactions on Medical Imaging*, 27:1515–1524, 2008.
27. Pastorelli, A., G. Torricelli, M. Scabia, E. Biagi, and L. Masotti. "A Real-Time 2-D Vector Doppler System for Clinical Experimentation". *IEEE Transactions on Medical Imaging*, volume 27, 1515–1524. 2008.
28. Qureshi, W.A., R.A.J. Khan, M. Ahmed, and A. Bashir. "An Efficient Approach for Target Tracking and Error Minimization by Kalman Filtering Technique". *Int. Conf. on Electrical Engineering*, 1–6. 2007.
29. Rohling, Hermann and Marc-Michael Meinecke. "Waveform Design Principles for Automotive Radar Systems". *CIE Int. Radar Conf.* 2001.

30. Rohling, Hermann and Christof Moller. "Radar Waveform for Automotive Radar Systems and Applications". *IEEE Radar Conf.* 2008.
31. Siouris, George, Guanrong Chen, and Jianrong Wang. "Tracking an Incoming Ballistic Missile Using an Extended Interval Kalman Filter". *IEEE Transactions on Aerospace and Electronic Systems.* 1997.
32. Smart Microwave Sensors. *Universal Medium Range Radar Documentation*, May 2010.
33. Stadnik, P.J. "Flight test of an Integrated Digital GPS Translator". *IEEE Position Location and Navigation Symposium*, 75-82. 1996.
34. Steel, Robin and Peter Fish. "Error Propagation Bounds in Dual and Triple Beam Vector Doppler Ultrasound". *IEEE Transactions on Ultrasonics, Ferroelectrics, and Frequency Control*, volume 49, 1222-1230. 2002.
35. Steel, Robin and Peter J. Fish. "Error Propagation Bounds in Dual and Triple Beam Vector Doppler Ultrasound". *IEEE Transactions on Ultrasonics*, 49:1222-1230, 2002.
36. Sweeney, Nicholas and Kenneth Fisher. "Air-to-Air Missile Vector Scoring". *IEEE Int. Conf. on Control Applications*, 579-586. 2011.
37. Tafti, Abdolreza and Nasser Sadati. "A Hybrid Fuzzy Dynamic Model for Maneuvering Targets". *IEEE Aerospace Conf.*, 1-6. 2009.
38. Thompson, T. "Demonstration of a Precision Missile Intercept Measurement Technique". *John Hopkins APL Technical Digest*, 19:513-23, 1998.
39. Titterton, David H. and John L. Weston. *Strapdown Inertial Navigation Technology*. The Institution of Electrical Engineers, 2nd edition, 2004.
40. Tu, Po-Jen and Jean-Fu Kiang. "Estimation on Location, Velocity, and Acceleration with High Precision for Collision Avoidance". *IEEE Transactions on Intelligent Transportation Systems*, volume 2, 374-379. 2010.
41. Veth, Michael. *Fusion of Imaging and Inertial Sensors for Navigation*. Ph.D. thesis, Air Force Institute of Technology, September 2006.
42. Xu, Jian-Zhong, Zu-Lin Wang, Yi-Huan Zhao, and Xu-Jing Guo. "A Distance Estimation Algorithm Based on Infrared Imaging Guided". *Int. Conf. on Machine Learning and Cybernetics*, volume 4, 2343-2346. 2009.

# REPORT DOCUMENTATION PAGE

Form Approved  
OMB No. 0704-0188

The public reporting burden for this collection of information is estimated to average 1 hour per response, including the time for reviewing instructions, searching existing data sources, gathering and maintaining the data needed, and completing and reviewing the collection of information. Send comments regarding this burden estimate or any other aspect of this collection of information, including suggestions for reducing this burden to Department of Defense, Washington Headquarters Services, Directorate for Information Operations and Reports (0704-0188), 1215 Jefferson Davis Highway, Suite 1204, Arlington, VA 22202-4302. Respondents should be aware that notwithstanding any other provision of law, no person shall be subject to any penalty for failing to comply with a collection of information if it does not display a currently valid OMB control number. PLEASE DO NOT RETURN YOUR FORM TO THE ABOVE ADDRESS.

<b>1. REPORT DATE (DD-MM-YYYY)</b> 22-03-2012		<b>2. REPORT TYPE</b> Master's Thesis		<b>3. DATES COVERED (From — To)</b> Sept 2009 — Mar 2012	
<b>4. TITLE AND SUBTITLE</b>  Air-to-Air Missile Vector Scoring				<b>5a. CONTRACT NUMBER</b>	
				<b>5b. GRANT NUMBER</b>	
				<b>5c. PROGRAM ELEMENT NUMBER</b>	
				<b>5d. PROJECT NUMBER</b>	
				<b>5e. TASK NUMBER</b>	
				<b>5f. WORK UNIT NUMBER</b>	
<b>6. AUTHOR(S)</b>  Nicholas Sweeney, Maj, USAF				<b>8. PERFORMING ORGANIZATION REPORT NUMBER</b>  AFIT/GE/ENG/12-38	
<b>7. PERFORMING ORGANIZATION NAME(S) AND ADDRESS(ES)</b> Air Force Institute of Technology Graduate School of Engineering and Management (AFIT/EN) 2950 Hobson Way WPAFB OH 45433-7765				<b>10. SPONSOR/MONITOR'S ACRONYM(S)</b>  83 FWS	
<b>9. SPONSORING / MONITORING AGENCY NAME(S) AND ADDRESS(ES)</b> 83rd Fighter Weapons Squadron Lt Col Kevin Calhoun 1287 Florida Ave Tyndall Air Force Base, FL 32403 (850) 283-0990; kevin.calhoun@tyndall.af.mil				<b>11. SPONSOR/MONITOR'S REPORT NUMBER(S)</b>	
<b>12. DISTRIBUTION / AVAILABILITY STATEMENT</b>  This material is declared a work of the U.S. Government and is not subject to copyright protection in the United States. Distribution A. Approved for Public Release; Distribution Unlimited					
<b>13. SUPPLEMENTARY NOTES</b>					
<b>14. ABSTRACT</b>  An air-to-air missile vector scoring system is proposed for test and evaluation applications. Three different linear missile dynamics models are considered: a six-state constant velocity model and nine-state constant acceleration and three-dimensional coordinated turn models. Frequency modulated continuous wave radar sensors, carefully located to provide spherical coverage around the target, provide updates of missile kinematic information relative to a drone aircraft. Data from the radar sensors is fused with predictions from one of the three missile models using either an extended Kalman filter, an unscented Kalman filter or a particle filter algorithm. The performance of all nine model/filter combinations are evaluated through high-fidelity, six-degree of freedom simulations yielding sub-meter end-game accuracy in a variety of scenarios. Simulations demonstrate the superior performance of the unscented Kalman filter incorporating the continuous velocity dynamics model. The scoring system is experimentally demonstrated through flight testing using commercial off the shelf radar sensors with a Beechcraft C-12 as a surrogate missile.					
<b>15. SUBJECT TERMS</b>  missile scoring, missile state estimation, missile test and evaluation, missile model					
<b>16. SECURITY CLASSIFICATION OF:</b>			<b>17. LIMITATION OF ABSTRACT</b>	<b>18. NUMBER OF PAGES</b>	<b>19a. NAME OF RESPONSIBLE PERSON</b>
<b>a. REPORT</b>	<b>b. ABSTRACT</b>	<b>c. THIS PAGE</b>			Kenneth A. Fisher, Maj, USAF
U	U	U	UU	248	<b>19b. TELEPHONE NUMBER (include area code)</b> (937) 255-3636, ext 4677; kenneth.fisher@afit.edu